JPL SP 43-21

PROCEEDINGS

SYMPOSIUM ON CHARGE-COUPLED DEVICE TECHNOLOGY FOR SCIENTIFIC IMAGING APPLICATIONS

March 6-7, 1975

Jet Propulsion Laboratory
California Institute of Technology
Pasadena, California 91103

June 15, 1975

Sponsored by
NASA Office of Aeronautics and Space Technology and Jet Propulsion Laboratory

JPL SP 43-21

PROCEEDINGS

SYMPOSIUM ON CHARGE-COUPLED DEVICE TECHNOLOGY FOR SCIENTIFIC IMAGING APPLICATIONS

March 6-7, 1975

Jet Propulsion Laboratory
California Institute of Technology
Pasadena, California 91103

June 15, 1975

Sponsored by
NASA Office of Aeronautics and Space Technology and Jet Propulsion Laboratory

SYMPOSIUM ORGANIZATION

CHAIRMAN

G. M. Smith	Jet Propulsion Laboratory

ORGANIZATION COMMITTEE

B. Rubin Co-Chairman	NASA Office of Aeronautics and Space Technology
M. I. Smokler Co-Chairman	Jet Propulsion Laboratory
H. D. Hendricks	Langley Research Center
M. K. Hendrix	Johnson Space Center
C. T. Huggins	Marshall Space Flight Center
J. T. Williams	Goddard Space Flight Center

COORDINATOR

M. I. Smokler	Jet Propulsion Laboratory

PREFACE

The past year has seen an increase in the pace of CCD imager development paralleled by an increase in application ideas and plans. With events in both areas moving rapidly, it appeared that a forum of device developers and device users would provide coordination which could lead to early fruition of both efforts. While the potential for CCD imaging in commercial and military applications is generally understood, it was believed that the type and number of potential scientific applications were not fully appreciated. As with many technological breakthroughs, new applications will be found and the scope of scientific applications will undoubtedly increase. These considerations were the genesis of this Symposium and of its joint sponsorship by NASA and JPL.

The objectives, scope, and technical organization of the Symposium are described in the introductory address given by Gerald M. Smith, the Symposium Chairman.

We wish to acknowledge the participation of the panel on "User Requirements for CCDs in Scientific Imaging Applications," consisting of W. A. Baum (Chairman) of Lowell Observatory, B. J. Oke of the California Institute of Technology, S. Sobieski of Goddard Space Flight Center, B. A. Smith of the University of Arizona, and V. T. Norwood of Hughes Aircraft Company.

Bernard Rubin
NASA Office of Aeronautics
and Space Technology

Melvin I. Smokler
Jet Propulsion Laboratory

CONTENTS

INTRODUCTION

G. M. Smith
Jet Propulsion Laboratory
Pasadena, California

The objectives of this Symposium, as stated in the program, are to stimulate the development of CCDs and related devices by the exchange of information on recent advances in CCD technology, and by the identification of applications requirements. The timing of the Symposium has been based upon the emergence of CCDs from the research stage, with devices which have practical scientific applications.

The use of electronic imaging sensors in scientific applications is a relatively new field. Most of the work has been done in the past 10 to 15 years as part of the space program. During this time, we have learned a great deal about how to calibrate and process imaging data, and the number of applications has multiplied. But the electronic sensor technology in use today is not very much different than it was 10 years ago. The recent development of large silicon sensors, and particularly CCDs, may change this situation in the near future.

Scientific imaging is distinct from nonscientific applications in that scientific work requires quantitative information from an image. In the simplest form, this involves being able to accurately measure the amplitude and position of each point in an image. Implicit in this measurement is the need to account for the distortion introduced by the measuring system, and especially the sensor. These simply stated needs translate into very specific requirements for each different application. The applications sessions are intended to discuss several of these applications and then, through a panel discussion, help formulate sensor requirements for various applications areas.

There are a few sensor characteristics which are fundamental to a large variety of scientific applications. These common characteristics include

(1) High sensitivity.

(2) Broad spectral response.

(3) Stable transfer function.

(4) Large format.

High sensitivity is desirable to achieve the most efficient detection of incident photons and minimize the degradation caused by system noise. This is particularly important when the incident energy is low, but even with bright objects, we usually find ways of reducing the useful light with narrowband filters or short exposure times, and in many applications, it is necessary to detect very low-contrast features.

Broad spectral response is needed in a large variety of applications. In most situations, sensor selection involves a tradeoff to achieve high quantum efficiency in one spectral region at the expense of another portion of the spectrum. An imaging sensor with a high quantum efficiency from the near-UV to the near-IR will be a major addition to the capabilities of available imaging sensors.

Stable transfer functions are of critical importance in making quantitative measurements. Most electronic imaging systems in current use do not have a stable, well-behaved relationship between input and output, and measurement accuracies of a few percent are very difficult to achieve. Silicon target vidicons have yielded the best results, but a considerable amount of computer processing is required to compensate for sensor distortions. Routine measurement accuracies of 1% or better will ultimately be needed.

In virtually all applications, it is desirable to have a format with a large number of picture elements. This has been a major limitation in electronic sensors and has been largely responsible for the continuing attractiveness of film in many applications. Sensors with formats of 10^6 to 10^7 elements will be needed eventually, but devices with 10^5 to 10^6 elements will be useful in many applications.

The development of electronic sensors for scientific imaging historically has involved a long, and mostly unsuccessful, struggle to improve sensors in these four characteristics. The development of CCDs should result in major improvements in three of the four areas. Only in format size will the CCD

suffer in comparison to present sensors. The solution to this limitation may come in time from improved processing technology or from mosaics of small format devices. In the meantime, devices of usable format size for many applications now appear practical.

There are many other factors, in addition to the four characteristics already discussed, which are very important in various applications. They include cost, useful lifetime, power, weight, size, and environmental sensitivity. The CCD offers dramatic improvement in some of these factors, while others, such as cost and radiation sensitivity, remain question marks.

The development of CCDs over the past 3 years has been very active. The devices have progressed from very simple demonstration models to the relatively complicated models which are emerging. In the course of this development, the early, optimistic estimates of device simplicity and performance have been moderated substantially by the facts of life learned in making and testing practical sensors. Many of the problems inherent in new technology are now being identified, and solutions are being worked out.

The session on device technology will cover the progress in CCD development and evaluation and bring potential users up to date on current device capabilities. While most of the development work in CCD technology has emphasized direct photon imaging, some very important work has been directed toward an electron bombardment mode for very low light applications; this work will also be reviewed. In spite of the problems and limitations which are now apparent, it is clear that CCD technology will play a major role in future scientific imaging. In some ways, CCDs available today surpass the best available electronic imaging devices, and future work should widen the gap.

In organizing and sponsoring this Symposium, JPL and NASA are providing a vehicle for communication between potential scientific users and device manufacturers which we hope will promote the earliest and most effective application of this new capability to scientific imaging.

AN X-RAY SHADOWGRAPH TO LOCATE TRANSIENT HIGH-ENERGY CELESTIAL SOURCES

G. J. Fishman and T. A. Parnell
Space Sciences Laboratory
NASA/Marshall Space Flight Center
Huntsville, Alabama

T. A. Rygg* and J. C. Gregory
University of Alabama
Huntsville, Alabama

A new technique has been developed to locate strong, transient x-ray sources such as the recently discovered gamma-ray bursts. The instrument, termed a "shadowgraph," locates sources by detecting the x-ray shadow cast by a large occulting mask pattern on an imaging detector. Angular resolutions of from 2 to 10 arc minutes are obtainable while essentially full sky coverage is maintained. The optimum energy range of operation is between 20 keV and 100 keV.

The high-efficiency x-ray imaging detectors, which make it possible to locate bursts with intensities down to ~10 photons/cm^2-sec, are capable of detecting single 20-keV photons with a spatial resolution of ~0.2 mm. The detectors consist of an x-ray to optical conversion phosphor, a multistage image intensifier, and a CCD image readout.

I. INTRODUCTION

The relatively new field of x-ray astronomy has led to the discovery of entirely new classes of celestial objects and has provided us with new insights into the final evolutionary stages of stars and the origin of high-energy processes in the galaxy.

*Dr. Rygg died on March 14, 1975.

Among the more interesting phenomena are the recently discovered gamma-ray bursts (Ref. 1). These infrequent, transient events produce intense fluxes of x-rays and gamma-rays relative to the background. Position data is poor, although the sources appear to have an isotropic distribution. Although many theories for the bursts have been proposed (Ref. 2), it appears that a satisfactory explanation may have to await accurate measurement of their positions so that they may be identified with a particular type of optical or radio object. Such a measurement presents a unique experimental problem. Because of their apparently random occurrence in space and their brief duration — as short as 0.1 sec — it is necessary to use a wide-field detector. Since observable bursts occur infrequently and apparently randomly in time, the detector must be in continuous operation above the atmosphere for long periods.

The instrument we have developed for locating discrete, brief bursts of x-rays and gamma-rays is termed a "shadowgraph" and combines the features of wide field, high efficiency, and good angular resolution. Image readout by a CCD confers an advantageous combination of simplicity, integrating capability, and energy discrimination of the x-ray spatial detector compared with other position-sensitive x-ray detectors. The x-ray system has thus far been tested only by photographic means rather than by CCD readout. Since CCD technology is expected to improve greatly before the first operational shadowgraph, this paper will stress the experimental techniques and capabilities of the shadowgraph and the specifications of CCDs optimized for this application.

II. PRINCIPLE OF OPERATION

The shadowgraph is composed of a large dome-like occulting shadow mask and a number of x-ray imaging detectors located inside to detect an x-ray shadow cast through any part of the shadow mask (see Figure 1). A typical mask is made from photoetched 0.5-mm-thick tungsten plate. This thickness would provide adequate opacity for x-rays with energies up to 150 keV. The solid angle subtended by the mask at the detectors determines the field of view of the instrument, which could, conceivably, cover 4π steradians.

Since it is assumed that the brief bursts arrive from a point source at a great distance (Ref. 1), the parallel incident x-ray beam would produce a sharp shadow of the coded mask on the face of an x-ray image detector. The x-ray

shadow projection angle is uniquely determined simply by finding the area on the mask which produced the shadow. The source direction is then derived from this shadow projection angle and the orientation of the spacecraft.

The angular resolution of the shadowgraph is $\Delta\theta \approx \Delta x/d$, where Δx is the spatial uncertainty of the image position and d is the distance between the image plane and the appropriate shadow mask section. There are several components which enter into Δx; among the most important are: (1) x-ray source photon statistics and background events, (2) flexing and thermal distortion of the shadow mask and image detector image system, and (3) uncertainty in the location of individual x-ray photon events. It is estimated that for a weak burst, with ~400 x-ray photons over a 100-cm^2 detector area, the value for Δx will be of the order ~1 mm. For a small Explorer-type satellite, an average value for d is ~70 cm, yielding a location uncertainty of $\Delta\theta \approx 1$ mm/70 cm = 5 arc minutes. Spacecraft motion during observation, and attitude uncertainty will increase the location error somewhat.

The uncertainty due to photon statistics and background events, Δx_1, has been examined in detail, both analytically and through computer simulations. Consider N_s photons incident on a shadow mask with a transmission factor r (ratio of open area to total area) and a characteristic pattern cell dimension ℓ. Also assume that there are N_b background events randomly spaced over the image detector area and that it is required to locate the pattern with a statistical uncertainty of n_σ standard deviations. Then

$$\Delta x_1 \approx \frac{n_\sigma^2 \ell (N_s + N_b)}{r N_s^2} \qquad (1)$$

Figure 2 shows the results of a simulation of x-ray images from various fluxes of signal photons from a point source incident on the shadow mask pattern, with r = 0.44. A portion of the pattern is shown at the top of the figure. The amount of random background or noise photons was also varied, being equal to 1/2, 1/5, or 1/10 of the number of signal photons, as indicated in the figure. A computer program was used to find the optimum fit between the total mask pattern and the discrete photon image pattern by shifting the image in small steps over the larger mask pattern and finding the minimum photon coverage.

Assuming that the image area is 10 cm × 10 cm, the optimized fit from the computer routine for the case of 200 signal photons and 100 noise photons was less than 0.6 mm, while the value obtained from Equation (1) is ~0.5 mm for a 2 σ error. Note that at this low signal level, the mask pattern is not visually recognizable. This demonstrates that relatively little information is required to ascertain the location of the source by this technique, since the image detected is a portion of a known pattern. Naturally, it would be impossible to reconstruct a meaningful image from only 200 photon locations.

Since the locating accuracy for weak x-ray or gamma-ray bursts is dependent mainly upon photon statistics, it is desirable to obtain the highest ratio of signal photons to background photons in a particular energy range. Among the considerations that determine the optimum energy range are: (1) the spectrum expected from the source object, (2) the spectra of various components of the background such as the diffuse x-ray background and secondary x-ray and gamma-ray fluxes produced by charged-particle interactions; and (3) the efficiency of the shadowgraph mask and image detector combination. A rather detailed analysis of the combined spectral effects yields an optimum x-ray energy range of ~20 keV to ~100 keV in which to make observations of gamma-ray bursts.

III. IMAGING DETECTORS

The imaging detector is the most critical component for the shadowgraph and other x-ray multiplex methods such as the scatter-hole or Dicke camera (Refs. 3, 4). For this application, the essential characteristics are: (1) good spatial resolution irrespective of angle of incidence of the x-ray photon, (2) high detection efficiency over the energy range of interest, (3) large sensitive area, and (4) capability for observing a large range of burst intensities.

After studying several alternatives, the phosphor-image intensifier system (Figure 3) was chosen as the most suitable wide-field image detector for the energy region up to 100 keV. In this system, the x-ray photon is first converted into optical photons in a relatively thick (0.5 to 1.0 mm) phosphor. Present phosphors under study include rare-earth phosphors and cesium iodide. The energy conversion efficiency of these phosphors is in the range from 5% to 15%, so that a 20-keV photon will result in ~10^3 photons in the range 4000 Å to 5000 Å. The optical signal having a spot size of ~1 mm^2 is intensified and

demagnified by a multistage, electrostatically focused image intensifier. The image is then transferred by a lens onto a CCD for image readout.

Overall image reduction is from 80 mm X 80 mm at the x-ray phosphor to about 6 mm X 6 mm at the CCD. Linear spatial resolution at the x-ray phosphor of 0.5 mm thus requires a 160 X 160 element CCD array of area about 6 mm square. Grey level encoding of 4 bits would be sufficient to provide coarse energy resolution for each detected x-ray. The energy information would be used in the data analysis to eliminate sources of background such as dark current, high-energy gamma-ray Compton events, and charged particles. It is anticipated that the x-ray image integration time will be of the order of 1 sec, which may require operating the CCDs at temperatures below 0° C. Such temperatures would also reduce the dark current of the image intensifiers. The total image data expected from a single x-ray burst is several megabits. Present CCD technology requires that this data be stored in a nonvolatile, onboard digital storage device (possibly a CCD memory) for later transmission to a ground station.

The pictures in Figure 4 are output images of an experimental setup in our laboratory to study properties of intensifiers and x-ray converter phosphors. Two three-stage image intensifiers (Varo models 8585 and 8605) were coupled by an f/1.4 lens. A 0.5-mm-thick rare-earth phosphor was placed directly on the fiber optic input of the first intensifier (25-mm diameter), and the output of the second intensifier was photographed on Tri-X film with a 35-mm single-lens reflex camera. Figure 4 shows three photographs obtained with this system: two with weak radioactive sources present and one with background only. Individual x-ray photons can easily be observed from Co^{57} (122 keV) and Am^{241} (60 keV). All three photographs were obtained under the same conditions, outlined in Figure 4. The centroid of the brighter x-ray images can be determined to within ~0.2 mm.

It appears that the imaging requirements for an x-ray shadowgraph in terms of array size, resolution, and dynamic range can be met by current CCD technology. For a space-borne experiment, a CCD image readout offers great advantages of simplicity, small size, low power, low weight, and image positional stability compared to any conventional TV tubes. Areas of potential concern include long-term gain stability, image degradation during integration, and reliability.

REFERENCES

1. Klebesadel, R. W.; Strong, I. B.; and Olson, R. A.: Astrophys. J., Vol. 182, p. L85 (1973).

2. Ruderman, M. A.: Proceedings Seventh Texas Symposium on Relativistic Astrophysics, New York Academy of Sciences (to be published, 1975).

3. Dicke, R. H.: Astrophys. J., Vol. 153, p. L101 (1968).

4. Ables, I. G.: Proc. Astron. Soc. Australia, #4, p. 1 (1968).

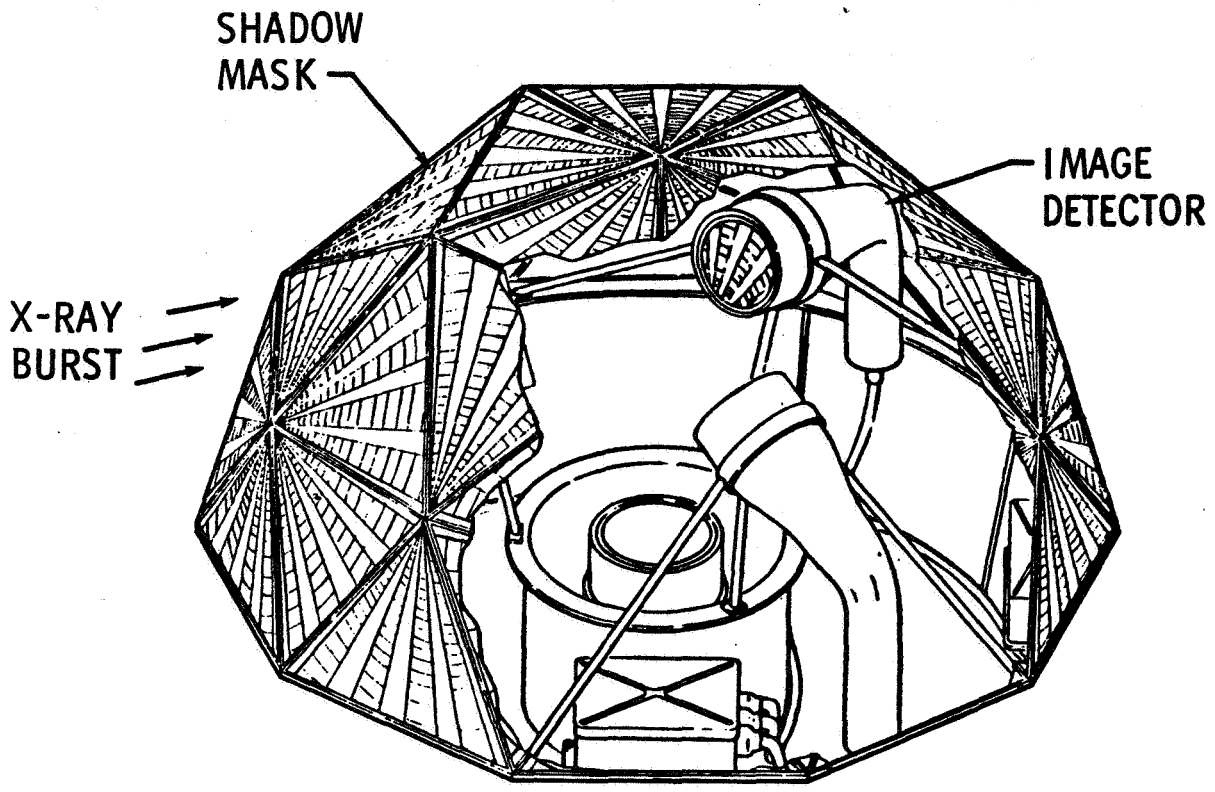

Figure 1. Shadowgraph experiment components (As shown, an x-ray burst incident from the left would cast an x-ray shadow on the forward-facing image detector.)

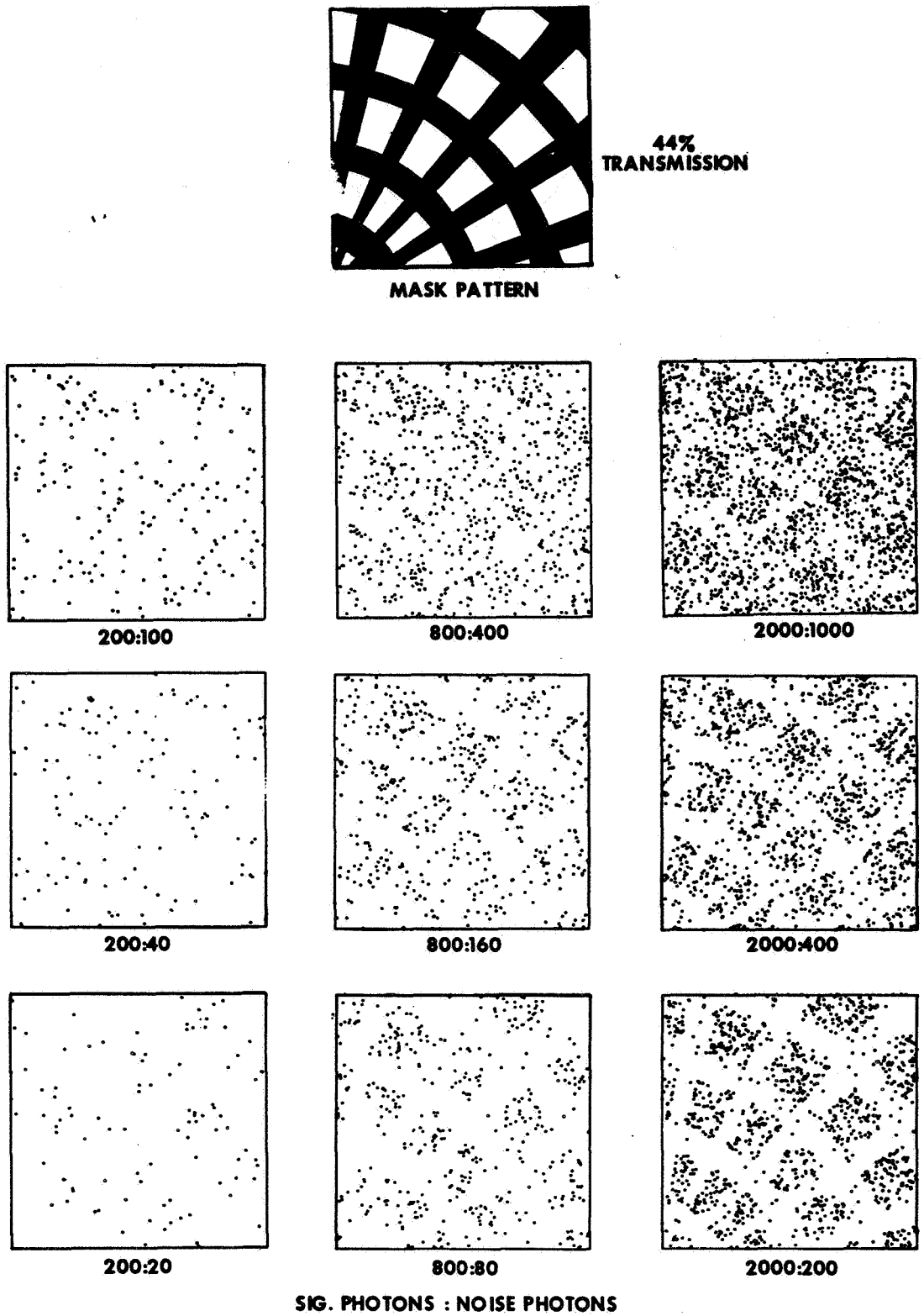

Figure 2. Simulated shadowgraph images showing effects of signal and noise photon statistics (The incident source photons are transmitted through the open areas of the mask pattern at the top, which represents a portion of the large shadow mask.)

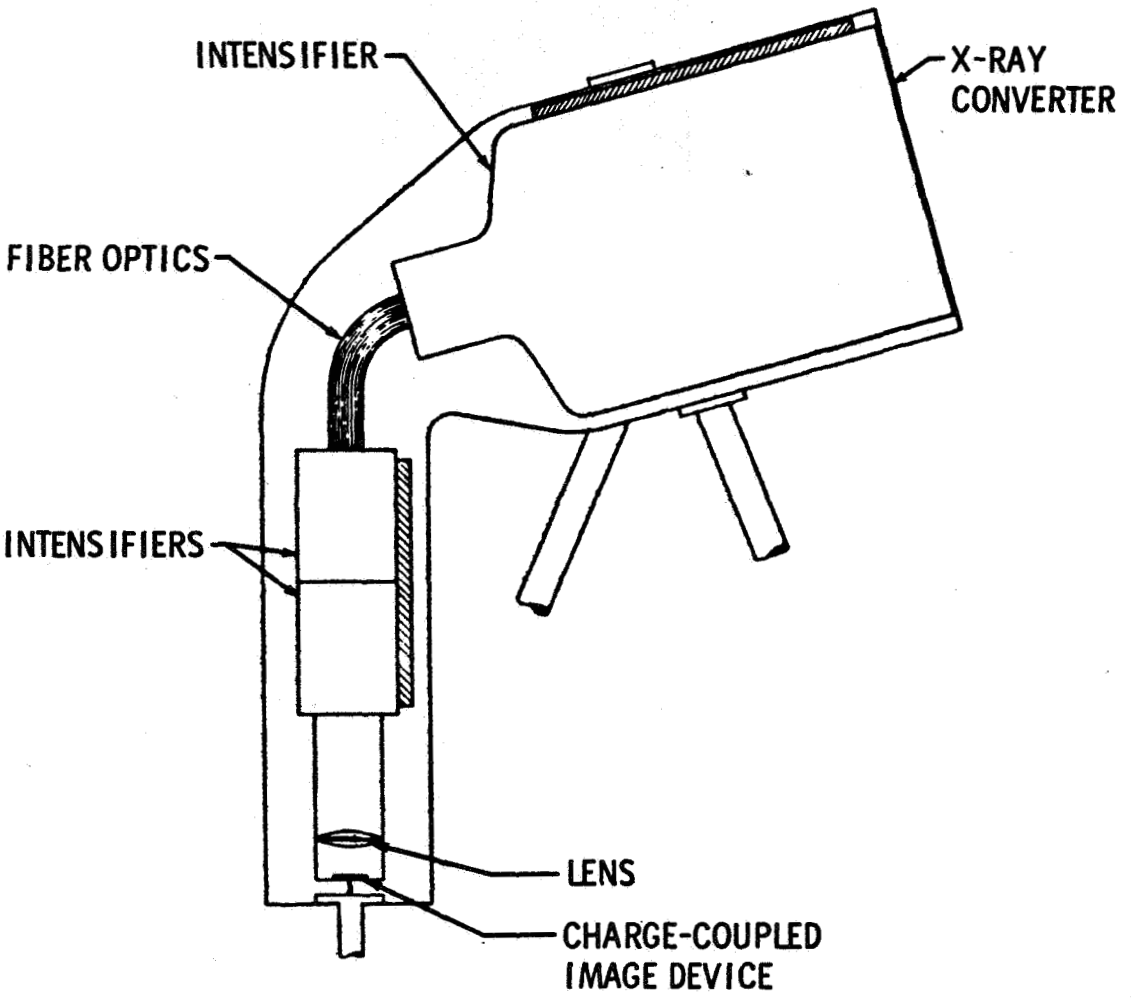

Figure 3. X-ray image detector schematic (The first-stage intensifier is an 80-mm/20-mm zoom-type intensifier. Additional stages are required to produce a suitable intensity for the CCD. It may be possible to improve the overall efficiency by coupling the CCD with fiber optics or even by locating the CCD internally in the last intensifier stage.)

X-RAY TEST PICTURES

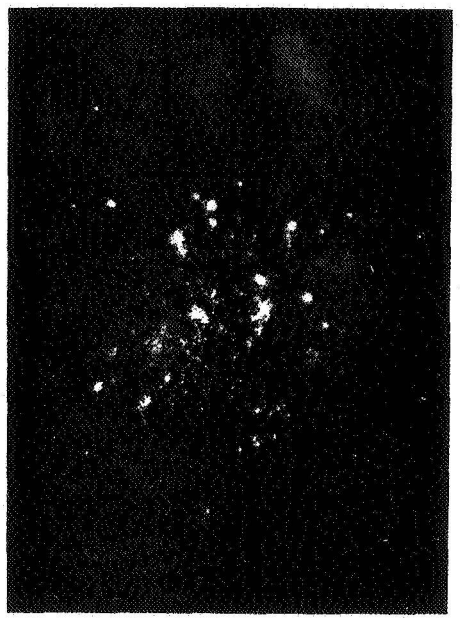

EXPOSURE: 0.125 sec
PHOSPHOR: RARE EARTH
THICKNESS: 0.5 mm
TEMP.: 20^0 C
GAIN: $\sim 10^6$
SCALE: ⊢ 1 mm

Am^{241} 60 KeV

Co^{57} 122 KeV

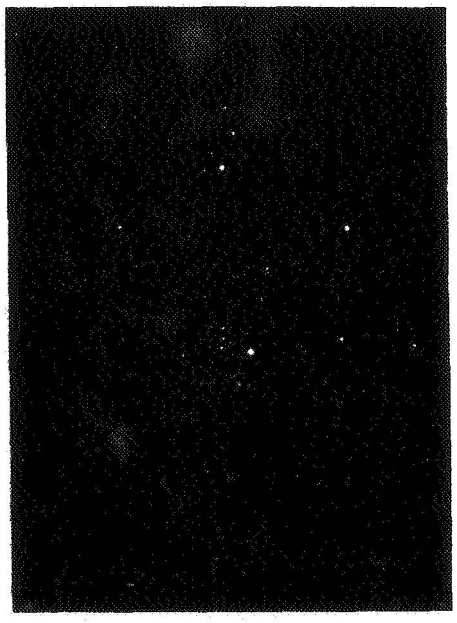

BACKGROUND

Figure 4. X-ray test photographs of a rare-earth phosphor/multi-stage intensifier system (Single x-ray photons at 60 keV and 122 keV are visible. Intensifier input diameter is 25 mm. X-ray spot size is ~0.5 mm. The centroid of each spot can be determined to less than 0.2 mm.)

A CCD IMAGE TRANSDUCER AND PROCESSOR SUITABLE FOR SPACE FLIGHT

Donald J. Michels

E. O. Hulburt Center for Space Research
Naval Research Laboratory
Washington, D. C.

A satellite-borne extreme-ultraviolet solar telescope under development at the Naval Research Laboratory makes use of CCD area arrays for both image readout and on-board data processing. The instrument is designed to view the inner solar corona in the wavelength band 170 - 630 Å, and the output video stream may be selected by ground command to present the coronal scene, or the time-rate-of-change of the scene.

Details of the CCD application to on-board image processing will be described, and a discussion of the processor's potential for telemetry bandwidth compression is included. Optical coupling methods, data storage requirements, spatial and temporal resolution, and nonsymmetry of resolution (pitch) in the CCD will be discussed. Laboratory simulations of system performance using solar data from previous space flights will be presented.

I. REQUIREMENTS OF SPACE IMAGING SYSTEMS

Increasing availability of stabilized, accurately pointed space platforms has accelerated development of sophisticated imaging systems designed to be used in a space environment and operated in automatic or remotely controlled mode. Requirements for space telescopes differ, in some respects, from those for ground-based imagers; therefore it is appropriate to comment briefly on system requirements before describing the telescope under development at NRL.

The components of a generalized space imaging system may be divided into three functional groups, viz.: the optical, the detection, and the processing subsystems. In Figure 1, the optical subsystem includes the first three blocks of the functional block diagram. Information, in the form of photons from a distant source, enters the system at the extreme left. The optics perform two vital functions, namely, collection of the light and formation of a real image at the focal plane. Diffraction limited optics are not yet common; thus the necessity for collecting suitable numbers of photons implies that collection efficiency is frequently the driving parameter in sizing the optics.

Because natural media do not generally intervene to limit the spectral range of radiation arriving at a space platform, and because radiations in widely different parts of the spectrum usually arise from distinct physical mechanisms, some method of passband limitation is almost always employed. This is indicated by the second block in Figure 1b. In some cases (third block), there may follow a stage of image intensification and/or conversion to visible wavelengths. It is possible to introduce considerable flexibility at this stage: for example, an amplified image containing a very broad range of irradiance values may be compressed by nonlinearity in the intensifier gain or the output phosphor. If this can be accomplished without blooming or other deleterious consequences, the effect may be to reduce demands on the detector.

In the detector subsystem, information is converted from the domain of quantum mechanical photons, or electron clouds, to macroscopic, or analog, electrical signals. Additionally, because the bandwidths required for parallel transmission of two-dimensional arrays are prohibitive, another necessary function of the detector subsystem is to serialize the picture

information. This reduces the data flow to a single sequential stream requiring only one telemetry channel. Both internal (self-) scanning and external (mechanical) rasters are widely used for this purpose.

In the processing subsystem are included the functions of amplification, on-board image processing (if any), digitization, formatting, buffer storage, and readout into the spacecraft telemetry system. The spacecraft system accepts data at times determined by appropriate readout gates, which it supplies, and also provides power, stabilization, timing, and other necessaries to the experiment.

The requirements for a space imaging system include sensitivities down to a few photons per picture element (pixel) per second, and dynamic range ≥ 100. Spatial resolution in excess of 10^5 pixels is frequently desired, though imagers of lower resolution also find application. In addition to total number of pixels, resolution element density is also of importance, because restrictions on telescope dimensions often limit the magnification possible. Other requirements include stability of gain and sensitivity, and the ability to put out data at a rate commensurate with spacecraft telemetry allocations. For video systems in small scientific satellites, this will almost always imply a capacity for image storage or slow-scan operation.

II. NRL EXTREME-ULTRAVIOLET VIDEO TELESCOPE

One configuration of the proposed NRL system is shown in Figure 1c. Designed to study the sun in the wavelength range 170 - 630 Å, this version is equipped with a Type II Wolter reflective lens. The first flight system, however, will use a normal incidence parabolic mirror in the off-axis Herschelian arrangement. The filter wheel carries six transmission filters consisting of unsupported thin films of evaporated metals. Passband is determined by the telescope reflectance folded into the transmittance curve for the filter selected.

Other than the optics and filter wheel, the remainder of the first, or optical section is largely empty; very careful attention must be paid to the nature and cleanliness of materials and surface finishes used within this compartment because of the extreme sensitivity of ultraviolet optical components to surface contaminants condensing from outgassed vapors. A second compartment, isolated from the first and third, contains the cooled

CCD detector. The third compartment contains that portion of the electronics that must be kept physically close to the detector. Remaining electronics may be housed in a separable electronics package.

III. DETECTION SUBSYSTEM

An enlarged view of the detector section is seen in Figure 2. At the focal plane of the telescope is placed a microchannel plate image intensifier (MCP) (Refs. 1 - 4). Output from this device is through a fiber-optic plate, sealed into the isolation bulkhead. A phosphor provides conversion to visible wavelengths after multiplication of the electron image by 10^3 or more in the MCP. The CCD is mounted on a substrate cooled by a simple heat radiator (Refs. 5 and 6). A second CCD, labeled B, is mounted on the same cooled pad. Chip B, which may actually be two or several discrete chips, is shielded from any light input. It is used for buffer storage and image processing. Optical coupling of the image from the MCP to CCD-A is achieved through a tapered fiber-optic, which will be discussed later.

IV. ON-BOARD IMAGE PROCESSING

Figure 3 presents, in conceptual form, the CCD readout and processing technique. The amplified, visible image (of the sun, in this application) is relayed to CCD-A for detection. The output register of chip A feeds the video data stream into an analog switching network that can route the signals into any of three paths. In the simplest case (path 1), the video image, after a suitable integration period, is clocked out, digitized, and sent through the spacecraft telemetry system to ground stations for analysis.

In a second mode, the two CCDs are used cooperatively as an optical comparator. At time t, chip A receives and records an optical image. On completion of image integration, the video signal is clocked out and routed (path 2) to the input register of chip B. After insertion, the image is stored in chip B, while a new image is recorded on chip A at time $t + \Delta t$. Then, using common clock pulse signals, the image of the scene at time t is gated out of chip B (path 4) simultaneously with readout of the scene at $t + \Delta t$ from chip A (path 3). The two signals are combined in a difference amplifier, whose output is an analog video image having the same dimensionality as

either of the two input images. The intensity values in this difference image will be zero for every picture point, unless the brightness of the scene at a given point has changed during the time Δt.

As a further refinement, when the two images are being simultaneously clocked into the difference amplifier, the signal from chip A (the scene at $t + \Delta t$) may be divided (path 2 and path 3) and used to replace the original image now being moved out of chip B. Continuous operation for a succession of images processed in this manner provides at the output of the comparator an analog video signal that displays the time-rate-of-change of brightness for each element in the scene viewed, with time resolution Δt, while retaining the full spatial resolution of a single image recorded by the same system.

The amplified difference signal may be utilized in a number of ways. Most simply, it may be entered into the telemetry data stream, particularly for use as real-time data during passes over ground stations (path 5). This allows reduction of the number of bits per data word (pixel) to that required to transmit changes only in the brightness in sampling intervals Δt.

The image points in the difference picture will, in general, have intensity values other than zero, the rms value being a measure of photon statistical noise, of system noise, and of imperfect matching of the two CCD chips. It will be useful therefore to include a discriminator (which may be located in either the analog or the digital portion of the circuitry). The discriminator will pass all signals whose difference value exceeds a certain threshold level (preset by ground command), while setting all other pixel values to zero. If the number of picture elements that are poorly matched between the two chips is so large as to be troublesome, a compensating filter may be required. This too may be constructed around a CCD (linear), which is ideally suited for matched transversal filtering.

After filtering and discrimination, the number of nonzero picture points remaining in each frame will be relatively small; it becomes a simple matter to store and operate on them for the purpose of automatic decision-making.

As mentioned earlier, the telescope presently under development is optimized for observations of the sun in the ultraviolet. An important problem in solar observations is the study of solar flares. The flare manifests itself

as a sudden, highly localized brightening throughout a broad spectral range; the energy release mechanism is unknown. One of the objectives of this system is to detect, locate, and predict the occurrence of solar flares. A "decision logic" package is indicated in the diagram (Figure 3), with logic circuitry sufficient to perform basic functions such as, e.g., generation of a flare-alarm signal whenever the intensity, or rate of increase of intensity, in one pixel or a group of pixels exceeds some presettable threshold. Note that by the simple expedient of counting readout-gate pulses, the x and y position of any pixel exceeding the discriminator threshold is uniquely determined (x-y counter). The flare-alarm signal sequence will contain information on location of the flaring point, and on the rate of change of the most rapidly increasing point. The more sophisticated functions required for flare prediction, such as analysis of the time-history of brightness fluctuations in certain XUV bright points, will require substantial amounts of storage and more versatile programming; automated analysis of this type would require an on-board spacecraft computer of modest capability. This central processor (CPU) is indicated in Figure 3.

Even analysis of fluctuating bright points, however, does not make exorbitant demands on the computer. Suppose, for example, that we assume a CCD matrix of 244 × 190 pixels: it desired to track the intensity variations of the ten most active pixels (in a raster of 46,360). This requires storage of 10 intensity values (8 bits each) for each sample, plus 10 x-position and 10 y-position words (8 bits each), or 30 data words for the first sample and 10 per sample afterwards, as the position designators need not be repeated; a check can be maintained so that if a given pixel becomes inactive during a certain number of sampling intervals, its history can be erased and the next most active pixel put in its place. Image integration times may be one second or several seconds, but sampling intervals may be more widely spaced. For detection of precursors that may precede the explosive phase of a solar flare by 5 to 10 minutes, 1/4-minute sampling intervals should be sufficient. Then storage of the indicated information over a time span of 10 minutes will require 420 8-bit data words. Programming should be correspondingly straightforward. The requirements reduce basically to ordering according to peak and gradient values, and comparisons with a table of ground-commandable threshold levels. After each picture readout, the appropriate comparisons will be carried out,

and a decision is made either to repeat the sequence or to actuate the flare alarm sequence.

V. DATA COMPRESSION

Another use of the discriminator and logic capability is as a powerful data compression tool. For this, the CPU is not needed. A digital comparator and buffer memory is included in the logic package, which is capable of storing perhaps 1% of the total 46K pixel values, along with their x and y coordinates. Then, as each difference-picture is processed, the 460 most significant (rate-of-change) pixels are stored. In this mode, a full picture is transmitted (path 1) at intervals, then changes only are transmitted until the next reference (full) picture is due. In this way, rapidly changing scenes can be recorded with high time resolution while using only a small fraction of the telemetry that would be required for the same information in a full transmission mode.

As a test for the concept proposed here, trial runs have been made on a laboratory computer, using broadband XUV data from the NRL instrument on OSO-7. The results of such a trial are shown in Figure 4. At the top of the figure are shown seven sequential pictures of the sun in 171 - 630 Å radiation. Spaced at 8-minute intervals, they were generated by an image dissector utilizing the mechanical raster of the OSO, with 64 horizontal scan lines of 48 data words each, for a total of 3072 8-bit words per frame. In reconstructing the data for presentation in the form shown here, this matrix has been expanded by a factor of 12, so that the resultant display of 36,864 pixels approximates the proposed matrix of 46K.

Shown in the lower row of Figure 4 are difference images generated by differencing, in the computer, pairs of images from the upper row. Note that alternate, rather than successive, images are differenced. This is because the OSO was in an interlaced raster mode at the time; successive rasters were displaced from each other by a small amount. Therefore, the time interval Δt covered by each of the lower pictures is 16 minutes. While this sampling interval is longer than would be desirable for some applications, the principle is clearly illustrated. Ground observatories detected a flare of importance -N on the west limb, beginning at 1342 UT. The flare is seen as a single bright spot in the third difference frame (1344 - 1328) and, in its later phase, in the

fourth frame (1353 - 1336). An apparent precursor brightening is seen in the first difference frame (1328 - 1312). The sensitivity of the method is made more apparent if one considers the difficulty of detecting the flare by inspection of the upper images, or by such methods as looking for a change in the integrated light from the entire solar image.

Examination of the first three difference images of Figure 4 should convince one that transmission of the most variable 1% of the total number of pixels will serve a useful purpose in tracking the progress of transient phenomena, particularly when the sampling interval is short. The fourth difference frame shows, in addition to the flare, a displacement of the entire solar disc. This is because the last picture in the upper row (1353 UT) was completed just before entering the earth's shadow. Atmospheric attenuation and scattering were sufficient to cause a slight shift in the spacecraft pointing error signals. This effect may have been sufficient also to alter slightly the appearance of the flaring region in the last difference image.

VI. OPTICAL COUPLING

Figure 5 illustrates the proposed method for coupling the MCP output into CCD-A. While a relay lens could be used, there are a number of advantages to the tapered fiber-optic. Among these are (1) compactness, (2) lower transmission losses, (3) inherent ruggedness and low weight, and (4) the ability to introduce image distortions that are desirable in order that the resolution capability of the CCD may be fully realized. The dimensions of a Fairchild 244 × 190 CCD are indicated in the upper portion of the figure (5a) (Ref. 7). Neither the linear dimensions nor the spacing (pitch) of sensing elements are equal along the two scan directions. There are 244 TV lines parallel to the 5.7-mm dimension (pitch = 18 μm), with 190 picture elements per line parallel to the 4.4-mm direction (pitch = 30 μm). [Horizontal scan lines, in the TV video raster sense, run vertically in the illustration. The orientation shown would pertain when the instrument z-axis is aligned with the heliographic polar axis, as shown in the lower portion (5b).]

The solar image formed by the optics at the MCP measures 7.1 mm. Tapering of the fiber optic will demagnify the image so that it just fills the chip's sensitive area. For a solar angular diameter of 1920 arc seconds,

the 190-pixel scan line then fulfills the design requirement to locate a point source to within 10 arc seconds. Distortion of the fiber optic into an elliptical cross section compresses the solar image along the equatorial axis, thus making the resolution parallel to the equator equal to that parallel to the polar axis.* In addition, the field of view for equatorial regions is then expanded to 42 arc minutes, thus facilitating observation of off-limb transient events, which are far more common at low and middle heliographic latitudes. The format of the reconstructed solar image is shown in Figure 5b. It is seen that the 32 × 41 arc minute field of view allows observation of coronal emissions over the entire solar disc, and above the limb to a distance of 5 or 10 arc minutes, except near the poles.

As indicated earlier, the CCD detector is mounted on a pad for cooling to approximately 200°K. The necessity for cooling to reduce thermal dark current arises from the requirements of this application, in which integration and storage times of tens of seconds are essential. A paper to be presented later in this symposium will give the results of preliminary cooling experiments using a 100 × 100 imager.

VII. CONCLUSION

Figure 6 shows how the inner solar corona may look through the eye of a CCD camera. Data from a rocket flight was imaged to simulate the scene. The camera used a Fairchild CCD-201 chip. Present plans call for launch in 1977 of a simple CCD imaging system of 10^4-pixel, or greater, resolution. This first prototype will utilize the MCP, tapered fiber optic, and cooled CCD imager, but will probably not have on-board image processing capability. The full system, with improved resolution and on-board processing, is proposed for a later flight.

*High-resolution tapered fiber optics having controlled distortion were obtained from Galileo Electro-Optics Corp., Galileo Park, Sturbridge, Massachusetts.

REFERENCES

1. B. W. Manley, A. Guest, and R. T. Holmshaw, Proceedings of the Fourth Symposium on Photo-Electronic Image Devices, London, 1968; Advances in Electronics and Electron Physics, Vol. 28 A, Academic Press, New York, 1969, p. 471.
2. J. Adams, Electro-Optical Systems Design 1, 46 (1969).
3. G. R. Carruthers, Astrophysics and Space Science 14, 332 (1971).
4. W. R. Hunter and F. E. Harlow, Appl. Opt. 12, 968 (1973).
5. R. V. Annable, Appl. Opt. 9, 185 (1970).
6. R. V. Annable, Appl. Opt. 11, 1495 (1972).
7. M. Vicars-Harris, Fairchild Camera and Systems Div., Syosset, New York (private communication).

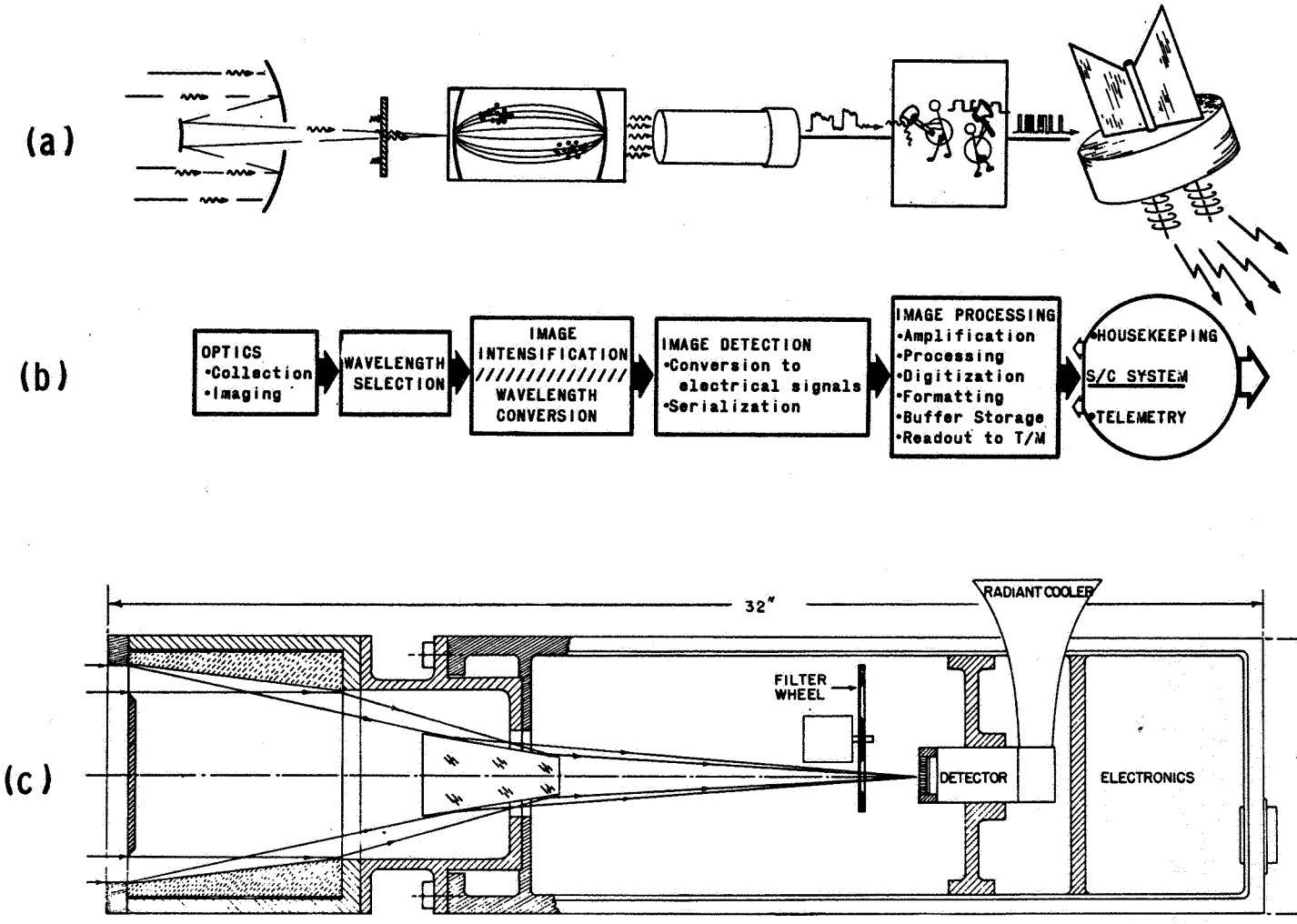

Figure 1. The various components of a generalized space imaging system in (a) diagrammatic and (b) functional block diagram form; (c) one version of the extreme-ultraviolet solar telescope under development at the Naval Research Laboratory

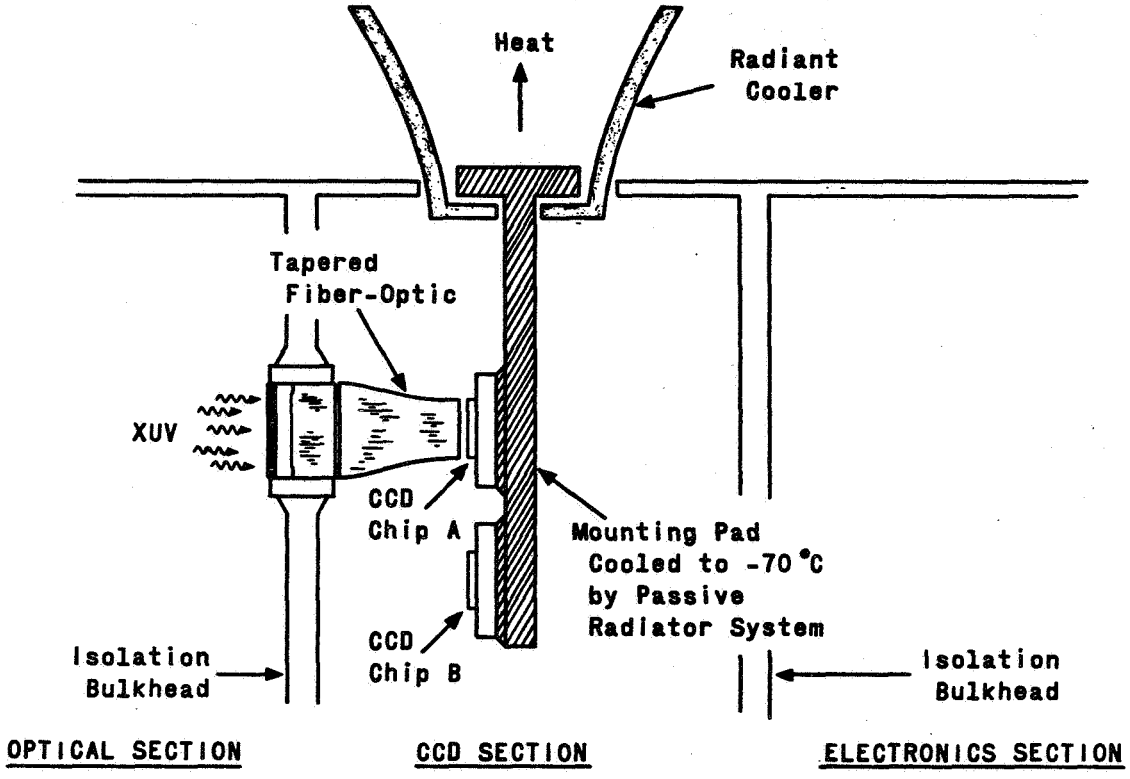

Figure 2. View of the detector section of the NRL telescope

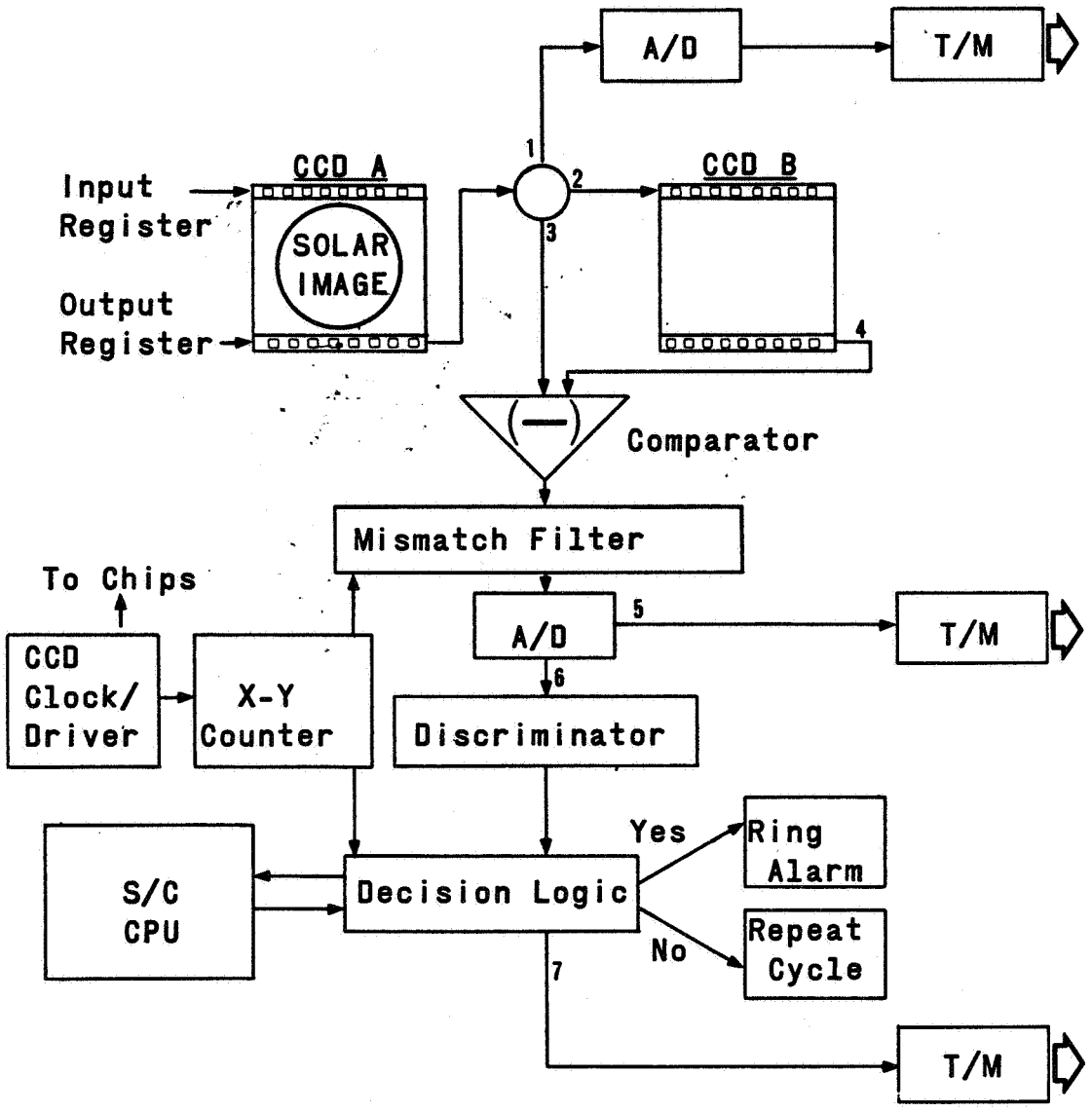

Figure 3. Functional block diagram of the CCD image transducer and processor (CCD-A is at the focal plane of the telescope; CCD-B is covered by an optical mask and receives image information only through the electrical input register.)

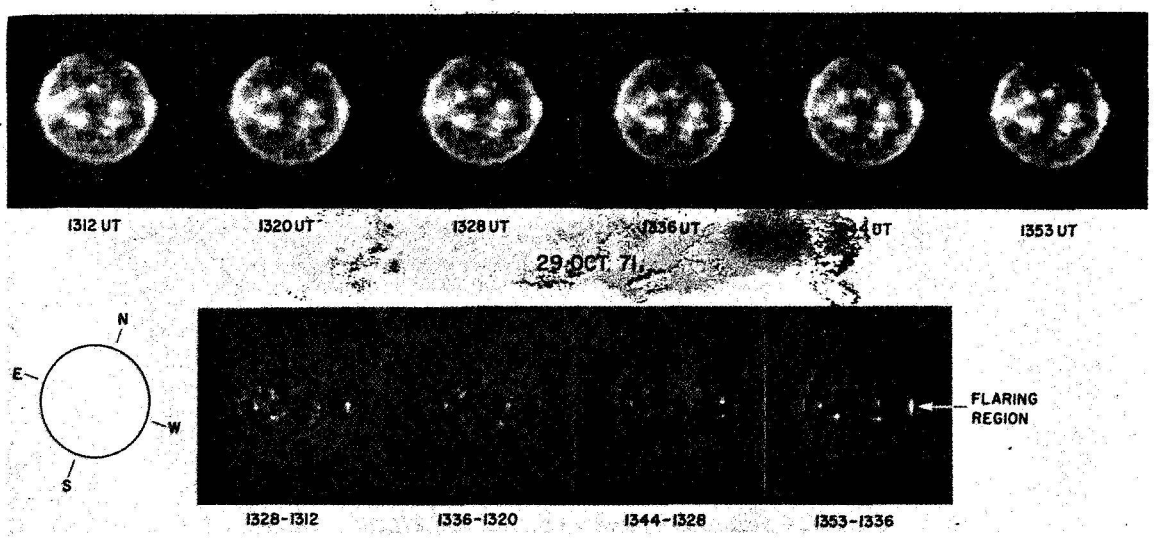

Figure 4. Laboratory simulation of optical comparator mode of operation, using solar data from the OSO-7 satellite (In the upper row are sequential 171 - 630 Å solar images; times shown are the starting times for each 8-minute raster. Below are shown differences between pairs of (alternate) images from the upper row.)

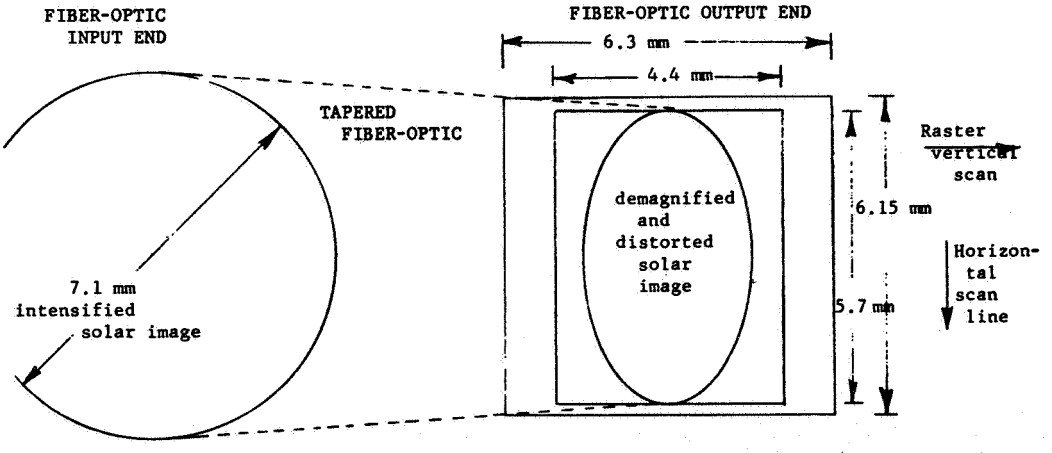

(a) FLIGHT INSTRUMENT IMAGE LAYOUT AND CHIP DIMENSIONS.

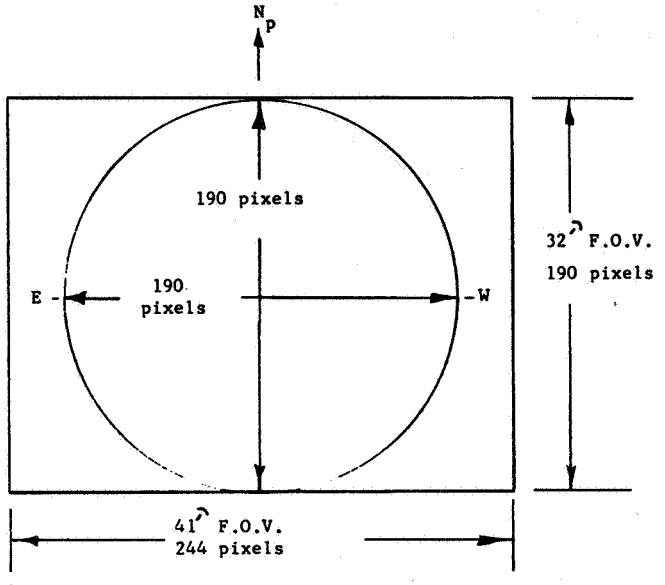

(b) RECONSTRUCTED SOLAR IMAGE.

Figure 5. Details of the optical coupling scheme, which makes use of fiber optics to both reduce and distort the image for optimum utilization of the CCD (Consult Section VI of the text for explanation.)

XUV SOLAR IMAGE AS READ OUT
BY 100X100 CCD CHIP

Figure 6. Laboratory simulation of solar telescope output

A SPECIALIZED CCD IMAGING AND ANALYSIS SYSTEM FOR EARTH RESOURCES APPLICATIONS PROBLEMS*

A. F. H. Goetz
Jet Propulsion Laboratory
Pasadena, California

Present-day satellite imaging systems such as LANDSAT are designed to accommodate users in many disciplines, but delight few of them. In particular, spectral band assignments are not optimized. For this reason, considerable image processing is required to extract a useful data set. Image processing on general-purpose computers is expensive and time-consuming. In addition, most users cannot obtain data in the proper form for processing until months after the image has been taken. These constraints exclude a potentially important group of users who need real-time data.

An imaging and analysis system based on CCD technology and containing a real-time data processing element is proposed which will satisfy needs for on-the-spot results in the areas of mineral exploration, oil slick, algal bloom, and blight detection. Preliminary tests with a 100 × 160 array partially demonstrate the feasibility of the system. **

*This paper presents the results of one phase of research carried out at the Jet Propulsion Laboratory, California Institute of Technology, under Contract No. NAS 7-100, sponsored by the National Aeronautics and Space Administration.

**Abstract only. Paper not received in time for publication.

CCD STAR TRACKERS*

W. C. Goss
Jet Propulsion Laboratory
Pasadena, California

This paper presents an overview of current activities at JPL directed toward the application of CCDs to star trackers and star mappers. The advantages and disadvantages of silicon CCD star trackers are compared with those of image dissector star trackers. It is concluded that although the image dissector provides somewhat greater sensitivity for tracking single stars, the CCD has adequate sensitivity for most single star tracking tasks and is distinctly superior in multiple star tracking or mapping applications. In addition, the CCD has major advantages in terms of size, weight, stability and growth potential.

The signal and noise figures of several current CCD configurations are discussed. The basic structure of the required signal processing is described, and it is shown that resolution in excess of the number of CCD elements may be had by interpolation.

CCD star trackers and star mappers now under development at JPL will utilize microprocessors for their signal processing. Some major advantages of the microprocessor approach are discussed and include the ability to use data which is in an interlaced field format.

*This paper presents the results of one phase of research carried out at the Jet Propulsion Laboratory, California Institute of Technology, under Contract No. NAS 7-100, sponsored by the National Aeronautics and Space Administration.

I. INTRODUCTION

JPL currently has two tasks funded by the NASA Office of Aeronautics and Space Technology to develop CCD star reference trackers for spacecraft and payload stabilization. One of these tasks is directed toward providing a single-axis star tracker which will be used for roll axis stabilization of Mariner-type spacecraft on missions subsequent to Mariner Jupiter-Saturn 1977. The other task is to develop a star pattern sensor having the capability of tracking ten stars simultaneously, providing two-axis coordinates and magnitude data for each and providing a video signal for display of the star field on a television monitor. The intended application is astronomer-supervised acquisition of infrared target bodies by the Shuttle Infrared Target Facility, a Shuttle payload now in the definition phase.

This paper presents the rationale for the choice of a charge-coupled image sensor for these tasks, discusses CCD star image signal processing techniques and outlines expected performance parameters.

II. IMAGE DISSECTORS VS. CCDs

Image dissectors have been in wide usage for more than a decade as the preferred star magnitude and position sensing elements in star trackers. Image dissectors are, very simply, photomultiplier tubes with an electron imaging and electron deflection section located between the photocathode and a sampling aperture which is at the entrance to the electron multiplier section. Image dissectors provide optical signal modulation and field of view gimballing without the use of moving parts.

Image dissectors can be almost completely signal shot noise limited. The large and comparatively noise-free gain in the multiplier section reduces the effect of subsequent leakage currents and amplifier noise contributions to an insignificant level. Modern photocathodes have thermal emissions of only a few electrons per second or less for typical image dissector electron aperture areas. Pulse height discrimination photon counting techniques exclude the majority of electrons thermally emitted within the multiplier structure and can ignore the multiplier gain distribution function. In the absence of a significant sky background or ambient radiation field, an image dissector can reliably detect a few photoelectron events per sampling period (Ref. 1).

However, image dissectors have a number of disadvantageous characteristics which have encouraged designers to consider alternatives; these characteristics principally include the non-storage feature which heavily penalizes sensitivity under multiple target or full frame search conditions, variable and unsymmetrical magnification across the field which necessitates elaborate calibration for precise offset pointing, fatigue and damage susceptibility of the photocathodes, relatively high weight and power demand, use of high voltages, fragility, susceptibility to magnetic fields and cost, to name a few.

Silicon photodiode or photovoltaic detectors have appeared attractive for some applications by contrast because of their low cost, small size, rugged construction, stability, insensitivity to magnetic fields and ability to operate at voltage levels compatible with microcircuits. Solid-state star trackers have been built and flown using silicon detectors despite their limited fields of view, relatively poor sensitivity, and inability to electronically gimbal or provide accurate star position information except in a very limited region about null.

Silicon CCD sensors now provide the designer with a superior alternative which exhibits all the strong points of the silicon detector, has few of its weaknesses and provides valuable capabilities not obtainable from either the image dissector or the silicon sensor. The minute area of the individual CCD elements along with the charge storage capability and the broad-band high quantum efficiency silicon response combine to produce an ultimate sensitivity, when cooled to moderately low temperatures, within one stellar magnitude or less of the threshold for an ideal image dissector, all other factors remaining the same. This number can be arrived at by comparing the response of silicon and an S-20 photocathode -- a ratio of typically 8/1 for a relatively hot type F star (Ref. 2) -- and the signal level at unity signal-to-noise ratio for the two detectors. Those numbers are typically 3 electrons per interval for an image dissector and presently about 150 electrons per element for a CCD. Including a duty cycle factor of 1/2 for the image dissector modulation, a threshold stellar irradiation ratio of 3 results, corresponding to 1.2 stellar magnitudes.

This slim margin in favor of the image dissector vanishes decisively if a cooler star is the target, or if the dissector is required to track multiple

targets or to scan the full field in search. Unlike the image dissector, the charge storage and full field readout features of the CCD make its star magnitude threshold independent of the number of targets.

A further advantage of the discrete detector configuration is that the sensor is relatively insensitive to nonsaturating levels of stray light or sky background. The only illumination which can interfere with the star target signals is that illumination which is intercepted by the same elements upon which the star is imaged. Background level subtraction in the signal processing can then remove the mean value of the interfering illumination. Fixed pattern variations and shot noise will remain.

Several problems are inherent in the use of CCDs for star trackers that are not encountered using image dissectors. Room temperature average dark charge generation rates are typically so high as to fill the CCD wells in a few seconds, and individual high dark charge elements may have generation rates several times the mean value. Cooling to moderately low temperatures, for example to -40°, will be necessary to reduce the dark charge and so provide a usable dynamic range. Experience at JPL with other space instruments, for example, the Mars Atmospheric Water Detector, shows that packages may be reliably cooled to even lower temperatures by utilizing passive radiation to space.

Several signal processing complexities arise because of the discrete detector array structure. A star image will not in general fall upon a single element at a time. Even a point image will often be quadrisected at the common corner of four cells. A very small image might, in fact, "fall into the crack" between elements if the CCD were an interline transfer device. For these reasons as well as others, it will often be useful to work with an image point spread function measuring two or more elements in width and to measure star magnitude by summing the signal from a small group of adjacent elements large enough to include all the signal from a star image.

A related problem is that the number of image elements now available in CCDs is smaller than the incremental resolution needed in most star tracker applications. The largest imaging CCD array commercially available at this time is RCA's Big Sid, a surface-channel device having 256 × 312 elements. Buried-channel arrays of about 400 × 400 elements are being developed by

Texas Instruments and Fairchild. Star tracker requirements frequently demand 1000 or more resolution elements across the field in order to provide offset pointing capability. Present CCD fabrication techniques can generate cell structures with adequate geometric accuracy, and as will be discussed further in this paper, simple interpolation techniques may be used to locate the centroid of an extended star image to within a small fraction of a pixel. These signal processing techniques require substantial memory capacity and logic capability since signals from as many as nine separate image elements must be processed in several ways to derive star magnitude and an interpolated image centroid position, and the signals will not all be located consecutively in the data stream. Use of an interlaced CCD data stream would, in fact, produce part of the data in one field and the rest in the other.

Signal processing is operationally much more complex than for an image dissector star tracker, which simply phase demodulates to obtain star position within the scan width and obtains a direct measure of star magnitude from the multiplier current or voltage. Signal processing circuitry then could be expected to be complex by comparison. Although this computational task is relatively complex in hardware, it is relatively simple in software, and use of a microprocessor provides at once a functional simplicity and a great flexibility in altering tracker characteristics to meet a variety of functional requirements.

A final consideration in the tradeoff between image dissectors and CCDs is the question of present and future availability. The image dissector is a mature device with fairly consistent and predictable characteristics, and commercial devices are readily available at prices of a few thousand dollars. The market is relatively small. This comment will probably still be correct 10 years from now. CCD devices, on the other hand, are still developing very rapidly and have a large growth potential. Very few devices are available on the commercial market today, and they must be regarded as forerunners of more capable devices yet to come. A very large commercial market is expected to develop, and price competition will be strong. In 10 years, if we should apply the experience of the integrated circuit industry, the CCD imagers which are available today will amost certainly be obsolete and unavailable. More sophisticated and more reliable devices will have replaced them at prices perhaps in the tens of dollars.

III. CCD SIGNAL CHARACTERISTICS

If we assume that the star image signal charges which are generated in adjacent elements are reconstituted by the signal processing circuits into a total value representing the entire image, then the detector response to a star can be characterized by

$$Q_S = \frac{aA\Delta T}{q} \int R(\lambda)S(\lambda)\, d\lambda \qquad (1)$$

where

Q_S = star signal in electrons
a = ratio, detector element area to unit cell area
A = objective lens area
ΔT = charge integration time
q = electronic charge
$R(\lambda)$ = detector response, amp/watt
$S(\lambda)$ = star irradiation spectral power density

Figure 1 illustrates the normalized spectral energy density of α-Carinae (Canopus) (Ref. 3), a type F star having an effective black-body temperature of 7000° Kelvin, and for comparison, spectral response curves for two differently structured CCDs. The lower curve, for the Fairchild CCD 201, has a peak response of nearly 0.3 amp/watt and effective short and long wavelength cutoffs of 0.45 and 1.1 microns. The upper curve plots spectral response measured by Texas Instruments on a promising backside illuminated and thinned device now under development for JPL. Peak response is 0.4 amp/watt, with a long wavelength cutoff of 0.1 micron and a short wavelength cutoff which was not measured but must be well below 0.4 micron.

Using the data of Figure 1 and a structural shadowing factor a = 0.5 for the Fairchild device, we obtain from Equation (1) a charge generation rate of 1.26×10^6 electrons/second for each cm^2 of objective lens area. A similar calculation for the Texas Instruments device, assuming a = 1.0, yields a generation rate of 7.1×10^6. It is of interest to note that this response is slightly greater than the value tabulated in Ref. 2 for the silicon detector response to Canopus.

IV. NOISE CHARACTERISTICS

Noise sources in CCDs which compete with the detected signal fall into several categories. Thermal generation of carriers within the bulk silicon and at the interfaces provides a temperature-dependent dark current that supplies, at best, a uniform background charge level in the storage elements and, at worst, a pronounced fixed pattern of spikes. Statistical variations in signal plus dark current electrons introduce the familiar shot noise. Transfer losses introduce highly correlated errors. Clocking and reset waveforms appear at the output, introducing coherent noise. Surface state trapping introduces yet another noise factor in surface-channel CCDs.

Dark current is a limiting factor in several ways. The accumulated charge can simply fill the potential wells and leave no room for storage of photo-generated signals. Lower-level uniform background charges may be subtracted by the signal processing circuits; however, shot noise proportional to the square root of the number of thermal charges in each element remains. Finally, individual high dark current elements produce signals which would be difficult to differentiate from star signals if of large enough amplitude.

Room temperature dark current generation rates for typical silicon diffusions, as used in buried channels, should be approximately 3 na/cm^2 (Ref. 4), or approximately 1.2×10^5 electrons per element per second, assuming element dimensions of 25 microns on a side. Many have much larger average rates, however; 10 na/cm^2 are not unusual with some individual elements having rates as much as 6 na/cm^2 above the mean. These high dark current elements would appear as bright stars and would seriously interfere with the star tracker operation. Fortunately, moderate cooling should reduce the accumulated dark charge to a level below the minimum detectable signal level, taken earlier to be 150 electrons. Data reported by Fairchild (Ref. 5) indicates that operation at -40° will reduce dark current rates by 600 times below room temperature rates. Assuming a 1.1-second integration time, the dark charge collected will be 100 electrons or less.

The principal noise constituents, then, assuming framing rates of 10 per second or greater, can be expected to be clocking and reset noise at low light levels and shot noise at signal levels higher than about 4% of saturation.

Improvements made in reducing clock waveform coupling and in developing low-noise output amplifiers will be directly translatable into an improved small signal sensitivity, although additional cooling might be required to realize the gain.

Taking 150 electrons as our threshold detectable signal, multiplying by three to account for summing nine total elements and multiplying again by four to achieve a reasonable signal-to-noise ratio, we decide on a criterion for threshold detection of stars of $N_t = 1800$ electrons accumulated during a single integration time. Extrapolating signal response for stars of magnitudes other than our example in Figure 1,

$$Q(m) = Q_S(2.512)^{(m_o - m)} \tag{2}$$

and, substituting into Equation (1), we can write a scaling expression for the diameter of lens which is required in order to detect a star of a given magnitude:

$$d = \left[\frac{4qN_t(2.512)^m}{(2.512)^{m_o} a \pi \Delta T \int R(\lambda)S(\lambda)\,d} \right]^{1/2} \tag{3}$$

This expression is plotted in Figure 2 for the Fairchild and Texas Instruments CCDs. Note that a 1-cm-diameter lens, for example, will collect light enough to see a magnitude 3 1/2 star with the Fairchild device and a magnitude 5 1/2 star with the Texas Instruments CCD.

V. INTERPOLATION

The previous discussion has explored star detection capabilities of the Fairchild CCD image sensor, which is commercially available now, and of a Texas Instruments sensor currently under development. The conclusion is that these devices have very useful star detection capabilities. However, detection and identification of a guide star are only prerequisites to the principal task of generating relative star position coordinates with adequate accuracy and resolution.

As noted earlier, present-day CCDs have fewer image elements than the total number of resolution elements often required. The following discussion will address the subject of an interpolation providing adequate accuracy for the present requirements, yet simple enough to be built into a flight instrument.

We will consider first CCDs which are organized with vertical transfer, and then discuss interpolation with devices which have interline transfer.

We will assume that charge is not lost between elements, and that the image point spread function is symmetrical and one or more element-widths in diameter so that charge levels in adjacent elements may be compared to determine the location of the image center. We will not consider a detector point spread function apart from the image spread function. Assume first that we have an arbitrary image point spread function

$$I = f_1(x, y)$$

If we can make detailed measurements of the function, we may obtain the line spread functions in x and y, I(x) and I(y), by integrating over the image width in the other direction. We may then calculate centroids along both axes; for example,

$$X_c = \frac{\int xI(x)\,dx}{\int I(x)\,dx} \tag{4}$$

Figure 3 illustrates how the point spread function might look to a CCD imager. The continuous point spread function has been integrated in steps over the sub-interval areas represented by the CCD elements. We can still form line spread functions by summing in one dimension, as shown in Figure 4; however, accurate calculation of centroids is frustrated by uncertainty as to the shape of the image function within the element boundaries. The difficulty is resolved if we have a priori knowledge of the shape of the line spread function, and calculation becomes appealingly simple if the line spread function is rectangular.

If we have an image of width greater than one element and less than two, the line spread function will be fully defined by three successive elements, which we designate F_{k-1}, F_k, and F_{k+1}, and the x-direction centroid position will be

$$X_c = \frac{F_{k+1} - F_{k-1}}{2F_k}, \quad \text{for } -0.5 \leq x_c \leq 0.5 \tag{5}$$

This expression is exact for a rectangular line spread function and very nearly so for some reasonable approximations. A point spread function of the form

$$I(r) = a + br^2, \quad r \leq 1 \tag{6}$$

can, in principle, be interpolated by Equation (5) to an accuracy of 1%.

Point spread functions of that form can be generated by several techniques, including defocusing the image formed by a folded mirror objective. Even line spread functions far removed from the rectangular shape are reasonably well interpolated by Equation (5). Figure 5 illustrates the interpolation accuracy of an image having a Gaussian spread function. Best results are obtained for the largest image, and indications are that the optimum size may be even larger. From smallest to largest, the maximum errors are 14.6%, 11.6% and 8.3%. A 0.6% step is observed to occur at the ends of the range for the largest image if the output is not rescaled.

Interpolation with devices having interline transfer is also feasible even though the interline transfer registers are opaque and strips of the image are lost. A variety of techniques are available; however, a calculationally simple approach similar to the one just outlined for vertical transfer devices will be described. We consider a symmetrical triangular line spread function of approximately 2 1/2 unit cell widths. We construct the sides of the triangle

from the measured element signals and calculate the intersection point. The centroid then will be

$$X_c = \frac{F_{k+1} - F_K}{F_{k-1} + F_k + F_{k+1}}, \quad -0.5 \leq x_c \leq 0.5 \tag{7}$$

This expression is not exact for a triangular line spread function; a maximum positional error of about 6% results. A Gaussian line spread function, which results from a Gaussian point spread function, is a fairly good approximation to a triangular form, and a maximum error of 8% results, as illustrated in Figure 6. The signal summation $F_{k-1} + F_k + F_{k+1}$ is constant to within about 3% over the full range of image positions.

VI. SUMMARY

In summary, the technical tradeoff between image dissectors and CCDs for star tracker applications provides a clear picture of major performance and configurational advantages in favor of CCDs, although the image dissector is somewhat more sensitive for tracking single hot stars. The outstanding disadvantages of the CCD are that it requires cooling and that the signal processing is more complex than for an image dissector. A close look indicates that these are not serious problems; passive radiation to space can provide the necessary cooling, and the signal processing, on close inspection, proves to be difficult for hardwired processing but straightforward for logical processing, as with a microprocessor. The CCD technology is immature at this time, and only a very limited selection of devices is available. Finally, measurement of the image position on an array by interpolation to an accuracy of 1/10 of an element appears feasible for both types of CCDs.

REFERENCES

1. E. H. Eberhardt, "Multiplier Phototubes as Quantum Counters," Applied Optics, Volume 6, No. 1, 1967.

2. F. F. Forbes and R. I. Mitchell, "Stellar Photometric Data For Six Different Photocathode Materials and the Silicon Detector," Communications of the Lunar and Planetary Laboratory # 141, 1968.

3. R. H. Norton, The Absolute Spectral-Energy Distribution of Canopus, JPL Technical Report 32-641, August 15, 1964.

4. Charge Coupled Device Image Sensor Study, Final Technical Report, JPL Contract 953674, Fairchild Camera & Instrument Corporation, February 1974.

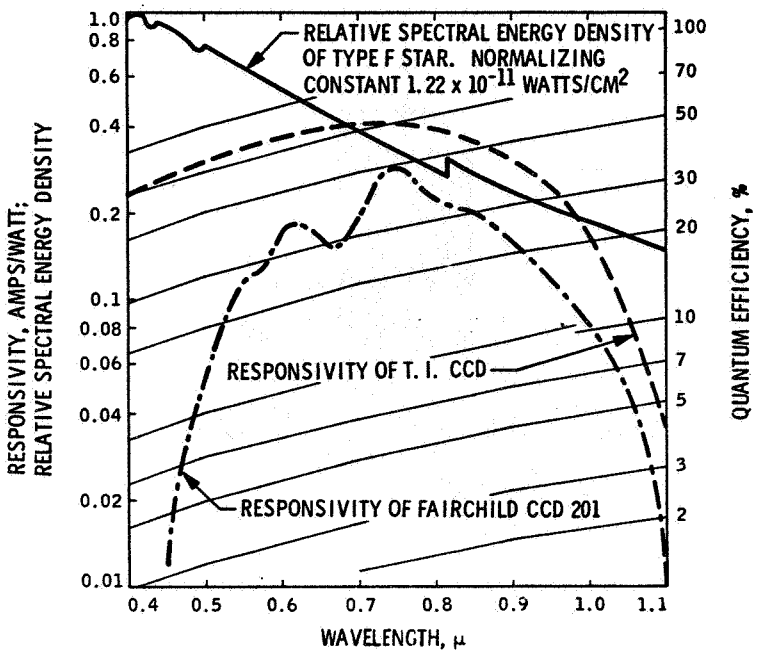

Figure 1. Typical star source and CCD response characteristics

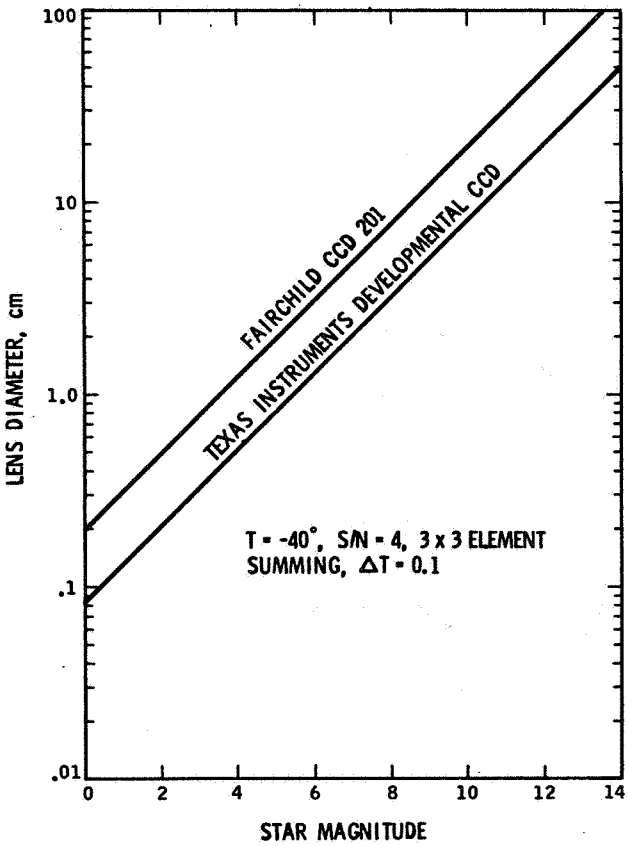

Figure 2. Star detection thresholds

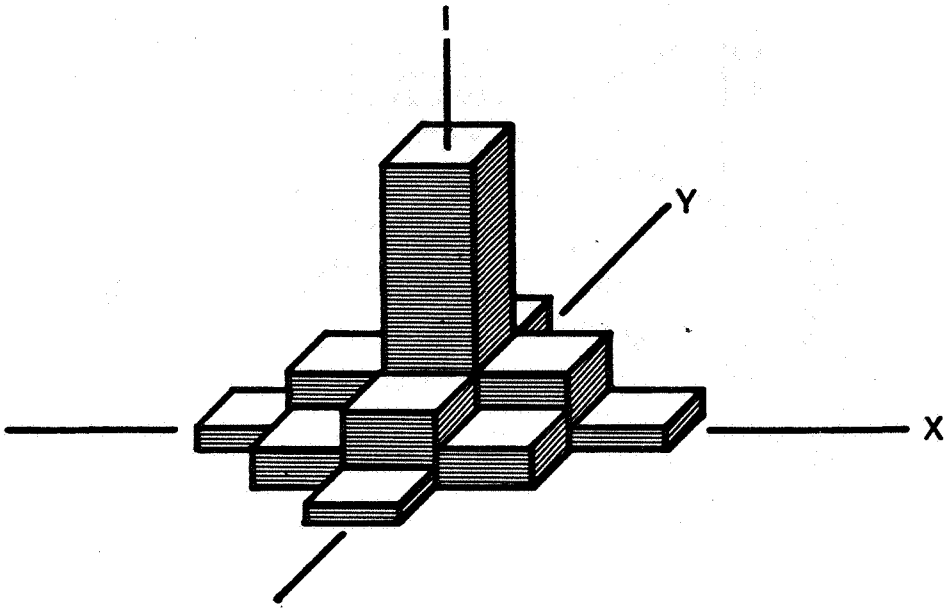

Figure 3. Image point spread function as seen by CCD array

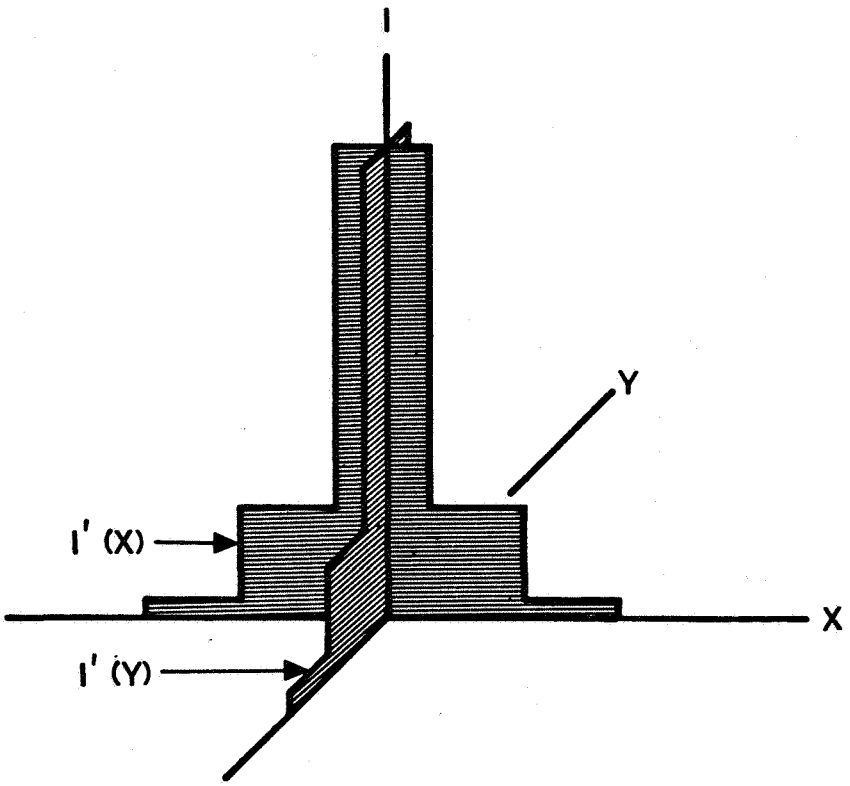

Figure 4. Image line spread functions as generated from CCD signals

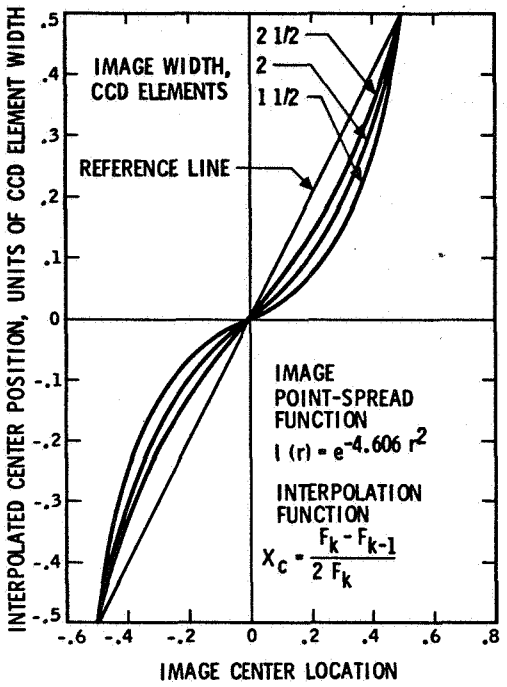

Figure 5. Interpolation of a Gaussian image by a vertical transfer CCD

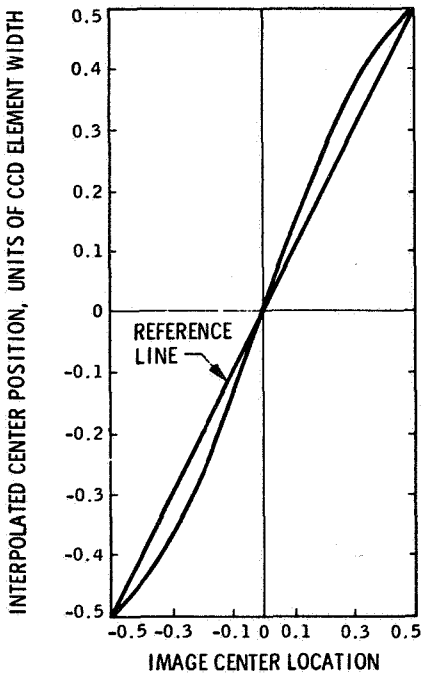

Figure 6. Interpolation of a Gaussian image by an interline transfer CCD

CCD IMAGING INSTRUMENTS FOR PLANETARY SPACECRAFT APPLICATIONS*

Terrence H. Reilly and Mark Herring
Jet Propulsion Laboratory
Pasadena, California

Aware of the great potential for improved planetary imaging, NASA has been an early and continuing supporter of CCD research. The purpose of this paper is to report on a companion effort, also sponsored by NASA, aimed at developing new spacecraft camera systems to be used in conjunction with the CCD sensors. We begin with a brief overview of the science objectives and engineering constraints which influence the design of cameras for deep space. This is followed by a review of two current development programs at JPL, one leading to a line scan imager and the other to an area array frame camera. For each of these, a general description of the imager will be given, with emphasis on the unique features. From the discussion, it will be evident that currently available CCDs fall short of our requirements in some respects. Therefore, we conclude by showing how the future of these CCD cameras is tied to the continued successful development of the sensors.

*This paper presents the results of one phase of research carried out at the Jet Propulsion Laboratory, California Institute of Technology, under Contract No. NAS 7-100, sponsored by the National Aeronautics and Space Administration.

I. DESIGN CONSIDERATIONS FOR PLANETARY IMAGERS

The camera on a planetary spacecraft is a compromise between the wishes of the science community and the constraints imposed by technology. The first section of this paper is given over to a review of these objectives and constraints. At the invitation of NASA, planetary scientists define imaging objectives for each new mission. The original objective might be stated as: Measure the equatorial diameter of the satellite Io to ±1/2%. Given the spacecraft trajectory, the camera designer then translates this science objective into the equivalent combination of angular resolution, geometric fidelity, and image format.

The science objectives may be either absolute or relative. Absolute objectives follow from natural phenomena. For example, to study absorption by methane in the clouds of Jupiter, the camera must respond at 890 nanometers. Relative objectives are tied to a previous accomplishment or an advance in the state of the art. The scientist accustomed to 800-line television pictures is reluctant to settle for a smaller format.

The following is a brief summary of typical science objectives stated in terms of camera and sensor parameters.

(1) Resolution. Objectives range from 100 to 10 microradians per pixel. For reasonable telescopes (focal length 1.5 m or less), this requires a sample frequency of 20-40 line pairs per millimeter on the sensor. Modulation transfer for the entire camera should be at least 20% at the sample frequency.

(2) Format. A square image with 1000 elements in each dimension is considered good by most scientists; 700 elements is OK. A smaller format will be considered if some particularly attractive tradeoff is available or in case of duress (e.g., a rigid weight limitation). Larger images can be built up by mosaicking several pictures, but the metric data in a mosaic does not compare with the accuracy of a single frame. Also, ground processing costs are proportional to the number of frames, thereby making many small pictures an unattractive solution.

(3) Spectral response. Figure 1 shows several spectral bands of interest, ranging from the near-UV to the near-IR. Typical spectral filters have passbands from 20 to 100 nanometers.

(4) Geometric fidelity. In decalibrated images, it should be possible to locate features to a fraction of a picture element. This is required for stereo measurements, color registration, mapping, and other photogrammetric applications.

(5) Photometry/polarimetry. Although difficult to achieve, the request is typically for 10% absolute and 1% relative photometry. This level of performance allows the scientist to study chemical composition of the planetary surface and to detect time-dependent variations in brightness.

(6) Dynamic range. Planetary scenes frequently have low illumination and contrast, so the image modulation does not fill the entire dynamic range of the sensor. The objective is to obtain enough distinguishable grey levels in the image to permit a strong contrast enhancement when the picture is displayed. If a particular image occupies only 1/8 of the sensor dynamic range, and the contrast will be stretched to fill 16 grey levels in a photographic print, then the camera dynamic range must be at least $8 \times 16 = 128$. A dynamic range in excess of 200 is preferred.

(7) Image processing. For reasons of time and cost, the scientist favors an instrument which does not require elaborate image processing to produce a usable picture.

The camera must also cope with the hardships of life on an unmanned spacecraft. Listed below are the major constraints imposed by the capabilities of the spacecraft and the nature of the missions.

(1) Minimum size/weight/power. Reasonable allocations for these parameters are:

Size:	$0.25 \times 0.25 \times 0.25$ to 1.0 m
Weight:	5 - 25 kg
Power:	10 - 20 W

These numbers apply to a single camera; some spacecraft carry two.

(2) Life and reliability. Typical life requirements are 5 - 10 years shelf, 3000 hours operating. The design must withstand up to 250 g of shock and 20 g of random vibration. Simplicity is sought after, and moving parts are used reluctantly. Use of the camera as a scientific instrument requires that it hold a calibration, and this implies long-term stability. In contrast to ground-based instruments, problems with drift cannot be solved with tweaks. Exceptions to this rule must be designed in at an early stage, and substantially increase the complexity of the camera.

(3) Data bandwidth. Because of the communication distance, digital data systems are used. Each picture element is quantized to 8 - 10 bits, so 25 kHz becomes 250 kilobits per second (kbps). The real-time capability of the downlink telecommunication channel is in the range 2 - 150 kbps. The actual rate used at any point in the mission depends on the design of the spacecraft, the earth-spacecraft range, and the signal-to-noise ratio required on the channel. Under these circumstances, the ideal camera is one capable of operating at several rather low data rates.

The traditional approach has been to operate the camera at a single rate in conjunction with an external buffer on the spacecraft. The buffering is often done by a digital tape recorder with rates to 2 Mbps and capacity to 5×10^8 bits. Solid-state buffers are faster (to 10 Mbps) but have less capacity (less than 10^7 bits). Since even the buffers do not operate as fast as we might like, a slow-scan camera is often required. This means that the sensor itself must be capable of storing a shuttered image for times ranging to tens of seconds. Once the data is in the buffer, however, it can easily be read onto the radio channel at any desired rate.

For reasons of reliability and increased data return, current spacecraft design permits a bypass of the data buffer when the real-time channel is operating at high rates. In the past, matching a single-rate camera to the real-time channel has been possible only with some loss of image size or quality. To take full advantage of this

real-time option, future cameras should operate in a variety of image formats and at several of the higher real-time rates.

(4) Environment. Irrespective of how the camera is mounted on the spacecraft, the electronics compartment will be at room temperature or slightly below. The telescope, on the other hand, is looking at cold space. The thermal design must control the gradients and maintain the components of the camera, particularly the telescope and sensor, within prescribed limits. The difficulty of this task depends on the temperature sensitivity of the sensor and whether or not it must be cooled.

For many current and future missions, there is a radiation hazard due to the planet, the spacecraft power generator, or both. A typical dose is 10^6 rads ionizing radiation and 10^{11} neutrons/cm^2 at 1 MeV.

(5) Low light. As planetary exploration turns toward the outer planets, the problem of low illumination level becomes severe. This is illustrated by comparing the solar illumination level at the superior planets with that at earth: earth = 1.00, Mars = 0.44, Jupiter = 0.04, Saturn = 0.01, and Uranus = 0.0025. At close encounter, integration times are limited to the millisecond range by the relative motions of spacecraft and planet. A broadband exposure at the farther planets can be less than 100 μJ/m^2 in 6000°K light.

The particular strengths and weaknesses of CCDs can be seen by measuring these imagers against the foregoing list of objectives and constraints. The spectral response, particularly in the red and near-IR, would greatly expand the scope of future imaging experiments. Geometric fidelity might well prove adequate without extensive decalibration. Dynamic range and low light sensitivity are remarkable by any standard. The life and reliability of solid-state devices are potentially very good. And the size/weight/power advantage over electron beam sensors is obvious.

The known shortcomings of the CCD are not too alarming for a device still in the developmental stage. The largest arrays currently available are still marginal for planetary work. The response nonuniformities must be offset by

computer processing to produce a research quality image. And the susceptibility to radiation damage has not been thoroughly explored.

On balance, therefore, NASA and JPL have found CCDs sufficiently promising to justify the camera development programs described in Sections II and III below.

II. LINE SCAN IMAGER

The objective of the line scan imager program is to develop a new camera for use on Pioneer-class missions to the outer planets. The current effort will lead to completion of a breadboard version of the instrument in 1976, and could result in a flight version for launch as early as 1979.

The Pioneer spacecraft is one-axis stabilized, i. e., it spins at a nominal 5 RPM about its roll axis. This motion permits the use of scanning-type cameras, which generally offer a weight advantage over the more familiar framing cameras. For this application, a line scan camera has been chosen, and the method of operation is illustrated in Figure 2. The camera sensor is a linear array of detectors, and this array is swept over the planet surface by the spacecraft rotation to produce a two-dimensional image. Each time the linear sensor advances by its own width, the integrated photo charge is sampled and recorded.

The line scan imager is configured in two parts: an electronic compartment located in the equipment bay of the spacecraft and a sensor/telescope package which extends outside. A stepper motor and reducing gears are used to point the telescope package fore and aft with respect to the spin axis. The second degree of freedom is obtained by allowing the rotating spacecraft to carry the telescope to the desired roll angle. Table 1 summarizes the principal characteristics of the line scan imager. Several entries in this table will require additional explanation.

The sensor chosen is a 160 pixel linear array CCD now under development at Texas Instruments, Inc. Buried-channel operation was specified to provide a higher threshold for radiation damage and better charge transfer efficiency. The sensor will be thinned and illuminated from the backside to maximize quantum efficiency. Three sensors are used in the image plane, each covering a different spectral band. The optical filters will be permanently affixed over the sensors.

For a simple line scan imager, the sensor would consist of a single line of 160 elements. The CCD, however, offers an opportunity to incorporate image motion compensation (IMC) with only a minor increase in camera complexity. On the Pioneer spacecraft, the major contributor to the image motion is the rotation of the spacecraft itself. This motion is quite uniform in rate and direction, so complex logic is not needed. As viewed in the image plane of the telescope, the scene appears to sweep over the linear sensor in a direction nearly perpendicular to the long dimension.

The image motion compensation is achieved by replacing the one-line sensor with another consisting of several lines (5 to 10). The charge transfer rate is then chosen to match the velocity of the optical image moving over the sensor. Thus, when the rotation of the spacecraft carries a point in the optical image from line 1 to line 2 of the sensor, the photo charge generated in line 1 is also transferred to line 2. After the image charge has accumulated over the space of several lines, it reaches the output register and is read by the sampling electronics. The scanning camera has no shutter, so the charge packet for line N + 1 immediately follows that for line N as they move across the CCD. Since the optical image is always present on the sensor, all parts except the active lines in the parallel registers must be covered by an opaque shield.

The effectiveness of the IMC is directly proportional to the number of active lines. For our application, approximately five accumulating lines will be used to increase the signal five-fold, with no loss of resolution. With the range of image motion velocities anticipated for this mission, 64 different charge transfer rates are needed to keep the mismatch between the optical and electronic image velocities below 3%. The runout mismatch depends on the number of IMC lines used. In this instance, the worst-case error would be 5 lines × 3% = 15% of one pixel overall error. Obviously, the larger the number of accumulation lines, the greater the demands on the CCD clock frequency generator.

The stepper motor is used with two stages of conventional gear reduction and a harmonic drive. The result is a step size of five pixels with an accuracy better than one pixel. The commandable look angles range from 10 to 185 degrees, but the instrument sees only the radio antenna at the low end of the scale.

Because of the large number of commands required to take a single picture, the imager will have a simple automatic sequencer. With this optional sequencer turned on, the camera will automatically take a series of pictures with a preselected look angle advance between frames.

The telescope focal length has been chosen to give an angular resolution of 100 μr per pixel. The optical aperture is limited to approximately 10 cm by weight restrictions.

The format of a full frame is 160 pixels × 640 lines. The short dimension is determined by the number of elements in the linear sensor. From a performance standpoint, it would be desirable to have a longer sensor, and linear CCDs many times this size have been built. However, the length of the sensor also determines the data rate out of the camera. (Recall that the line time is determined by the use of the IMC, and not by dark charge buildup or some other controllable factor.) With only 160 elements in the sensor, the maximum data rate is already 8 megabits per second. Rates higher than this would significantly increase power consumption in both the camera and the spacecraft data system.

The long dimension of the frame is determined by the capacity of the spacecraft data buffer. The imager could continue to sample the scene indefinitely, but when the buffer is filled, a pause of 2 - 8 minutes is required to relay the data to earth. Current projected capacity for a solid-state buffer on the Pioneer is 10^6 bits.

The camera can be commanded to record a quarter or half frame. The chief utility of this option is for multispectral work. The three sensors are arranged in the focal plane to permit recording of a quarter frame in three registered colors or a half frame in two registered colors.

The noise equivalent exposure is projected to be 2 $\mu J/m^2$ in 2854°K illumination, and about three times better than that in sunlight. The dynamic range should be several thousand. Digital encoding of 8 bits has been chosen to provide compatibility with existing data handling systems on the ground. Variable gain and offset values will permit assignment of the 256 grey levels to all or part of the camera's dynamic range.

III. AREA ARRAY CAMERA

The other instrument development effort is directed toward demonstrating the feasibility of an area array CCD camera for use on 1979 and later flights, such as the proposed Mariner Jupiter/Uranus mission. This camera will be compatible with the traditional Mariner spacecraft design, particularly the more recent versions (Mariner Venus/Mercury, Mariner Jupiter/Saturn). In addition to the broad requirements discussed above, specific constraints on camera design are imposed by Mariner-class missions in general, and by outer planet missions in particular.

For the present development effort, a maximum data rate of 250 kbps has been established. This corresponds to a frame readout time of approximately 6.5 seconds, which in turn requires sensor cooling to reduce dark current to an acceptable level. With dark current suppressed, the sensor itself must be capable of image storage to prevent degradation during the long readout, and to allow a pause between exposure and readout.

Unlike standard-rate television and the line scan imager, exposure (or integration) time for the area array camera is not simply the period between successive readouts. In this application, both exposure and readout times must be separately commandable from the ground. In keeping with recent practice, the camera will have variable readout rate to allow continued real-time operation as the communication channel rate falls off with distance.

Medium- and narrow-band optical filters have been an important part of past Mariner imaging experiments. CCD sensors for future missions should also maintain good image quality when narrow spectral filters are used.

Radiation tolerance is an important consideration for outer planet spacecraft, particularly for missions involving Jupiter. The cameras and other hardware must continue to operate predictably after exposure to the radiation dose integrated over the life of the mission. Allowance must be made for the possibility that the radiation flux at Jupiter will temporarily saturate the sensor, precluding any imaging during that period.

To demonstrate that these requirements can be met with a CCD imager, a feasibility model of the camera is being developed in three stages. First, a 500-element line array camera was constructed, using a Fairchild sensor (CCD-101). This camera served primarily as a learning tool, providing familiarization with general CCD operating characteristics and constraints.

The second phase of development is a breadboard area array camera, to be followed by the feasibility model itself. The feasibility model camera will be designed to use a 400 × 400 element sensor being developed for JPL by Texas Instruments. This will be a thinned, backside illuminated device for maximum quantum efficiency, particularly in the blue and near-ultraviolet. The sensor will also be a buried-channel type, which is expected to provide higher transfer efficiency, lower noise, and improved radiation tolerance compared to a surface-channel device. This is accomplished with the penalty of increased dark current and lower saturation level.

The breadboard camera will initially use a high-performance version of the recently announced RCA 320 × 512 element sensor. This is a surface-channel, front illuminated device developed primarily for standard-rate television applications. It does not, in its present form, offer all of the performance advantages projected for the Texas Instruments sensors but has the distinct advantage of being currently available. Most of the operational characteristics and circuitry requirements are similar to those of the Texas Instruments sensor.

The feasibility model camera will be a single package comprising test optics, electromechanical shutter, CCD sensor with cooling mechanism, and signal processing electronics. External optical filters will be used to demonstrate the camera properties for specific spectral bands. Table 2 summarizes the characteristics of the area array camera, including some parameters specific to the Mariner Jupiter/Uranus application. Figure 3 is a functional block diagram of the camera. A brief description of the various blocks is given in the following paragraphs.

The sensor housing contains the optics, shutter, sensor, cold plate, and cooling radiator. For an acceptable dark signal at the longer frame times, it is anticipated that a sensor temperature of -40°C will be required. This must be accomplished with the surrounding structure at -30°C to +50°C, and while maintaining the position of the sensor relative to the optical focal plane within ~50 μm.

The cooling radiator will provide cooling of the sensor in a simulated space environment, with additional cooling hardware required for bench operation. Also in bench operation, the sensor housing will be purged with dry nitrogen to prevent condensation of moisture.

The signal processor performs dc restoration and filtering of the raw sensor output signal prior to conversion to a serial digital data stream by the analog/digital converter. The sensor uses the standard "gated-charge" pre-amplifier, and one of the primary functions of the signal processor is minimization of the reset noise associated with this type of device. The performance of the signal processor is expected to be independent of the sample frequency (sensor clock frequency), thus simplifying the implementation of variable-rate operation. The analog/digital converter is a commercial 10-bit unit. CCD cameras are expected to have a larger dynamic range than can be encoded in 10 bits, so the signal processor will have adjustable gain.

The balance of the circuitry provides timing and control and bias to the sensor and shutter, and multiplexes the digital video with camera status data to create the composite serial data.

Table 3 lists the projected performance specifications for the camera. The camera performance will be highly dependent on the sensor characteristics, and is therefore somewhat speculative. (One goal of the program is to provide a test vehicle for assessment of sensor performance in a typical spacecraft application.)

The feasibility model camera will be subjected to a test program designed to verify and demonstrate the suitability of a CCD camera for a Mariner-type mission, including performance and environmental considerations. This testing will include characterization of the performance parameters listed in Table 3: temperature, thermal-vacuum (space simulator), vibration, and radiation.

The emphasis will be on identifying and solving problems. Specific areas of concern are sensor cooling and mounting, gradients in the sensor, focal plane shifts, and radiation compatibility (both damage and interference effects).

IV. CONCLUSIONS

We have described the general constraints placed on camera design for a planetary spacecraft, the potential advantages of CCDs in meeting these constraints, and two specific camera implementations. Success of these camera development efforts will be largely dependent upon progress in sensor development.

Current sensors exhibit a high degree of spatial nonuniformity of response. Significant improvement in this area will be required to meet the stated instrument performance goals.

Another concern is temporal stability. While CCD sensors are ultimately expected to have the inherent stability of a silicon device, this has not been realized in current devices.

Perhaps the most difficult problem is the development of sensor thinning technology to achieve high quantum efficiency and blue/UV response. Potential problems are warping and distortion of the sensor due to thermal gradients and other effects, and mounting and cooling problems.

Finally, radiation tolerance is an important problem for most projected planetary missions. Devices must be developed which minimize radiation effects, and those effects must be well understood to allow appropriate shielding and other precautions.

For future camera development, expansion to larger formats will be the primary goal. If this is to be accomplished with larger monolithic arrays, improvements in dark current and transfer efficiency will be required. Also, larger arrays will aggravate the thinning problem. An alternate implementation of the larger format involves the use of multiple sensor mosaicking, either by mounting the sensors side by side in the image plane, or by the use of optical image splitting. Neither method is completely satisfactory, the first leaving gaps in the image and the second resulting in greater optical system complexity and sensor mounting problems.

In summary, it appears that CCD cameras can play an important role in future planetary explorations, and that the potential performance advantages justify continued intensive development effort.

Table 1. Line scan imager characteristics

Sensors	Three 160 × 5 CCDs, buried-channel, backside illuminated, three-phase, double-level aluminum gates
IMC	Compensates for spacecraft roll
Multispectral	Three bands
Telescope	Focal length 229 mm, f/2.3
Stepper	Five-line increments through 165 deg
Sequencer	Automatic stepping in look angle
Size	0.25 × 0.25 × 0.50 m
Weight	7 kg
Power	10 W
Angular resolution	100 μr/pixel
Frame format	160 × 640 pixels, quarter and half frame allowed
Field of view	1 × 4 deg full frame
Noise equivalent exposure	2 $\mu J/m^2$ in 2854°K illumination
Encoding	8 bits/pixel
Data rates	Sixty-four rates from 0.5 to 8 Mbps

Table 2. Area array camera characteristics

Sensor	Texas Instruments, buried, backside
Image (raster) format	400 × 400 elements
Pixel pitch	23 μm
Image size	9.2 × 9.2 mm
Signal processing	Baseband, filtered, dc restored
Signal encoding	10 bits/pixel
Spectral filters	External to camera
Exposure times	2 - 2048 ms, 2× steps
Serial data rates	7.81 - 250 kbps, 2× steps
Frame readout times	210 - 6.56 s, 2× steps
Operating modes	1. Expose and read 2. Expose and hold 3. Read without exposing 4. Inhibit
Optics*	Focal length 1500 mm, f/8.5
Angular resolution*	15.3 μr/pixel
Shutter*	Two-blade electromechanical
Sensor cooling*	Nominal -40°C, external radiator
Size*	3000 cm^3
Weight*	4 kg (plus optics weight)
Power*	12 W

*Mariner Jupiter/Uranus application.

Table 3. Area array camera performance specifications

Saturation charge	$\sim 5 \times 10^5$ electrons
Saturation exposure	$< 10^4$ $\mu J/m^2$ at 2854°K
Noise equivalent exposure	< 2 $\mu J/m^2$ at 2854°K
Dynamic range	$> 2 \times 10^3$
Dark charge	< 5% of saturation at 13 s, -40°C
Squarewave response	> 30% at 22 lp/mm
Quantum efficiency	> 20% at 400 nm > 50% at 600 nm > 50% at 800 nm > 5% at 1000 nm

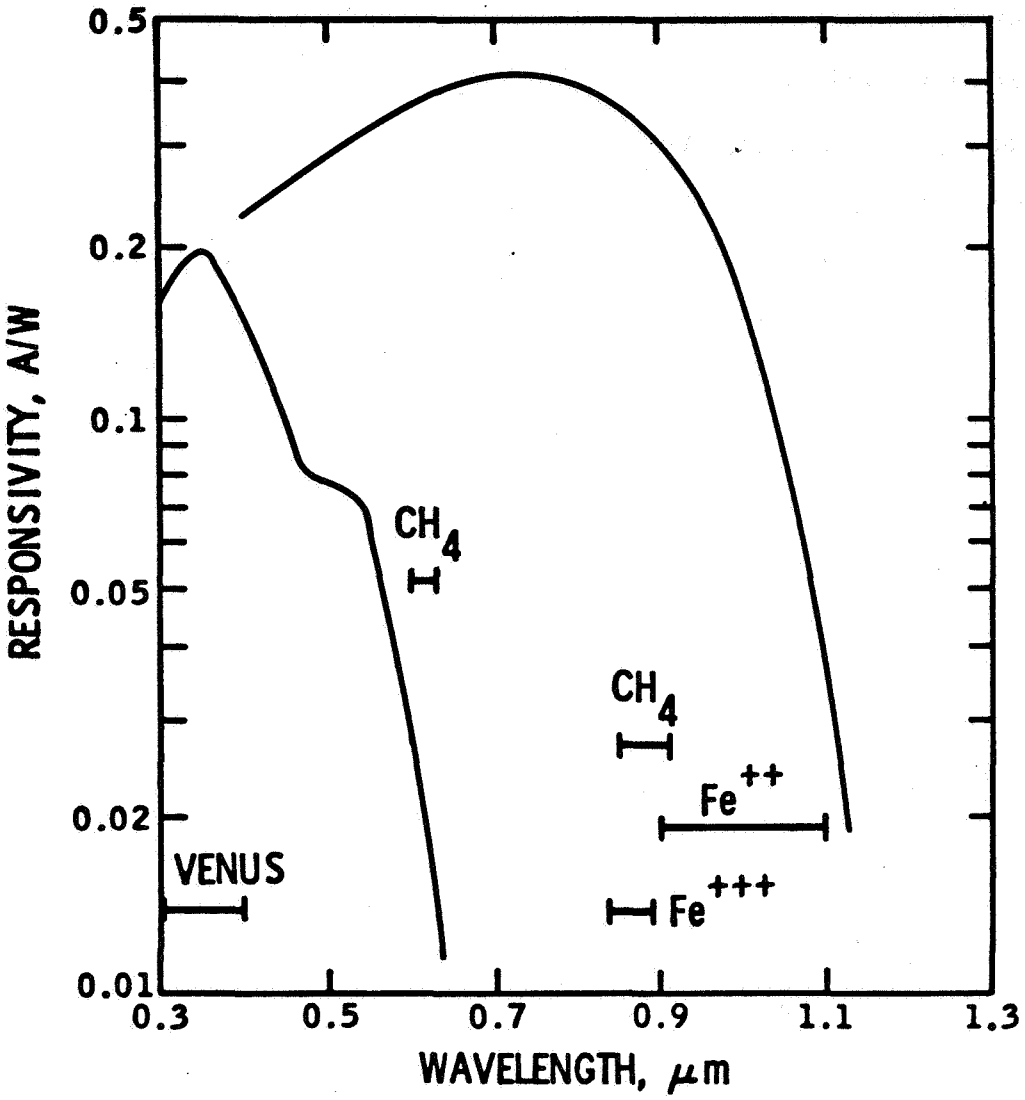

Figure 1. Typical spectral bands of interest to planetary scientists (Response curves for selenium-sulfur vidicon and CCD are superimposed.)

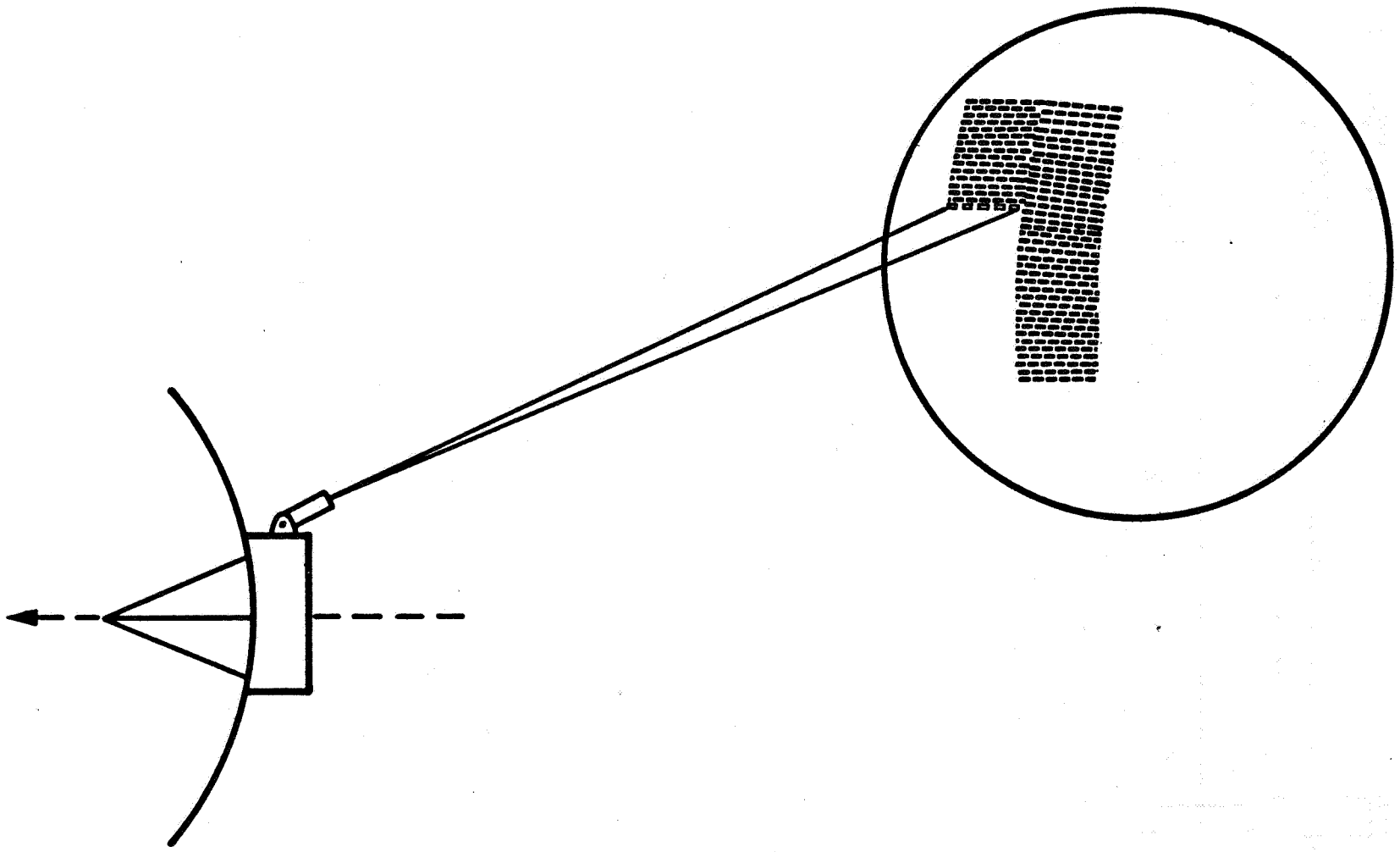

Figure 2. Method of image formation by line scan camera (Scan is from top to bottom.)

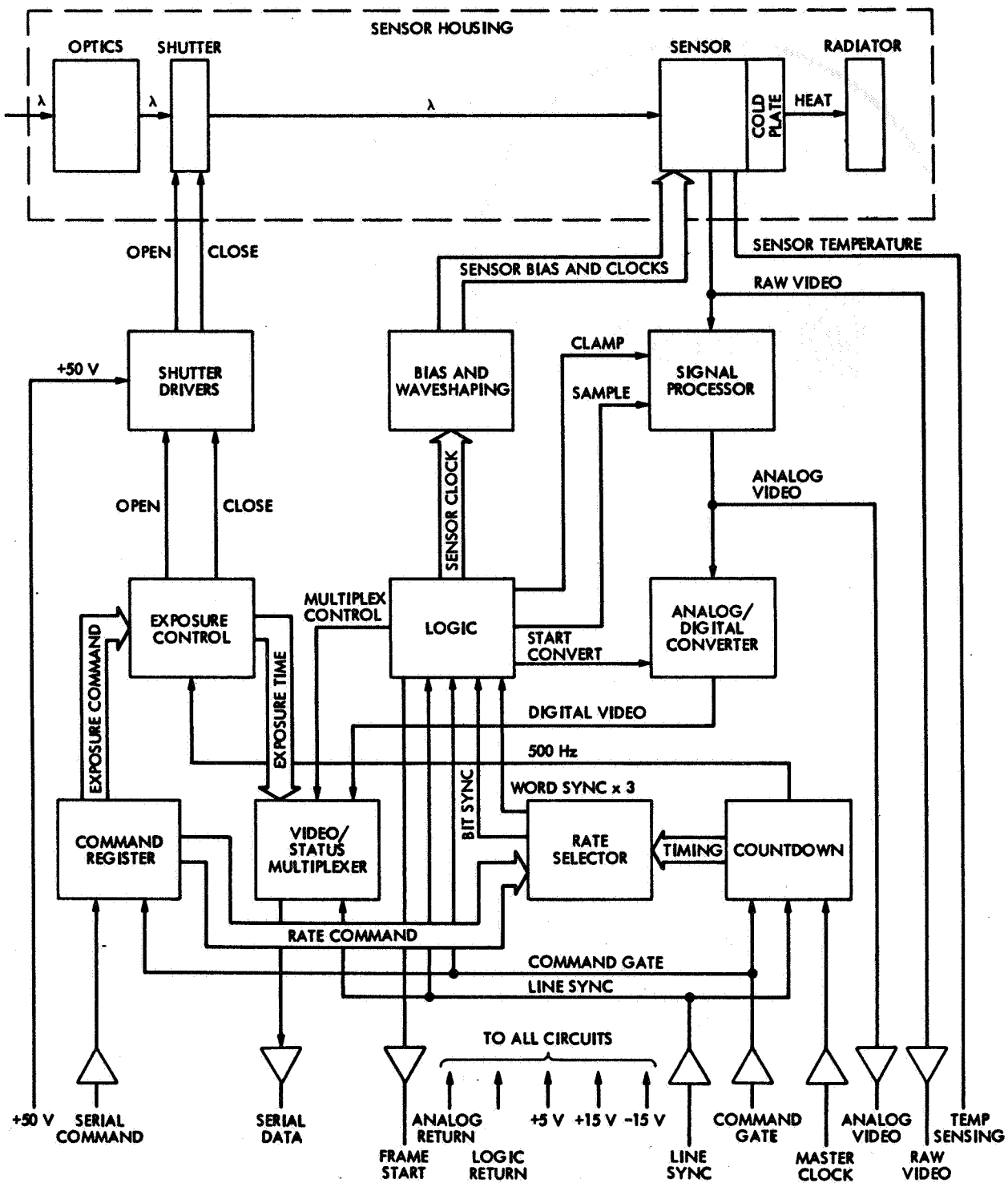

Figure 3. Functional block diagram for feasibility model area array camera

POTENTIAL USEFULNESS OF CCD IMAGERS IN ASTRONOMY

Thomas B. McCord and Jeffrey P. Bosel
Massachusetts Institute of Technology
Cambridge, Massachusetts

Two-dimensional detectors have been important in astronomy since the earliest days of the science. Recently, the requirements for greater photometric accuracy, sensitivity and spectral coverage have driven the search for better imaging devices. Electron-beam readout devices with a variety of target materials and intensification schemes, including the SEC and silicon vidicons, have been used successfully. The CCD as an image detector has several potential advantages over electron-beam read-out devices; low noise, simple construction and geometric stability are among them.

Two-dimensional photo-detectors have been used extensively in astronomy since its beginning. The human eye and later the photographic films were used almost exclusively. In the past 10-20 years, a variety of electronic detectors have been tested and a few have been used for actual observations at the telescope. These devices are used for finding, tracking and general field viewing as a substitute for the human eye. More importantly, they are used for quantitative measurement of the direct image as well as of the spectrum of extended objects and point sources.

The charge-coupled device (CCD) is the latest in a series of photon-to-charge-carrier conversion devices and is one that may come closest to being the "perfect" detector. I have been asked to discuss briefly what detector properties are important to the groundbased astronomer and how the CCD might satisfy the astronomer's needs.

The CCD is a silicon wafer onto which a structure of electrodes has been deposited. The silicon wafer is the photo-sensitive material in which photons are converted to charge carriers and the optical properties of the detectors are to first order those of silicon. The charge carriers are collected and stored in potential wells created on the silicon wafer by potentials on the electrodes. At an appropriate time, the stored charge can be shifted across the wafer through a charge-sensitive amplifier and converted to a video signal. Because the potential wells are discrete elements in an array across the wafer, the detector becomes, in effect, an array of discrete abutting photosensors.

Experience with two-dimensional silicon photo-detectors has been gathered through study of the silicon diode array vidicon. This device has recently been put to use in astronomy (Ref. 1). Several at-the-telescope testing programs have been reported (Refs. 2 and 3) and the device is now in routine service for scientific use (Refs. 4 and 5).

Many problems with the silicon vidicon have to do with the electron beam readout and the external preamplifier. The CCD is read out directly and its preamplifier is manufactured on the silicon wafer. Considering the high performance of silicon vidicons, the CCD is potentially quite useful to the astronomer. In fact it is my impression that the center of effort of the image detector development program in astronomy is rapidly shifting to the CCD.

Although I will center my attention on groundbased astronomical needs, I should mention that CCD detectors almost surely will find their way into the new spacecraft-borne telescope programs. The properties which make the CCD useful here on earth will also apply in space. In addition, as I am sure will be discussed elsewhere in this program, the small size and the low power requirement of the CCD will help make it suitable for space.

The variety of observations made by astronomers assures that no one single detector will ever satisfy all requirements. Point source images (stars) and extended sources (planets, nebulae, galaxies) are observed. Spectra of all these objects are imaged like extended sources. The size of the point source is limited by the magnification and diffraction of the telescope optics and by atmospheric turbulence. The spectral range is limited by atmospheric adsorption at short wavelength and by background thermal emission at long

wavelength. Table 1 lists the range of conditions under which imaging might be carried out.

The properties and performance for several currently used two-dimensional imaging devices are given in Table 2. These values are often approximate and in some cases there is disagreement among astronomers about the performance. We give our impression of the present state of the art.

The quantum efficiency and spectral range are limited by the photo-cathode for the SEC and SIT and by silicon and its surface coatings for the silicon vidicon and the CCD. Maximum signal is limited by charge storage; capability and minimum signal are equal to preamplifier noise. The range of linearity, the slope of the response curve γ and the photometric precisions are a property of the entire detector-readout system.

The CCD compares favorably with the other detectors. Unless unexpected problems arise, it will be an important device in astronomy. The most important properties to improve, we believe, are the minimum detectable signal and the array size. Spectral coverage and quantum efficiency are also very important.

Table 1. An attempt at defining the range of conditions under which telescope observations may be carried out

Measurement precision	0.1 - 10%
Object size	$\geq$10 μm
Field	1 - 300 mm
Intensity	10 - 10^6 photons/pixel
$\lambda\lambda$	0.3 - 3.0 μm
$\nabla\lambda$	10^{-2} Å - 10^4 Å
Exposure	10^{-2} - 2×10^4 seconds

Table 2. Performance of several two-dimensional detectors as gleaned from personal contact with a variety of astronomers working with experimental systems intended for use in astronomy

Properties	Film	Sec	SI vidicon	SIT	CCD (present)	CCD (future)	Desirable
Q.E. (%)	≤1	1 - 15	1 - 70	1 - 15	~1 - 50	≤60	100
Spectral coverage (μm)	≤0.9	0.4 - 0.85	0.34 - 1.10	0.37 - 0.85	0.4 - 1.0	≤1.10	≤3
Max. signal (photoevents/pixel)	$\leq 5 \times 10^4$	2000	$\sim 10^6$	$\sim 10^3$	$10^5 - 10^6$	$\sim 10^6$	10^6
Min. det. sig. (photoevents/pixel)	≥500	4	300	2	~300	~10	1
Linear range	$10^2 - 10^3$	~500	$\geq 10^3$	$\geq 10^3$	?	$\geq 10^5$	10^6
Gamma	varies	?	1.00 (0)	0.97	?	1.00	1.00000
Photometric prec.	Few percent	1.2 × photon noise	Photon noise limited	Photon noise limited	≤1%	Photon noise limited(?)	Photon noise limited
Array size (pixels)	$3 \times 10^4 - 3 \times 10^4$	$10^3 \times 10^3$	500 × 500	500 × 500	100 × 100	500 × 500	$10^4 \times 10^4$
Pixel size (μm)	10	25	25 - 50	25 - 50	25	25	10
Digital readout	No	Yes	Yes	Yes	Yes	Yes	Yes
Cooling	No	No	Yes	Yes	Yes	Yes	No
Fragility (1 - 3)	3	1	2	2	3	3	3
Cost	Cheap	1000	250	1200	500	≤1000	Cheap
Prestorage gain	—	50 - 100	1	1000	1	1	1

ACKNOWLEDGEMENTS

The authors thank P. Crane, J. Westphal and S. Colgate for helpful comments on Table 2. This work was supported by NSF Grant GP31516.

REFERENCES

1. McCord, T. B., and J. A. Westphal. "Two-Dimensional Silicon Vidicon Astronomical Photometer," Applied Optics, 11, 522-526 (1972).

2. Crane, P., and M. Davis. "Characteristics of the Silicon Diode Vidicon," Astron. Soc. Poc., in press (1975).

3. McCord, T. B., and M. Frankston. "Observational Experience with Silicon Diode at the Telescope," Applied Optics, in press (1975).

4. Pieters, C., T. B. McCord, M. Charette, and J. B. Adams. "Dark Mantling Material in the Apollo 17 Soil Samples," Science, 183, 1191-1194 (1974).

5. Schild, R., M. Frankston, and T. B. McCord. "Observation of a Red Nuclear Halo in NGC 4565," Ap. J. Letters, in press (1975).

PLANETARY INVESTIGATION UTILIZING AN IMAGING SPECTROMETER SYSTEM BASED UPON CHARGE INJECTION TECHNOLOGY

R. B. Wattson, P. Harvey, and R. Swift
American Science & Engineering, Inc.
Cambridge, Massachusetts

An intrinsic silicon charge injection device (CID) television sensor array has been used in conjunction with a $CaMoO_4$ co-linear tunable acousto-optic filter, Harvard's 61-inch reflector, a sophisticated computer system, and a digital color TV scan converter/computer to produce near-IR images of Saturn and Jupiter with 10-Å spectral resolution and ~3-inch spatial resolution.

The CID camera has successfully obtained digitized 100 × 100 array images with 5 minutes of exposure time, slow-scanned readout to a computer (300 ms and digitized to 12-bit accuracy), and has produced this data at near dry ice temperature and in conjunction with other state-of-the-art technology instrumentation. Details of the equipment setup, innovations, problems, experience, data and final equipment performance limits are given, so that those people who plan to utilize solid-state TV sensor arrays will be able to judge, at least in part, which technology, CCD or CID, they should choose. Twelve spectral images of Saturn are shown, 40 Å apart (centered at 8500 Å), which will illustrate the type of data now obtainable with present CID technology. It is our belief that the

data represents the first instance of truly three-dimensional astronomical data that has been obtained.

I. INTRODUCTION

Figures 1a and b are images of Saturn having ~3-inch spatial resolution. Each image represents a 10-Å spectral bandpass in the near infrared, and required about 5 minutes of exposure due to the narrow bandpass. The twelve spectral images of Figure 1a are generally 40 Å apart, as indicated by the central wavelengths shown below each image (the first image should indicate 9400 Å). Although some corrections for background and noise have been applied, it is not valid to compare the overall intensities of different spectral images. However, the variation of ball-to-ring intensity ratios for the different images is significant. The absence of Saturn's ball at 8900 Å and 8860 Å and the depression of the ball relative to the rings near 8700 Å is clearly evident. Note also the bright equatorial bulge in the planet seen at 8780 Å. This may be caused by higher clouds and hence less methane absorption near Saturn's equatorial region. It is interesting to compare the relative ball-to-ring intensities vs. wavelength with the reflectivity spectrum of Jupiter shown in Figure 2, from Pilcher et al. (Ref. 1). The dots, indicating the wavelengths of the Saturn images of Figure 1a, encompass a methane double absorption feature with a strong dip at 8900 Å and a more moderate dip at 8700 Å. The spectral resolution is 10 Å in both Figures 1 and 2.

Figure 1b shows both a spectral image of Saturn (8660 Å) and a spatial intensity plot for a line through the planet. The location of the line is indicated by tick marks on the image. Note the good S/N (~20:1) of the plot. The intensity scans for Saturn's ball are essentially limb-darkening curves. These curves are being analyzed by fitting to Minnaert functions for various wavelengths.

These and other spectral images of Saturn, ranging from 7200 Å to 10,600 Å (i.e., essentially the range covered by Figure 2), and a similar set of images of Jupiter, were obtained from data taken at Harvard's 61-inch reflector during December 1974 and early January 1975. They were acquired by the use of a new type of instrumentation, an imaging spectrometer, which is the subject of this paper.

II. DESCRIPTION OF INSTRUMENTATION

Figure 3a shows a schematic of the imaging spectrometer. Figure 3b is a picture of the instrument, which is about 2 feet long. It consists of two principal parts: a tunable acousto-optic filter (TOF) (Ref. 2) and a charge injection device (CID) camera (Ref. 3). The TOF is similar in throughput and transmission characteristics to an interference filter of comparable resolution, except that it is electronically tunable over a 2:1 wavelength range. The TOF utilizes a pair of crossed calcite Glan-Thompson polarizers, between which is placed a bi-refringent $CaMoO_4$ crystal. Acoustic waves, produced by a voltage-controlled oscillator and piezo-electric transducer, are propagated axially through the bi-refringent crystal and absorbed at the opposite end. Polarized light transmitted through the crystal in a direction co-linear with the acoustic waves interacts with the acoustic field in such a way that only a narrow range of wavelengths, related to the acoustic frequency, is scattered into the other polarization state and is thus transmitted by the output polarizer. The filter's bandpass is basically determined by the same characteristic that determines the bandpass of a diffraction grating monochromator: the number of grating rulings; correspondingly, in the TOF, the number of acoustic waves in the crystal determines its resolution. Computer control of the rf driving frequency is possible.

The other optics of the imaging spectrometer include relay lenses to transmit the primary telescope image through the TOF and onto the CID chip; a beam splitter, reticle and eyepiece which are used for manual guidance of the telescope during exposure; and a cylindrical lens to correct for the astigmatism produced by the TOF's bi-refringence.

The CID camera is basically an intrinsic silicon 100 × 100 sensor array, wherein each sensor is ~0.1 mm square. Each sensor has a quantum efficiency of ~50% at 9000 Å and, at -40° C, shows only moderate integrated dark current after 5 minutes exposure time. The CID, like the CCD cameras, employs a passive solid-state digital readout mode instead of either the active digital readout mode of photodiode arrays such as Reticon arrays or an electron-beam readout mode as exemplified by the silicon target vidicon cameras. Highly monochromatic radiation, such as is used in this system, may produce interference effects in a vidicon system. No such effect has been observed with the present TOF/CID system having a 10-Å bandpass.

The charge injection device readout employs the injection of a particular sensor's charge into the silicon substrate via the voltage change across a row/column addressed capacitor at the sensor site. Other sensor sites along the particular row or column only have their charges shifted. With this technique, random sensor interrogation could be achieved if desired. Charge-coupled technology, on the other hand, requires many transfers via capacitor plates to translate the entire charge pattern resulting from the image to a storage area for line-by-line readout, thereby requiring extremely high transfer efficiency.

The GE CID camera, which was originally designed for standard TV frame rates, had a readout rate fixed at about 300 kHz continuous, and used a triggered analog sweep system, so that after injection significant amounts of signal remained uncollected. At AS&E, the camera was modified by installing interrupt circuitry to hold the digital camera sweep at the beginning of the first field until triggered by a computer, one sweep at a time. The injection time was increased and the internal readout clock rate decreased; a digital monitor sweep system was constructed which would track the camera sweep regardless of rate. The output signals were amplified, DC restored, digitized, and sent via line drivers to the computer.

The CID chip was found to saturate on dark current in about 3 seconds at room temperature. Since the expected signals would require integration for much longer periods of time, it was necessary to cool the CID chip to reduce both the dark current and its associated shot noise. The characteristics of reverse-biased Si are such that the dark current can be expected to decrease by approximately a factor of two for every 10° C cooling. Thus, at the temperature of dry ice, or some 100° C below room temperature, we would expect to be able to integrate for about half an hour without dark current saturation.

In order to achieve such cooling, the CID chip was removed from its socket in the camera body and mounted on an ~1-inch extender, so that it could be located within a cooled, insulated enclosure. The extender was fabricated from a spare header and socket, provided by GE, sandwiched around a block of lucite. The interconnections were made by means of fine (#30) wire to minimize heat conduction. The enclosure is (literally) a peanut can, lined with polystyrene foam and provided with a double-paned window, evacuated between the panes to provide a thermal barrier that does not frost. The assembly was

attached to the camera body at the normal lens location. The enclosure was continuously purged with dry nitrogen gas to prevent fogging.

Cooling was done by thermally coupling the CID to a brass heat sink, through which cold alcohol was pumped. Anhydrous, denatured alcohol and 1/4-inch tubing were used to prevent the fluid viscosity from restricting the flow. Several coils of copper tubing immersed in a dry ice/alcohol slurry served as a heat exchanger through which the coolant was circulated. The slurry temperature was about -55° C. This operating temperature for the CID chip is consistent with dark current saturation after ~20 minutes. Dark current buildup was hardly detectable after 5 minutes of integration time.

Experience with the CID camera, operated under extremely cold (-15° C) and also under humid ambient conditions, showed that modification and refurbishment of both the prototype electronics and the CID sensor array were needed. With strong cooperation from GE, both were done. Because of the longer injection times and the small capacitances involved in the readout circuitry, the printed circuit board became a significant leakage path due to condensation or humidity in the telescope environment. The problem was overcome by thoroughly cleaning and drying the board and spraying it with Krylon clear plastic. Hermetic sealing of the CID chip, to overcome moisture contamination problems, was done at GE. Very little difficulty with the CID camera has been experienced since these changes were made. The data and accumulated experience indicate that the expertise now exists to allow reliable field use of CID cameras, at least for ground-based observational purposes.

Frame integration time was determined by the operator, who had control of the system via an alphanumeric computer terminal. When the program determines that an exposure is complete, the computer initiates the CID readout mode. The 10^4-word, 12-bit readout of the CID camera was read directly into the 32K core of a NOVA 1200 via the data channel. The data were then stored on digital tape and, for random access to spectral image frames, stored also on magnetic discs.

One of the main design philosophies of the system was real-time display of the data, allowing the operator to exercise his judgment to repeat exposures and/or modify or improve the data acquisition parameters based upon the observed results. Hence, a display computer/scan converter and a color TV

monitor were used to immediately view the images as they were acquired. The use of color can enhance the observer's ability to discriminate against improper data. Some degree of processing can also be accomplished before display. Various other display modes such as alphanumeric information and plots are available at the operator's command. The images shown in Figure 1 were produced directly via this display system.

Finally, the entire computer support facility (shown in Figure 4) is portable. It is sufficiently small and reliable to be transported and operated anywhere, having already been used at several sites without major difficulty.

III. CONCLUSIONS

The data displayed here represents only the first very preliminary and relatively crude data obtained by an imaging spectrometer system designed for astronomical observations. Improvements of factors of 3 or more in instrumental sensitivity, spatial resolution and demonstrable spectral resolution can be made by improved CID preamp design, reduced residual bi-refringent aberrations and extended observation time. Careful photometric calibration and spatial, spectral and vignetting corrections, combined with use of observation sites more suited to planetary observations (i.e., observation sites where relatively long exposures can be accomplished with 1-inch or better "seeing" and guiding characteristics), will provide very useful new planetary results. Extension of the spectral response to the 5-μm region is possible by the use of InSb CIDs and TeO_2 TOFs. Observation sites located above the earth's atmosphere would eliminate atmospheric interference in that spectral region, and would extend the spatial resolution to the diffraction limit. Finally, sophisticated radiative transfer algorithms employing anisotropic, inhomogeneous atmospheric modeling will enable one to construct, via planetary atmospheric molecular absorption features, truly three-dimensional pressure, temperature, constituent and aerosol maps of planetary atmospheres. Such pixel-by-pixel "sounding" maps can be made with the existing equipment for CH_4 and NH_3 on Jupiter and Saturn, CO_2 on Venus and, in fact, the present spectral resolution may even allow 1-inch maps separating the J-manifolds of the R-branch $3\nu_3$, CH_4 band! Hence, one could say that the technique described above represents the beginning of true 3-D planetary astronomy.

ACKNOWLEDGEMENTS

Much appreciation is extended to the directors and staff of the Harvard Observatory for their strong cooperation in the observational program. The authors would also like to thank Dr. Edwin Frederick and Dr. Saul Rappaport as co-observators, and Richard Cabral and Douglas Hill for their very helpful engineering in this effort.

REFERENCES

1. C. B. Pilcher, R. G. Prinn, and T. B. McCord, J. Atmos. Sci., 30, 302 (1973).

2. S. E. Harris, S. T. K. Nieh, and D. K. Winslow, "Electronically Tunable Acousto-Optic Filter," Applied Physics Letters, 15, 325 (1969).

3. G. J. Michon and H. K. Burke, "Charge Injection Imaging," IEEE International Solid-State Circuits Conference Digest, 138-139 (1973).

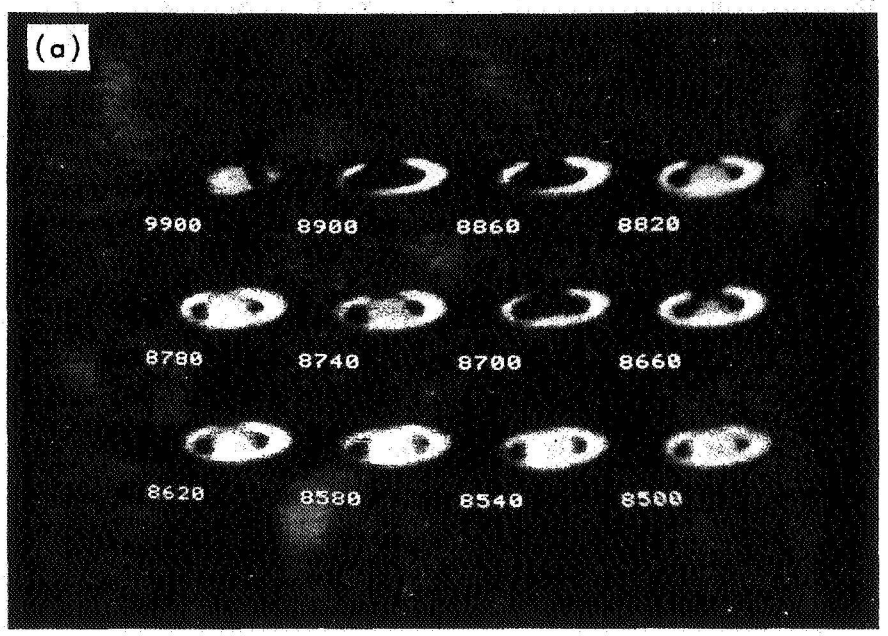

Figure 1a. Twelve images of Saturn at wavelengths ranging from 8500 to 9400 Å

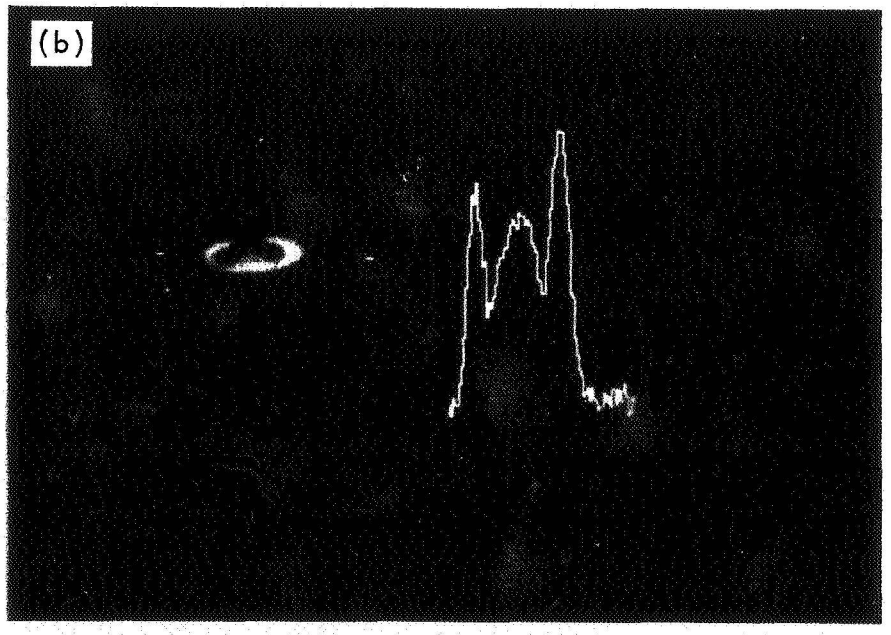

Figure 1b. Spectral image and cross-sectional intensity plot of Saturn at 8660 Å

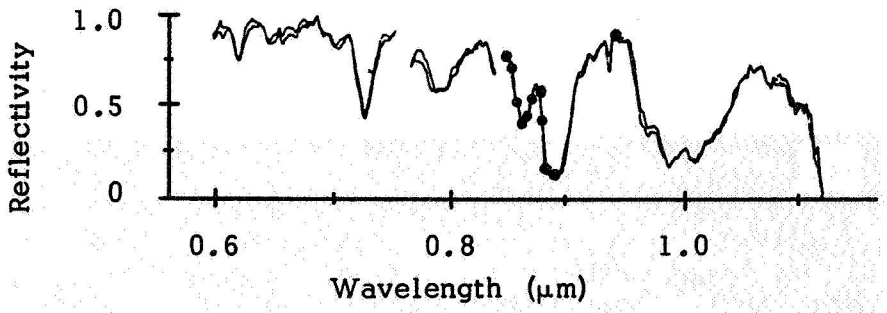

Figure 2. Absolute reflectivities of Jupiter (Ref. 1)

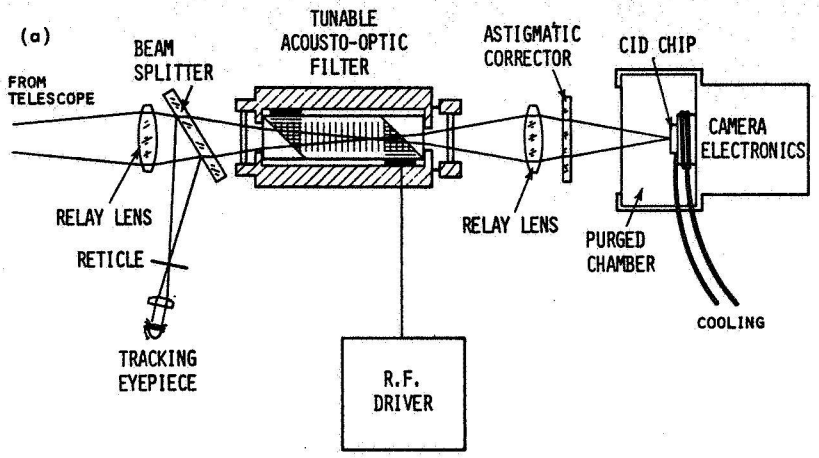

Figure 3a. Schematic diagram showing principal components of the imaging spectrometer

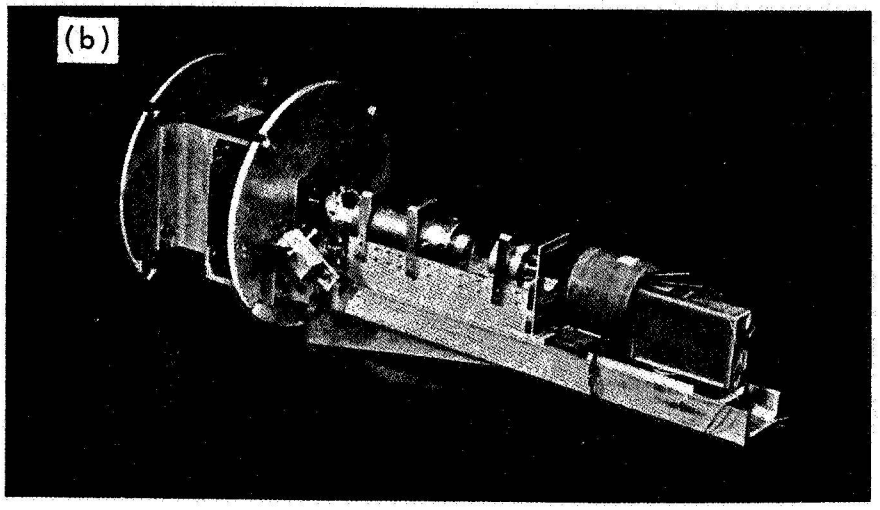

Figure 3b. Photograph of the imaging spectrometer

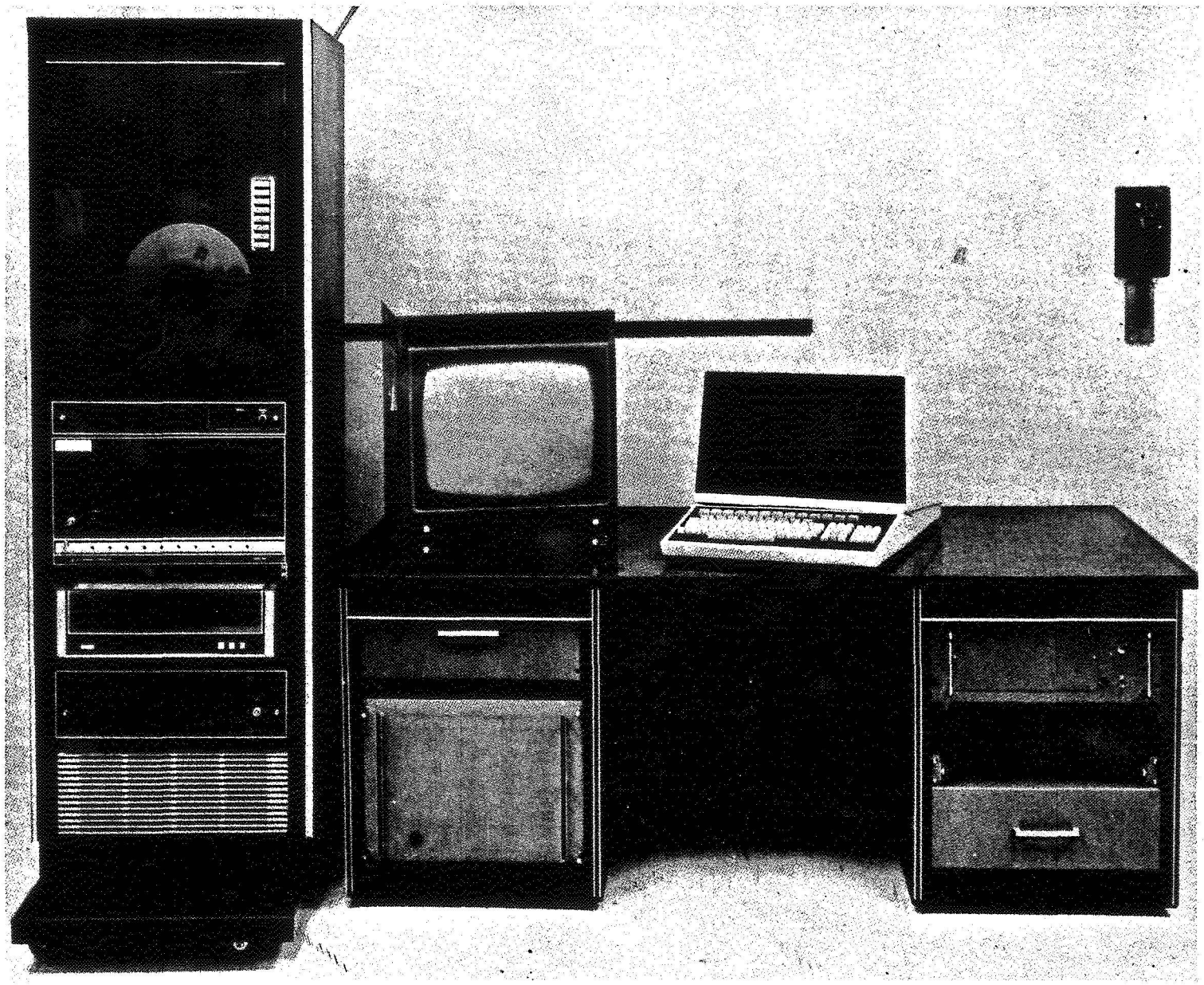

Figure 4. Processing and display facility

ON A PHOTON-COUNTING ARRAY USING THE FAIRCHILD CCD-201

D. G. Currie
University of Maryland
College Park, Maryland

Current work on the evaluation of certain performance parameters of the Fairchild CCD-201 and the proposed method of operation of an electron-bombarded charge-coupled device will be described. This device will be used in two different applications in the multi-aperture amplitude interferometer now being fabricated at the University of Maryland. The first application uses an array of sensors in the aperture plane of a telescope. The requirements are: discrimination between single, double, and triple photoelectron events in a pixel frame scan time of a few milliseconds, and an array of at least 60 × 30 pixels. The second application, which is in the focal plane and operates with very high contrast illumination, should have a single photoelectron sensitivity and a minimum of blooming and lag. Theory of operation of a device which uses the Fairchild CCD-201 and satisfies both of these requirements will be discussed. The expected blooming characteristics will also be considered. Work in progress at the University of Maryland on the evaluation of the parameters relevant to remote, low-noise operation of the Fairchild CCD-201 will be described. These tests have been conducted using light input. The video data from the CCD are amplified, digitized, stored in a minicomputer core memory, and then recorded on magnetic tape. The frames of data are then analyzed on a Univac 1108 using a set of specialized programs which

permit a statistical analysis of the variation of the single level across a single frame. These programs also permit evaluation of the performance of a given pixel in a sequence of frames, followed by an "across the frame" evaluation of the statistical properties. To handle the data from the ICCD, a circulating semiconductor memory has been designed and fabricated to handle five frames of data with an accuracy of 16 bits at a 4-MHz data rate. This operates in conjunction with a minicomputer, which controls the operation of the circulating semiconductor memory and serves as an intermediate data storage.

I. INTRODUCTION

In the following, we discuss the work being done at the University of Maryland on the internally intensified charge-coupled device (ICCD). The details of the actual tube, which is being fabricated by the Electronic Vision Company, are described in detail in the paper by John Choisser (Proceedings of this Symposium). The ICCD will be operated as a photon-counting array detector.

An incident photon is converted to a photoelectron with a standard photocathode (S-20, for example). This photoelectron is then accelerated to an energy of about 15 keV and electrostatically focused onto the front surface of a Fairchild CCD-201. Within a particular photosite on the CCD, the photoelectron creates many hole-electron pairs by ionization. These charges for a single photoelectron are collected and produce an easily detectable charge packet. These charge packets are "scanned" from the CCD by the conventional clock pulse trains. After on-chip amplification, the signals leave on a single video output line. This data is then electronically processed to detect the charge packet produced by each photoelectron. The information is then processed on-line and stored in a special memory, which can operate at video data rates.

II. PHOTO SENSOR REQUIREMENTS

This development effort with the ICCD is motivated by two different applications with significantly different requirements.

A. Amplitude Interferometer Requirements

The primary application of the ICCD will be as the light sensor for a special instrument, the multi-aperture amplitude interferometer (MAAI). This instrument is a multi-channel version of a similar instrument, which has been used in an astronomical observation program over the last few years (Refs. 1, 2, 3). Basically, this application requires an array of photosensors, each of which acts as a photomultiplier. Thus, the requirements are:

(1) The ability to discriminate on single photoelectrons
(2) The scan of an entire frame in a few milliseconds
(3) Very low lag, or memory from one frame to the next frame
(4) Minimal crosstalk between spatial channels (or pixels)
(5) The ability to distinguish reliably among zero, one, two, or more photoelectrons per pixel per scan.

B. Imaging Camera Requirements

The other application, which is related to the MAAI, consists of an imaging camera in the focal plane of the telescope. For this application, the requirements consist of items 1, 2, 3, and 4 listed in Section A, as well as

(1) Very large dynamic range
(2) Very low blooming

The electronic operating conditions for the ICCD will be somewhat different in order to satisfy the different requirements of the two applications.

III. METHOD OF CCD OPERATION

A. Theory of Operation of the CCD

The Fairchild CCD-201 will be bombarded by electrons arriving in the front of the CCD. The transfer registers, which carry the charge from the photosensitive sites to the on-chip preamplifier, operate independently and at the same time as the integration of charge at the photosites. Thus, the transfers or "scanning" can take place during the integration period, and eventually the array is sensitive all the time. These transfer registers are protected by a layer of aluminum, so that the bombarding electrons cannot produce any ionization or "noise" in the registers. In the operational data system, the scanning procedure is controlled by an external device [the cir-

culating semiconductor memory (CSM)], which may be programmed to scan a portion of the 100 × 100 array, or the entire array.

B. Operation of the CCD

In order to operate the light sensor on the telescope, a long cable from the electronics to the camera head is required. To handle this, a special camera head has been fabricated which minimizes the crosstalk and coherent noise. The pulse trains are transmitted to the telescope on high-impedance lines. These are converted to the required high-current pulses by clock drivers in the camera head. The camera head also contains amplifiers, a sample and hold circuit, and a discriminator.

C. Noise Sources in the Charge-Coupled Device

There are three types of electronic noises which are most significant with respect to ideal photoelectron discrimination operation. These are "random charge noise," "thermal leakage charge," and the variation of the thermal leakage current or the "thermal leakage noise."

1. Random Charge Noise. The random noise is indicated by the variation of the voltage level, from one frame to the next, at a given pixel. For measurements of the random noise, the illumination is presumed to be constant or, as for most of these tests, no illumination. The random noise is characterized by the standard deviation of the voltage at a given pixel for a number of successive frames. This type of noise behaves as if it were Johnson noise dominated by the capacitive input of the on-chip preamplifier. The value of the random noise is essentially independent of temperature (more precisely, it varies inversely as the temperature). At a data rate of 0.5 MHz, the random noise has been measured by Dyck and Jack (Ref. 4) to be about 300 electrons per pixel per scan.

2. Thermal Leakage Current. This "dark current" or thermal leakage current is due to thermally generated charge pairs which are created within the active silicon. The leakage current is parameterized by the average number of electrons which collect at a given pixel during the integration interval (usually the scan or frame time). The value of the thermal leakage charge varies across the frame from pixel to pixel. It decreases by a factor of two when the temperature of the CCD is reduced by 6 or 7°C and decreases

linearly as the integration time is decreased. The average leakage charge across the frame does not significantly affect the ICCD operation, but its variation across the chip may create a problem. The variation of the thermal leakage charge from frame to frame (Poisson noise) would properly be a component of the random noise, but its value is negligible for normal ICCD operation.

3. Thermal Leakage Noise. The thermal leakage noise is the variation of the thermal leakage charge across the array. This will be parameterized by the standard deviation of the thermal leakage charge across the array. More precisely, it is the variation of the mean (over many frames) thermal leakage charge across the array. This latter form of the definition removes the random noise as a component of the thermal leakage noise. It should decrease with temperature at the same rate as the thermal leakage charge and decrease in proportion to the increased data rates. In order to permit single photoelectron discrimination without a change of discriminator level for each pixel, this noise must be reduced by about 100 photoelectrons. This may safely be accomplished by cooling to approximately -20°C.

D. Array Display

In order to study these quantities, an image processing system has been developed at the University of Maryland which permits computer processing of many scanned frames and the determination of these quantities by a standard procedure.

IV. OPERATION OF INTENSIFIED CCD

A. Theory of Intensification

The photoelectron is accelerated to 14.6 keV prior to impact on the CCD. This value is sufficient to produce a large enough charge by ionization to permit the detection of a single photoelectron, but is not sufficient to penetrate the aluminum (and other) layers which form the protection for the transfer registers. Since different regions covering the transfer registers have different thicknesses, the accelerating voltage is chosen so the photoelectron cannot penetrate the thinnest region. In fact, the energy has been further reduced so the photoelectron will not penetrate into the final layer of SiO_2 insulation above the active silicon of the transfer registers. For a photoelectron which impacts the CCD over a photosite, some of the energy is lost in the layers of silicon and silicon dioxide which lie over the photosite. The 14.6-keV electron will encounter either of

two regions over the photosites, which have different thicknesses. Therefore, the photoelectron may have either 8.5 or 9.6 keV upon entry to the active silicon. These detailed calculations are based on a specific model of the CCD architecture which was obtained from R. Dyck of the Fairchild Corporation. For any given device from a particular run, it is expected that there will be significant variations. Thus, these numbers may be considered as a sample calculation.

As a result of the energy of the photoelectron entering the active silicon, we will have the production of charge packets containing 2300 or 2600 electrons, depending on how many layers it has penetrated. The variation of these numbers is relatively small, especially when compared to noise in the on-chip amplifier of 300 electrons.

V. ADVANTAGES OF SINGLE PHOTOELECTRON DISCRIMINATION

In this section, we distinguish between single photoelectron sensitivity and single photoelectron discrimination in a photodetector. In a conventional photomultiplier, this distinction is the difference between operating in an analog or "DC" mode and operating with a discriminator set to trigger at the single photoelectron level. In order to illustrate this distinction more clearly for a television or scanning system, several parameters will now be defined. The nominal CCD-201 has a saturation level of 75 millivolts, which is equivalent to 0.4×10^6 electrons. Under operating conditions similar to those discussed in the previous section, a single photoelectron will produce a charge packet of 2000 electrons.

We presume for the sake of discussion that the thermal leakage charge and the thermal leakage noise are zero. Let us now consider the dynamic range and the noise level for such a detector system. The maximum number of photoelectrons per pixel version is thus 200. If the "random noise" has a value which is larger than 2000 electrons, then the dynamic range is linearly related to the noise level. However, as the noise level decreases, we have the option of a different type of detection based upon the discrete character of the photoelectron. Thus, we may introduce the discriminator and operate in a mode in which, intuitively, the discriminator will never be tripped when there are no photoelectrons. The dynamic range would then be infinite.

From a more practical point of view, a finite noise distribution has a "tail," so there are occasional times when the discriminator is actuated, producing an "electronic dark current." However, the value of the electronic dark current or the probability of tripping this discriminator decreases far more rapidly than linearly with a decreasing noise level. Thus, if the discriminator is set equal to 1000 electrons and the random noise has a value of 1000 electrons (giving an effective collection efficiency of 84%), the probability of tripping the discriminator by the noise in each pixel in a given scan is about 0.16, so the dynamic range is about 1300. If the random noise level is one half as large (500 electrons), then collection efficiency is 98% and the probability of tripping the discriminator is about 2.3%. Thus, the dynamic range is increased by a factor of seven to 2,000,000. This general relation presumes Gaussian statistics for the random noise. Thus, we see the critical importance of decreasing the noise and operating in a single photoelectron discrimination mode, since small reduction in random noise increases the dynamic range by several orders of magnitude rather than by proportional factors.

VI. SATURATION, BLOOMING, AND LAG

In this section, we briefly mention several problems which normally affect scanning sensors.

A. Saturation

Saturation is defined as the departure from a linear relation between input light intensity and output electrical signal. For the moment, we ignore the processes analogous to the computer processing methods which are used to get "linear" results from film by unfolding an H-D curve. The single photoelectron discriminator curve which relates input to output has a break point at 1 photoelectron per pixel per scan. Actually, for normal MAAI operation, this break point occurs at 3 photoelectrons per pixel per scan. This value then parameterizes the single photoelectron discrimination (SPD) saturation. However, if a parallel analog channel is used, the break point for the "analog saturation" is defined by using the nominal 75-millivolt saturation of the CCD-201. For the parameters of the earlier section, this occurs at about 200 photoelectrons per scan per pixel.

B. Blooming

The term "blooming" is used in this discussion to describe the appearance of apparent photo response in pixels which receive no light but are located near pixels which are receiving illumination. There are three types of blooming:

(1) Radial bloom is normally seen in conventional low-light-level devices. It is caused by various mechanisms, including the electron beam spread. There is almost no radial bloom in the CCD due to internal structures in the silicon and the lack of an electron beam.

(2) Vertical bloom occurs due to spilling of charge from an overloaded photosite into the transfer register locations which are "passing by." This occurs at an illumination beyond the analog saturation level, which, in turn, is well beyond the normal operating levels for single photoelectron discrimination.

(3) Horizontal bloom occurs primarily due to a lower transfer efficiency for the horizontal transfer registers operating at 4 MHz. This type of blooming occurs as apparent light in one horizontal line only. Existing data may be used to place an upper limit on the magnitude of this effect. It will produce excess light in a horizontal line which is fainter than the "diffraction spikes" which occur due to the spider in a reflecting astronomical telescope.

C. Lag

Lag describes the residual charge left at a photosite from the previous frame. This is not significant below saturation and should be small above saturation, but it has not yet been measured.

VII. DAMAGE MECHANISMS

When a CCD is bombarded on the front surface by photoelectrons with an energy of 10 to 20 keV, there may be radiation damage which interferes with proper semiconductor operation. While there are a variety of different damage mechanisms, proper operating conditions and some of the special properties of the CCD-201 will prevent a number of these problems. The mechanism which remains most important is related to the effect of holes left in the SiO_2 when

the photoelectron causes ionization in the insulating layers. General radiation damage measurements which have been conducted at the Naval Research Laboratory (Ref. 5) indicate that this type of damage will result in a significant operational lifetime problem. The actual lifetime will depend upon details of operating procedures and conditions. Several further techniques are now being investigated for extending the operating life of the ICCD. One of these techniques consists of increasing the thickness of the aluminum protection. This is one aspect of reducing, as much as possible, the amount of ionization in the critical layers. In addition, there are several procedures that have shown promise in annealing or removing the damage. These techniques have been successful in other types of devices but have not been properly tested on the CCD-201.

VIII. TEST SYSTEM DESCRIPTION

A basic description of the single-scan data system is presented in this section. The voltage sequences which are required to drive the CCD are developed in the video driver unit. This is a separate rack-mounted unit. In addition to the high-impedance pulse trains, this unit also develops the required voltages for driving the CCD. Clock drivers within the camera mount, on the video drive board, convert the high-impedance pulse train into the high-current pulse trains required for the CCD. The actual performance of the CCD, as well as a detailed description of the electronic system will appear in a separate report.

In the Mark II camera head (upgraded), the video output from the CCD is processed in a separate chamber, which is electrically isolated from the chamber in which "scanning" pulse currents are generated. This video processor card contains a preamplifier, a sample and hold amplifier which is gated from the video driver unit, a second amplifier, and a DC restoration circuit.

The output of the video processor card may be amplified and used for a direct CRT display, using special outputs from the video driver unit to provide the proper voltages to form a raster.

The video signal from the video processor card then proceeds to an input/output card in the NOVA 2/10 computer. Here the signal is again sampled and converted from analog to digital form. A special multiplexing circuit then

compacts the 8-bit or 4-bit data from the A/D converter into 16-bit NOVA words. This permits the use of the NOVA direct memory data rate of 1.2 MHz for 16-bit words or a CCD data rate of 4.8 MHz with 4-bit digitization (2.4 MHz for 8-bit digitization).

The control of the NOVA, which includes the storage and selection of the array data, is handled by a Lexiscope CRT terminal. While this data is stored in the NOVA 2/10 core, with the Lexiscope terminal, one can command a bar chart display of a single line in the array. This permits the inspection of the data within the NOVA core prior to recording on magnetic tape. Following this inspection, on command from the Lexiscope, the data is transferred from the NOVA core to the Precision Instruments magnetic tape unit for recording on 9-track magnetic tape.

The magnetic tape is then read by a special program written for the UNIVAC 1108 which unpacks the NOVA words into FORTRAN-readable 36-bit words and/or writes these pictures into an image processing system picture format file. The arrays of data are then processed by the image processing system (IPS), which has been written for the Amplitude Interferometry Program. The output for the IPS employs several of the I/O devices of the Computer Science Center, in particular, teletype display, CRT display, line printer output, or the Computer Science Center digital optical scanner. The image processing system will be described in more detail in separate publications.

The entire single-scan data system is rack-mounted in special shipping containers to permit convenient field operation.

IX. OPERATING DATA SYSTEM

For normal operation of the ICCD on a telescope, there are several additional requirements placed on the data processing system. Since we expect to operate the ICCD at a data rate of 4 MHz, this will require some method of data storage and successive frame addition which has a cycle time of 350 nanoseconds. In order to satisfy the requirements for the MAAI application, a circulating semiconductor memory (CSM) has been fabricated. This unit has five independent tracks, each of which has an ultimate capacity of 12,288 words containing 16 bits. The data is entered through five arithmetic units, which are presently programmed either to add the new data word to the existing word

or to produce a zero. However, the arithmetic unit has the capability of being programmed for a total of 32 logical operations on its two inputs. The data which is circulating in the CSM may be removed on data buses. The data buses from each of the five tracks are multiplexed to a common data bus. This common data bus is connected to the NOVA 2/10 minicomputer core by the direct memory access mode. Thus, the data can be transferred directly from the CSM to the NOVA 2/10.

In this mode, the CSM is serving as a temporary high-speed storage device. However, it serves another purpose. By placing a "skeleton" of control words in the CSM and certain logic and control functions in the hardware, the CSM controls, in detail, the voltages used in scanning of the CCD. In this mode, the CSM controls the horizontal and vertical scanning and inserts the data words between the cortrol words in the CSM. Since this "skeleton" is entered to the CSM via a program contained in the NOVA 2/10, one may enter special skeletons to cause special scanning modes (i.e., scanning a small rectangle in the CCD array). These control modes are defined by interjecting a new control skeleton into the CSM from the NOVA 2/10. The CSM has been completed and presently is operating in stand-alone mode. The interface to the minicomputer has been completed and is being tested. With a modification in a control card, the CSM can also do real-time subtraction of sky background.

REFERENCES

1. D.G. Currie, "On a Detection Scheme for an Amplitude Interferometer," NAS-NRC Woods Hole Summer Study on Synthetic Aperture Optics, 1968.

2. D.G. Currie, "On the Atmospheric Properties Affecting an Amplitude Interferometer," NAS-NRC Woods Hole Summer Study on Synthetic Aperture Optics, 1968.

3. D.G. Currie, S.L. Knapp, and K.M. Liewer, "Four Stellar-Diameter Measurements by a New Technique: Amplitude Interferometry," Astrophys. J., Vol. 187, No. 1, Part 1, January 1974.

4. R.H. Dyck and M.D. Jack, Low Light Level Performance on the CCD-201, Fairchild Corp. Internal Report.

5. J.M. Killiany, W.D. Baker, N.S. Seks, and D.F. Barbe, "Effects of Ionizing Radiation on Charge Coupled Device Structure," IMEE Transactions on Nuclear Science, Vol. NS-21, December 1974, p. 193.

SOFT X-RAY DETECTION WITH THE FAIRCHILD 100×100 CCD

George Renda and John L. Lowrance
Princeton University Observatory
Princeton, New Jersey

Princeton has measured the soft x-ray sensitivity of the Fairchild 100×100 element CCD for possible use as a detector in plasma physics research. This paper will explain the experimental setup and the laboratory results. The paper will also present data on slow-scan operation of the CCD and performance when cooled. Results from digital computer processing of the data to correct for element-to-element nonuniformities will also be discussed.

I. INTRODUCTION

Plasma physics research related to nuclear fusion is becoming increasingly interested in diagnostic measurements in the 1-Å to 500-Å spectral region. This region is also of interest in astrophysics. There is particular interest in the CCD type of detector because the intense magnetic fields associated with plasma containment in nuclear fusion research make it awkward, if not impossible, to use more conventional television type image sensors. We have begun a program to measure the soft x-ray sensitivity of CCD image sensors. This paper reports our initial results with the Fairchild 100×100 element CCD. Results from digital computer processing of the video to correct for element-to-element nonuniformities are also discussed. It should be noted that the video signal in this case was obtained with the CCD illuminated with visible wavelength light. The results from computer processing of the x-ray video will be reported in a later paper.

II. SLOW-SCAN, VISIBLE LIGHT PERFORMANCE

A. Test Setup and Tests

Uniform illumination tests were conducted to ascertain the noise characteristics of the CCD with computer processing. Figure 1 shows the test arrangement consisting of the CCD and associated electronics, LED light source, cold chamber, A/D converter and digital tape recorder.

To eliminate dark current and dark current nonuniformities, the CCD was operated at -80°C. The uniform illumination tests covered a range of approximately 60,000 electrons/pixel to 600,000 electrons/pixel, which corresponds to 10 to 100% of full scale for the CCD. The tests were conducted at a pixel clock rate of 5.2 kHz, which resulted in a frame rate of approximately 0.5 frames/sec. The period of integration was varied from 2 seconds to 20 seconds. The LED light source was controlled by a current regulator preset at one specific level.

As a result of the testing, it was found that the predominant noise was coherent. This coherent noise was assumed to be caused by the gain variations in the silicon detectors and charge transfer inefficiency.

The straight line equation ax + b seems to adequately fit the individual pixel data. The "a" term corresponds to the gain or sensitivity of each pixel, and the "b" term corresponds to an initial "zero exposure" offset. This model was assumed, and a computer program was written to find the a's and b's of each pixel element. This full frame set of a's and b's was then used to process other data files.

B. Data Processing

In order to solve for the a and b values of the individual pixels, it is necessary to have two uniform field exposures. As indicated above, the photoresponse equation for each pixel is taken to be

$$Y_k = a_n X + b_n \tag{1}$$

where Y_k represents the total number of signal electrons measured at pixel n in file k.

X is used as a scaling factor. For this specific program, X is chosen such that full scale equals 10,000 counts. For example, if Y_k represents, on the average, 25% of full scale, then X is set equal to 2500.

The equation for the second file is

$$Y_{k2} = Na_nX + b_n \tag{2}$$

where Y_{k2} represents the signal measured at pixel n in file k2, and N represents the increase in exposure over Y_k.

The following equations show the steps the computer program goes through to solve for the value of a and b:

$$a_n^X = \frac{Y_{k2} - Y_k}{N - 1} \tag{3}$$

where N - 1 is a data input card to the program; i. e., if Y_{k2} is 4 times greater than Y_k, then N - 1 = 3.

$$a_n = \frac{a_n^X}{X} \tag{4}$$

and

$$b_n = Y_k - a_n^X \tag{5}$$

The values of a_n and b_n for every pixel are then stored as a file on tape. We now have a calibration matrix for the entire CCD array.

The next step is to use these values to remove the coherent noise in a data file of interest.

$$Y_p = \frac{Y_r - b_n}{a_n} \tag{6}$$

where Y_r is the raw (unprocessed) data file of interest and Y_p is the processed data file.

C. Standard Deviation in Computer Processed Data

The following is the general equation for the variance of a sum:

If

$$A = a_1 + a_2$$

then

$$\sigma_A^2 = \sigma_1^2 + \sigma_2^2 \tag{7}$$

and the general equation for the variance of a product is (Ref. 1)

$$A = c_1 a_1^m a_2^n a_3^r \ldots \tag{8}$$

$$\left(\frac{\sigma}{A}\right)^2 = \left(\frac{m\sigma_1}{a_1}\right)^2 + \left(\frac{n\sigma_2}{a_2}\right)^2 + \left(\frac{r\sigma_3}{a_3}\right)^2 \ldots \tag{9}$$

Rewriting Equation (6) in terms of the data used to develop the calibration coefficients a and b,

$$Y_p = \frac{Y_r - b_n}{a_n} = X\left(\frac{(N-1)\left(Y_r - Y_k\right)}{Y_{k2} - Y_k} + 1\right) \tag{10}$$

and, making the following substitutions,

$$C_1 = X(N-1) \qquad a_2 = Y_{k2} - Y_k$$

$$m = 1 \qquad \sigma_1^2 = \sigma_r^2 + \sigma_k^2$$

$$n = -1 \qquad \sigma_2^2 = \sigma_{k2}^2 + \sigma_k^2$$

$$a_1 = Y_r - Y_k$$

one obtains from Equation (9)

$$\sigma_p = \frac{X\,(N-1)}{Y_{k2} - Y_k} \left(\sigma_r^2 + \sigma_k^2 + \frac{\left(Y_r - Y_k\right)^2 \left(\sigma_{k2}^2 + \sigma_k^2\right)}{\left(Y_{k2} - Y_k\right)^2} \right)^{1/2} \tag{11}$$

which has the general form

$$\sigma_p = C_1 \left(\sigma_r^2 + \sigma_k^2 + C_2 \left(\sigma_{k2}^2 + \sigma_k^2\right) \right)^{1/2}$$

The signal-to-noise ratio is

$$S/N = \frac{Y_p}{\sigma_p} = \frac{\left(Y_r - Y_k + \frac{Y_{k2} - Y_k}{N-1}\right)}{\left(\sigma_r^2 + \sigma_k^2 + \frac{\left(Y_r - Y\right)^2 \left(\sigma_{k2}^2 + \sigma_k^2\right)}{\left(Y_{k2} - Y_k\right)^2} \right)^{1/2}} \tag{12}$$

This ratio can be written in a simplified form. Since $Y_{k2} \approx NY_k$, then

$$S/N = \frac{Y_r}{\left(\frac{\sigma_r^2 + \sigma_k^2 + \left(Y_r - Y_k\right)^2 \left(\sigma_{k2}^2 + \sigma_k^2\right)}{\left(Y_{k2} - Y_k\right)^2} \right)^{1/2}} \tag{13}$$

D. Experimental Data for Visible Illumination

Figure 2a shows the raw unprocessed video signal for one 100-pixel line at an exposure of 24% of full scale. Figure 2b shows the same line after computer processing. Figures 2c and 2d show the same type of data for an exposure that is 84% of full scale (saturation).

For a more quantitative comparison, the standard deviation was computed over a 50 × 50 pixel patch near the center of the 100 × 100 array.

Table 1 shows the improvement in signal-to-noise ratio after point-by-point calibration of the data. This is compared with the signal-to-noise ratio that one would calculate from Equation (13), assuming that the noise is gaussian; i. e., σ = (number of electrons)$^{1/2}$. The predicted signal-to-noise calculation also includes a readout noise factor of 200 electrons rms per pixel. The actual readout noise characteristics are still under investigation.

Table 1. S/N characteristics (50 × 50 pixel area)

Exposure level, % full scale	S/N raw data	S/N processed data	S/N predicted from Eq. (13)	Ideal, (photoelectrons)$^{1/2}$
24	62	195	236	380
84	71	313	446	710

The standard deviation was also calculated for the 100 pixels along a single line. These results are shown in Table 2.

Table 2. S/N characteristics (100 pixel line)

Exposure level, % full scale	S/N raw data	S/N processed data	S/N predicted from Eq. (13)	Ideal, (photoelectrons)$^{1/2}$
24	62	207	236	380
84	116	438	446	710

The discrepancy between Table 1 and Table 2 for the 84% file may be due to a small number of pixels in the 50 × 50 pixel patch that were several sigmas away from the mean.

The processed data S/N is remarkably close to the predicted S/N in Table 2. Therefore, the assumption of (photoelectron)$^{1/2}$ noise is valid.

This implies that by averaging calibration data frames to achieve higher S/N in the calibration frames, one can closely approach the ideal case. This makes the CCD uniquely attractive for low-contrast applications, such as imagery of solar granulation.

III. SOFT X-RAY DETECTION

In nuclear fusion research, it is important to measure the impurities in the plasma and the total energy being radiated. The sensitivity of silicon over a broad spectral range makes it very attractive, and when configured as a CCD, it is even more attractive because of its relative insensitivity to strong magnetic fields associated with plasma containment. The Fairchild CCD-201 has been illuminated with x-rays from a copper target to explore its applicability for x-ray imagery. A block diagram of the experiment for the x-ray sensitivity measurements is shown in Figure 3.

A. Fairchild CCD-201

The photosensitive area of the CCD-201 is covered by about 1.5 microns of silicon and silicon dioxide that is "dead" in terms of visible radiation. That is, photons absorbed in this layer do not contribute to the signal. The shift registers are covered by an additional layer of aluminum 1.2 microns thick that is opaque to visible radiation. Figure 4 shows the transmission characteristics of the aluminum and silicon layers in the soft x-ray spectral region. As can be seen by the aluminum transmission characteristics, the shift register circuits behind the aluminum are sensitive to the x-ray photons. We have found that the problem of the photosensitive shift register can be circumvented by rapid scanning of the shift registers during the exposure time. One would expect that x-ray exposure of the shift register regions may cause permanent damage as well, but this has not been investigated. With regard to this problem, a back illuminated device would be much better. A back illuminated device would also allow a thinner dead layer, with corresponding improvement in long-wavelength response.

B. X-Ray Data

The equation for the continuous x-ray intensity per unit energy interval is (Ref. 2)

$$I_E = K_1 Z \left(E_o - E\right) + K_2 Z^2 \tag{14}$$

For light elements, the Z^2 term can be neglected, since typically $K_2/K_1 = 0.0025$. N_E, the number of photons per unit energy interval, can be written

$$N_E = KZ \frac{\left(E_o - E\right)}{E} \tag{15}$$

where

E_o is the high energy limit of the spectrum (eV)

E is any energy between E_o and 0 (eV)

Z is the atomic number of the element

K is the continuous x-ray efficiency constant of the element $\left(eV^{-1}\right)$.

In the case of the CCD, the x-rays are attenuated by the beryllium filter and by the polysilicon and silicon dioxide layers on the CCD. From Figure 4, one notes that the transmission is a function of E. The equation for the number of x-rays per unit energy interval reaching the active silicon is

$$N_{EI} = KZ \frac{E_o - E}{E} \exp\left(-u_1 x_1 E^{-Y_1}\right) \exp\left(-u_2 x_2 E^{-Y_2}\right) \tag{16}$$

where $\exp\left(-u_1 x_1 E^{-Y_1}\right)$ is the transmission function for the beryllium, and the silicon transmission is expressed by a similar term.

The silicon has a conversion efficiency of one electron-hole pair per 3.5 electron volts of energy. The number of photoelectrons per unit energy is then

$$N_{pe} = KZ \frac{E_o - E}{3.5} \exp\left(-u_1 x_1 E^{-Y_1}\right) \exp\left(-u_2 x_2 E^{-Y_2}\right) \tag{17}$$

And for a given electron accelerating voltage E_o, the response of the CCD is

$$\sum_{o}^{E_o} N_{pe} = \frac{KZ}{(3.5)(4\pi)} \int_{o}^{E_o} (E_o - E) \exp\left(-u_1 x_1 E^{-Y_1}\right) \exp\left(-u_2 x_2 E^{-Y_2}\right) dE$$

$$\text{photoelectrons steradian}^{-1} \text{ electron}^{-1} \tag{18}$$

The characteristic x-ray spectra of interest are the L shell lines $L_{\alpha 1,2}$ and $L_{\beta 1}$ at 0.928 and 0.948 keV, respectively. The other L series lines are either weak compared to these lines or are sufficiently attenuated by the beryllium filter so that they are negligible in these measurements.

The empirically derived equation (Ref. 3)

$$N = n\left(E_o - E^*\right)^{1.63} \text{ photons electron}^{-1} \tag{19}$$

gives the characteristic line strength, where E^* is the line of interest (keV) and n is the efficiency coefficient. Efficiency coefficients for $L_{\alpha 1,2}$ are published for heavier elements and have been extrapolated to yield a value of 3.4×10^{-5} for copper. The ratio of $L_{\alpha 1,2}$ to $L_{\beta 1}$ is 2. Therefore, the combined characteristic line strength is given by the equation

$$N = \frac{3.4 \times 10^{-5}}{3.5 \times 4\pi} \left(K_\alpha \left(E_o - E_{L_{\alpha 1,2}}\right)^{1.63} E_{L_{\alpha 1,2}} + \frac{K_\beta}{2} \left(E_o - E_{L_{\beta 1}}\right)^{1.63} E_{L_{\beta 1}} \right)$$

$$\text{photoelectrons steradian}^{-1} \text{ electron}^{-1} \tag{20}$$

where K_α and K_β are the attenuation factors for the filter and dead layer at the characteristic line energy.

Figure 5 shows the sum of Equations (18) and (20) plotted as a solid line and the experimental results plotted as points. There is a close agreement between the experimental data and the calculated response from 1.7 to 6 keV.

The rolloff in response at lower energies is readily attributed to a somewhat thicker beryllium filter and/or thicker layers of polysilicon and silicon dioxide on the CCD.

The actual CCD signal current, when converted to photoelectrons in the silicon per steradian per incident electron on the x-ray target, agrees with the calculated value when one uses a value for the continuous x-ray efficiency constant K/2 of 1.3×10^{-9} eV^{-1} and an active CCD area of 7 mm^2 out of a total area of 12 mm^2.

ACKNOWLEDGEMENTS

The authors wish to thank Edward Loh and Patrick Murray for their aid in obtaining the experimental data, and Paul Zucchino for assistance in the data analysis. We also wish to thank Dr. Martin Green for his assistance in understanding the characteristic x-ray production efficiency. This work was supported by the Energy Research Administration.

REFERENCES

1. L. Tuttle and J. Satterly, The Theory of Measurements, Longmans, Green and Co., London, pp. 215-220 (1925).

2. N. A. Dyson, X-rays in Atomic and Nuclear Physics, Longman Group Limited, London, pp. 7-61 (1973).

3. M. Green and V. E. Cosslett, Brit. J. Appl. Phys. (J. Phys. D.), 1, 425 (1968).

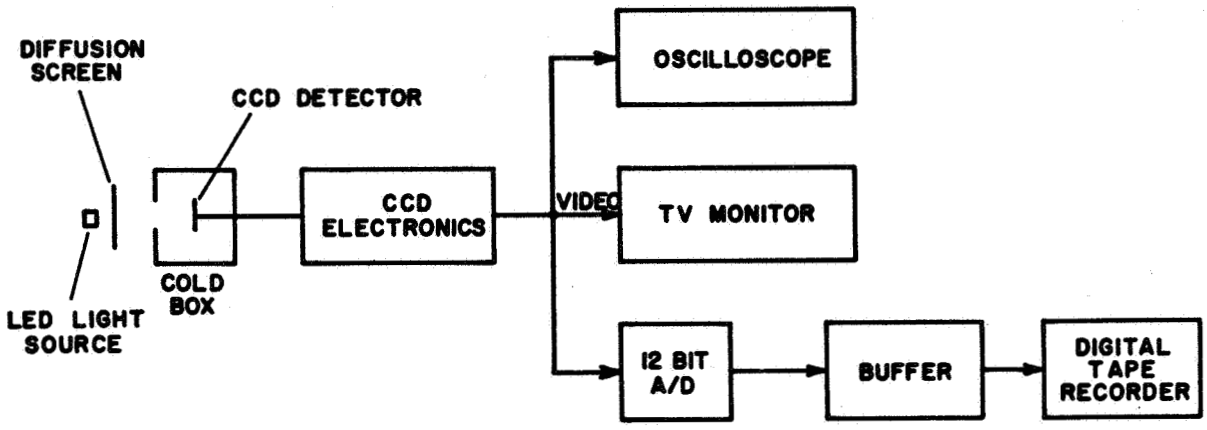

Figure 1. CCD test block diagram

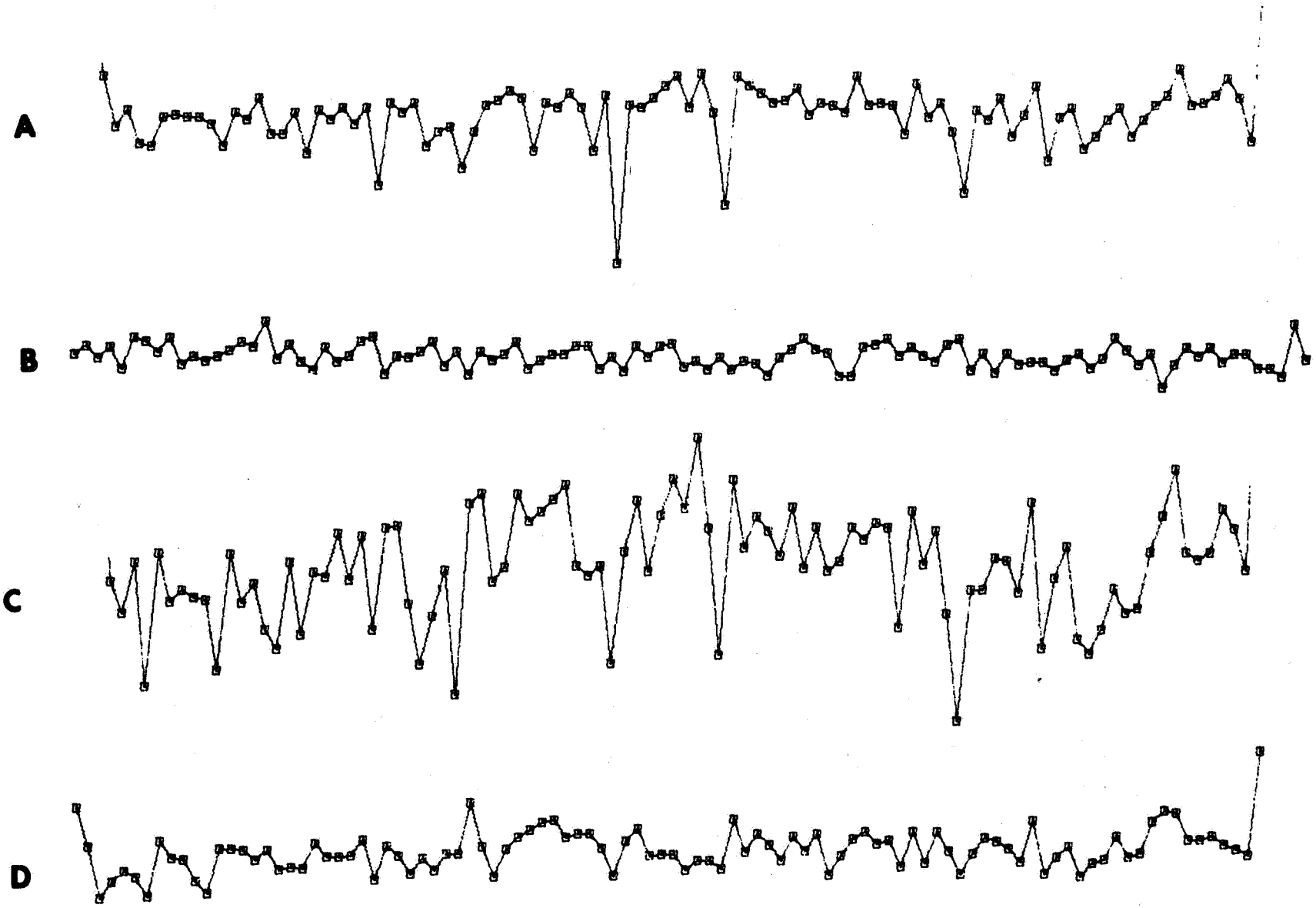

Figure 2. Computer plots of 100-pixel line of video: (a) raw, 24% full scale, (b) processed, 24% full scale, (c) raw, 84% full scale, (d) processed, 84% full scale

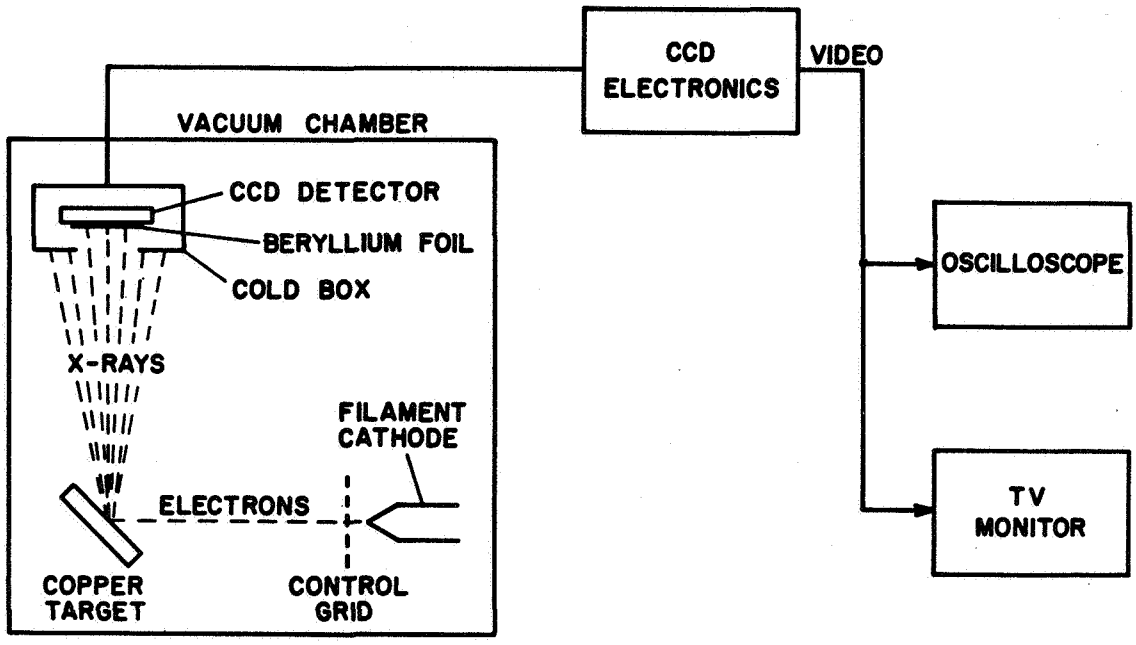

Figure 3. CCD x-ray experiment block diagram

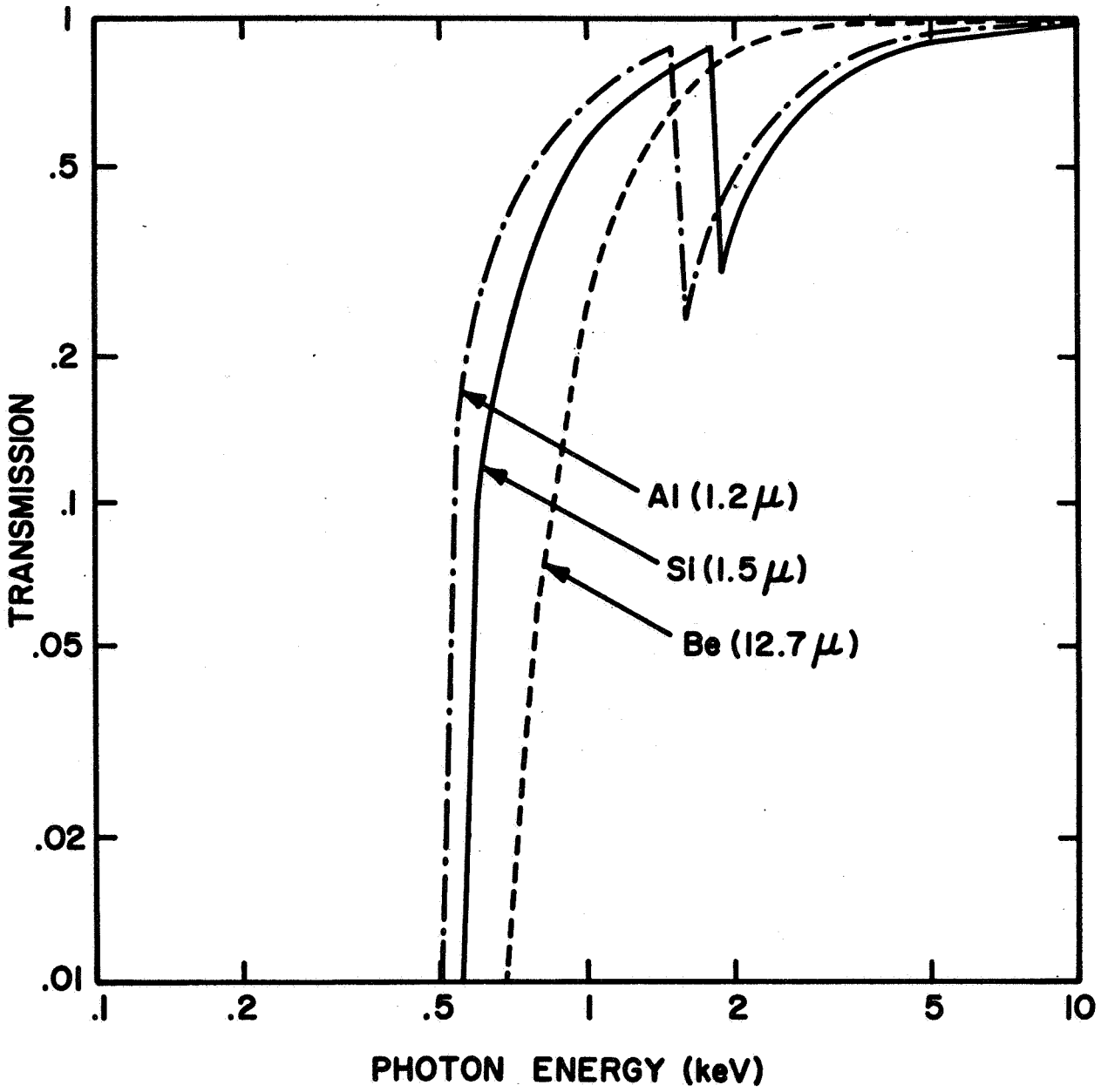

Figure 4. Soft x-ray transmission characteristics of beryllium, aluminum, and silicon

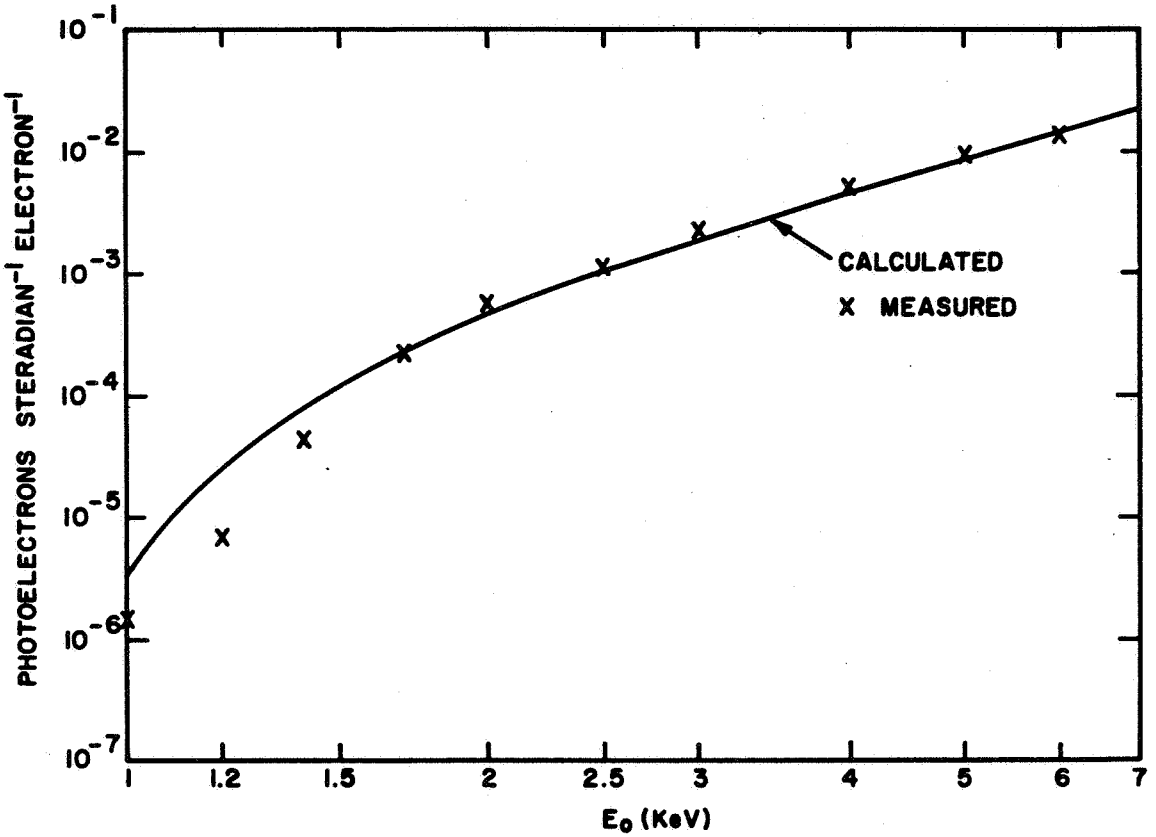

Figure 5. Fairchild CCD-201 response to soft x-rays, calculated and measured

RECENT DEVELOPMENTS IN CID IMAGING

G. J. Michon, H. K. Burke, and D. M. Brown
General Electric Company
Corporate Research and Development
Schenectady, New York

Readout of CID imaging arrays was first performed by injecting and detecting the signal charge from each sensing site in sequence. An epitaxial structure was used to provide a buried collector for the injected charge to allow high-speed operation and to eliminate crosstalk of the injected charge. This technique is also compatible with nonsequential scan formats (random-scan).

A new readout method, termed "parallel injection," has been developed in which the functions of signal charge detection and injection have been separated. The level of signal charge at each sensing site is detected during a line scan, and during the line retrace interval, all charge in the selected line is injected. The injection operation is used to reset (empty) the charge storage capacitors after line readout has been completed. Nondestructive readout is possible by deferring the injection operation.

The parallel injection technique is well adapted to TV scan formats in that the signal is read out at high speed, line by line. A 244-line by 248-element TV-compatible imager, employing this technique and including an on-chip preamplifier, has been constructed and operation demonstrated. The performance level that can be achieved is presented.

An additional improvement in the CID structure has been the replacement of the opaque aluminum electrodes with transparent conductors. Devices fabricated in this way have achieved quantum efficiencies in the order of 70% over the spectral range of 4000 Å to 8000 Å, front illuminated.

I. BASIC DESCRIPTION

The CID solid-state image sensors use an X-Y addressed array of charge storage capacitors which store photon-generated charge in MOS inversion regions. Readout of the first self-scanned arrays was effected by sequentially injecting the stored charge into the substrate and detecting the resultant displacement current to create a video signal (Refs. 1,2). The charge storage sites can be read out in any arbitrary order. Arrays can be designed with integral digital MOS decoders for X and Y line selection to allow "random" access. The integration time as well as the scan sequence could then be externally programmed for special applications.

An array designed for raster scan which includes integral shift registers is diagrammed in Figure 1a. Each sensing site consists of two MOS capacitors with their surface inversion regions coupled such that charge can readily transfer between the two storage regions. A larger voltage is applied to the row-connected electrodes so that photon-generated charge collected at each site is stored under the row electrode, thereby minimizing the capacitance of the column lines. The sensing site cross-sections (Figure 1b) illustrate the silicon surface potentials and locations of stored charge under various applied voltage conditions.

A line is selected for readout by setting its voltage to zero by means of the vertical scan register. Signal charge at all sites of that line is transferred to the column capacitors, corresponding to the "row enable" condition shown in Figure 1b. The charge is then injected by driving each column voltage to zero, in sequence, by means of the horizontal scan register and the signal line. The net injected charge is measured by integrating the displacement current in the signal line over the injection interval. Charge in the unselected lines remains under the row-connected electrodes during the injection pulse time (column voltage pulse). This corresponds to the "half select" condition of Figure 1b.

The array is constructed on an epitaxial layer so that the reverse biased epitaxial junction can act as a collector for the injected charge. This effectively prevents the charge injected at any site from being collected by neighboring sites.

II. PARALLEL INJECTION

A new readout technique, termed "parallel injection," has been developed in which the functions and signal charge detection and injection have been separated. The level of signal charge at each sensing site is detected during a line scan and, during the line retrace interval, all charge in the selected line can be injected.

A diagram of a 4 × 4 array designed for parallel injection is illustrated in Figure 2, with the relative silicon surface potentials and signal charge locations included. As before, the voltage applied to the row electrodes is larger than that applied to the column electrodes to prevent the signal charge stored at unaddressed locations from affecting the column lines. At the beginning of a line scan, all rows have voltage applied, and the column lines are reset to a reference voltage V_S by means of switches S_1 through S_4 and then allowed to float. Voltage is then removed from the line selected for readout (X_3 in Figure 2), causing the signal charge at all sites of that line to transfer to the column electrodes. Voltage on each floating column line then changes by an amount proportional to the signal charge divided by the column capacitance. The horizontal scanning register is then operated to scan all column voltages and deliver the video signal to the on-chip preamplifier Q_1. The input voltage to Q_1 is reset to a reference level prior to each step of the horizontal scan register.

At the end of each line scan, all charge in the selected line can be injected simultaneously by driving all column voltages to zero through switches S_1 and S_4. Alternately, the injection operation can be omitted and voltage reapplied to the row after readout, causing the signal charge to transfer back under the row electrodes. This action retains the signal charge and constitutes a nondestructive readout operation.

The parallel injection approach permits high-speed readout and is thus well adapted to TV scan formats, and offers optional nondestructive readout. A 244-line by 248-element imager, employing this technique and including an on-chip preamplifier, has been designed, fabricated, and evaluated in both the normal and nondestructive readout modes.

For TV-compatible operation, a line time interval of 63 μsec (5 MHz element rate) is used, and the vertical scan rate is 60 scans per second. The imager is completely read out during each interlaced field of the standard TV frame such that video is displayed on all 488 active lines of the 525-line system.

The parallel injection technique, in general, retains the high performance characteristics of CID imaging (Ref. 2) such as low dark current, wide dynamic range, and high modulation transfer function. Significant differences exist, however, with regard to nondestructive readout and overload immunity.

A. Nondestructive Readout

The nondestructive readout characteristics of the 244 × 248 array have been evaluated by operating the device at low temperature to minimize dark current and thereby achieve long storage time intervals.

Two experiments were performed to identify the limiting factors in nondestructive image readout. First, a charge pattern of an image was generated and stored by momentarily opening a shutter, and then the image was read out continuously at 30 frames per second, until image degradation was noted. At a chip temperature of -70°C, images were read out for 3 hours (324,000 NDRO operations) with no detectable charge loss. The charge lost during each NDRO operation was, on the average, much less than one carrier per pixel per frame.

The second experiment was performed to insure that charge could be generated and stored at very low light levels under continuous (30 frames per second) NDRO conditions. A series of time exposures were made at successively lower light levels, and the time required to reach a given level of signal voltage was measured. The results (Figure 3) show that the exposure time is inversely proportional to light level, with no measurable reciprocity loss for exposure times up to 3 hours. The lowest light level used was equivalent to about two carriers per pixel per frame in the highlight regions of the image. Here again, the readout loss was not measurable and was much less than one carrier per pixel per frame.

B. Blooming

Unlike the sequential injection approach, this new technique exhibits relatively little blooming in the displayed image as a result of sensing site overload. This is because the half-select and injection operations occur during the horizontal blanking interval.

While excess charge can accumulate during a line scan interval and cause column brightening for overloads occurring in the right-hand portion of the image field, this effect is attenuated by the line-to-frame integration time ratio.

For NDRO operation, virtually no blooming occurs, since the charge is not injected. The affected sites simply saturate and cease collecting charge.

In all cases, radial spreading of excess charge is prevented by the underlying charge collector.

III. TRANSPARENT ELECTRODES

The incorporation of transparent metal oxide electrodes into a self-scanned CID high-density imager has recently been reported by Brown, Ghezzo, and Garfinkel (Ref. 3). This development is reviewed here because of its significance in scientific imaging applications.

The use of metal oxide (tin, antimony, indium oxide) electrodes in imaging array structures presents significant advantages because of three important physical properties:

(1) The index of refraction (~2) is a close match to silicon dioxide (~1.46) and silicon nitride (~2), the commonly used dielectrics in MOSFET integrated circuits.

(2) The spectral transmissivity of these materials is very high in the visible spectrum (~80%) and extends from 4000 to 9000 Å.

(3) The conductivity of these materials is good, being as good as or better than doped polysilicon (≤ 100 Ω/square).

The incorporation of this material in a self-scanned CID array imager has been successfully carried out, as shown by the photomicrograph. In Figure 4, the central array is the imager array (32 × 32) using 1.7 × 1.3 mil cell spacing, with lines fanned out to the scanning circuits on the chip's periphery.

The spectral quantum efficiency of this high-density self-scanned array is given in Figure 5. The high and nearly constant visible wavelength spectral efficiency is due to the fact that the major portion of the array is covered by metal oxide electrodes, and photon conversion can occur in the underlying depletion layer of each CID cell. These arrays have excellent blue response, nearly uniform spectral response from 8000 Å to 4000 Å, and very high sensitivity (~70% quantum efficiency.)

IV. CONCLUSIONS

High-density, high-speed CID imaging arrays with wide spectral response characteristics, when front-illuminated, are now practical.

Nonsequential addressing, now being explored, promises interesting new applications.

The capability of repeated readout, during or subsequent to exposure, allows a number of system functions not previously possible, such as exposure monitoring and extended time image processing.

ACKNOWLEDGEMENTS

Development of the 244 X 248 imager was partially funded under the sponsorship of the Advanced Research Projects Agency (ARPA) and the Air Force Systems Command, US Air Force.

REFERENCES

1. G.J. Michon and H.K. Burke, "Charge Injection Imaging," 1973 IEEE International Solid State Circuits Conference, pp. 138-139, THPM 11.6.

2. G.J. Michon and H.K. Burke, "Operational Characteristics of CID Imager," 1974 IEEE International Solid State Circuits Conference, pp. 26-27, WAM 2.2.

3. D.M. Brown, M. Ghezzo, and M. Garfinkel, "Transparent Metal Oxide Electrode CID Imager Array," 1975 IEEE International Solid State Circuits Conference, pp. 34-35, WAM 2.6.

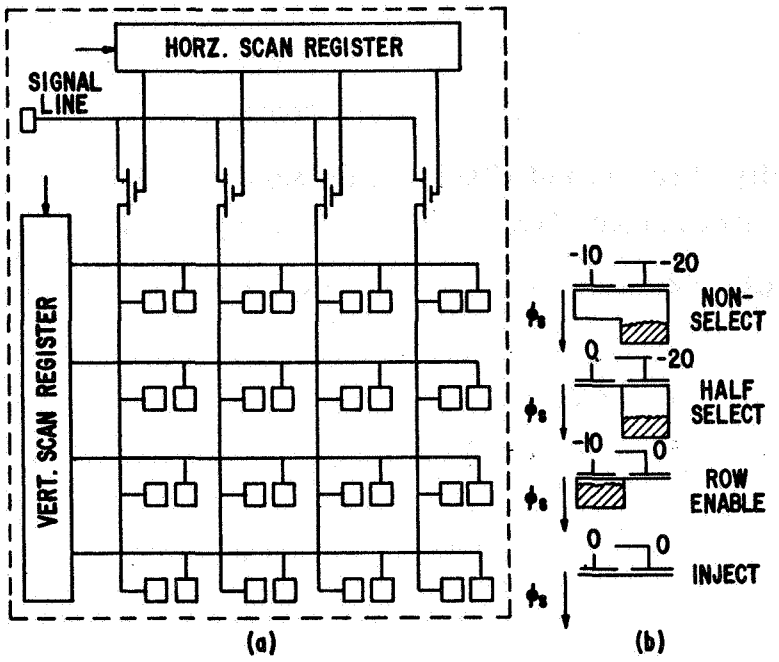

Figure 1. Sequential injection CID imager: (a) array diagram, (b) sensing site cross-sections illustrating surface potential (ϕ_s) and location of stored charge under various bias conditions

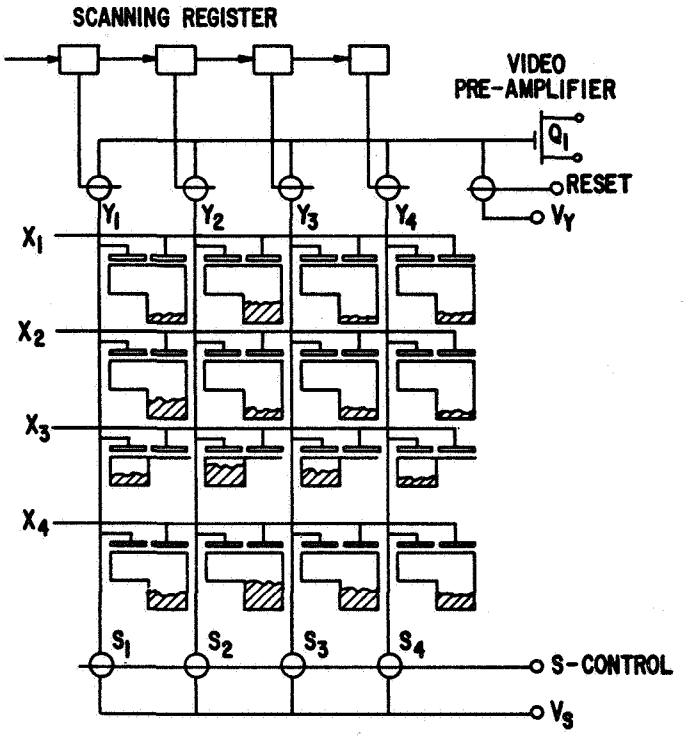

Figure 2. Parallel injection array schematic illustrating location of stored charge in selected (X_3) and unselected (X_1, X_2, X_4) rows

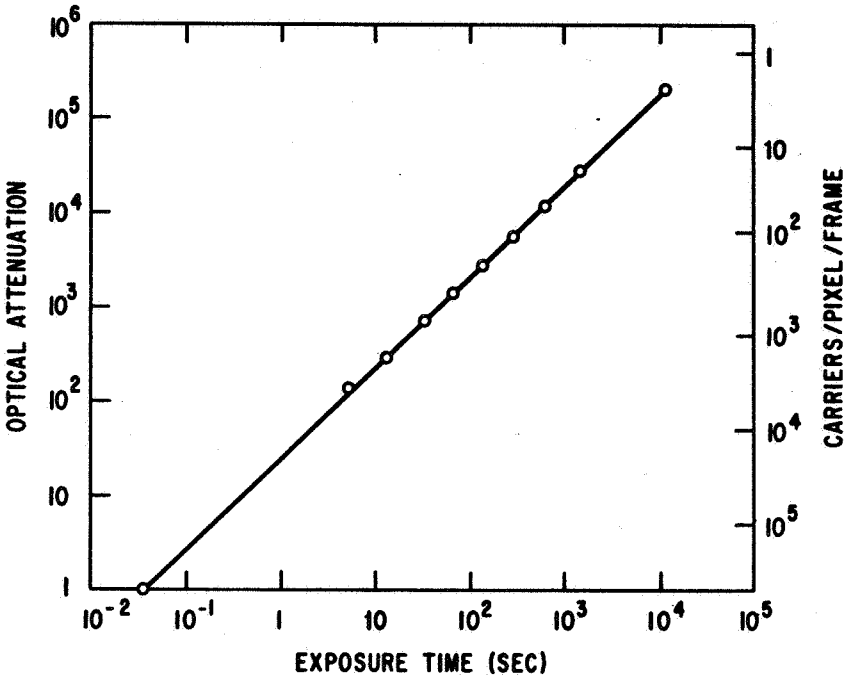

Figure 3. Exposure time required to reach a given level of output signal, as a function of optical attenuation (inverse light level), under continuous, 30 F/S nondestructive readout

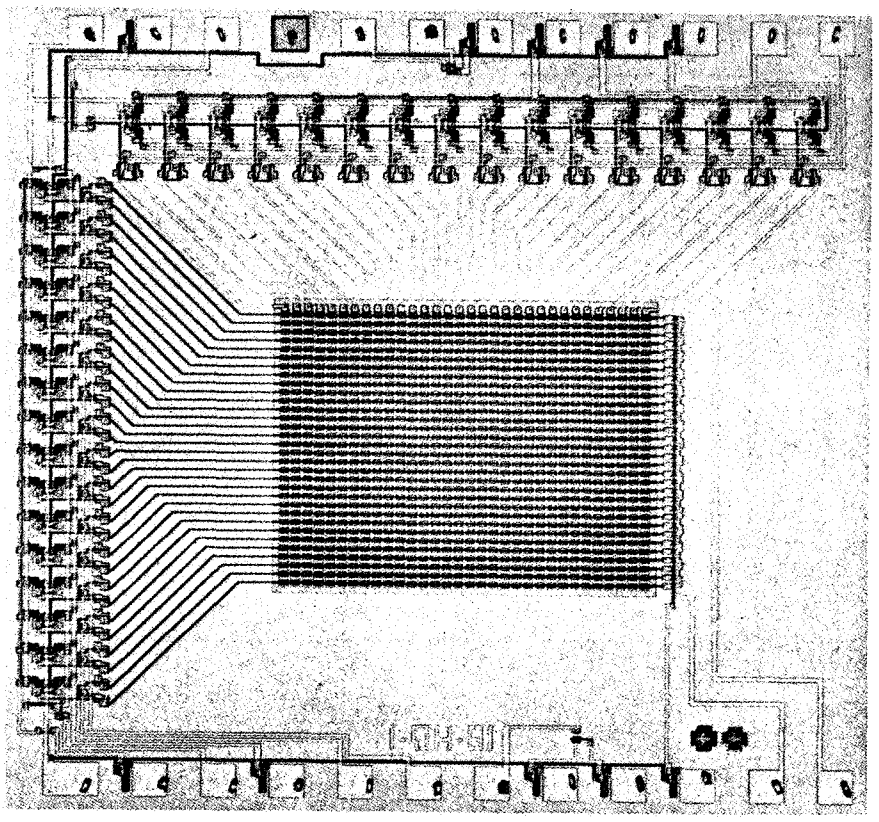

Figure 4. Photomicrograph, 32 X 32 self-scanned imager incorporating a high-density, transparent electrode image sensing array

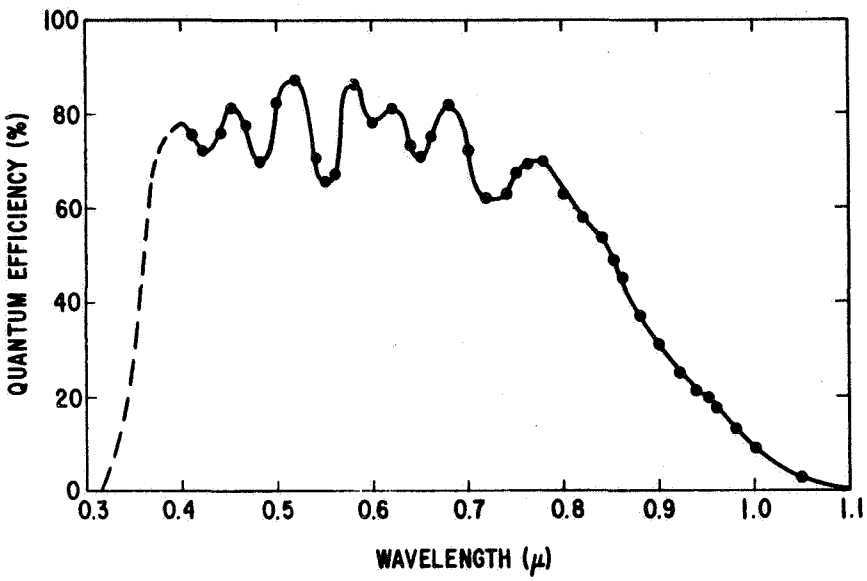

Figure 5. Measured spectral quantum efficiency of transparent electrode CID imager

COOLED SLOW-SCAN PERFORMANCE OF A 512 × 320 ELEMENT CHARGE-COUPLED IMAGER*

R. L. Rodgers III and D. L. Giovachino
RCA Corporation
Electronic Components
Lancaster, Pennsylvania

A 512 × 320 element charge-coupled imager has been fabricated and tested under cooled slow-scan conditions to evaluate the device's performance under a variety of long integration and slow-scan readout conditions. Operation in a low-blooming mode of operation enables the sensor to be exposed with portions of the image heavily overexposed, without those areas spreading into adjacent picture areas. This paper describes the device design, layout, and operating mode, and presents experimental results, including displayed images taken under cooled slow-scan operation.

A 512 × 320 element imager based on charge-coupled device (CCD) technology has been fabricated for use in a variety of television applications, including those applications requiring slow-scan operation. The choice of this cell count has been described previously (Ref. 1). This device utilizes a single-layer doped polysilicon gate structure (Ref. 2). The individual gates are formed by doping N^+ regions in a P-layer of polysilicon on top of the channel oxide. This results in low leakage between gates. Since there are no exposed gaps, a stable sealed channel structure results. The polysilicon layer is transparent to most wavelengths, and there are no opaque areas to cause aliasing. The useful spectral response range extends from 420 nM to 1100 nM (Ref. 3).

*This work was performed for the Jet Propulsion Laboratory, California Institute of Technology, sponsored by the National Aeronautics and Space Administration, under Contract No. NAS 7-100.

The device is organized into a three-phase vertical frame transfer system (Ref. 3). N-surface channel operation is utilized. An electrical bias charge (fat zero) is inserted into the horizontal register to improve horizontal resolution. An optical bias light is used to introduce bias charge into the body of the image area.

Conventional television requirements involve observation of objects in motion in real time in a similar fashion to motion picture filming. This results in relatively short exposure times to avoid image motion smearing and flicker in the display. A large number of picture elements must be read out each frame at a fast readout rate to keep up with the picture rate (i. e., 30 frames/sec and a 6-MHz data rate). In many scientific imaging applications, the requirement to record, transmit, or process video at high data rates presents a problem. In those applications where a single frame of video is sufficient, slow-scan readout may be used following an exposure to reduce the data rate. Also the exposure time may be lengthened to expose faint images, as is done with film. Both of these techniques place severe requirements on the dark charge generation rate and signal handling capability of the sensor. Buried-channel devices have experimentally exhibited smaller signal handling capability and higher dark current generation rates than surface-channel devices. This has led to the choice of a surface-channel structure for the 512 × 320 element sensor being described. Sensor cooling is required for very slow readout rates and/or long exposure times to reduce the thermal generation of dark current. The device is packaged in a hermetic, edge-contacted, 24-connection ceramic dual in-line package. The package contains an optical glass window to allow the image to be focused onto the sensor. The packaging has a low thermal impedance to the chip and facilitates easy cooling.

There is no residual image remaining after the picture has been read out. This means that no special prepare or erase cycles are required for proper slow-scan operation. All that is required is proper setting of the exposure. The sensor is normally operated in a run-stop-run mode of operation for slow scan. The sensor is set up to operate at the desired readout rate and is left continuously reading out the dark signal until it is desired to make an exposure. The vertical clocks are stopped during the time the shutter is open to expose the image. After the shutter is closed, the slow-scan readout at the preset

rate begins. The horizontal clocks are kept running during the exposure to read out any dark or light charge buildup in this register.

Many scenes are low contrast and do not present small area overload problems to the CCD sensor. Other scenes may contain strongly overloaded areas (e.g., star fields). Containment of charge during overloads can be a problem with CCD imagers. Figure 1 shows the performance of the 512 × 320 sensor operating in its low-blooming mode of operation (Refs. 3, 4). All of the small circular images in the scene are 0.25 mm in diameter on the sensor. The one on the right center is exposed at saturation and represents the original image size. The image at the upper left is at a 10X overload. The remaining four images are at a 100X overload. It can be seen that the image size grows less than a factor of two in diameter with this 100X overload. Part of the enlargement is known to be from the lens itself.

Figure 2 shows what would have happened if the low-blooming mode of operation had not been used. The blooming takes place in the vertical direction because it is confined by the channel stop diffusions in the horizontal direction. The low-blooming mode of operation is accomplished by accumulating the substrate under the two-phase gates next to the phase gate collecting charge during picture exposure. This electronically extends the channel stops around each sensing site, preventing charge spreading. The sensor's phase gates are then biased into depletion during the normal readout transfers. Buried-channel devices cannot use this method of charge confinement during exposure since the surface cannot be accumulated (Ref. 2). This was another reason for choosing a surface-channel structure instead of a buried-channel structure for this 512 × 320 sensor.

The pictures shown in Figures 1-6 were all taken with a 10-second picture frame readout time. The sensor was cooled to -6°C for all of the pictures. All of the pictures were made in the low-blooming mode of operation except Figure 2, in which blooming was allowed to occur to demonstrate the effectiveness of blooming control. Figures 3 and 4 show live imaging of the authors. Figure 3 was taken with a 1/4-second exposure. Figure 4 was taken with a 2-second exposure. Figures 1, 2, and 5 were taken with a 30-second exposure, followed by the 10-second readout. Figure 5 is a picture of two different star fields taken from a book. The white line in the middle is the

division between the two pages of the book. Figure 6 is a picture of the earth. It was exposed for 67 seconds, followed by a readout of 10 seconds. The equivalent illumination on the sensor in the highlights is approximately 5×10^{-5} - 1×10^{-4} fc of 2856-K illumination. The sensor was measured to have a dark current density of 2 nA/cm^2 at 24°C. The sensor exhibited cell-limited resolution in all parts of the picture (i. e., 512 × 320 cell resolution). However, the Tektronix 604 display used for the pictures cannot resolve individual raster lines. All of the photographs exhibit a horizontal line structure. This is not generated by the 512 × 320 imager. This background pattern is present in the display even when the video is disconnected and varies with scan rate. It is believed to be due to 60-cycle modulation in the 604 display unit.

Figure 7 shows a portion of one video line of information at the output of the imager (16-kHz data rate, corresponding to 10-second readout). The video is shown with white negative. The output floating diffusion is reset at the end of each clock period so that the next cell output will be present for most of the next clock phase. This presents the data in a pseudo sample and hold output. No further video processing or filtering was necessary to make the displayed photos. The reset pulses that are present merely blank off the beam for a small part of an element time and are not resolved in the displayed picture.

In summary, it has been shown that a 512 × 320 element CCD imager may be operated at scan rates much slower than standard television (i. e., 10-second frame time compared to 33-msec frame time) and integrated for much longer times (i. e., 67 seconds compared to 16 msec) by slowing down the scanning and using a modest amount of cooling.

These results do not represent the limiting performance possible from such a sensor even at this temperature as regards frame time and integration time. The ultimate performance will be limited by the dark current generation rate at the lowest operating temperature.

REFERENCES

1. R. L. Rodgers, III, "Charge-Coupled Imager for 525-Line Television," IEEE Intercon Proceedings, New York, N. Y., March 1974.

2. R. L. Rodgers, III, "512 × 320 Element Silicon Imaging Device," IEEE ISSCC Proceedings, Philadelphia, Pa., February 1975.

3. RCA SID51232 Data Sheet, January 1975.

4. W. F. Kosonocky, J. E. Carnes, M. G. Kovac, P. Levine, F. V. Shallcross, and R. L. Rodgers, "Control of Blooming in Charge-Coupled Imagers," RCA Review, Vol. 35, No. 1, March 1974.

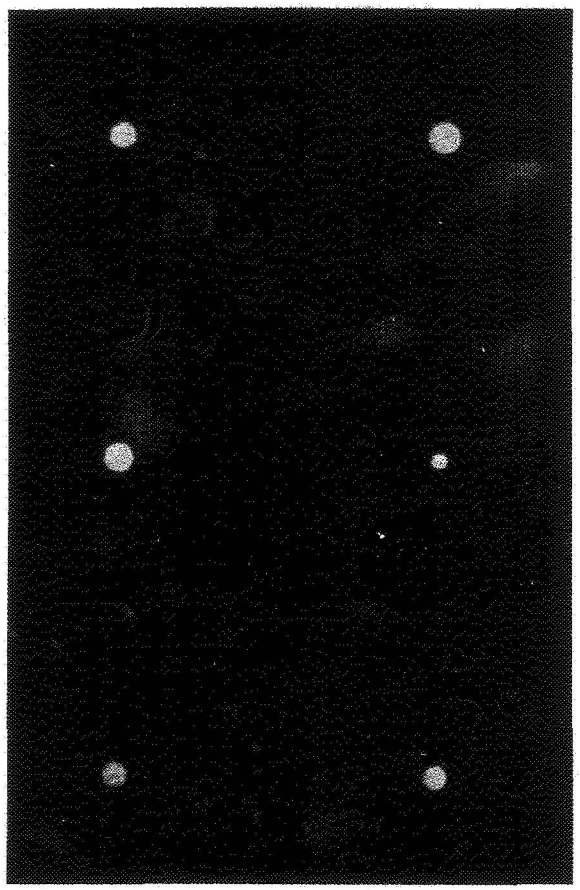

Figure 1. Low-blooming imaging of 0.25-mm images (10-sec readout, 30-sec integration, -6°C temp.)

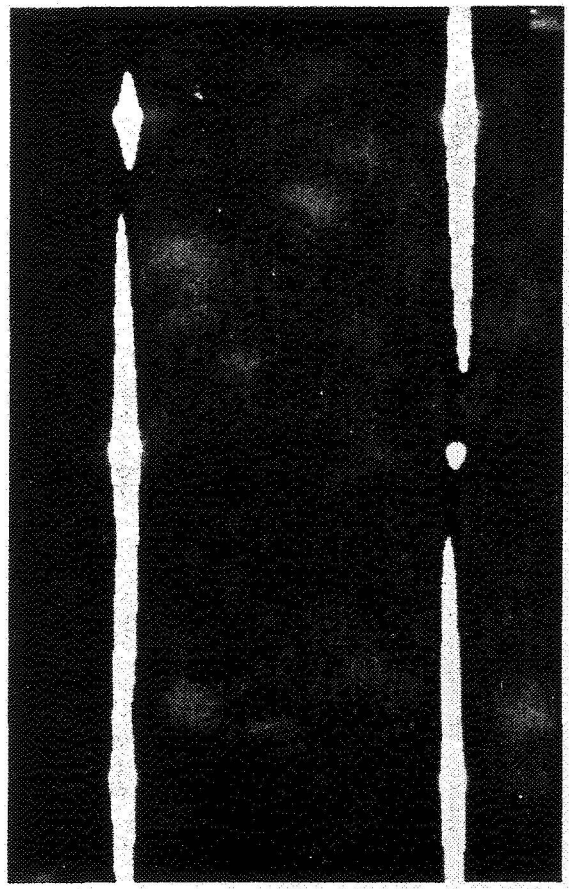

Figure 2. Blooming imaging of 0.25-mm images (10-sec readout, 30-sec integration, -6°C temp.)

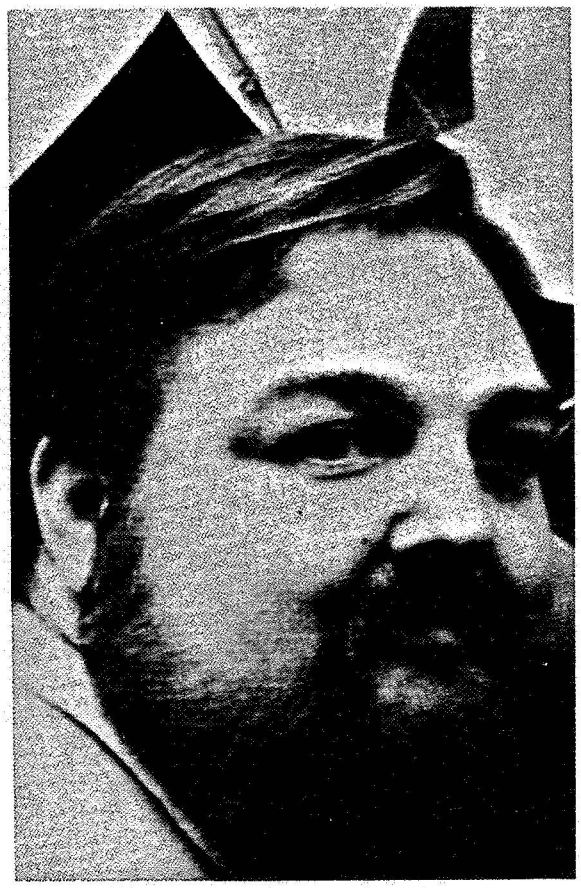

Figure 3. Live imaging of R. L. R. (10-sec readout, 1/4-sec integration, -6°C temp.)

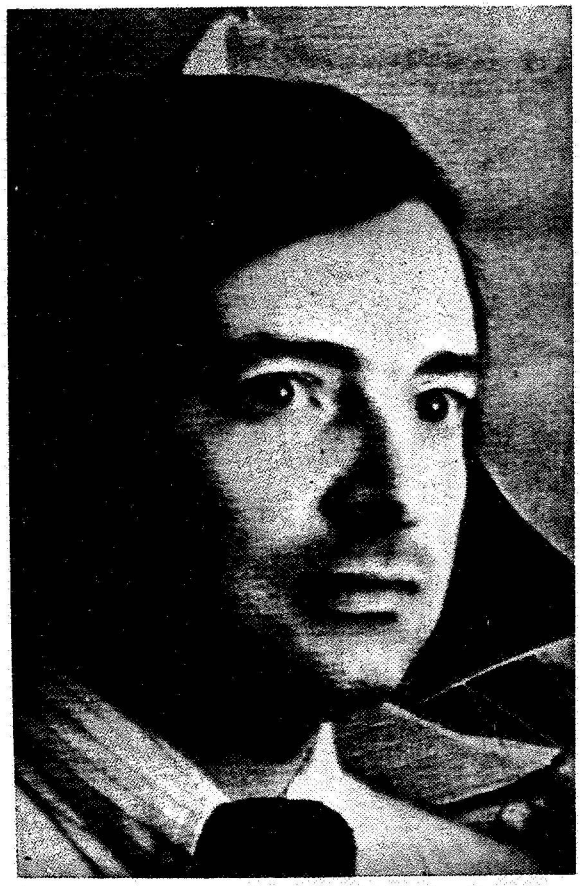

Figure 4. Live imaging of D. L. G. (10-sec readout, 2-sec integration, -6°C temp.)

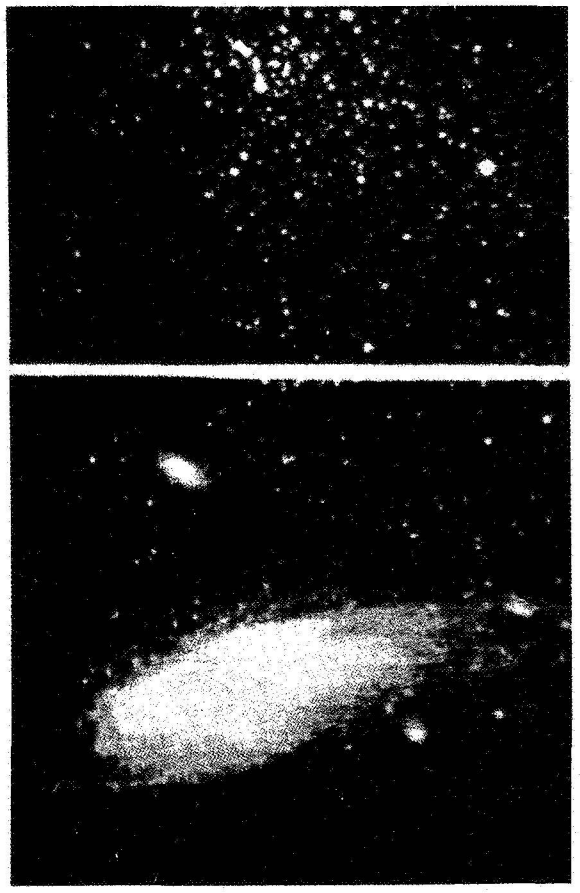

Figure 5. Star field imaging (10-sec readout, 30-sec integration, -6°C temp.)

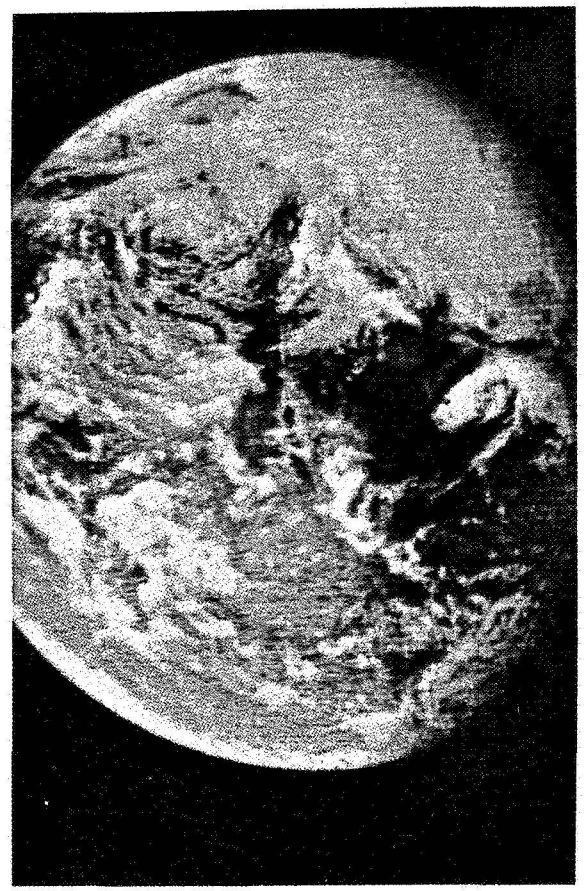

Figure 6. View of earth (10-sec readout, 67-sec integration, -6°C temp.)

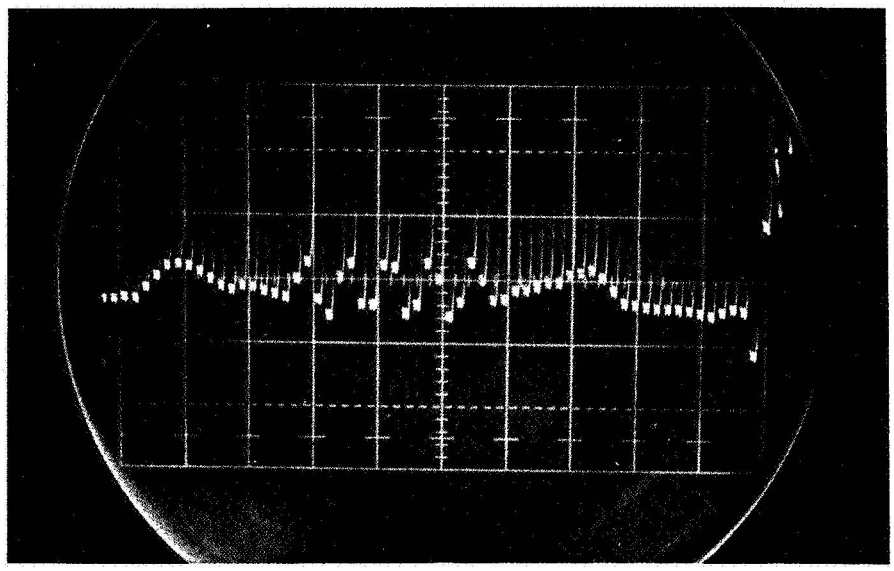

Figure 7. Expanded video output (white negative, 16-kHz data rate, 10-sec readout)

LARGE-AREA CCD IMAGERS FOR SPACECRAFT APPLICATIONS*

G. A. Antcliffe, L. J. Hornbeck, J. M. Younse,
J. B. Barton, and D. R. Collins
Texas Instruments Incorporated
Dallas, Texas

Backside illuminated CCD imagers with 100 X 160 resolution elements have been fabricated using double-level metal technology. Detailed study of the optical performance of such arrays has been performed between 24° C and -40° C using data rates from 10 kHz to 1 MHz. A 400 X 400 array is presently being fabricated.

I. INTRODUCTION

Large-area charge-coupled device (CCD) imagers can be fabricated with any of several existing technologies (Refs. 1, 2, 3). Since a completely sealed electrode structure is very desirable to optimize device electrical performance, many arrays use polysilicon electrodes which are sufficiently transparent to allow optical radiation to enter the active region of the CCD. Electrode absorption and interference effects related to the device structure itself can result in a degradation of the optical performance, particularly at short wavelengths. Illumination of the CCD from the backside (Ref. 4) eliminates this problem but requires that the silicon chip be thinned to about 10 μm for optimum performance. This paper will discuss the characteristics of backside illuminated, three-phase (3 ϕ) (Ref. 5), buried-channel imagers fabricated using the double-level anodized aluminum technique (Ref. 6). A completely sealed structure with high charge transfer efficiency (CTE) and optimum optical responsivity is obtained. The electrical and optical performance of arrays with 160 × 100 resolution elements will be presented to confirm that this technology can be successfully

*This work was performed for the Jet Propulsion Laboratory, California Institute of Technology, sponsored by the National Aeronautics and Space Administration, under Contract No. NAS 7-100.

applied to fabricate high-performance CCD imagers. The unique aspects of the double-level, backside illuminated structure will be discussed with emphasis on a 400 × 400 array presently being fabricated.

II. DESIGN AND FABRICATION

The 160 × 100 imager is an n-channel device designed to have a resolution element size of 0.9 × 0.9 mil^2. The organization is serial-parallel-serial, which allows the input of electrical signals to the parallel section. A double-level aluminum metallization separated by approximately 2500-Å $A\ell_2O_3$ forms the transfer electrode structure. Three-phase clocking is used so that in both the parallel and serial sections of the array a given phase occurs alternately on first-level and second-level metal electrode (Ref. 5). The signal charge packets are transferred to the (ϕ_3) output serial register electrodes through a composite gate region of width 0.3 mil. Overlap of first- and second-level electrodes is nominally 0.05 mil to achieve a 0.9 × 0.9 pixel. This requirement places extremely tight tolerances on photomask perfection, particularly for 400 × 400 size arrays.

An output amplifier is provided for both upper and lower serial registers to allow forward or reverse operation of the imager. This can increase array yield in the event of a malfunction of one amplifier. A balanced sample-and-hold design takes the precharge output from a source follower through a sampling MOSFET and to a second source follower, giving an amplifier bandwidth greater than 10 MHz. On-chip load MOSFETs are used in this design. A correlated clamping circuit is provided at the upper serial output to investigate on-chip low-noise video processing. This amplifier has a bandwidth of about 1 MHz. A micrograph of the 325 × 325 mil^2 chip is shown in Figure 1. Bond pads are extended some 50 mils from the active area so they remain over the thick silicon after a region slightly bigger than the array itself (90 × 144 mil^2) has been thinned. Thinning was performed by chemical etching either after the individual chips had been mounted on ceramic 40-pin headers or by etching a whole slice using an etch mask around each individual array. In this latter case, the slice was then scribed into individual chips and each subsequently mounted on headers. Either technique can provide uniformly thin membranes of thickness 10-12 μm. The surface of the membrane is highly reflective, although a light surface haze is sometimes found after removal from the etch. Membrane

stability is such that repeated temperature cycles from 24° C to -40° C do not fracture the CCD. Distortion of the membrane is observed in some cases at -40° but can be minimized by avoiding temperature gradients.

The imagers were operated in the full frame mode, and the readout sequence occurred while light was incident on the device. To reduce streaking in the displayed image, the ratio of integration time to readout time should be $\gtrsim$3:1, and a 5-second exposure at an output rate of 10 kHz (1.6-second readout) was used at -40°. A shuttered mode of operation is simulated by illuminating with a short light pulse during the integrate period only, and the imagery of a 160 X 100 operating in this mode at 24° C is shown in Figure 2.

High charge transfer efficiency is achieved by using a phosphorus implantation to achieve a 0.5-1.0 μm deep buried channel in nominally 10 Ω-cm p-type silicon. Typical buried-channel arrays operate at 6-8 volt clocks with a CTE of ≥0.9999 (measured in the serial register) with no electrically introduced fat zero. Equally good CTE in the parallel section is inferred from the square-wave amplitude response (SWAR) data discussed below. It does not appear that the transfer gate region to the output serial register is affecting array performance.

III. IMAGER CHARACTERISTICS

The successful incorporation of the CCD imager into a spacecraft system will require that a given array meet many performance specifications. High CTE and spectral responsivity must be combined with a low blemish count and dark current. Uniformity of both responsivity and dark current are very desirable. The arrays discussed in this paper are intended for operation at long exposure times and a 10-kHz data rate at -40° C. Array dark current is expected to decrease with the temperature T at $T^{3/2} \exp(-E_g/2kT)$ or a factor of 895 between 24° C and -40° C. Storage times of $\gtrsim$200 seconds should therefore be possible at -40° C without appreciable filling of the potential wells.

Performance parameters of two buried-channel 160 X 100 arrays are indicated in Table 1. The consistent achievement of high CTE requires tight control over substrate resistivity and implant dose to achieve the desired buried channel. Any metallization defects, particularly in the serial output registers, will also degrade CTE from the optimum for the buried channel. Using a voltage contrast mode with a scanning electron microscope allows correlation of

such defects with array CTE and allows processing optimization. There does not appear to be any significant effect of temperature (25° C to -40° C) or frequency (10 kHz to 1 MHz) on the measured transfer efficiency.

The dark current I_D of the buried-channel arrays is in the range 10-20 nA/cm^2 at room temperature as measured by a picoammeter in the precharge line of the output amplifier. While this method of measurement is generally reliable at 25° C, it fails completely at lower temperatures, where I_D becomes lower than the CCD leakage currents. Our measurements (Table 1) at -40° C are taken using an integration technique that allows the dark current to build up over a long period (~200 seconds at -40° C) to give a significant well population which results in an easily measured video voltage output. The CCD/amplifier is calibrated using a (large) current injected at the input diode in a separate measurement. This technique gives a decrease of 1000× between 24° C and -40° C in satisfactory agreement with that predicted above. In contrast, the precharge technique gives a decrease of 80-100, which merely reflects the degree of spurious dc leakage current from the CCD and ceramic package.

One advantage of the backside illuminated mode is high responsivity and smooth spectral responsivity (Figure 3). The log-log plot of signal current versus incident power has a slope (γ) of 1 ±0.1 under all operating conditions. The wideband responsivity to 2854-K radiation with no AR coating is 90 mA/watt with a 70% quantum efficiency at 4000 Å. Decreasing temperature to -40° appears to decrease the responsivity at all wavelengths below about 6000 Å by about 30% as measured on a device with peak QE of 40% at 8000 Å. This effect may be related to a change in surface recombination velocity and suggests that a passivation layer or antireflection coating be applied to the thin membrane surface. For a 100-μJ/m^2 exposure at the array during a 5-second exposure time, the ratio of signal to dark current (-40° C) implied by the data is 18.6 for 2854° radiation.

The squarewave amplitude response of the imager taken with a high-contrast bar chart is shown in Figure 4 out to the Nyquist frequency f_N = 21.9 line pairs/mm. The results in Figure 4 were taken at 1 MHz and -40° C, since detailed comparisons at 10 kHz (where data is less accurate) and 24° and -40° show no consistent change in the SWAR. This result would indicate that any distortion of the thin CCD membrane at -40° C is not sufficient to affect device resolution. High array CTE is reflected by measuring a constant SWAR across

the array (Figure 4), and only a very small SWAR loss can be attributed to CTE degradation. At f_N, the SWAR is 40% and 30% for bars parallel and perpendicular respectively to the serial register. The lower value for perpendicular bars is due to a bandwidth limitation in the external electronics in the 1-MHz data and is not a CCD effect. Without this limitation (device II), the SWAR for parallel bars is found to be 0.04 below the perpendicular value.

An estimate of the SWAR for device I can be made as follows: Using a substrate resistivity of 5 Ω-cm, and a buried-channel dose of 1.5×10^{12} cm^{-2} and drive-in of $2\sqrt{Dt} = 0.6$ μm, where D = diffusion coefficient for implanted phosphorus and t = drive time, one can calculate the depletion layer width to be 3.2 μm from the SiO_2-Si interface for 8-volt clocks. If the substrate has been thinned to 10 μm, this results in a neutral bulk layer thickness of 6.8 μm. By first substituting these values into the Crowell-Labuda formula (Ref. 7) for diffusion MTF, which has been shown by Seib (Ref. 8) to be an adequate approximation to the CCD case in essentially all instances; next, multiplying by the pixel collection aperture MTF ($\sin \pi fd/\pi fd$, d = pixel pitch = 0.0229 mm) and the lens MTF; and finally, substituting this total MTF function, $R_o(f)$, into the formula for SWAR,

$$\mathrm{SWAR}(f) = \frac{4}{\pi} \sum_{m=0}^{\infty} \frac{(-1)^m}{2m+1} R_o[(2m+1)f]$$

one finds the SWAR at the Nyquist limit (f_N = 21.9 lp/mm) to be 0.53 for illumination having a 0.8-μm wavelength, the wavelength of peak sensor response. This is somewhat above the experimental value of 0.40 but possibly results from the monochromatic assumption in the model.

Isolated light blemishes in the arrays have been reduced to a low level by bulk gettering and annealing processes (Figure 2). Bulk lifetimes after processing are ~50 μsec, and interface states at the Si-SiO_2 boundary are $\lesssim 10^{10}$/cm^2-eV. However, the uniformity of response to 2854-K illumination has been found to depend on the thinning process itself. Nonuniform thinning can result in bands of higher (or lower) sensitivity, which in some cases correlate with a light surface haze remaining after the chemical thinning. The uniformity of the imager response (and also of dark current) is determined by sampling each pixel video

with a multichannel analyzer, and is defined as the standard deviation divided by the mean. This parameter is equal to 0.19 at 5% of full well and 0.14 at 50% of full well for a 2854-K source measured at 10 kHz and -40° C. Uniformity of 0.08 both for 2854-K and 4000-Å radiation at 24° C have been measured in a device at the 20% saturation level (Table 1). Uniformity of dark current is 0.96 at -40° C and 10 kHz. Device II is more uniform at 24° C but degrades at low temperature. It should be noted however that the array dark uniformity is affected by an apparent heating effect in the membrane from the on-chip load MOSFETs.

Preliminary measurements of dynamic noise of isolated pixels using the balanced sample-and-hold amplifier indicated about 400 electrons of noise at 1 MHz and -40° C, which is considerably higher than expected from a buried-channel device. More recent results (Ref. 9) using improved measurement technique indicate a noise as low as 67 electrons at 24° C and 1 MHz. However, even with a noise level of 400 electrons, the dynamic range of the imager is 3500:1 (full well 1.6×10^6 electrons with 7-volt clocks).

IV. DISCUSSION AND CONCLUSIONS

The performance of the 160 X 100 arrays appears sufficiently promising to allow fabrication of a larger 3 ϕ, double-level imager of similar basic design. Fabrication of this array is in progress, and several problems peculiar to this 0.5 X 0.5 chip have become apparent. Photomask perfection is extremely difficult to maintain over such large areas, and a single defect in a metal level mask can cause a fatal intralevel metal short in the array. This problem can be minimized in slice processing but at the expense of additional steps. The integrity of gate oxide is important, since a 400 X 400 will have 101,000 mil^2 of thin oxide. Defect (pinhole) levels of <0.5 cm^2 have been observed on test slices using dry-wet-dry or HCℓ doped oxides. The integrity of anodic $A\ell_2O_3$ is well recognized, but pinholes do exist and will give rise to interlevel shorts. This effect is minimized by the 0.05-mil overlap, but care must be exercised to maintain some overlap in order to allow buried-channel operation. These yield loss mechanisms are all expected to be of prime importance for the 400 X 400. The performance of such an array is expected to be comparable to that of the 160 X 100. Uniformity of thinning and membrane planarity for areas near 1 cm^2 may require further development, and some form of support for the membrane may be necessary to maintain planarity. The uniformity of response and of dark

current may also depend on silicon slice perfection and the effectiveness of bulk gettering over extended areas.

In conclusion, the results presented have shown that the double-level anodized aluminum technique can be used to fabricate high-performance 3 ϕ CCD imagers which operate at reduced temperatures and 10-kHz data rates.

REFERENCES

1. C. H. Sequin, F. J. Morris, T. A. Shankoff, M. F. Tompsett and E. J. Zimany, Jr., IEEE Trans Electron Devices ED-21, 712 (1974).
2. R. L. Rodgers, III, "Imaging with Charge Transfer Devices," Digest of Technical Papers, 1974 IEEE Intercon, p. 1 (1974). Also R. L. Rodgers, III, and D. L. Giovachino, Proceedings of this Symposium.
3. L. R. Walsh, Proceedings of this Symposium.
4. D. R. Collins, S. R. Shortes, W. R. McMahon, R. C. Bracken and T. C. Penn, J. Electrochem Soc. 120, 521 (1973).
5. G. A. Hartsell and A. R. Kmetz, Digest of Technical Papers, 1974 IEDM, p. 59 (1974).
6. S. R. Shortes, W. W. Chan, W. C. Rhines, J. B. Barton and D. R. Collins, App. Phys. Letters 24, 565 (1974).
7. M. H. Crowell and E. F. Labuda, Bell System Tech. J., pp. 1481 ff, (May-June 1969).
8. D. H. Seib, IEEE Trans. Electron Devices ED-21, 210 (1974).
9. C. G. Roberts, Private communication.

Table 1. Performance parameters of two buried-channel 160 × 100's

	I	II
CTE	0.9999 (7-V clocks)	>0.9999
Saturation level	1.6×10^6 electrons at 7 V	2×10^6 electrons
Dark current	0.0078 nA/cm^2 (-40° C)	–
	7.8 nA/cm^2 (+24° C)	6.5 nA/cm^2
Responsivity (2854 K)	90 mA/watt (24° C)--No AR coating	99 mA/watt
Quantum efficiency (4000 Å)	70% (24° C)	10% (24° C)
SWAR		
Parallel to serial	40%	37%
Perpendicular to serial	29%*	41%
Signal to dark current ratio (100-μJ/m^2 exposure for 5 sec at -40° C)	18.6	–
Response uniformity	0.14 (-40° C)	0.08 (24° C)
	50% full well	20% full well
Dark uniformity	0.96 (-40° C)	0.24 (24° C)

*Electronic limitation.

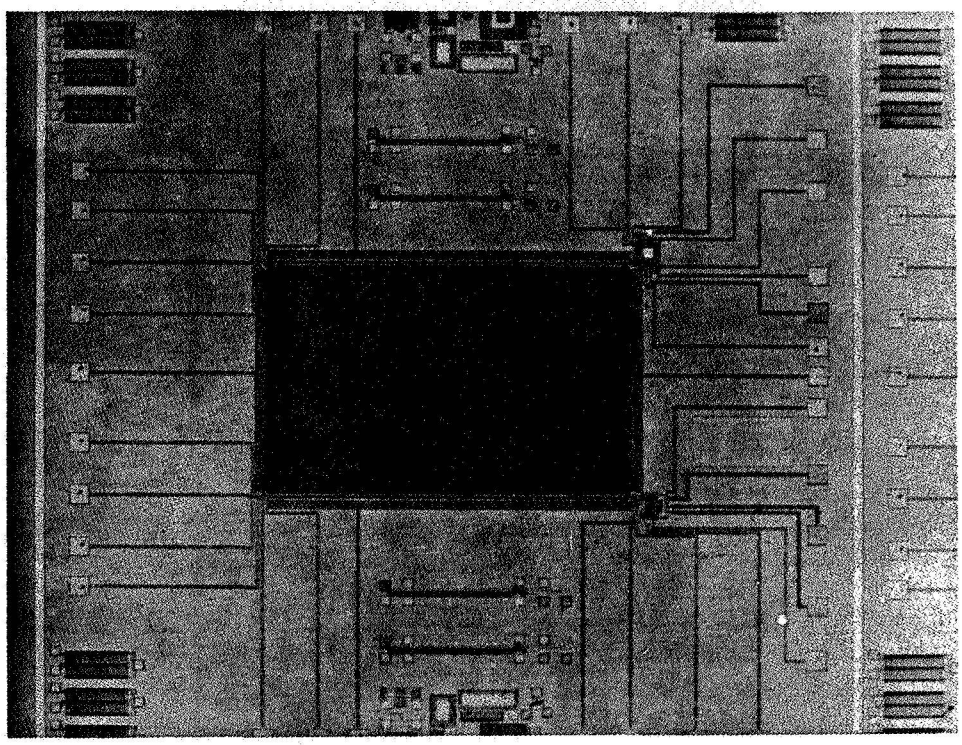

Figure 1. Photomicrograph of 160 × 100 CCD imager (Active area is 144 × 90 mil^2 and total chip is 322 × 325 mil^2.)

160 x 100 BURIED CHANNEL IMAGER

DATA RATE 1 MHz
TEMPERATURE 22°C
ILLUMINATION STROBED

Figure 2. Imagery at 24°C with buried-channel array using a strobed source to simulate shuttered operation

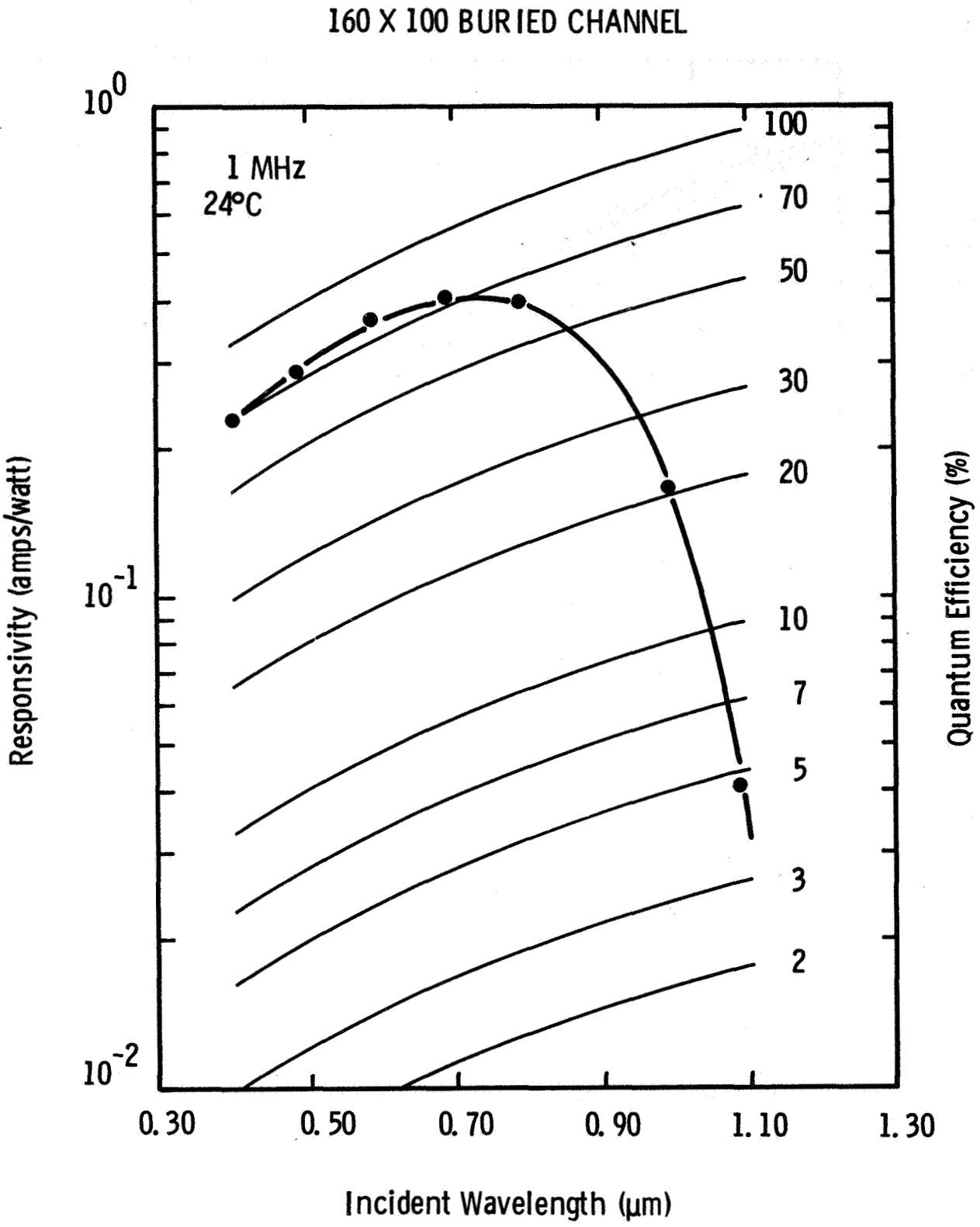

Figure 3. Spectral responsivity of 160 × 100 array (At -40°, there is an apparent decrease in responsivity below about 6000 Å by about 30%.)

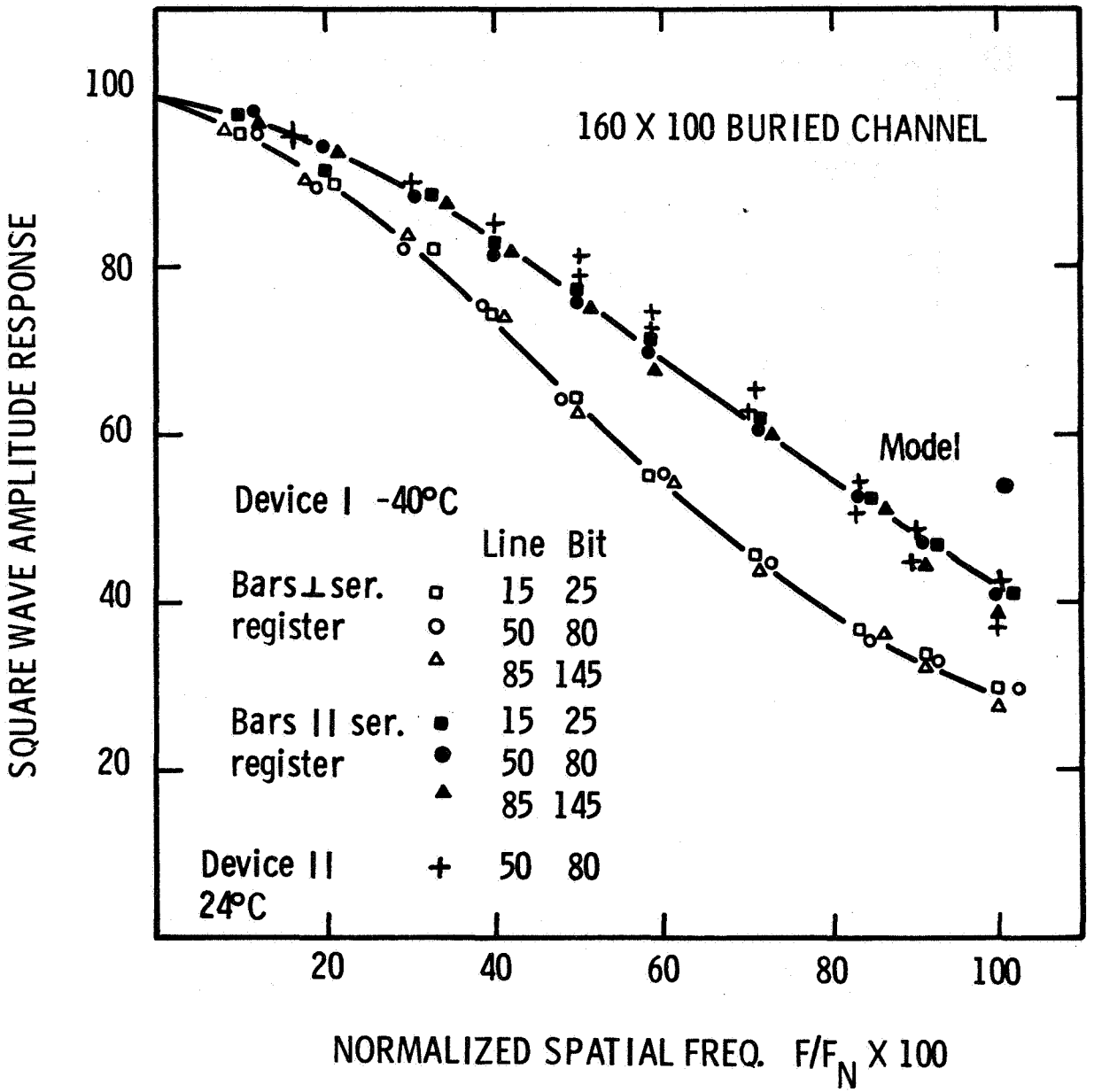

Figure 4. Squarewave amplitude response using a high-contrast bar chart (Essentially no change across the array is observed. The corrected value at the Nyquist frequency indicates the theoretical model for SWAR discussed in the text for device I.)

A 190 × 244 CHARGE-COUPLED AREA IMAGE SENSOR WITH INTERLINE TRANSFER ORGANIZATION

L. R. Walsh
Fairchild Camera and Instrument Corporation
Research and Development Laboratory
Palo Alto, California

A 190 × 244 element charge-coupled area image sensor has been designed, fabricated and tested. This sensor employs an interline transfer organization and buried n-channel technology. It features a novel on-chip charge integrator and a distributed floating-gate amplifier for high and low light level applications. The X-Y element count has been chosen to establish the capability of producing an NTSC-compatible video signal. The array size is also compatible with the Super-8 lens format.

The first few sample devices have been successfully operated at full video bandwidth for both high and low light levels with the charge amplifier system.

I. DEVICE ARCHITECTURE

The successful development at Fairchild in 1973 of the CCD-201, a 100 × 100 element CCD area imaging device, led to the decision to follow it with a larger structure based on essentially the same design philosophy. This device is a 190 × 244 element buried-channel charge-coupled area imager designed with interline transfer organization and using topside illumination. The element count on the 190 × 244 was chosen to establish compatibility with the Fairchild type 3261 sync generator in order to facilitate the generation of TV compatible video. The X-Y format was selected to approximate that of the Super-8 movie camera. With the interline transfer organization employed, 50% of the imaging area is photosensitive.

Figure 1 shows a functional layout of the device. The area array portion is similar in architecture to that of the CCD-201, except for the number of elements involved and a higher packing density. There are 190 vertical register columns in the array, one corresponding to each column of photosensors. The vertical registers are of the 2ϕ implanted barrier type. Their outputs parallel-couple into a high-speed output register which drives the amplifier system. Another high-speed register is located at the opposite end of the area array and permits the circulation of electrical information through the array. Both the input and output registers are of the four-phase type.

The amplifier section contains four separate amplifiers, enabling one to make sensitive performance comparisons between them. These amplifiers are (1) a gated charge integrator (GCI), (2) a distributed floating-gate amplifier (DFGA), (3) an input floating-gate amplifier (FGA1) located at the input to the DFGA and (4) an output floating-gate amplifier (FGA2) located at the end of the input channel of the DFGA. There are two charge steering gates, one located at the input to the GCI and the other at the floating-gate devices so that the array output can be channeled through either system.

A view of the 190 × 244 die is shown in Figure 2. It contains 33 bonding pads. The pad count is not minimal but reflects the desire to have maximum operating flexibility for the evaluation of the amplifiers. The die size is 248 × 242 mils. One of the design objectives was to constrain both the X and Y dimensions to ≤250 mils so that the masks would not have to be photocomposed. This resulted in the necessity to fold back the output register so that the amplifiers used space in the Y direction.

Figure 3 shows the portion of the output register which interfaces with the amplifier structure. Photo carriers are integrated at photosites 'A' for one frame time and moved to vertical register sites 'B' during one field and to sites 'C' during the next field. All vertical register columns are clocked simultaneously, transferring a row of data to the output register at the end of each horizontal scanning line.

II. AMPLIFIER DESIGN

In Figure 3, two separate control gates are shown (shaded) which enable one to direct charges either to the GCI or to the DFGA channel itself. This channel was made approximately half the size of the output channel so that

noise could be minimized. This sacrifice in charge handling ability was justified on the basis that the DFGA is primarily designed for low light level operation. A useful feature of this layout is that excess charge occurring while the DFGA is being used can be drained off to the GCI; therefore the GCI can function as a saturation control. Also it should be noted that DFGA analysis can be facilitated by injecting signals electrically into the DFGA through the reset circuit.

The GCI structure consists of an MOS signal amplifier and a reset circuit for resetting the amplifier gate after each charge packet has been sampled. In addition, there is a compensation amplifier, which does not receive the signal but is subjected to the reset transients seen by the signal amplifier. By taking the difference between the two outputs in an external amplifier, reset transients can be suppressed.

The theory and operation of the DFGA have been discussed previously (Ref. 1). In summary, the operation of a single floating-gate amplifier is based on the principle that the signal charge of a CCD channel can be nondestructively sensed by a floating-gate electrode. In a distributed floating-gate amplifier, the same signal charge is repeatedly sensed, thereby increasing the signal-to-noise power ratio by a factor equal to the number of times it is detected.

Figure 4 shows a view of the floating-gate amplifier system. Charge packets are transferred into the floating-gate input channel from the area array output register where they are first sensed by FGA1. As they are clocked through the input channel, they are subsequently sensed by the 12 floating-gate structures associated with the DFGA. Finally, they are detected by another single floating-gate amplifier (FGA2) and then terminate in a sink at the end of the channel.

Each of the twelve floating gates modulates its source-drain current, which flows under the large gates in the DFGA output channel. Charges clocked through the output channel are detected by a large floating gate at the end, which couples it to a large single floating-gate amplifier, designated FGA3. The current which flows into the output channel is under the control of a gate clocked at the data rate running between the two. Adjacent to it is a second gate, which is dc biased to reduce transient coupling from the clocked gate to the input channel.

III. PHOTOCELL DESIGN

A plan view and cross-section through a typical cell of the area array are shown in Figure 5. A photosite is defined on three sides by a P+ channel stop region and on the fourth by a barrier controlled by the vertical clock phases. Running vertically over columns of photosites is a first polysilicon layer, the photogate, which performs the carrier integration function and is clocked at the frame rate. Adjacent to each photosite is a vertical shift register cell, characterized by a carrier storage region bounded by channel stops and by gated barriers. Transfer in and out of a vertical cell is controlled by a gate made from a second polysilicon layer and clocked at the television scanning rate.

The signal saturation charge level for the cell is 0.07 pc, based on barrier heights of 3 volts. The photogate has a terminal capacitance of 2200 pF and a time constant of 120 nsec. The total capacitance of the vertical gates is 1500 pF with a time constant of 230 nsec.

IV. STRUCTURAL DETAILS

In the fabrication of the device, nine mask levels are involved. As Figure 4 indicates, the surface topography consists of two polysilicon layers with silicon nitride and thermal oxide dielectrics insulating them from each other and from the substrate. The vapox dielectric functions as a substrate for the aluminum, which in the area array serves to opaque the vertical registers.

In fabricating the device, the most critical process steps are the two masking operations, where the horizontal register gate structures are defined. The major phases, ϕ_{H1} and ϕ_{H2}, are formed from the first polysilicon layer, while the minor phases, ϕ_{H3} and ϕ_{H4}, are made from the second polysilicon layer. The overlap between the two sets of gates is 2 μm, which is the minimum design rule tolerance for all layers.

The definition of the floating-gate structure in the DFGA is also critical. In order to maximize sensitivity, the capacitance of the floating gates must be kept low. In this design, they are 5 μm wide and are defined in the first poly. The phase gates on either side of them are defined in the second poly and should ideally be positioned so that there is no gap on either side of the floating gates. This requirement results in a separation between the phase gates of 3 μm at this point.

In contrast to the etched gate structures which form the photogate and horizontal register gates, the vertical gates are formed by selectively doping the second polysilicon layer. Thus the gaps between vertical gates are bridged with undoped poly.

V. DRIVE CONSIDERATIONS

The input register, output register and DFGA are driven from the same four-phase clocking circuit. While a line of information is clocked out of the array, another line can be clocked in. There are 190 information bits in each horizontal line. The longest path from the output register is that to the DFGA output. There are 24 transfers for each phase in the DFGA, and 19 in the connecting channel. The total number of high-speed transfers for each phase is therefore $190 \pm 43 = 233$.

For a horizontal clock rate of 7.16 MHz, the element time is 140 nsec; thus the high-speed sections are emptied in 32.6 μsec. Since the horizontal interval is 63.5 μsec for standard TV, the inhibit time is 30.9 μsec. The horizontal registers can be clocked in either a two- or four-phase mode.

In the vertical registers, there is a vertical gate per sensor row, i.e., 244, plus three extra to allow for the incorporation of circuitry at either end. The vertical clock rate is 15.75 kHz for a scan time of 15.6 msec/field and a vertical inhibit time of 1.07 msec (60-Hz field rate).

Figure 6 shows a four-phase timing diagram suitable for driving the device. In this implementation, 260 CCD bit pulses are generated. During the horizontal inhibit period, all horizontal phases except ϕ_{H1} are kept low until the next line of video has been transferred in from V_1, which is also low at this time. One hundred and twenty-eight vertical pulses are generated per field. One hundred and twenty-three are needed as a minimum.

Charges are transferred from the area array to the output register during the horizontal inhibit interval, and from the photosites to the vertical registers during the vertical inhibit interval.

VI. PERFORMANCE

A number of 190×244 runs have been successfully fabricated to date. Good high light level imaging has been demonstrated. At very low light levels, the utility of the DFGA for the detection of signal levels on the order of 30 electrons has been confirmed. Figure 7 shows high light level images from the DFGA and

FGA1. The DFGA can handle approximately 90% of the saturation charge level of the area array. When all on-chip output amplifiers are biased as source followers with R_S = 1 K, typical saturation output voltages are 30 mV for the GCI, FGA1 and FGA2, and 150 mV for the DFGA. These pictures were taken at data rates of 10 MHz. Transfer inefficiency is negligible to 20 MHz. Horizontal resolution is approximately 142 lines/picture height. Vertical resolution is approximately 244 lines/picture height.

Representative low light level images are shown in Figure 8. Here the DFGA output is being viewed at five different light levels, at a date rate of 10 MHz, and in a +25°C ambient. Figure 8a shows a high light level image of approximately 140,000 electrons. In the subsequent pictures, the light source was attenuated using neutral density filters, the final attenuation resulting in an image of about 70 electrons.

VII. SUMMARY

A 190 × 244 CCD buried-channel area imaging array has been developed. An on-chip 12-stage distributed floating-gate amplifier significantly enhances the detectability of low light level images. Good array performance has been achieved at data rates up to 20 MHz.

ACKNOWLEDGEMENT

The development of this imaging array was in part supported by the Naval Electronic Systems Command.

REFERENCE

1. D. D. Wen, "A Distributed Floating Gate Amplifier in Charge Coupled Devices," ISSCC, 1975.

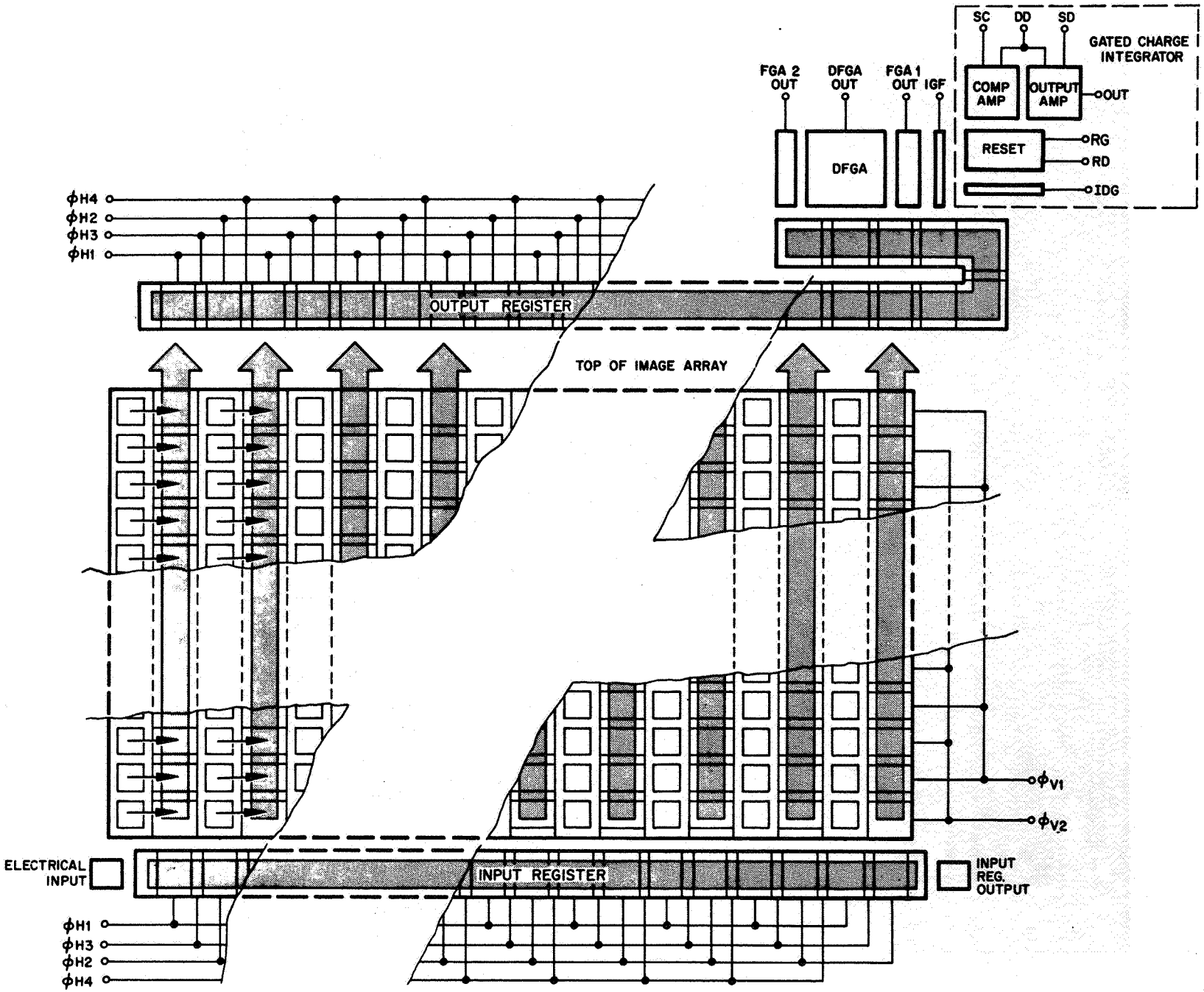

Figure 1. Functional layout of 190 × 244 array

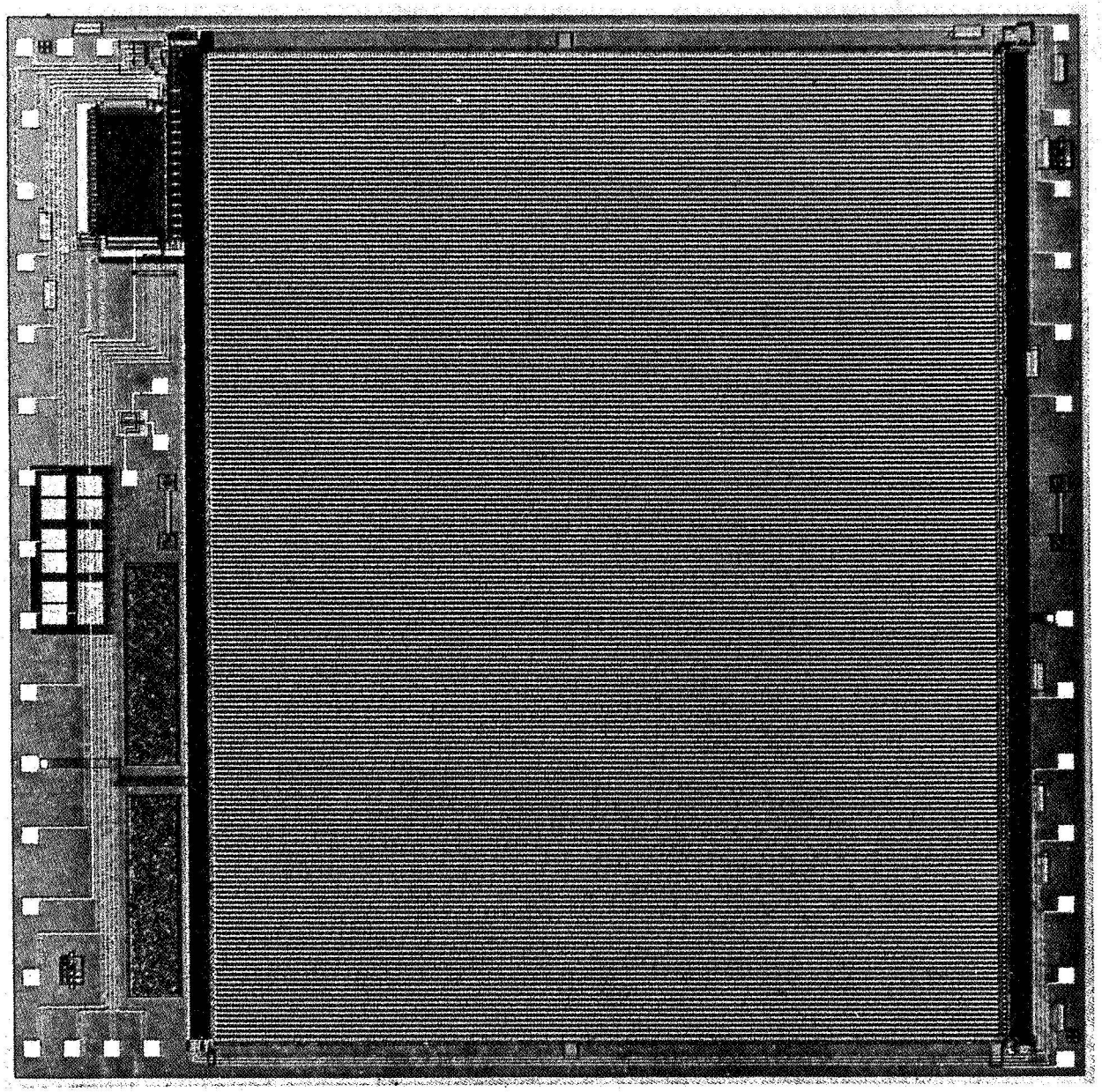

Figure 2. Photograph of die

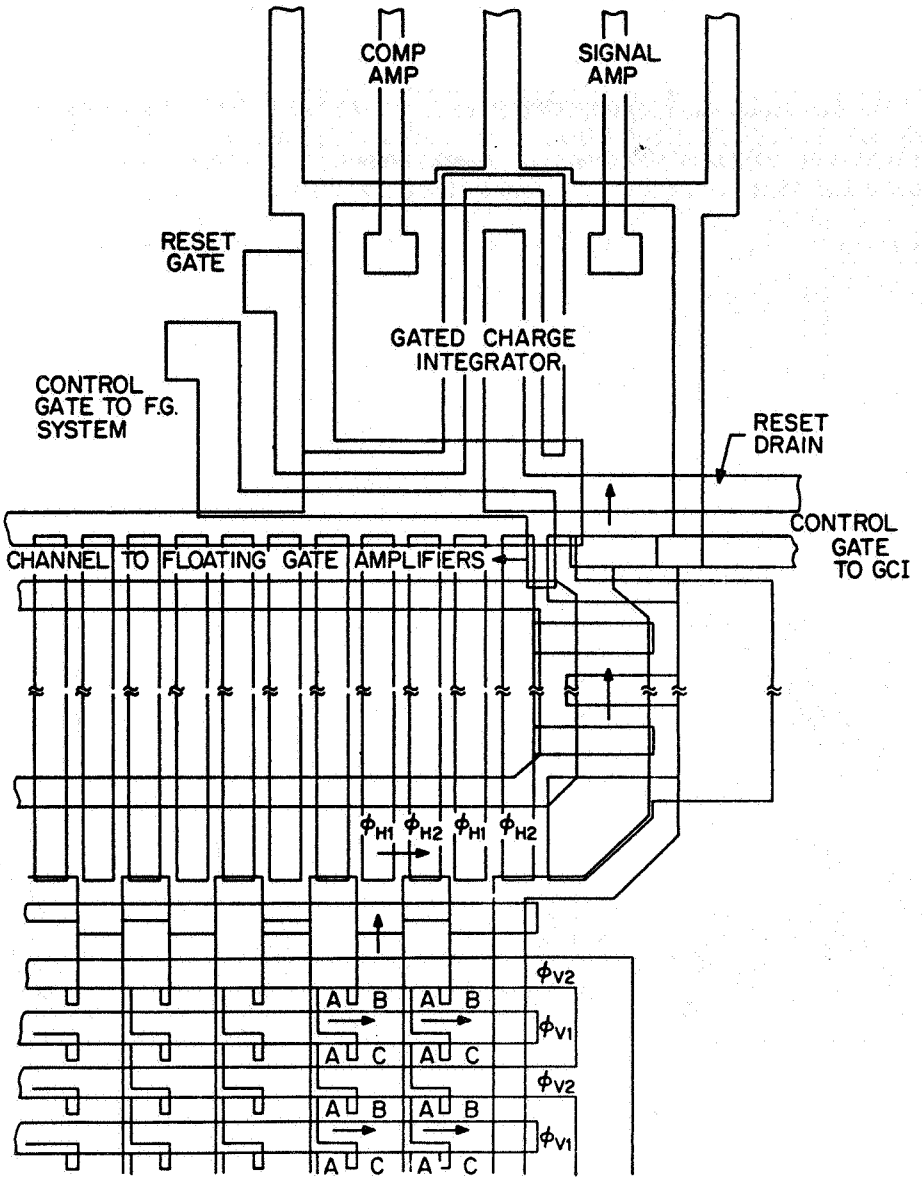

Figure 3. Detail view of array at amplifier interface

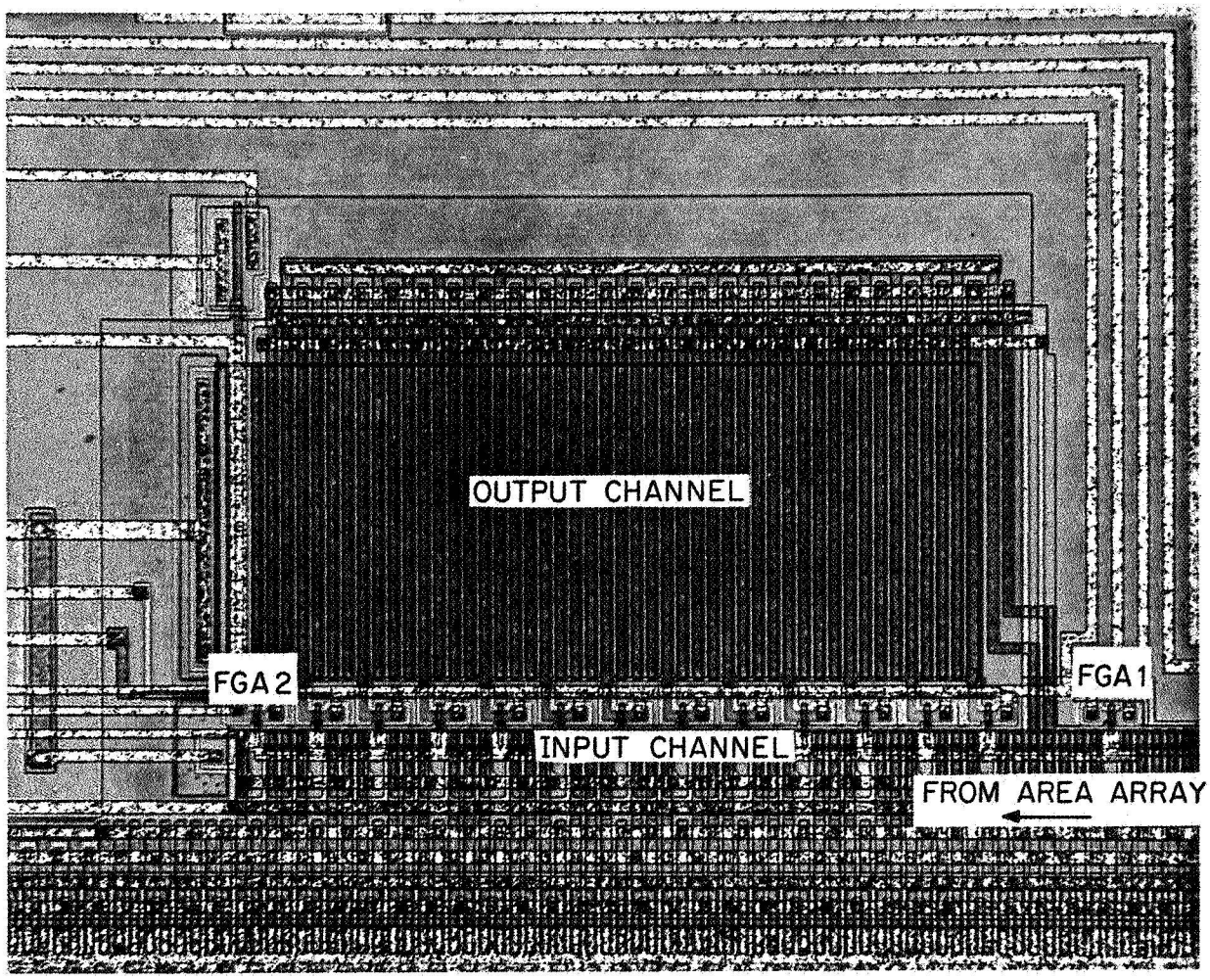

Figure 4. Floating-gate amplifier system

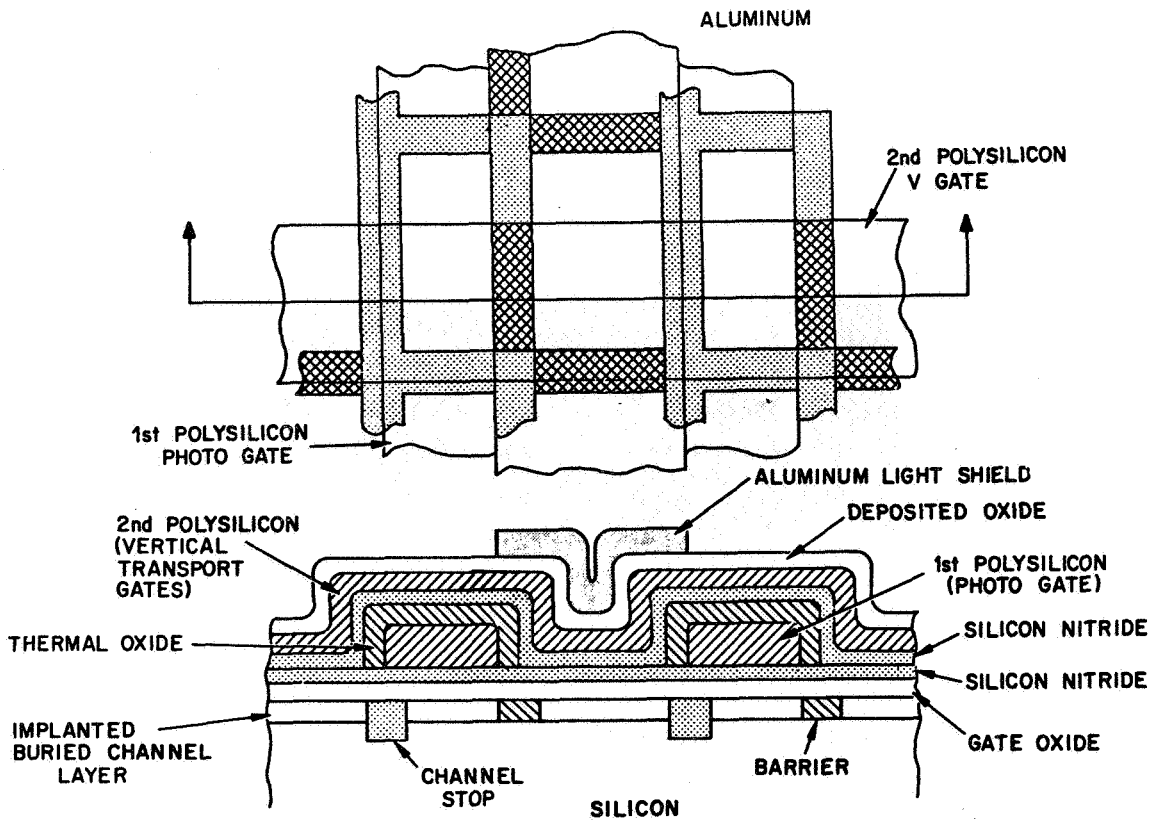

Figure 5. Cell structure in area array

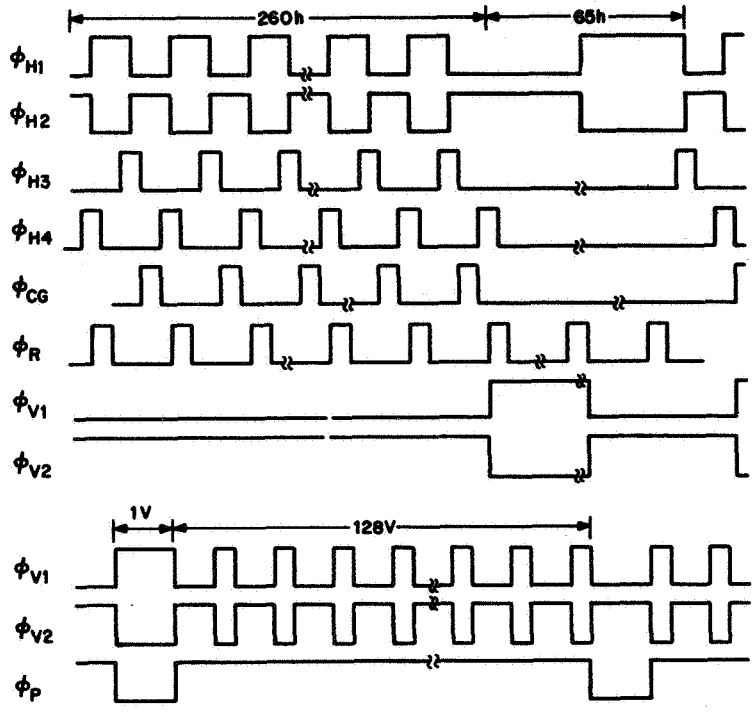

For 2ϕ Operation, ϕ_{H1} and ϕ_{H3} are in Phase; also ϕ_{H2} is in Phase with ϕ_{H4}

Figure 6. Timing diagram

(a)

(b)

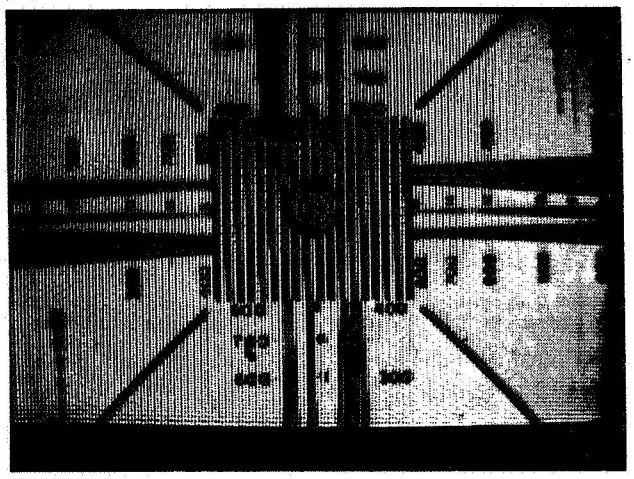

Figure 7. High light level images from (a) the DFGA and (b) FGA1 (To read the effective resolution, divide the test chart numbers by two.)

(a) ND=0, 140,000 electrons

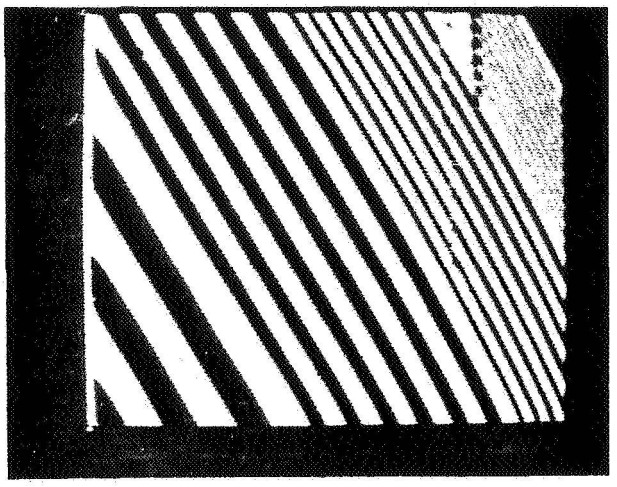

(b) ND= 1.0, 14,000 electrons

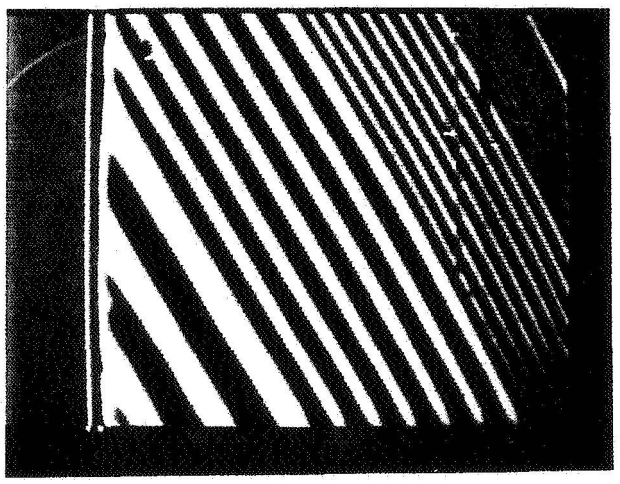

(c) ND=2.0, 1400 electrons

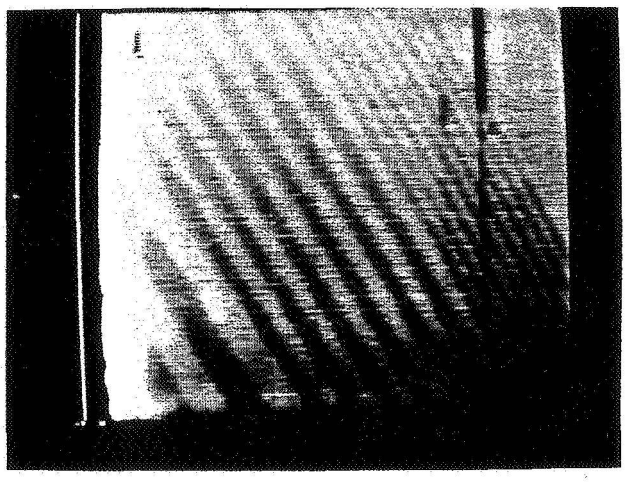

(d) ND=3.0, 140 electrons

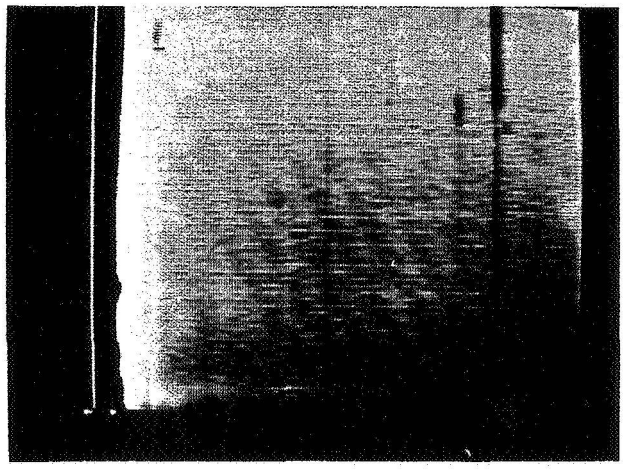

(e) ND=3.3, 70 electrons

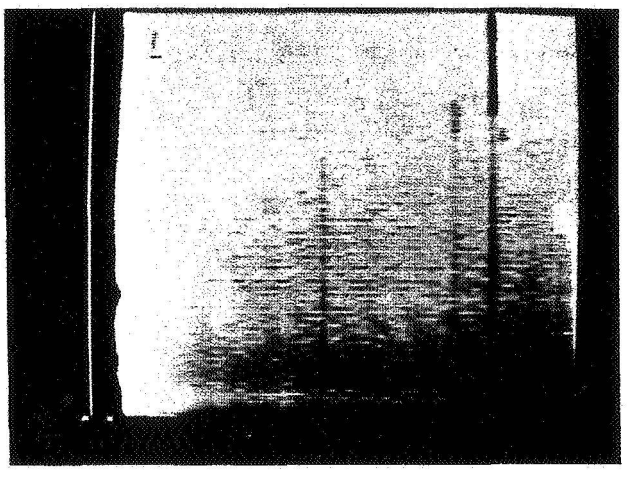

Figure 8. DFGA images at +25°C ambient, showing the effect of progressive light attenuation on image quality

EXPERIMENTS ON THE USE OF CCDs TO DETECT PHOTOELECTRON IMAGES

John P. Choisser
Electronic Vision Company
A Division of Science Applications, Inc.
San Diego, California

This paper will discuss the image tube design and processing requirements for building an ICCD. Work is under way at EVC for building an ICCD using the Fairchild CCD 201 (100 × 100) array, and progress will be reported. Demountable tests have been made, exposing parts of a CCD 201 to 15-kilovolt electrons over five radiation levels from approximately 10 to 10^6 rads. Other tubes built by EVC over the last few years which successfully use semiconductors to detect photoelectrons will be described briefly.

I. DIGICON AND PHOTOSIL

Two basic configurations of tubes we have built with semiconductor anodes are shown in Figure 1. The Digicon, which is on the right, is a magnetically focused tube, and the Photosil, on the left, is electrostatically focused. The tubes are, respectively, approximately 2 inches in diameter by 6 inches long and 1 inch in diameter by 2 inches long. Both types of tubes are built using externally processed molecular-beam-formed photocathodes, a process we believe to be important in avoiding poisoning of the semiconductors by alkali metals.

The design, fabrication, and use of Digicons have been described previously (Refs. 1-7). Both parallel output and self-scanned diode arrays have been used. Because one important facet of ICCD design concerns means for mounting CCDs, some Digicon headers will be shown as examples.

Figure 2 shows a header built for a 212-channel Digicon for Beaver at USCD. The ceramic (alumina) header is of multi-layer construction, so that the geometry of the diode leads can be different on the vacuum side and the air side. The basically circular contact configuration shown here is transformed into a rectilinear array of pins on 0.100-inch centers on the backside. The lateral travel of the lead paths between ceramic layers also permits an excellent hermetic seal, since the layers are metallized before the ceramic is pressed and fired. The diode manufacturer, in this case United Detector Technology, brazes the silicon chip to the header and attaches the lead wires from the substrate to the diodes. Figure 3 shows a similar header for Serkowski at the University of Arizona using a different array of 200 diodes. Figure 4 shows encapsulated and unencapsulated 200-channel Digicons.

The Photosils have been developed primarily for four-quadrant photon-counting for guiding on faint objects (Refs. 8 and 9). This is the basic tube configuration that will be used for the CCD 201. When encapsulated, the Quadrant Photosil is 2 inches in diameter and 5 inches long, including space in the rear for preamplifiers (Figure 5). One- and two-channel Photosils are planned for use in general photometry.

All of the previously described tubes have parallel outputs, and it is natural to consider the use of self-scanned arrays to permit the use of increased numbers of pixels. This has been done in the case of the Digicon, and Figure 6 shows a header for tubes using the Reticon 1024 B array. The first of these tubes was built 1 year ago for Tull of the University of Texas, and has been used successfully at the coudé spectrograph of the 107-inch telescope at McDonald Observatory.

To prevent damage to the circuitry on the chip, a mechanical mask is mounted over the chip to permit photoelectron bombardment only of the diodes. Radiation damage to the diodes in the Reticon array causing increased dark currents up to a maximum of a factor of about 15 has been measured, and is reported by Tull, Choisser, and Snow in Reference 6. Similar damage to CCDs which may increase leakage currents and adversely affect charge transfer efficiency is an important consideration in designing, building, and using ICCDs.

II. DEMOUNTABLE TESTS

In cooperation with Currie at the University of Maryland, EVC irradiated a Fairchild CCD 201 with 15-kilovolt electrons in an ultrahigh vacuum system. A mask was fabricated with five 0.020-inch-diameter holes, spaced so that they would have no rows or columns of the array in common. A second mask, with a single larger hole, was used to select the irradiation site for a particular run. The leads from the array were shorted together and grounded through a picoammeter. Photoelectrons were provided by a palladium photocathode, which was illuminated by a low-pressure mercury lamp.

Four exposures were made, representing approximately 10^3, 10^4, 10^5, and 10^6 rads. A fifth exposure was made with the mercury lamp on and the high voltage off. The array was then sent to Currie for tests.

Observation of the operating array showed no visible effect on dark current except for the spot which had received the highest irradiation. The increase in dark signal at this point was of the same order as the variations in dark current which occur normally over the area of the array.

Although these results appear encouraging, they should be considered somewhat inconclusive. The tests would have been more realistic, and possibly more damaging to the array, if the array were operating during irradiation. In addition, it was unfortunately not possible to make the tests at higher voltage, and there is some possibility that the 15-kilovolt electrons could not penetrate to the regions where damage would be more pronounced. In any case, additional more carefully controlled tests will be possible soon with the array in a tube, and with the protective oxide surface over the array removed.

III. ICCD DESIGN AND FABRICATION

Due primarily to the availability of the array, and because of the potential advantages of frontside bombardment if damage mechanisms permit (i.e., economics and cooling simplicity), it was decided to build an ICCD using a modified Fairchild CCD 201 and a Photosil tube design. The project is in cooperation with Currie at the University of Maryland, who will perform the test and analysis of the first devices (Ref. 10). The tubes are being built for a project sponsored by the Air Force Space and Missiles Systems Organization.

As previously stated, the tube will be made using the design of the electrostatically focused Photosil, shown in Figure 1. A 1-inch-diameter header has been built which conforms to Fairchild specifications in the die attach and wire bond region. The contact leads descend to a subsurface layer, where they are brought out to a pin circle near the perimeter of the header. This leaves the center area of the air side of the header clear for a cooling probe, and leaves most of the vacuum side available for brazing the copper sealing washer and Kovar anode cone mounting ring. The header is shown in Figure 7, along with a partially finished 2-inch header to be used in a Digicon with two parallel Reticon RL-1024 B arrays.

Later this month (March 1975), the headers will be sent to Fairchild for attachment of the arrays. The first tube is scheduled to be built in April, and tests will commence immediately.

IV. SUMMARY

Because of the number of successful image tubes built over the last few years at EVC using semiconductors of various types as anodes, we feel that the technology is at hand to build ICCDs as suitable arrays become available. In his paper (Ref. 11), for example, Collins will describe CCD arrays built at Texas Instruments specifically designed and mounted for rear illumination by photoelectrons. We are in hopes that, as future arrays are designed by the semiconductor manufacturers, the potential advantages to their use as photoelectron detectors will be kept in mind.

REFERENCES

1. Edward A. Beaver and Carl E. McIlwain, "A Digital Multichannel Photometer," Review of Scientific Instruments, Vol. 42, No. 9, September 1971.

2. Edward A. Beaver, Carl E. McIlwain, John P. Choisser, and Walter Wysoczanski, "Counting Image Tube Photoelectrons with Semiconductor Diodes," Fifth Symposium on Photoelectronic Imaging Devices, London, 1971, Advances in Electronics and Electron Physics, Vol. 33B, Academic Press, 1972.

3. John P. Choisser and Walter Wysoczanski, "A Multi-channel Image Tube for Photoelectron Counting," Proceedings of the Society of Photo-optical Instrumentation Engineers, Vol. 28 - Astronomy, Tucson, Arizona, 1972.

4. Edward A. Beaver, E. M. Burbidge, C. E. McIlwain, H. W. Epps, and P. A. Strittmatter, "Digicon Spectrophotometry of the Quasi-Stellar Object PHL 957," Astrophysical Journal, November 1972.

5. Edward A. Beaver, R. J. Harms, and G. W. Schmidt, "Digicon Applications in Astronomy," Sixth Symposium on Photoelectronic Imaging Devices, London, 1974 (to be published).

6. R. G. Tull, John P. Choisser, and E. H. Snow, "The Self-Scanned Digicon: A Digital Image Tube for Astronomical Spectroscopy," September 1974 (to be published).

7. John P. Choisser, "Recent Developments on the Use of Parallel and Self-Scanned Diode Arrays to Detect Photoelectrons," Sixth Symposium on Photoelectronic Image Devices, London, 1974 (to be published).

8. John V. Jelley, "Semiconductor Image Devices for Spectroscopy, Auto-guiding and Photometry," Cambridge Conference on Astrophysics, July 1972, The Observatory, Vol. 93, p. 9, 1973.

9. J. V. Jelley, and A. N. Argue, "A Quadrant Photosil Autoguider for the 17/24 Inch Schmidt Telescope at the Institute of Astronomy, Cambridge," Proceedings of the Society of Photo-optical Instrumentation Engineers, Vol. 44 - Astronomy, Tucson, Arizona, 1974.

10. D. G. Currie, "On a Photon-Counting ICCD Using the Fairchild CCD 201," Proceedings of this Symposium.

11. D. R. Collins, C. G. Roberts, W. W. Chan, W. C. Rhines, J. B. Barton, and S. Sobieski, "Development of a CCD for Ultraviolet Imaging Using a CCD Photocathode Combination," Proceedings of this Symposium.

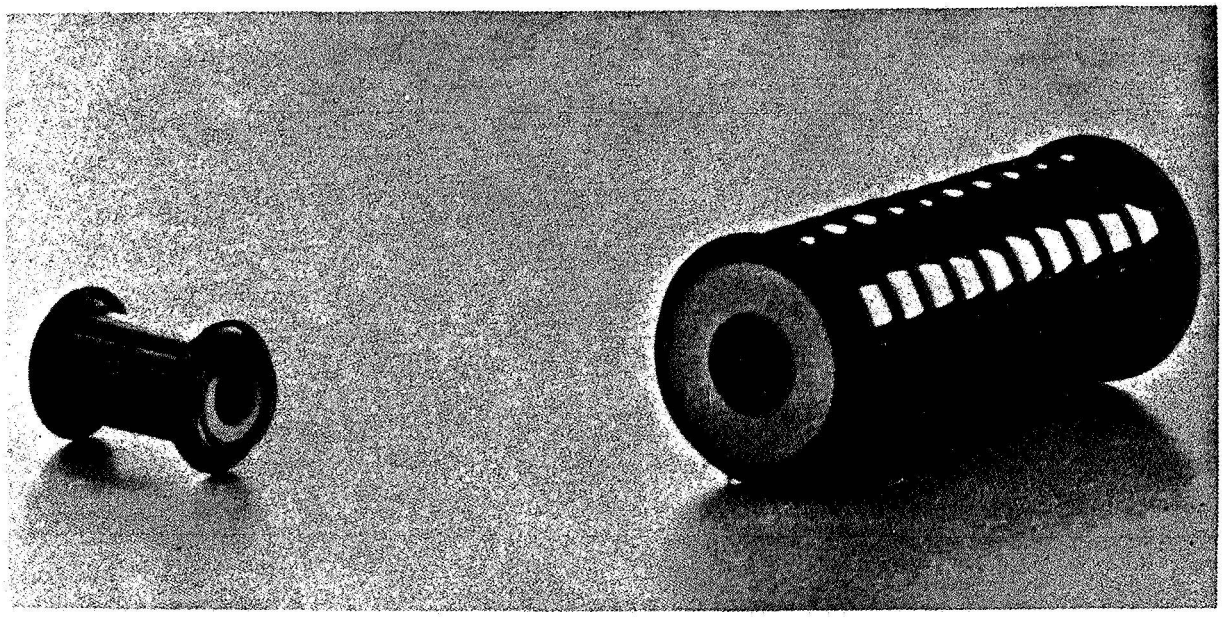

Figure 1. Magnetically focused Digicon (right) and electrostatically focused Photosil (left)

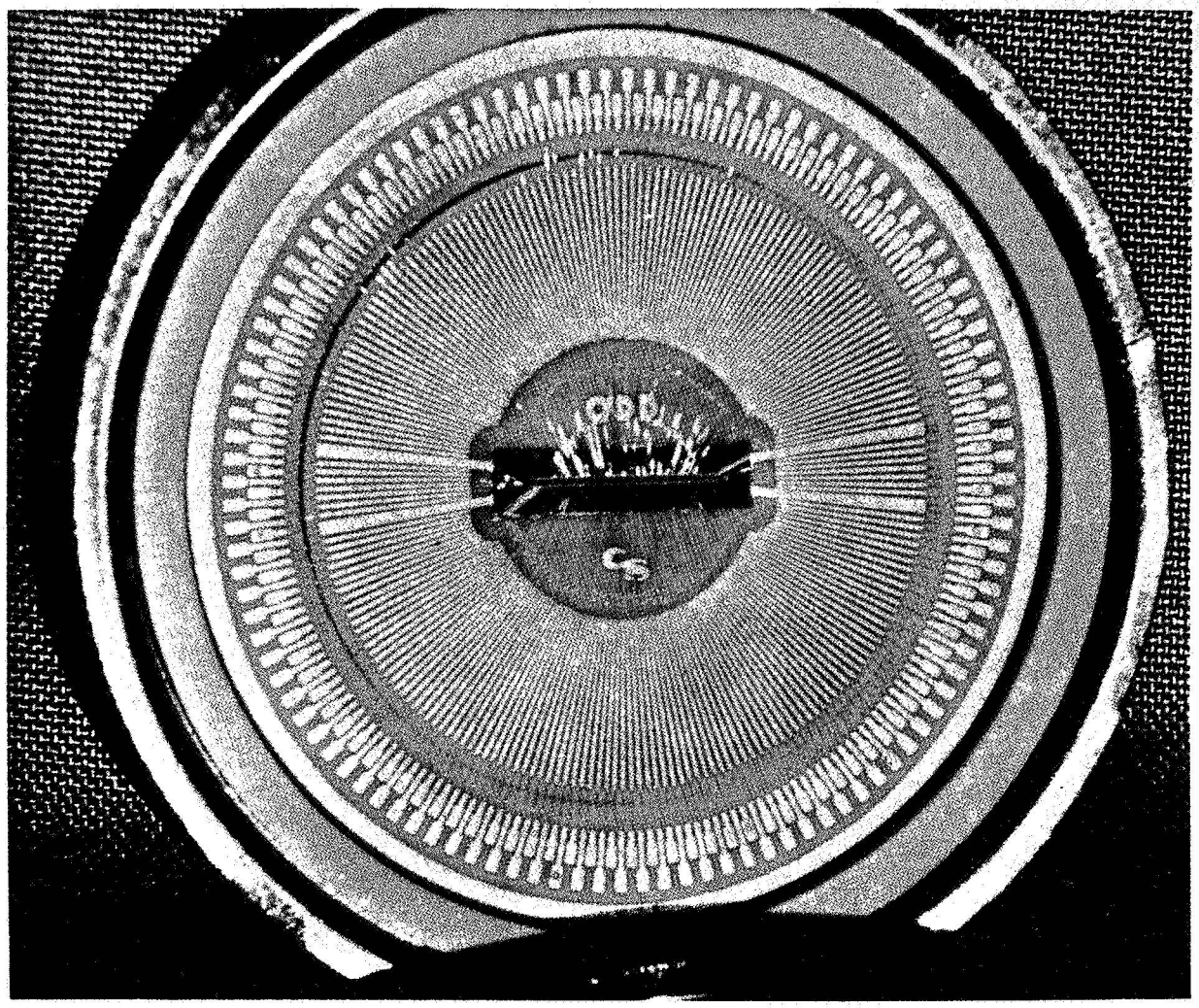

Figure 2. Multilayer ceramic header for a 212-channel Digicon

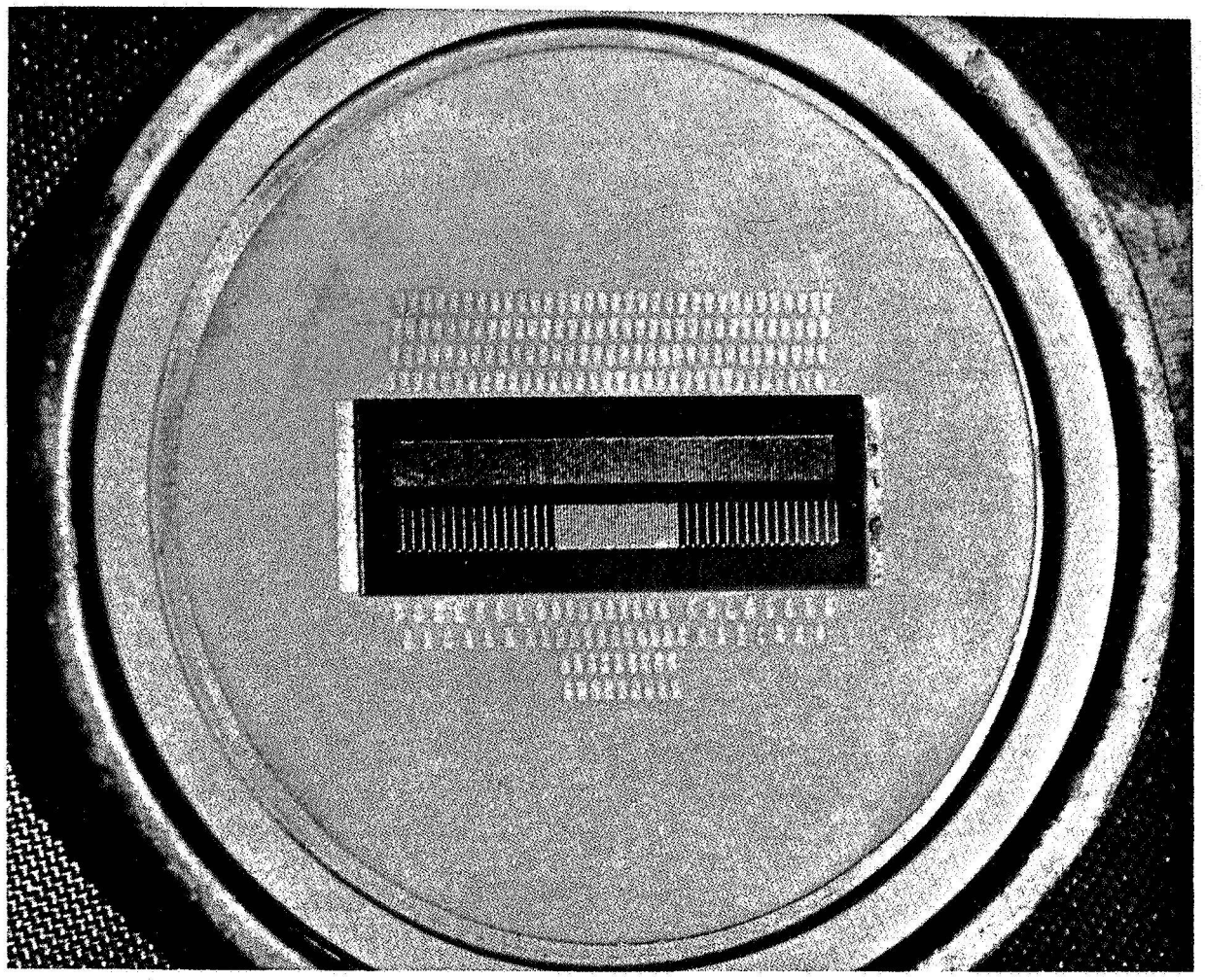

Figure 3. Multilayer ceramic header for a 200-channel Digicon

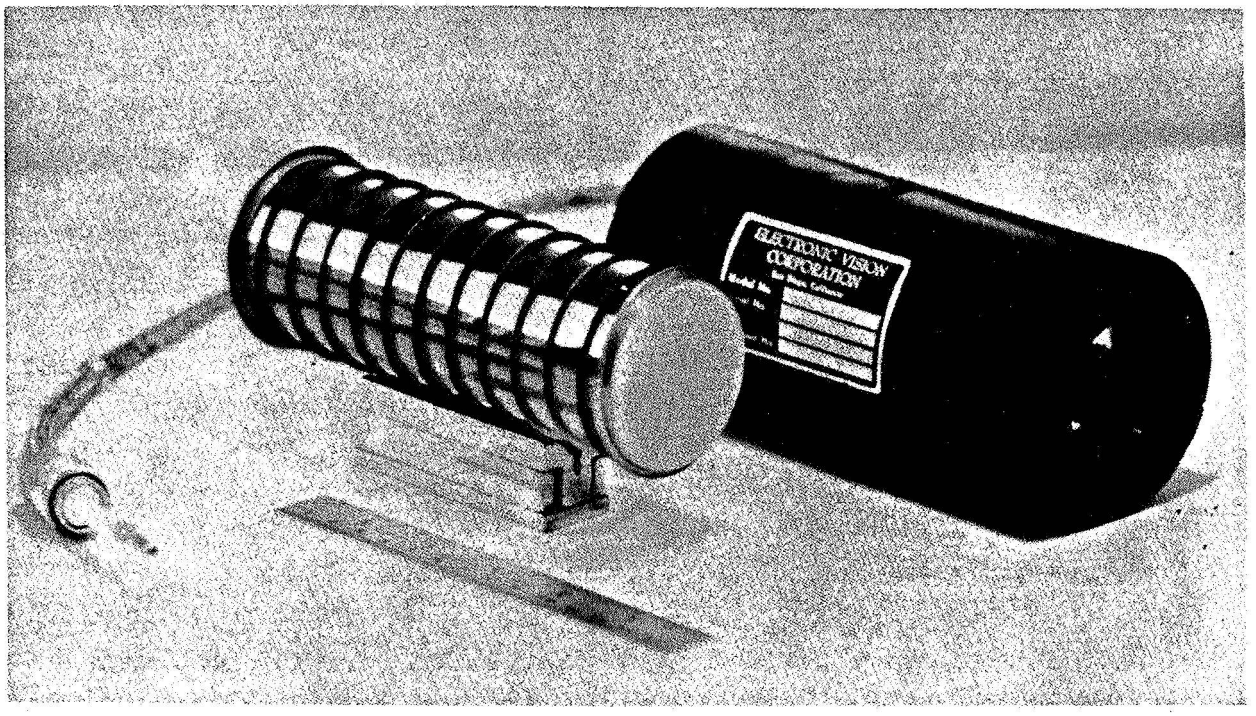

Figure 4. Encapsulated and unencapsulated 200-channel Digicons

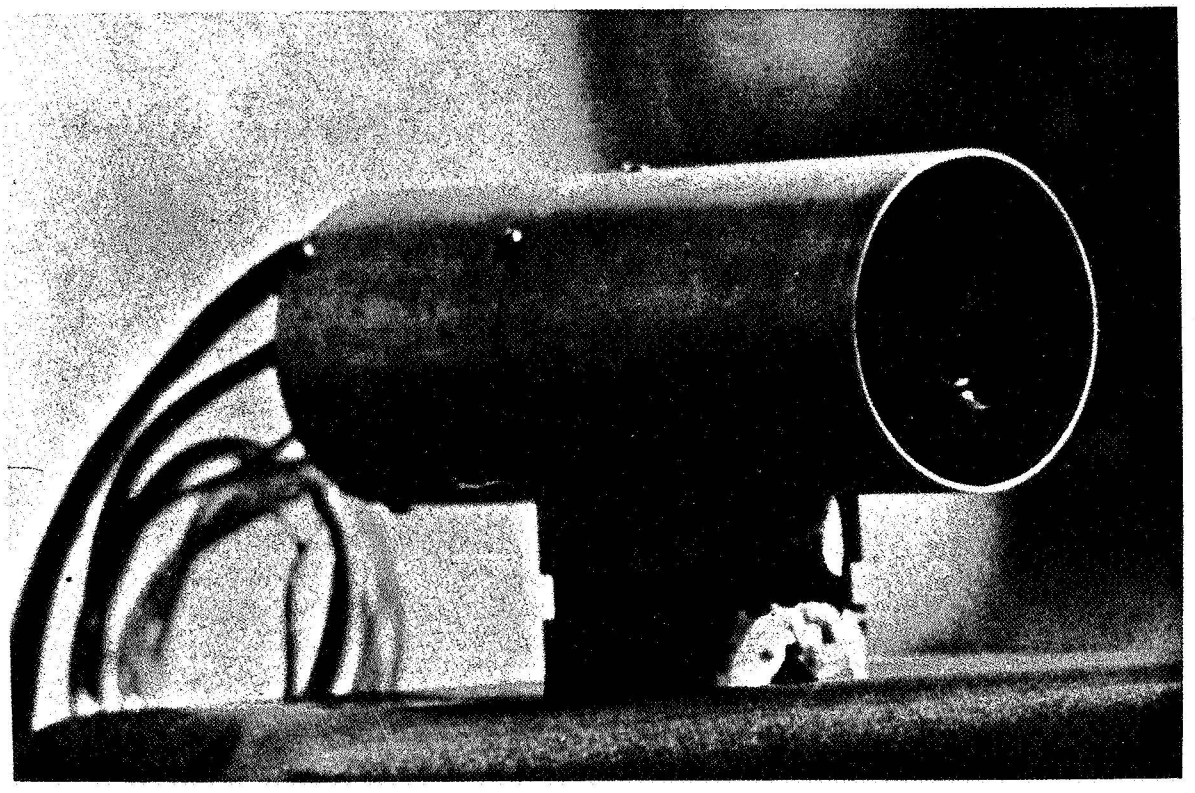

Figure 5. Quadrant Photosil for autoguiding on faint images

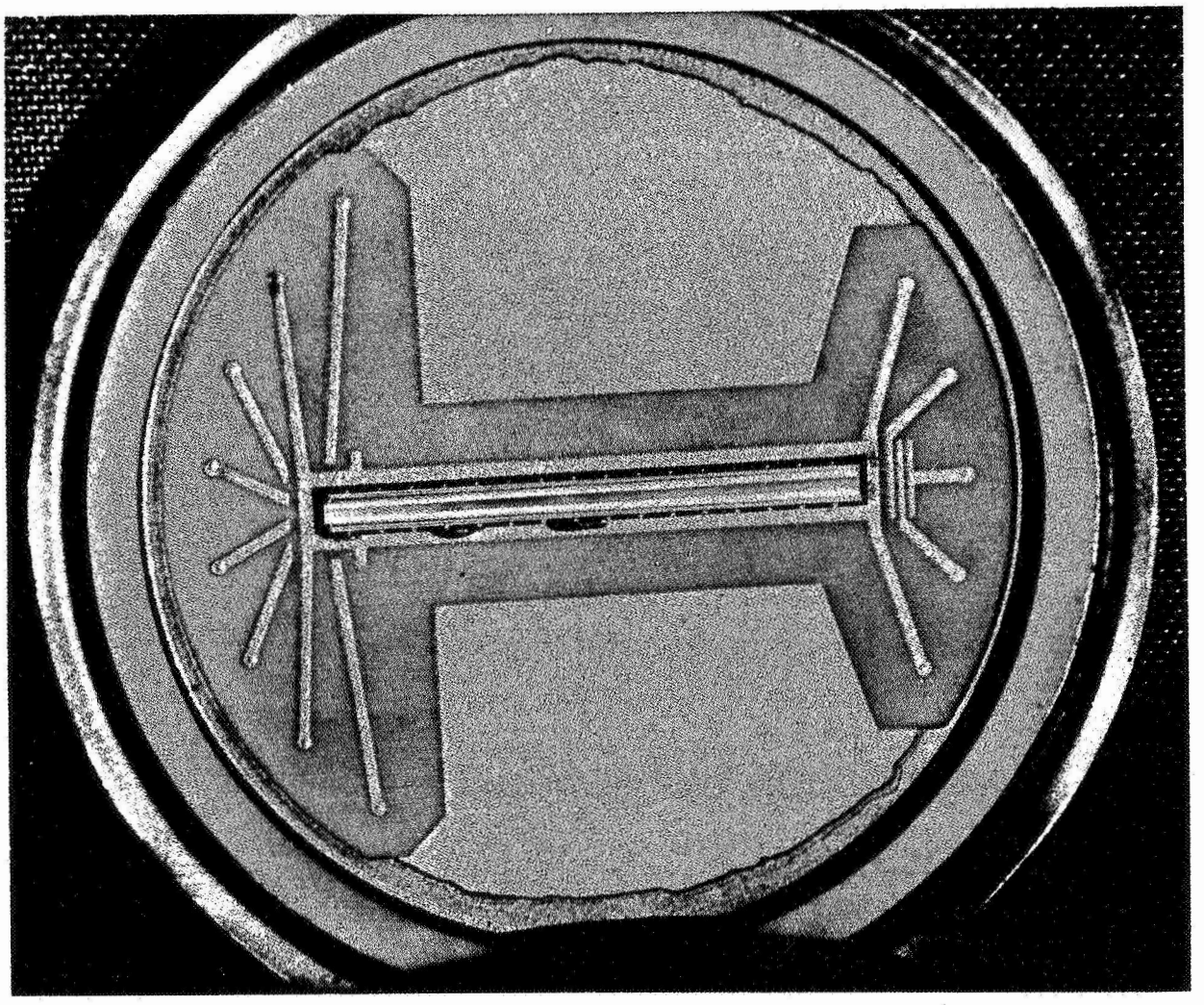

Figure 6. Multilayer ceramic header for a Digicon using the RL-1024 B Reticon array

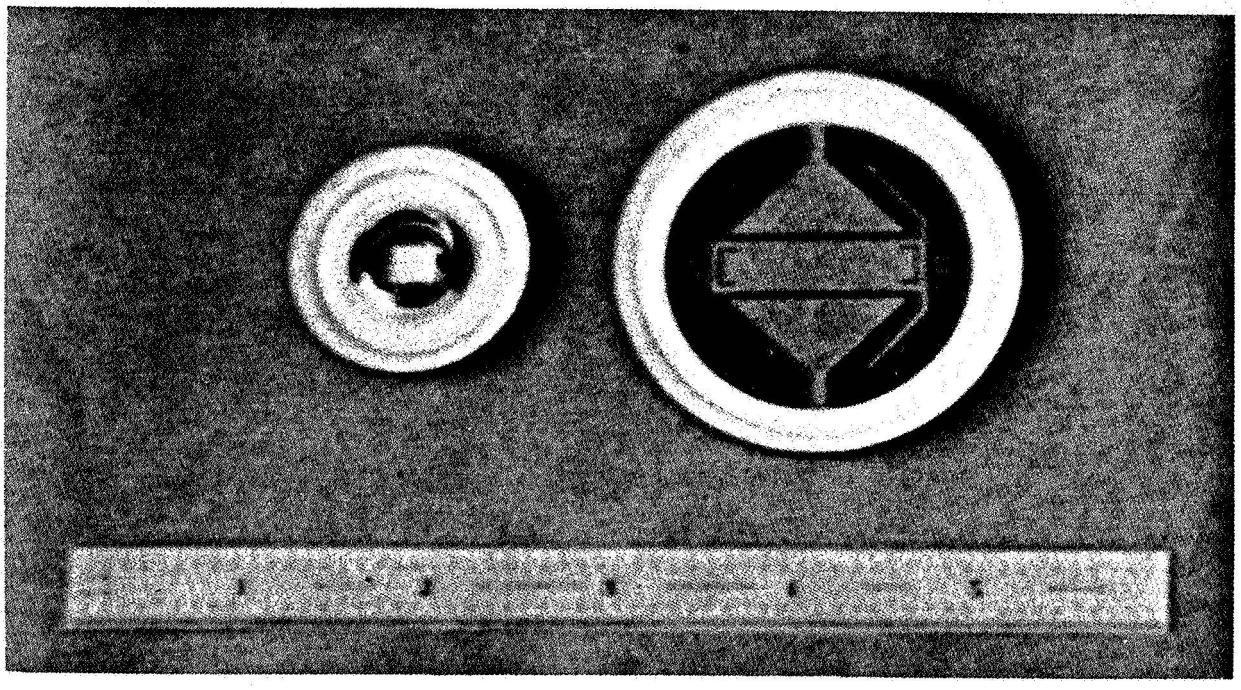

Figure 7. 1-inch-diameter Photosil header made for the Fairchild CCD-201 (left) and 2-inch-diameter Digicon header for two parallel Reticon RL-1024 B arrays (right).

DEVELOPMENT OF A CCD FOR ULTRAVIOLET IMAGING USING A CCD PHOTOCATHODE COMBINATION*

D. R. Collins, C. G. Roberts, W. W. Chan, W. C. Rhines, and J. B. Barton
Texas Instruments Incorporated
Dallas, Texas

S. Sobieski
Goddard Space Flight Center
Greenbelt, Maryland

For many space experiments, imaging and spectroscopy require excellent ultraviolet sensitivity. CCD imagers are promising sensors because of their low power, light weight, and high reliability. However, high responsivity at wavelengths below 0.4 micron is difficult to achieve with silicon CCDs even using thinned backside illumination. The use of a CCD in the electron-in mode, coupled with a bi-alkali photocathode to produce UV photon conversion, will provide the following desirable features:

(1) High UV response of the bi-alkali photocathode
(2) Excellent imaging quality of a CCD area array
(3) High signal-to-noise ratio due to the EBS (electron bombarded silicon) gain of the CCD operating in a tube configuration

This paper describes the rationale and progress made in developing a CCD for use as an UV imager.

*This work is partially supported by the U. S. Army NVL and NASA Goddard (DAAK02-74-C-0359).

The CCD area array geometry, and electrical and optical characteristics are described along with the technology used to fabricate the sensor. The advantages of using a thinned backside illuminated CCD in order to maintain MTF (modulation transfer function) and gain for the electron-in mode of operation are explained. Experimental data obtained using a scanning electron microscope as the signal source is presented on gain vs. accelerating voltage and MTF degradation due to lateral carrier diffusion from the back surface. Detailed discussion is given on the method of mounting the CCD within a tube structure to achieve backside illumination, cooling, multiple electrical connection to the CCD in the tube vacuum, and minimal cross-contamination between the CCD and the photocathode.

I. INTRODUCTION

Ultraviolet imaging and spectroscopy are primary mission goals for a number of planned space experiments. The capability for observing in the ultraviolet from a platform above the absorbing terrestrial atmosphere (0.3-micron cutoff) affords a number of advantages, including: (1) increased angular resolution, (2) extended wavelength baseline, (3) accessibility of important spectral resonance transitions, and (4) data on extremely hot or nonthermal sources nearer to their peak. The imaging of faint sources through band-limiting optical filters and spectroscopy, coupled with spatial resolution perpendicular to the wavelength dispersion direction, will also provide important new information. Representative planned programs include the study of stellar evolution, particularly by observations of the stars in hot-terminal stages of evolution, spatial characterization of the physical conditions within hot extended interstellar clouds, and the delineation of the physics and structure of the central regions of normal and high-excitation galaxies.

Figure 1 shows the spectral responsivity of photon-in (direct view) thinned backside illuminated CCDs. It may be seen that typical responsivity is unsatisfactory below 0.4-micron wavelengths. But it is possible to fabricate devices

with near-ideal backside accumulated surfaces and obtain near-theoretical quantum efficiencies at 0.4 micron (absorption length 0.13 micron in Si). However, examination of spectral resonance transitions below 0.3 micron (50-Å absorption length), such as the Lyman α line at 0.1216 micron, is not feasible with a photon-in CCD.

The purpose of this paper is to describe recent work in the development of an ultraviolet converter tube which will be particularly suited for space imaging or imaging spectroscopy. The tube uses a photocathode/window combination to convert ultraviolet (and visible) photons into photoelectrons, which in turn are focused by an applied electrostatic field onto a thinned charge-coupled device in close proximity to the photocathode. In this electron bombardment mode, the CCD provides a target for the photoelectrons with an inherent gain depending upon the accelerating voltage applied.

II. PHOTOCATHODE/TUBE SELECTION

A number of different photoemissive materials/window combinations can be used to produce the photoelectrons. Figure 2 illustrates the quantum efficiencies* of several combinations involving semi-transparent coatings which are suitable for UV applications. The Bi-alkali/MgF_2 combination has been selected for the developmental tube since it provides sensitivity in the visible and UV, thereby simplifying testing and evaluation. Immediate application at a ground-based telescope is therefore possible.

Quartz has an optical cutoff at approximately 0.2 micron and hence is of limited use as window material. This 0.2-micron cutoff of quartz also prevents the use of conventional curved fiber optic windows used in electrostatic inverter tubes. Hence, for UV applications, the flat window requires the use of either a proximity, magnetically focused, or pentode tube. From the standpoint of size, the proximity tube, has a distinct advantage since the photocathode and CCD are separated by only ~0.1 inch. However, the electric fields developed in such a tube structure may limit the accelerating potential that can be applied.

*Ref. EMR Photoelectric, wall chart.

III. CCD TARGET FABRICATION

The CCD imager chosen to be incorporated with a photocathode is a 160 × 100 resolution element, n-channel, buried-channel, double-level Aℓ-$Aℓ_2O_3$-Aℓ metallization, thinned, backside illuminated structure. This CCD imager is discussed in detail in a companion paper (Ref. 1). A cross section of the sensor is shown in Figure 3. The silicon membrane serves as the target for impinging electrons, and thinning is necessary to maintain spatial resolution near the Nyquist limit. Although in principle, the electrons could impinge upon the CCD from the front (metallized) side, the presence of the necessary gate oxide layer would eventually result in the buildup of charge in the oxide layer and drastically affect operation of the CCD. The performance of a single-level Aℓ metallization surface-channel CCD was found to degrade within a few seconds when operated while being irradiated on the front (metallized) side in a SEM (scanning electron microscope, 15-kV acceleration voltage). The same device could be operated in the SEM for a period of days with no degradation, with the electrons impinging on the thinned back surface.

IV. DESIRABLE PROPERTIES OF A CCD MOUNTED WITHIN A TUBE

The features desired or necessary for incorporating a CCD into a photocathode tube are listed below:

(1) Conventional semiconductor integrated circuit techniques for mounting the CCD.

(2) Parallel photocathode and CCD surfaces.

(3) Multiple electrical connections (~30) from the CCD to the tube exterior.

(4) Sturdy electrical connections (pins) at the rear rather than the side of the tube for ease in electrical testing.

(5) Simple CCD header, which is part of the vacuum tube wall.

(6) Minimization of cross contamination between the CCD/header and the photocathode.

(7) Header construction to facilitate cooling the CCD.

(8) Header construction to allow pressure equalization across the thin membrane, especially during vacuum evacuation of the tube.

(9) Header construction to withstand the tube temperature bake cycles (~350 to 400°C) without harming the CCD.

The ease with which the above properties can be achieved involves complicated tradeoffs in mounting and header, CCD, and tube fabrication.

V. HEADER CONSTRUCTION

Mounting a thinned backside illuminated CCD within a tube structure presents additional problems over those encountered in mounting a frontside illuminated device. The thinned surface must face the photocathode and yet allow electrical connections to be made to the CCD. An obvious method of mounting the CCD in such a fashion would be to flip-chip mount the CCD to a circular ceramic header with electrical feedthroughs. However, the concept of flip-chip mounting a CCD, much less a thinned CCD, would require a substantial CCD fabrication development effort. Hence the ceramic substrate on which the CCD is mounted must have an opening in it to expose the thinned silicon surface to the electron flux. Since the thin membrane will not withstand the pressure differential of the vacuum, the CCD itself cannot be part of the vacuum wall. This requires an additional vacuum wall element. However, the desire for ease in making multiple external electrical connections requires the substrate to be part of the vacuum wall. This feature in turn requires that the header have both a "cover" over the CCD and pressure relief vents between the main tube volume and the cover cavity.

A proposed CCD header configuration is shown in Figure 4. The ceramic substrate is brazed to a Kovar reentrant flange. The ceramic substrate itself is formed in two layers, providing a buried metallization path from the bond pads to the connector pins, which eliminates a potential vacuum leakage path. An alloy stage is brazed to the bottom of the ceramic substrate for mounting the thinned CCD. A seal flange is brazed to the top of the ceramic substrate. After the CCD has been alloyed to the alloy stage and bonded to the bond pads, a Kovar cover is heliarc welded to the seal flange, providing the outer vacuum wall. A small hole through the ceramic substrate provides the pressure relief vent between the main part of the tube and the CCD cavity. After the cover has been sealed, the tube flange may be heliarced to the main tube body.

This header design has all of the desirable features listed above. The alloy stage provides a good thermal expansion match to the silicon CCD during

the prolonged 350-400° C tube fabrication process. The only possibility for cross contamination between the CCD and the photocathode is through the small vent holes. While the contamination of the CCD MOS structure by alkali vapors is a real concern, remote processing of the photocathode can reduce the probability of this occurrence. Should cross contamination prove to be a problem, it is possible to eliminate the vent holes and evacuate the two regions separately. Attaching a thermoelectric cooler to the Koval cover will permit easy cooling of the CCD. Accurate registration and planarity of the CCD to the photocathode are assured by maintaining a flat surface on the alloy stage, and by proper alignment of the tube flange to the alloy stage.

VI. SIMULATED TUBE OPERATION USING A SCANNING ELECTRON MICROSCOPE

In order to obtain information on the electron-in mode of CCD operation prior to actual tube operation, a SEM was utilized. While no imaging could be performed in this experiment, critical performance in the 8- to 20-kV accelerating potential range was obtained. Figure 5 shows a plot of EBS (electron bombarded silicon) gain vs. acceleration voltage for three different CCDs. For comparison, both theoretical and typical SIT (silicon intensified target) tube gains are presented. The gains obtained are less than ideal; however, the devices were tested with the electron beam at a 45-deg angle of incidence to the target, increasing the effective "dead voltage." These devices were also fabricated with blue responses (0.4 micron) of less than 10%, indicating insufficient back surface accumulation. It is anticipated that sensors with near-ideal blue response will provide lower dead voltages and higher gains.

The effect of lateral carrier diffusion on the MTF (modulation transfer function) for the electron-in mode of operation is similar to the results obtained with blue light. For the resistivity of the p-type substrate used (8 Ω-cm), the depletion depth is approximately 4 microns. The thickness of the thinned membrane is approximately 10-12 microns. Thus the undepleted silicon is only 6-8 microns in thickness, compared to the 23-micron center-to-center separation of the resolution elements. Thus the degradation in MTF due to lateral charge diffusion is small. This may be seen in Figure 6 from a plot of output signal vs. beam position, as a beam is traversed across adjacent resolution elements.

VII. CONCLUSIONS

While the operation of a CCD in conjunction with a photocathode for UV imaging remains to be demonstrated, many problems concerned with this concept have been satisfactorily addressed. The thinned electron-in backside illuminated CCD has demonstrated gains of 3000 and excellent resolution. Furthermore, the difficult technology needed for mounting a thinned CCD within a tube appears feasible. Major questions still to be resolved involve operation and reliability of the photocathode and CCD once the tube is activated.

While the major emphasis of this paper has been UV imaging, it is appropriate to comment on the much broader consequences of this EBS CCD operation. The gains possible with a CCD/photocathode combination are not only useful for faint UV imaging but are also extremely important for all LLLTV (low light level TV) applications. Due to the high gain preceding the CCD and the inherent low noise of the CCD (less than 100 electrons/pixel at room temperature), a simple CCD/photocathode proximity tube should provide equivalent preformance to an ISIT (intensified SIT) tube. Furthermore, by maintaining the gain G of the EBS CCD at a sufficiently high level and reducing the noise such that G is approximately ten times the rms noise equivalent number of electrons per packet, one should be able to sense individual photon events, since the signal charge per packet resulting from a single photoelectron will be approximately G.

REFERENCE

1. G. A. Antcliffe, L. J. Hornbeck, J. M. Younse, J. B. Barton, D. R. Collins, "Large Area CCD Imagers for Spacecraft Applications," Proceedings of this Symposium.

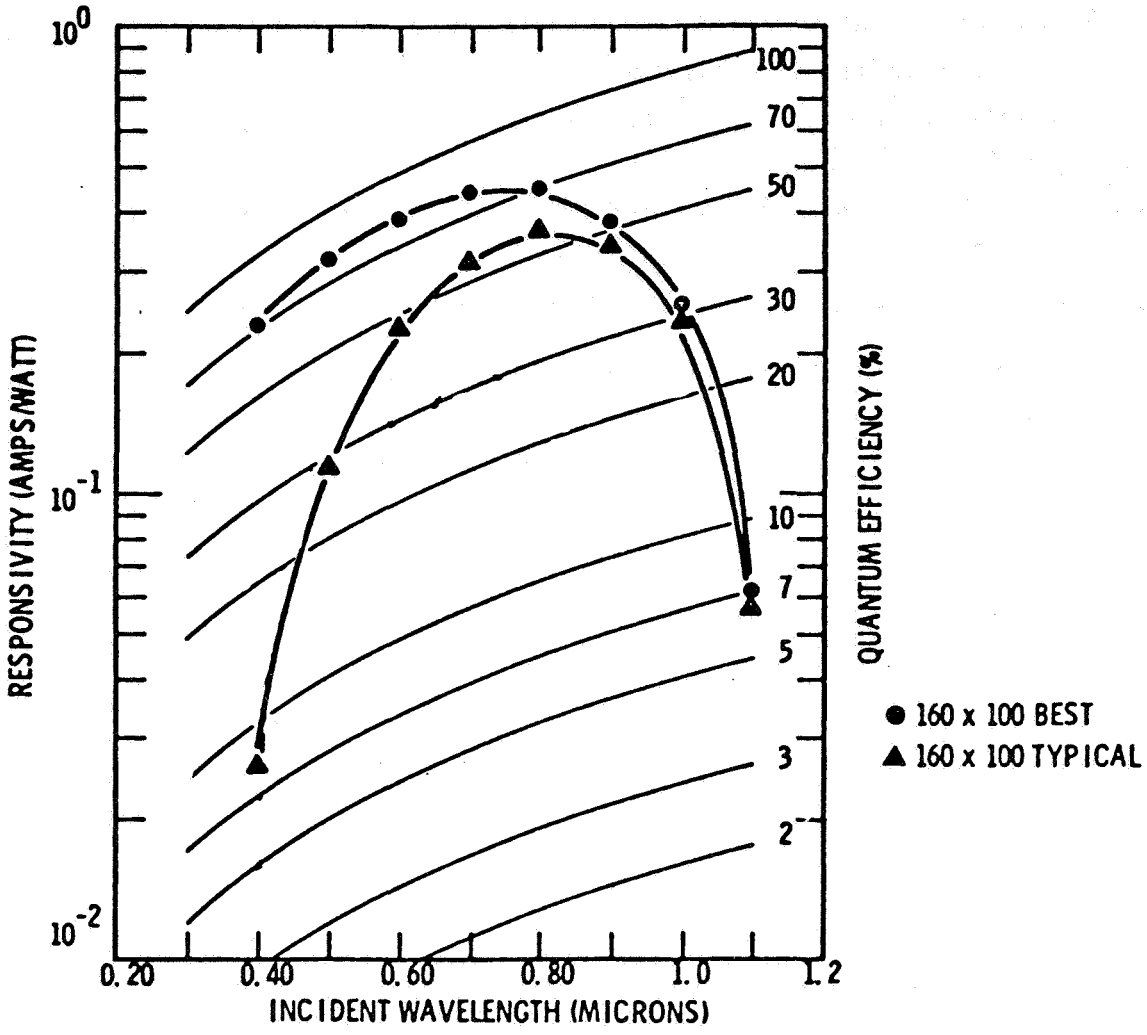

Figure 1. Spectral responsivity of near-ideal and typical thinned backside illuminated CCD area imagers

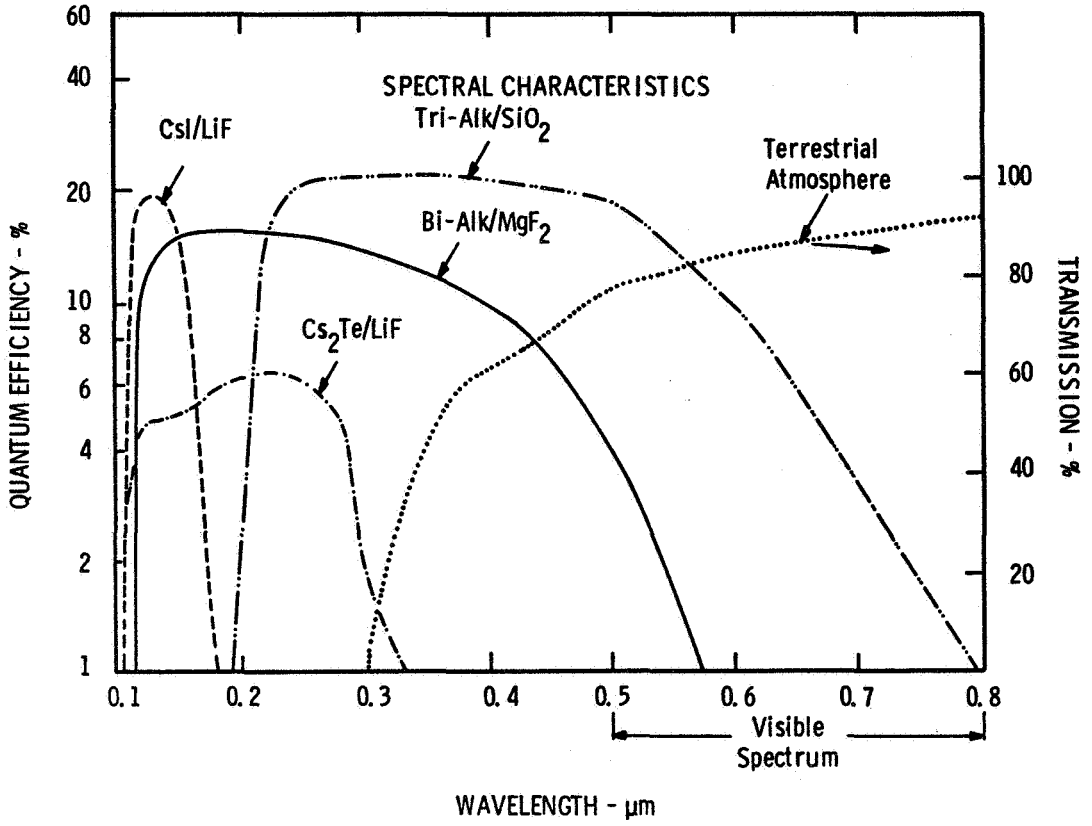

Figure 2. Quantum efficiencies of different photocathode/window combinations as a function of wavelength (Transmission of the earth's atmosphere as a function of wavelength is also presented.)

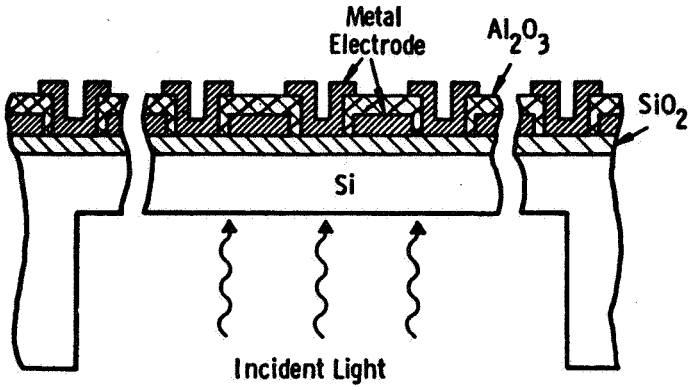

Figure 3. Cross section of a thinned CCD area imager (Membrane thickness is approximately 10-12 microns.)

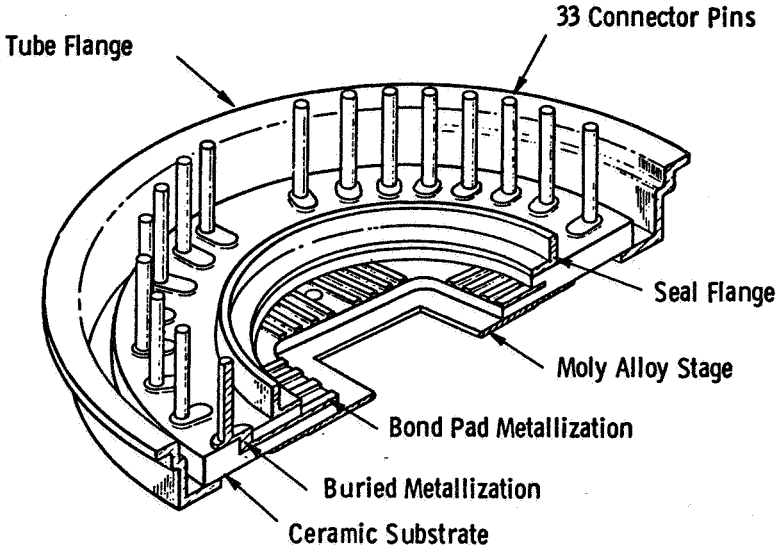

Figure 4. CCD header configuration

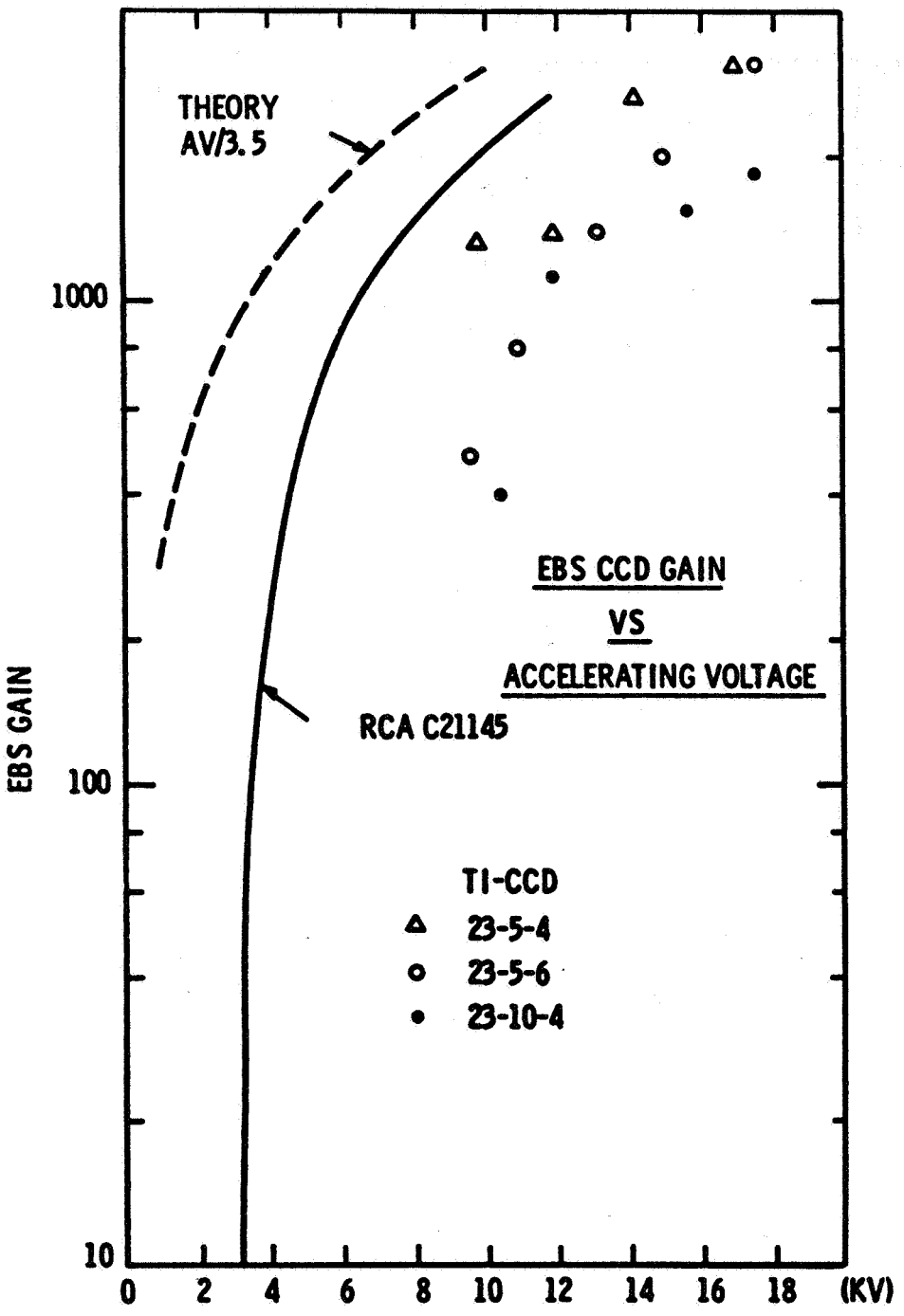

Figure 5. EBS gain of three CCDs vs. acceleration voltage. Theoretical and typical SIT data shown for comparison (Data taken with e-beam at 45° incident angle to the thinned silicon surface.)

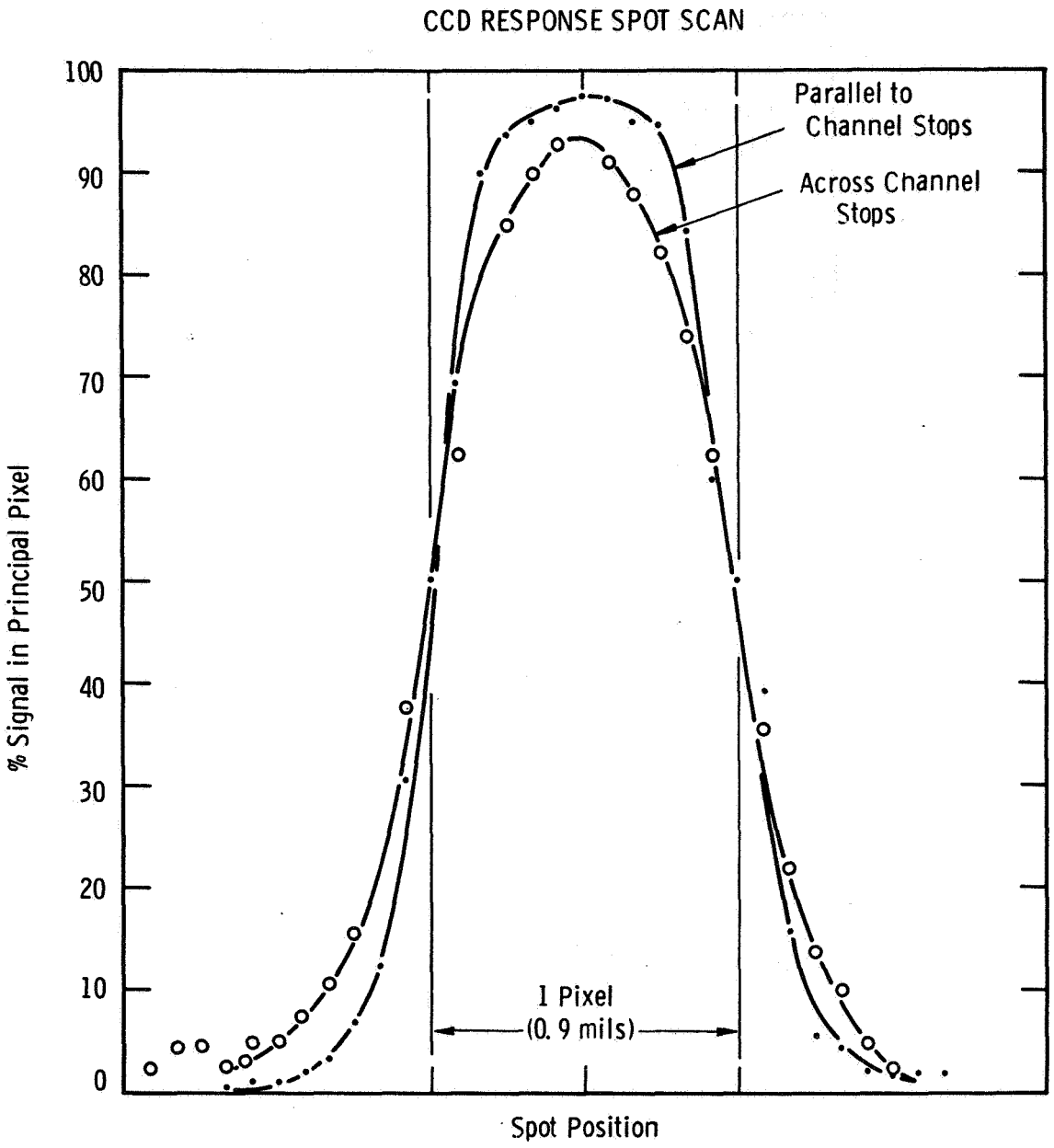

Figure 6. Plot of output signal vs. e-beam position relative to the pixel boundary for a 0.9 × 0.9 mil pixel (Data is presented for e-beam motion both parallel and perpendicular to the channel stops; e-beam acceleration voltages of 8-10 kV were used with effective range of approximately 1 micron. Variation in data between the parallel and perpendicular data may be primarily due to inaccuracy in focusing of the e-beam on the silicon surface.)

SLOW-SCAN OPERATION OF LONG LINEAR CCD ARRAYS

Michael Vicars-Harris
Fairchild Space and Defense Systems
Syosset, New York

The performance and characteristics of Fairchild long linear CCD arrays present a unique design input to slow-scan imaging systems. Slow-scan imaging generally results from requirements for either very high resolution or for very long integration times, or both. Linear CCD arrays used singly or in optically butted assemblies permit practical implementation of long line array systems with 6000 or more picture elements per line with readout rates in excess of 5 MHz. Display and tape recording of slow-scan imagery with over 1000 picture elements per line also presents unique challenges. This paper discusses performance results and the operation of the Fairchild 1728-element CCD arrays for generation of high-resolution slow-scan imagery and some approaches for recording and display of the imagery. The implication of dark current and its control is discussed.

I. INTRODUCTION

Current CCD technology is limited to area arrays no larger than approximately 500 X 400 photo sensors. For system applications which require higher-resolution imagery, CCD linear arrays provide a practical solution.

The Fairchild 1728-element CCD linear array is a two-phase buried-channel device with 1728 photo elements on a 13-μm pitch (Ref. 1). Readout registers and video amplifier are included on the chip, and the device offers

wide dynamic range. A summary of measured performance of this array is given in this paper, together with a review of some system applications and parameters.

"Slow-scan" operation is defined in this case as operation at frame rates much less than 30 frames per second. This includes both high-resolution slow-scan security systems, in which sequential frames are panned at a slow rate, and "push-broom" type cameras, in which the array is contained in a moving vehicle and is used to scan a continuous strip. The latter approach would cover wide-angle high-resolution strip reconnaissance cameras, multispectral earth resources systems, and environmental monitoring systems.

II. MEASURED PERFORMANCE OF 1728-ELEMENT ARRAYS

Figure 1a shows the typical signal transfer characteristics for a CCLID-1728, with the array output voltage in mV plotted against exposure in $\mu J/m^2$. Saturation for this array occurred at approximately 160 mV, at which point responsivity becomes nonlinear, with blooming occurring at about 180 mV.

Table 1a gives average results of characterization tests of 1728-element arrays at room temperature and at -20°C. As expected from theory, dark current (I_D) approximately halves for every 10°C reduction in chip temperature over this range, while parameters such as responsivity are essentially unchanged.

Spectral response is shown in Figure 1b for two devices from the same wafer. The photosensors on the 1728 arrays are covered by a transparent polysilicon electrode with a silicon dioxide insulator. These layers produce interference patterns in the incident light which result in the peaks and valleys that are seen in these response curves. These are dependent upon the relative thickness of the layers and also the angle of incidence of the rays. Quantum efficiencies of 10%, 30%, and 60% are shown on the same figure for reference purposes.

Figure 2 shows the combined MTF curves for a CCD 1728 array and a B & L Super Baltar 3-in. f/2 lens, measured at four different bands. At the array limiting resolution of 38.5 lp/mm, the MTF is 38% in the band 0.5 - 0.6 μm, 35% in the band 0.6 - 0.7 μm, 23% in the band 0.7 - 0.8 μm, and 18% in the band 0.8 - 1.1 μm. Measurement of the wideband MTF is

limited by the ability of the lens to focus simultaneously over the full silicon response of the array.

Transfer inefficiency was measured at 1 MHz both at room temperature and at -20°C. Transfer inefficiency in the readout register results in some charge being left behind after each clock transfer, and this can result in smearing of the information which is being read out as well as in degradation of MTF. Measurements were made using a light spot 5 μm in diameter to image onto one photosensor. The amplitude of the output signal and the trailing pulse signal were measured from each end of the array. The range of transfer efficiencies for all devices was between 0.99995 and 0.99998 per transfer for both temperatures. The effect on MTF for $\eta = 0.99998$ would be to reduce an MTF of 40% for the first elements read out to 38.6% at the opposite end of the array; i.e., the effect on MTF is negligible with these efficiencies.

Crosstalk was measured using the same light probe as in the transfer inefficiency measurements. Results are shown in Table 1b. As expected, crosstalk rises with increasing wavelength because of the deeper penetration of photons at longer wavelengths.

On the 1728 devices, signal charge is integrated in the photo elements during a line integration, then transferred in parallel from the photosensor to the readout registers. If all of this charge is not transferred, there will be a residual image. The efficiency of this transfer is a function of transfer time. Typically this should exceed 1 μs, and if a 10-μs transfer pulse is used, residual image will be negligible.

III. SYSTEM APPLICATIONS

Several slow-scan cameras have been built at Fairchild Space and Defense Systems using 1728-element arrays. For a typical camera which generates a 1728 X 1728 element picture in 4 seconds, the total power required is under 2 1/2 watts and the camera volume is under 20 cubic inches, excluding the lens. In some of these cameras, provision was made for array cooling using a thermoelectric cooler underneath the CCD array. Cooling of an array is only beneficial when the noise equivalent exposure for the system is being limited by dark current noise (Ref. 2).

Dark current noise falls into two categories, temporal and coherent. Temporal noise is random and results from the average I_D for the device, which is of course temperature-dependent. Coherent noise is defined in this instance as the dark current signature which results from the nonuniform dark signal generation from photosensor to photosensor. Variation across an array can be up to ±50% of I_D. At signal levels approaching the noise equivalent exposure, this signature appears as striation across the image in the direction of mechanical scan or motion. Though this coherent noise can be cosmetically objectionable, a useful signal which is below this level can still be extracted.

In a typical application, where the CCD array temperature could exceed 45°C and an integration period of more than 2 milliseconds per line is required, cooling is accomplished using a thermoelectric device (TED). A 1-watt, single-stage TED which is only slightly larger than the CCD package (24 pin DIP) provides a temperature depression of approximately 25°C between the chip and ambient.

A larger temperature depression, approximately 40°C, has been achieved using a 4-watt TED. In this case, care is required to thermally isolate the CDD package from losses through the DIP pins to the printed card, and to adjacent components. Also, in this case chip dissipation is held to under 100 mW total. At low clock frequencies, chip dissipation is determined principally by the I^2R losses of the on-chip amplifier, which is of the order of 50 mW. Power dissipation P due to clocking can be determined from the formula $P = CV_c^2 fc$, where C is the total capacitance of the clocking gates, V_c is the clock voltage amplitude, and fc is the clock frequency. Typically $P \approx 30$ mW at 1 MHz.

For "push-broom" applications requiring very high resolution, many thousands of picture elements are required in a single line. For these situations, optical butting of several arrays can be achieved. One approach, which uses a beam splitting prism to optically align three arrays, is shown in Figure 3. Longer scanners are practical because of the high geometric accuracy of the arrays. For an array with a photosensor pitch of 13 μm, accuracy is better than ±0.2 μm, noncumulative, and the optical alignment between arrays can be made better than ±10 μm. Data reduction techniques can be applied to reduce the effect of the signatures of the arrays, which are caused by small

variations in responsivity and transfer characteristics, since these are stable and repeatable for any one device. Thus they can be predetermined for each device used in the scanner. No abnormal characteristics have been observed for the end elements on any device; therefore, optical butting can be contiguous and does not require any overlap or combining of photo elements.

IV. VIDEO RECORDING AND DISPLAY

For a single 1728 array operating at clock rates up to 2 MHz, data has been stored successfully using a standard Sony rotating head video recorder. In this case, the recorder will make several head rotations for each 1728 X 1728 frame, and requires insertion of a pseudo sync pulse after each head rotation to maintain synchronism. Figure 4 shows a recording made with a 1728-line scanning camera, which was then played back using a slow-scan electrostatically deflected CRT display. In this particular example, detailed analysis of the recorded picture was made possible by playing one slow-scan frame, or portion of a frame, into a scan converter operating at a 30 frame per second output. Since even the best monitors start to degrade resolution at over 1000 lines, it is important to be able to expand selected portions of the frame for viewing at full resolution.

When multiple arrays are used simultaneously, the video output requires more complex mass data storage techniques. For instance, for ten 1728 arrays simultaneously being clocked at 5 MHz, the video bandwidth will be 1/2 X 50 MHz, i.e., one half of the fundamental clock frequency. Storage and display of video at a 25-MHz bandwidth clearly require special equipment for both recording and display. Real-time viewing of the total scene can be done at a lower resolution, with detailed analysis performed by either electronically "zooming" in on the area of interest, or by transferring the recording to film.

V. CONCLUSION

Systems configured around the 1728-element CCD array have been successfully built and demonstrated in Fairchild Syosset. A brief summary has been given in this paper. All of these systems share the advantage inherent in the use of CCDs of having low power consumption, small size, high metricity, and a wide operating dynamic range.

ACKNOWLEDGEMENT

The author would like to thank the many people who were involved in these programs, and in particular I. Hirschberg for many useful discussions, and A. Green and F. Moy for performance data and testing.

REFERENCES

1. C. K. Kim, "Two-Phase Charge Coupled Linear-Imaging Devices with Self Aligned Implanted Barrier," IEDM Technical Digest, Dec. 1974, p. 55.

2. C. K. Kim and R. H. Dyck, "Low Light Level Imaging with Buried Channel Charge Coupled Devices," Proc. IEEE, Aug. 1973, p. 1146.

Table 1. Measured performance characteristics of CCLID 1728 arrays (clock frequency = 1 MHz, integration time = 1.8 ms)

(a) General characteristics

AVERAGE VALUES	TRANS. EFF. η	DARK CURRENT I_D nA	DARK CURRENT NON-UNIFORM % I_D	SAT. EXPOSURE $\mu J/M^2$	NEE $\mu J/M^2$	DYNAMIC RANGE	RESPONSIVITY-mA/W .5-.6	.6-.7	.7-.8	.8-1.1	2854°K .4–1.2
AT +25°C	.99995	2	±25	2060	1.5	1441	171	254	304	180	156
AT -20°C	.99995	.1	–	2060	1.5	1441	–	–	–	–	156

(b) Element-to-element crosstalk

IRRADIANCE BANDPASS μM	CROSSTALK (%) ADJACENT ELEMENT	2 ELEMENTS AWAY	3 ELEMENTS AWAY	4 ELEMENTS AWAY
.5 TO .6	5%	0	0	0
.6 TO .7	7%	1%	0	0
.7 TO .8	12%	2%	1%	0
.8 TO 1.1	21%	7%	3%	1%

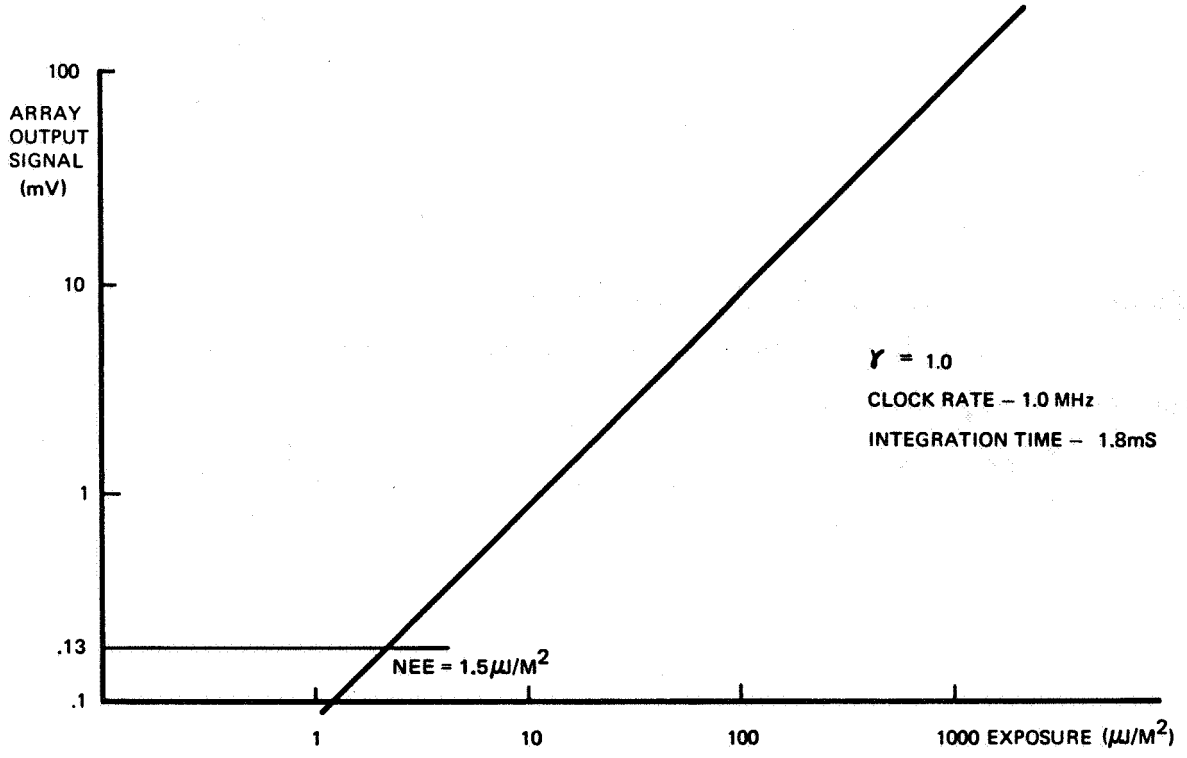

Figure 1a. Signal transfer curve

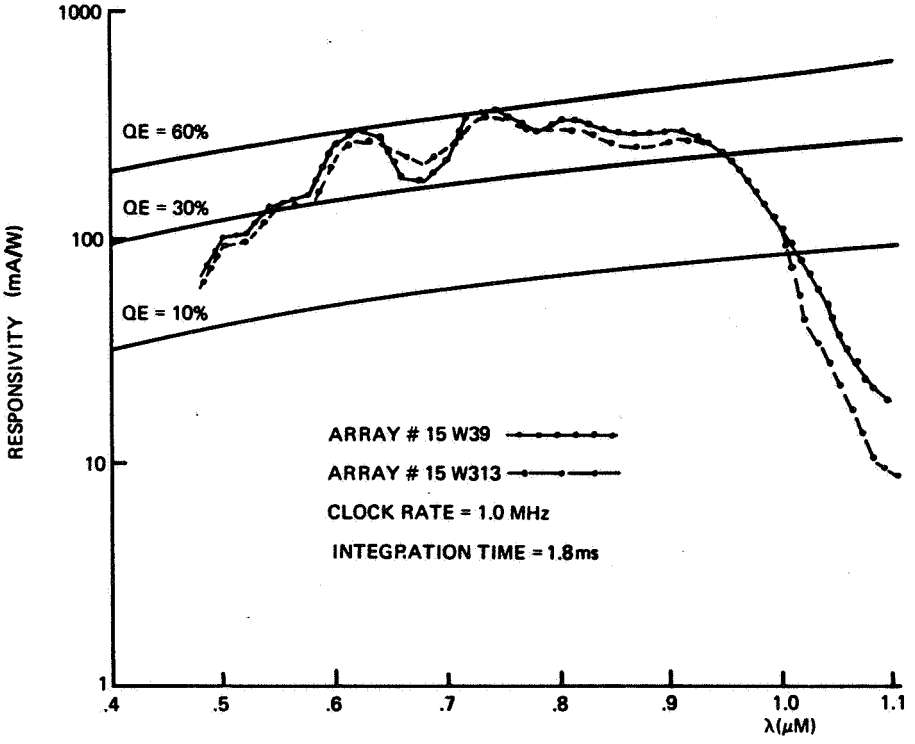

Figure 1b. Spectral response of two arrays from the same wafer

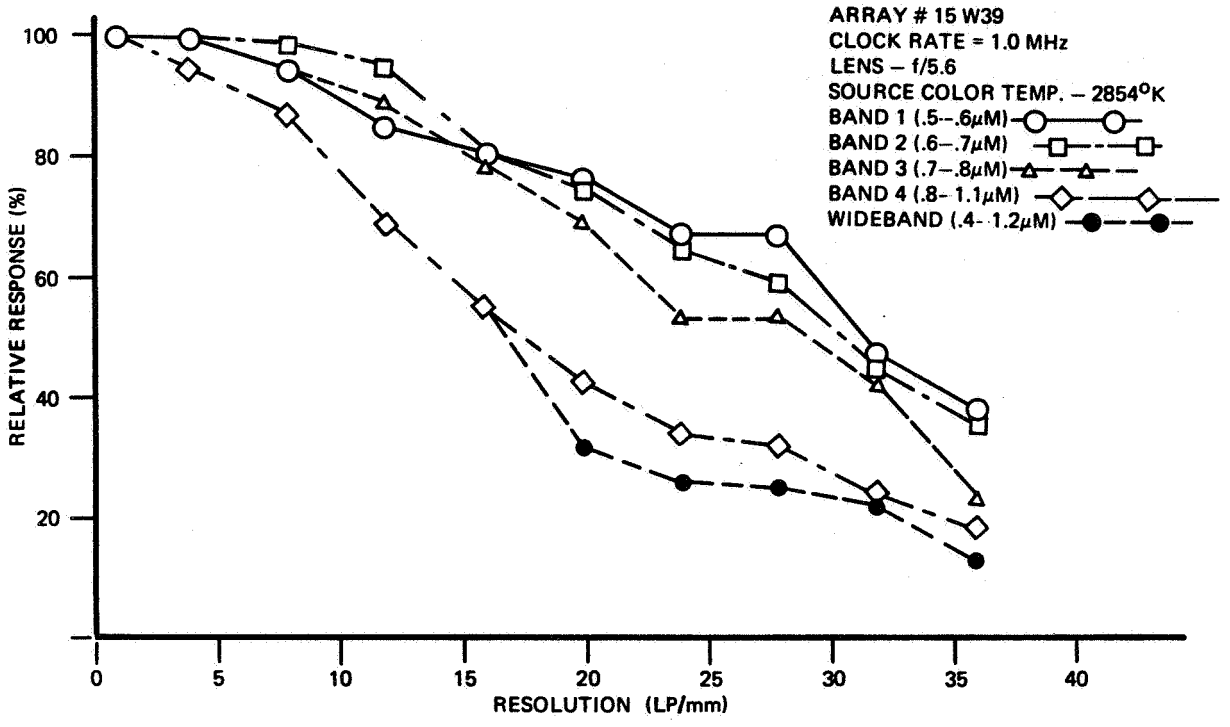

Figure 2. Squarewave response -- in phase

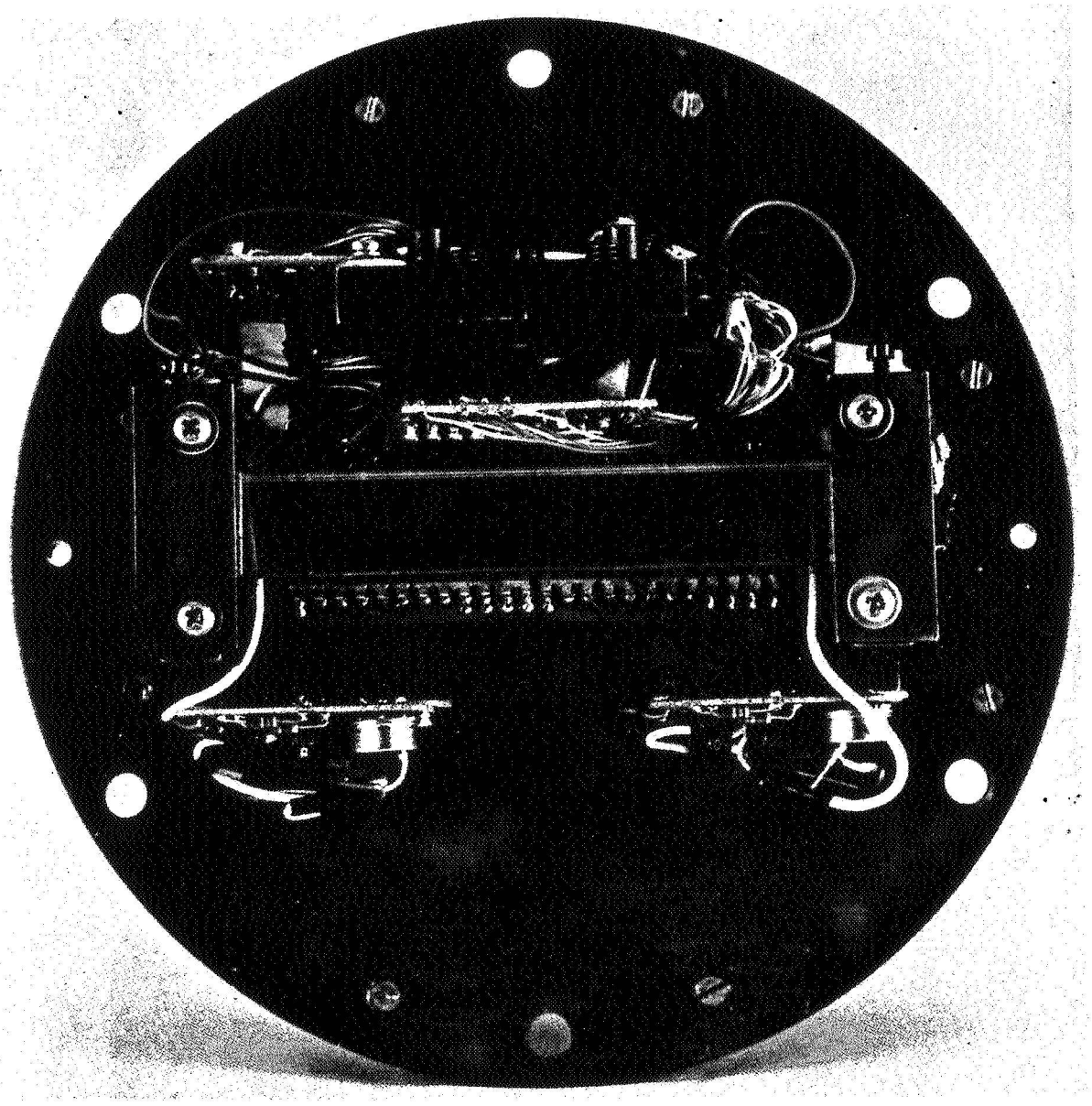

Figure 3. EWACS optical butting assembly

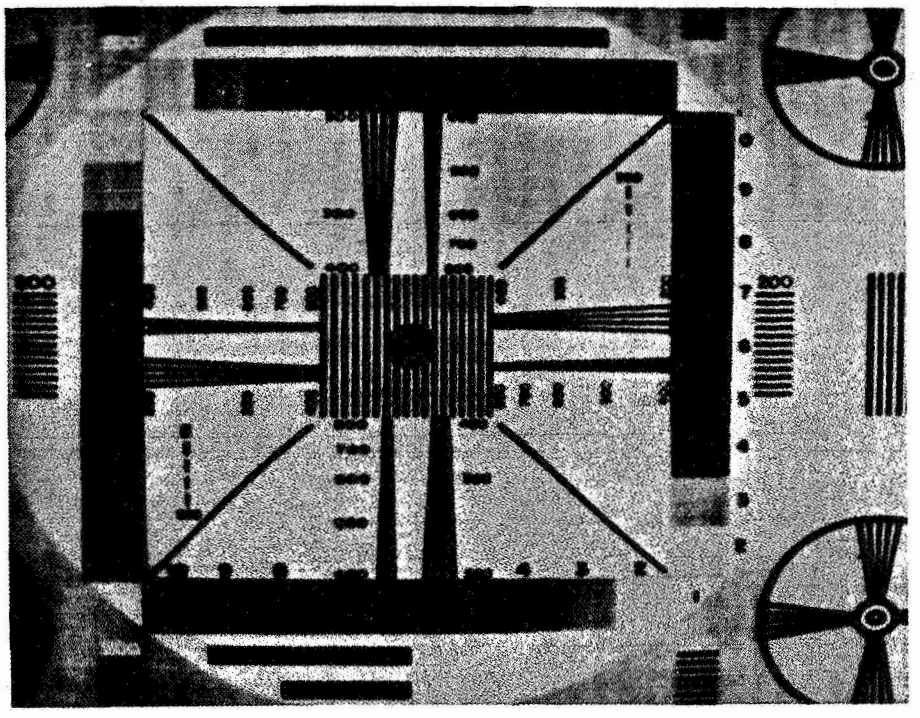

Figure 4a. Camera output image

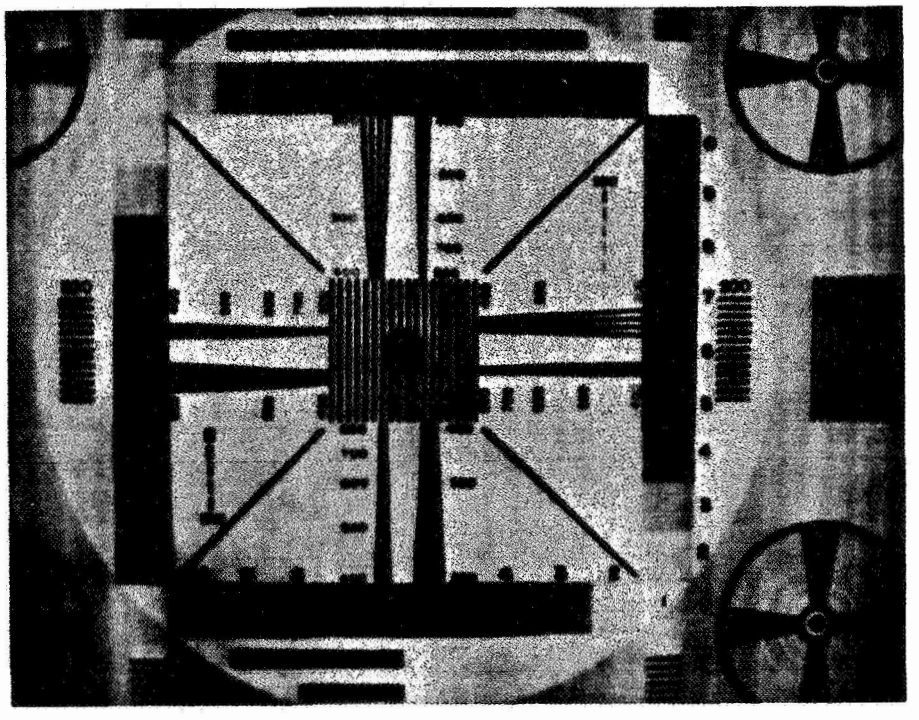

Figure 4b. Tape recorder output image

IMAGING PERFORMANCE OF A CCD AREA ARRAY AT 200°K

W. D. Baker and D. J. Michels
Naval Research Laboratory
Washington, D. C.

The performance of a 100 × 100 charge-coupled device imager was evaluated in the vicinity of 200°K. A set of operating conditions was determined which permits satisfactory operation of the imager from 300°K to 150°K while assuring maximum tolerance to ionizing radiation. Good imaging has been obtained for integration times in excess of 10 seconds at 200°K. Preliminary results on image storage indicate that storage times of many seconds are possible at 200°K.

I. INTRODUCTION

Charge-coupled device (CCD) area array imagers are attractive for many applications due to their small size, low power consumption, and inherent metricity. We have been engaged in an effort to evaluate the feasibility of using a CCD area imager to develop a space-qualified camera system with an on-board image processing capability. As a part of that effort, we have investigated the operation of a 100 × 100 CCD imager (Fairchild CCD 201) in view of the system requirements for the proposed camera.

The system requirements place several constraints on the CCD performance. For this system, both long integration times and long image storage times (up to 30 seconds or more) are desired in order to obtain sufficient sensitivity and to simplify telemetry electronics. To achieve such long integration and storage times, the device must be cooled to reduce the effects of thermally generated dark current. The amount of power available for cooling during a space-flight mission is, of course, quite limited. The use of a passive radiator to provide cooling is very attractive provided that the

heat load is not excessive, that a cold temperature of about 200°K is adequate, and that the requirements on temperature accuracy and stability are not too severe. Since the 100 × 100 CCD imager dissipates only about 50 mW in its package, it could be cooled by a passive radiator. What we have attempted to determine, then, is if the CCD imager can meet system requirements when operated at 200°K and if good imaging performance can be maintained over a reasonable range of temperatures around 200°K without changes in the CCD operating conditions.

An additional system requirement is that the imager must be capable of tolerating the anticipated radiation dose which it would encounter over the life of a mission. This means that the operating conditions for low-temperature operation must be compatible with the operating conditions for radiation tolerance.

Also, from the standpoint of power conservation, it is desirable that the number of different voltage levels required for CCD operation be as few as possible.

II. EXPERIMENTAL TECHNIQUE

The experimental apparatus used to collect the data for this investigation is indicated schematically in Figure 1. A collimated light source was used to illuminate a transparency (either a standard resolution chart or some other scene). A filter was used in the light path to remove the infrared component from the incandescent light source. The image was focused onto the CCD imager using a trinocular microscope with an appropriate lens combination. The CCD was mounted in a Teflon (TM) cold cell, which was continually flushed with dry nitrogen to prevent moisture condensation. Cooling was accomplished by mounting the CCD on a copper finger attached to a copper block through which cold nitrogen gas was passed. The temperature was regulated by a controller driving a small heater mounted in the copper block. Thermocouples were mounted to the copper finger for monitoring the temperature. The temperature could be controlled within ±3°C. We estimate that the temperature of the CCD is at most 5°C warmer than the finger temperature as a result of imperfect thermal contact and power dissipation in the CCD. The light source intensity was adjusted to give a saturation response in the

CCD for an integration time of 8 msec. Neutral density filters were used to adjust the light intensity to any level desired. Long integration times were obtained by inhibiting the transfer of charge from the photosites into the scanning shift register. All shift registers were continuously run at a rate compatible with a 120 frame per second TV display.

III. RESULTS

A set of operating conditions was established which gave satisfactory imaging performance over the range from 300°K to 150°K without changes in the conditions. These operating conditions are also compatible with the maximum radiation tolerance possible for these devices. The conditions used are given in Table 1, along with the manufacturer's nominal and limiting values. Under these conditions, only three clock driver supply voltages are required and only one bias voltage. The approximate limiting resolution measured both at room temperature and 150°K was 15 lp/mm vertical and 11 lp/mm horizontal. This compares to geometrical limitations of approximately 16 lp/mm and 12 lp/mm based on the vertical and horizontal element pitch, respectively.

Integration times of 10 seconds have been used with good results and no evidence of dark current buildup. Modification of timing circuits to extend the integration time up to 1 minute is in progress. Estimates of the dark current at 200°K indicate that the desired integration times of at least 30 seconds are possible with almost no dark current contribution to degrade image quality. Preliminary measurements of image storage have been made by using a shutter to allow light on the CCD for a short period and then delaying the readout for several seconds. From these preliminary results, no loss mechanisms have been seen which could prevent image storage times comparable to the integration times.

These measurements indicate that the combination of a CCD area imager and a passive radiation cooler can meet the system requirements described earlier.

ACKNOWLEDGEMENTS

The authors would like to acknowledge the contributions of Dr. J. Killiany and Dr. G. W. Anderson to this work.

Table 1. CCD imager operating conditions

Parameter	Manufacturer			This work
	Min	Typical	Max	
Horizontal clock LOW	-10	-8		-8
Horizontal clock HIGH		2	10	+1
Vertical clock LOW	-10	-8		-8
Vertical clock HIGH		2	10	+1
Reset clock LOW	-10	-8		-8
Reset clock HIGH		2	10	+10
Photogate clock LOW	-10	-8		0
Photogate clock HIGH		2	10	+10
Reset drain		12	15	+15
Output drain		12	15	+15
Reset gate		12	15	+15
Compensation drain		12	15	+15

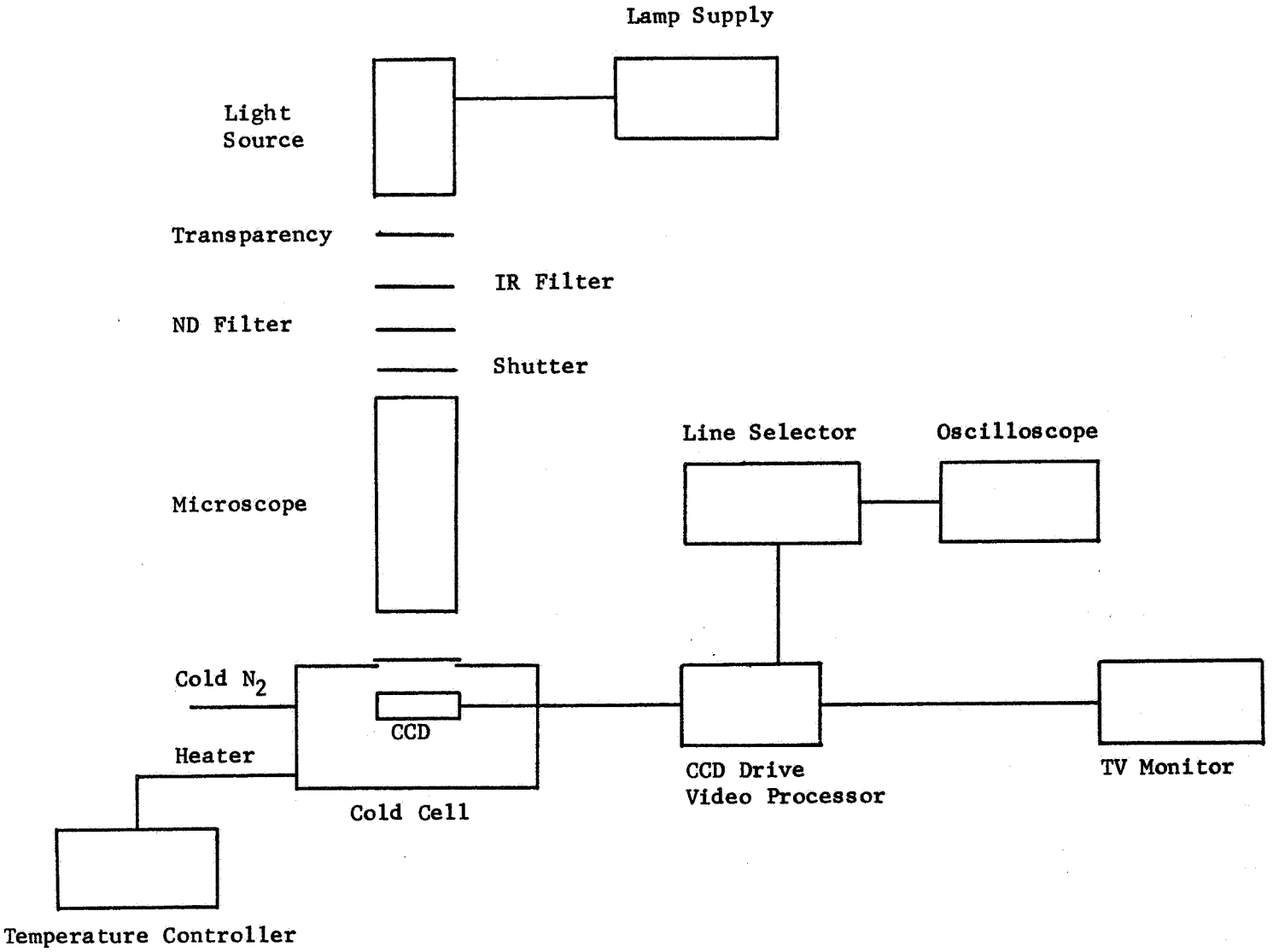

Figure 1. Experimental apparatus

MTF AND POINT-SPREAD FUNCTION FOR A LARGE-AREA CCD IMAGER*

K. J. Ando
Jet Propulsion Laboratory
Pasadena, California

In the present work, utilizing the Crowell and Labuda model, the MTF degradation due to lateral diffusion is calculated for a back-illuminated CCD imager for typical device parameters. The discrete nature of the CCD and finite size of the photosensitive elements, with its less than ideal collection efficiency for photogenerated charge, result in an additional MTF degradation. The Fourier transform approach is utilized to calculate the effective point-spread function for these processes in the time domain. Experimental data is presented on the point-spread function for a three-phase, double-level anodized aluminum 160 X 100 thinned and back-illuminated CCD imager and compared with the theoretical results. A simple modification of the Crowell and Labuda model suggested by these results is presented. Finally, the effects of the less than ideal charge transfer efficiency in practical devices are calculated and applied to predict the anticipated MTF and point-spread function for a 400 X 400 large-area CCD imager currently under development.

I. INTRODUCTION

The charge-coupled device offers a new and significant approach to achieving the once elusive goal of a viable large-area solid-state imager

*This paper presents the results of one phase of research carried out at the Jet Propulsion Laboratory, California Institute of Technology, under Contract No. NAS 7-100, sponsored by the National Aeronautics and Space Administration.

possessing the format size and element density comparable to a conventional vidicon. Considerable progress has been made towards achieving this goal, as reflected by the performance data presented at this Symposium on large-area array imagers. This paper discusses the MTF, point-spread function, and the effects of charge transfer inefficiency for such large-area arrays. Expressions for the MTF and point-spread function are derived and applied to a thinned, back-illuminated 400 X 400 area imager (Ref. 1). The results indicate the anticipated performance levels for such a CCD and the significant role of charge transfer efficiency for large-area arrays.

II. MTF AND POINT-SPREAD FUNCTION FOR LATERAL DIFFUSION

Figure 1 illustrates the simplified model utilized by Crowell and Labuda (Ref. 2) to calculate the quantum efficiency η_0 and the MTF for a silicon diode array target. The depletion region of width $L_b - L_a$ is assumed to be totally depleted and a region of zero lateral conductivity. η_0 and the MTF are calculated by evaluating, for a sinusoidal optical input, the steady-state diffusion current

$$J_p = -D\frac{\partial p}{\partial x}\Big|_{y = L_a} \tag{1}$$

flowing into the depletion region from the field-free region and adding the photogenerated current from the direct photon absorption in the depletion region. J_p is evaluated from the solution of the continuity equation

$$-D\nabla^2 p + \frac{p}{\tau} = G(x, y, z) \tag{2}$$

subject to the boundary conditions

$$\begin{aligned} Sp &= \frac{\partial p}{\partial x}\Big|_{y = 0} \qquad \text{(input surface)} \\ p &= 0\Big|_{y = L_a} \qquad \text{(depletion region edge)} \end{aligned} \tag{3}$$

where

p = minority carrier density in excess of thermal equilibrium

τ = minority carrier lifetime

D = minority carrier diffusion constant (cm^2/sec)

$G(x, y, z)$ = minority carrier generation rate per unit volume

S = surface recombination velocity (cm/sec)

The photogeneration rate $G(x, y, z)$ is assumed to vary sinusoidally in the transverse direction and exponentially in the y direction, and is given by

$$G(x, y, z) = \frac{N_0}{2}(1 - R)\alpha \exp(-\alpha y)(1 + \cos kx) \tag{4}$$

where

N_0 = peak incident photon flux

α = silicon absorption coefficient at the wavelength of interest

R = reflectivity of silicon at the wavelength of interest

$k = 2\pi/\lambda$ = spatial frequency of the optical input

The resulting solution can be written in the form

$$J_p(x) = \frac{N_0}{2}(\eta_0 + \eta_k \cos kx)$$

with

$$\eta_k = \frac{\alpha L(1 - R)}{\alpha^2 L^2 - 1}\left[\frac{2(\alpha L + SL/D) - (\beta_+ - \beta_-)\exp(-\alpha L_a)}{\beta_+ + \beta_-} - \frac{1}{\alpha L}\exp(-\alpha L_a)\right]$$

$$-(1-R)\exp(-\alpha L_b) \tag{5}$$

and

$$\eta_0 = \eta_{k=0}$$

where

$$\beta_{\pm} = \left(1 \pm \frac{SL}{D}\right) \exp \pm \frac{L_a}{L}$$

$$L_0 = \text{diffusion length} = (D\tau)^{1/2}$$

$$L = \frac{L_0}{\left(1 + k^2 L_0^2\right)^{1/2}}$$

The MTF, defined to be the peak-to-peak minority carrier current entering the continuous p region normalized with respect to the response for uniform light, is simply the ratio η_k/η_0. The resulting MTF can be written as a sum of a frequency-dependent component and a constant,

$$\frac{\eta_k}{\eta_0} = \frac{\eta(\omega)}{\eta_0} + \frac{C}{\eta_0} \tag{6}$$

where

$$C = \exp(-\alpha L_a)\left\{1 - \exp\left[-\alpha(L_b - L_a)\right]\right\}$$

$\eta(\omega)/\eta_0$ is the output modulation due to absorption in the field-free region and decreases due to lateral diffusion as the input spatial frequency is increased. C/η_0, on the other hand, is equal to the fraction of the total collected charge contributed by direct photon absorption in the depletion region and contributes a constant output modulation. This latter term arises from the total depletion approximation.

The above results can also be applied to a thinned, back-illuminated CCD imager such as that shown schematically in Figure 2. For a typical oxide thickness, clock voltages, and substrate resistivity, the maximum depletion depth is

approximately 5 μm. The depletion depth x_d, however, is not constant throughout the unit cell but varies schematically, as illustrated in Figure 2. Typically, for a three-phase CCD, only approximately 1/3 of the unit cell is depleted to the maximum depth, with the remainder of the unit cell being only partially depleted. The exact profile can be obtained from the surface potential profile $\varphi_s(x)$, since

$$x_d = \left(\frac{2\epsilon\varphi_s(x)}{qN_a}\right)^{1/2} \tag{7}$$

where ϵ is the dielectric constant of silicon and N_a is the acceptor density of the substrate. Additionally, $\varphi_s(x)$ is, in general, anisotropic, with the doping and width of the channel stops being important factors in the direction perpendicular to the channel stops. However, the quantum efficiency is relatively insensitive to the detailed shape of the potential wells. Although partial depletion introduces a transition region of charge collection uncertainty and cross modulation between the unit cells, the total collection efficiency remains unity since the recombination loss is small in this region.

Finally, at wavelengths greater than 0.8 μm, one can expect interference effects due to multiple reflections from the structured side of the CCD. Seib (Ref. 3) has extended the Crowell and Labuda model to include the effects of multiple reflections for normal incidence. His results show that for wavelengths greater than 0.8 μm, although the calculated η_0 is increased over the single pass case, the resulting MTFs are nearly identical. Thus, although the total depletion condition is not realized in practice by a back-illuminated CCD, and multiple reflections are not considered at the longer wavelengths, one nevertheless should obtain a reasonable estimate of the quantum efficiency η_0 and the MTF degradation due to lateral diffusion from the single-pass Crowell and Labuda model. Equation (6) has been evaluated utilizing typical CCD parameters for two substrate thicknesses, and the results are shown in Figures 3 and 4. For a thinned array, the results are relatively insensitive to the value of L_0 and to S. The key parameter, especially at short wavelengths, is the thickness of the field-free region. MTF (∞) is the constant to which the curves converge and is equal to C/η_0.

The results can also be expressed in the time domain by calculating the inverse Fourier transform of Equation (6) to yield the point-spread function for lateral diffusion,

$$PSF(x) = \mathcal{F}^{-1}\left\{\frac{\eta_k}{\eta_0}\right\} = \frac{1}{2\pi}\int_{-\infty}^{\infty}\frac{\eta(\omega)}{\eta_0}\exp(-i\omega x)d\omega + \frac{C}{\eta_0}\delta(x) \qquad (8)$$

Since the lateral diffusion process possesses even symmetry, it is only necessary to evaluate the real part of the complex Fourier transform. Equation (8) was evaluated by numerical integration. The results are shown in Figures 5 and 6 and represent the spatial charge spread (impulse response) of the field-free region to a delta optical input.

III. EFFECTS OF SAMPLING AND THE FINITE PIXEL SIZE

In addition to the MTF degradation resulting from lateral diffusion, the discrete and finite aperture of a CCD imager imposes a further geometric limitation on the MTF. The resulting MTF loss can be estimated by assuming total depletion and dividing the depletion region into contiguous pixels of width d, where d is the pitch of the pixels, as shown in Figure 2. Under these simplifying assumptions, the MTF for the sampling and collection process is given by

$$R_P = \text{sinc}\frac{kd}{2} \qquad (9)$$

The total pixel MTF becomes $\eta_k/\eta_0 \times R_P$ and is plotted in Figure 7 for a typical pixel size of 1 mil. Note that in the spatial frequency range of interest ($f < f_{NYQ}$), the pixel size is the dominant factor. Additionally, the spectral dispersion in the MTF curves has been reduced. The corresponding point-spread function has been calculated by first truncating the MTF expression to zero at f = 4000 c/mm and numerically integrating up to this limit. The results are shown in Figure 8. The error introduced by truncation is negligible for λ = 0.4 and 0.6 μm, whereas for λ = 0.8 μm, the actual point-spread function should be slightly more rectangular than calculated.

The response of a single pixel is given by

$$R(x) = K\int_{-\infty}^{\infty} I(x')PSF(x' - x)dx' \qquad (10)$$

where I(x') is the spread function for the optical input. If I(x') is narrow in comparison with PSF(x), it follows from the sifting properties of the delta function that

$$R(x) \cong PSF(x) \qquad (11)$$

Thus, by measuring the response of a single pixel as a point or narrow slit light source is scanned across the pixel, the point-spread function of the device can be experimentally determined. The next section will describe the results of such a measurement on a thinned, back-illuminated CCD imager.

IV. EXPERIMENTAL RESULTS

The characteristics of the tested CCD and the operating conditions for these measurements, respectively, are summarized below. Design and general performance data has been presented previously on this type of CCD imager (Ref. 4).

(1) CCD imager characteristics

- (a) Three-phase, double-level anodized aluminum
- (b) Surface channel
- (c) Thinned and back-illuminated
- (d) Array size - 160 pixels horizontal by 100 pixels vertical (160 × 120 mils)
- (e) Pixel size - 1.0 × 1.2 mils

(2) Operating conditions for pixel sensitivity profile measurements

- (a) Serial clock frequency = 100 kHz
- (b) Serial fat zero ≈ 10%

(c) Exposure time = 250 msec (shuttered)

(d) Total frame time = 423 msec

The point-spread function measurements were made with the apparatus shown in Figure 9. The point light source was a 5-mil Xenon arc lamp, which was imaged through a 10 × F/2 microscope objective. The CCD was approximately 200 cm from the light source. Spectral and neutral density filters were inserted into the optical path to vary the spectral passband and intensity of the light spot. The light spot could be viewed simultaneously through a microscope eyepiece via a beam splitter as it was being focused on the CCD input surface. The diameter of the minified light spot, as visually determined by focusing the light spot onto a stage micrometer placed in the same plane as the CCD input surface, was less than 4 μm. The light spot was stepped across the CCD in the parallel transfer section in 2.2-μm increments in the image plane. The output from a 20 × 20 area (400 pixels) was recorded after a 12-bit A/D conversion by a digital tape recorder after each 2.2-μm increment. The data was taken from a computer printout of the 20 × 20 area. Figure 10 shows the typical video output as the spot was scanned across three adjacent pixels. The assymetric response is due to the redistribution of a fraction of the charge from the primary pixel into the trailing pixels because of charge transfer inefficiency.

Typical results showing the simultaneous output from three adjacent pixels as a function of spot position are shown in Figures 11 and 12, respectively. A Beck glass filter with a long-wavelength cutoff of 0.45 μm was utilized. The spot intensity was adjusted to be approximately one-half of full well. The spot was positioned as close as possible to the output to minimize charge transfer efficiency effects. The peak amplitude increased from pixel to pixel because of the localized shading in the region near the output. The slight assymetry in the measured profiles is due to charge transfer inefficiency. The solid lines enclosing the sensitivity profiles are the boundaries of the respective pixel. Similar measurements were also made with a Beck red glass filter, and essentially identical results were obtained.

Comparison of the sensitivity profiles with the calculated point-spread functions of Figure 8 shows that the measured profile is narrower at the center and exhibits more response outside the pixel than predicted by the Crowell and

Labuda model, indicating some pixel overlap. A simple modification of this model is suggested by these results, as shown in Figure 13. The collection regions defining the pixels are assumed to be overlapping and trapezoidal in shape to account for the less than ideal isolation between pixels. The total collection efficiency for the depletion region remains unchanged since the sum of the collection efficiencies in the overlap region is unity. Because of this overlap, the MTF due to the collection process is reduced from R_P to R_T, where

$$R_T = \text{sinc}\frac{\omega b}{2}\,\text{sinc}\frac{\omega(a+b)}{2} \tag{12}$$

V. CHARGE TRANSFER INEFFICIENCY EFFECTS ON A LARGE-AREA ARRAY

In an image sensor such as a vidicon, the electron beam provides a direct readout of each pixel. On the other hand, in a CCD, the signal charge from each pixel must first be transferred to the output for readout. In practical devices, the transfer process is less than perfect, with some charge redistribution and loss occurring in the transfers and the dispersion increasing with the number of transfers. The key characteristic of a CCD is its charge transfer efficiency. The frequency-dependent distortion introduced by charge transfer inefficiency for a CCD delay line for the case where the fixed loss is negligible has been calculated utilizing both Z transform (Refs. 5 and 6) and Fourier analysis (Refs. 7, 8, and 9). The transfer function, derived from the transform of the impulse response in the time domain, for such a delay line is given by (Refs. 5 and 7)

$$H(\omega) = A(\omega)\exp\left[-i\varphi(\omega)\right] \tag{13}$$

where

$$\left|A(\omega)\right| = \left[\frac{(1-\epsilon)^2}{1+\epsilon^2-2\epsilon\cos\omega d}\right]^{n/2}$$

and

$$\varphi(\omega) = n \tan^{-1} \frac{\epsilon \sin \omega d}{1 - \epsilon \cos \omega d}$$

where ϵ is the fraction of charge left behind per transfer, n is the number of transfers, and d is the pitch of the pixels. The modulus $A(\omega)$ is the attenuation factor, and the argument $\varphi(\omega)$ is the phase shift. For $\epsilon << 1$, these expressions can be approximated by (Refs. 7 and 10)

$$\begin{aligned} \left|A(\omega)\right| &\cong \exp(-n\epsilon)(1 - \cos \omega d) \\ \varphi(\omega) &\cong n\epsilon(\omega d - \sin \omega d) \end{aligned} \tag{14}$$

In the time domain, which is the more suitable domain to calculate pulse train dispersion effects, the charge $Q_N(nt_0)$ in a charge packet at a time nt_0, transferred through N pixels, is given by (Ref. 11)

$$Q_N(nt_0) = (1 - \epsilon)^N Q_0[(n - N)t_0] + Q_R(nt_0) \tag{15}$$

where

$$Q_R(nt_0) = (1 - \epsilon)^N \sum_{m=1}^{\infty} \binom{N+m}{m} \epsilon^m Q_0[(n - N - m)t_0]$$

Here t_0 is the clock period, $Q_0(nt_0)$ is the size of the charge packet inserted at the input at time nt_0, and Q_R is the contribution from the trailers from the preceding charge packets.

Utilizing Equations (14) and (15), the effects of charge transfer inefficiency on the MTF and point-spread function for a large-area CCD imager can be calculated. The results are shown in Figures 14 and 15. Figure 14 is the calculated MTF for a 400 × 400 three-phase CCD imager with a 0.9 × 0.9 mil pixel size

currently under development (Ref. 1) for three locations in the image plane. Overlapping pixels with trapezoidal collection profiles are assumed as shown. Charge transfer efficiencies in the anticipated range for a buried-channel device were used. For $f \ll f_{NYQ}$, the output modulation for a sine-wave input will be identical to the MTF. For optical inputs near f_{NYQ}, however, phasing effects become significant and the output modulation will depend upon the phasing (Δx) between the optical input and the CCD, as shown in Figure 16, where the relations between the MTF and device response for sine- and square-wave inputs have been summarized (Ref. 12).

Figure 15 is the corresponding charge dispersion at the same locations for various optical inputs. The first column shows the effects of charge transfer inefficiency on a single 1, which would roughly be the point-spread function for this array. For a single 1, the ratio of the first trailer to the primary charge packet is equal to $n\epsilon$. Column 2 indicates the output modulation at the Nyquist limit for the in-phase condition. Figures 14 and 15 indicate how the MTF and point-spread function can be expected to vary continuously across the image plane and represents the ideal case, where the charge transfer loss is uniformly distributed. In practical large-area devices, however, charge dispersion will usually occur because of the presence of isolated regions of poor charge transfer efficiency. For such a case, the results shown in Figures 14 and 15 can still be applied by determining an effective $n\epsilon$ product for the region in question.

VI. CONCLUSIONS

The MTF and point-spread function for a large-area CCD imager have been calculated. Both the theoretical model and the experimental results show that the MTF loss due to lateral diffusion in the frequency range of interest ($f < f_{NYQ}$) is minimal for a back-illuminated CCD thinned to 10 μm, with the size of the pixel and its geometric collection profile being the dominant factor. These results suggest that the MTF could be increased by a further reduction in device geometry before diffusion effects become significant. The key role of charge transfer efficiency has been shown. A charge transfer efficiency η of 0.9999/transfer or better will be necessary to minimize charge dispersion effects and obtain a device where the MTF and point-spread function are limited only by pixel size.

ACKNOWLEDGEMENTS

The author wishes to thank C. J. Mahoney and G. R. Root for their assistance in the experimental phase of this work.

REFERENCES

1. G. A. Antcliffe, L. J. Hornbeck, J. M. Younse, J. B. Barton, and D. R. Collins, Proceedings of this Symposium.
2. M. H. Crowell and E. F. Labuda, Bell Systems Tech. J, 48, 1481 (1969).
3. D. H. Seib, IEEE Tran. Elec. Devices, ED-21, 210 (1974).
4. G. A. Hartsell and A. R. Kmetz, IEDM Tech. Digest, 1974 International Electron Devices Meeting, Washington, D.C., p. 59 (1974).
5. G. F. Vandstone, J. B. G. Roberts, and A. E. Long, Solid State Electronics, 17, 889 (1974).
6. D. D. Buss, W. H. Bailey, and D. R. Collins, Proc. IEEE Int. Symp. Circuit Theory, April 3-7, 1973, pp 3-7.
7. R. D. Nelson and W. P. Waters, Proceedings of the CCD Applications Conference, San Diego, Sept. 18-20, 1973, p. 207 (1973).
8. W. B. Joyce and W. J. Bertram, Bell Systems Tech. J., 50, 1741 (1971).
9. K. K. Thornber, Bell Systems Tech. J., 52, 1453 (1973).
10. M. F. Tompsett, J. Vac. Sci. Technol., 9, 1166 (1972).
11. K. K. Thornber, IEEE J. Solid-State Circuits, SC6, 285 (1974).
12. J. W. Coltman, J. Optical Soc. Am., 44, 468 (1954).

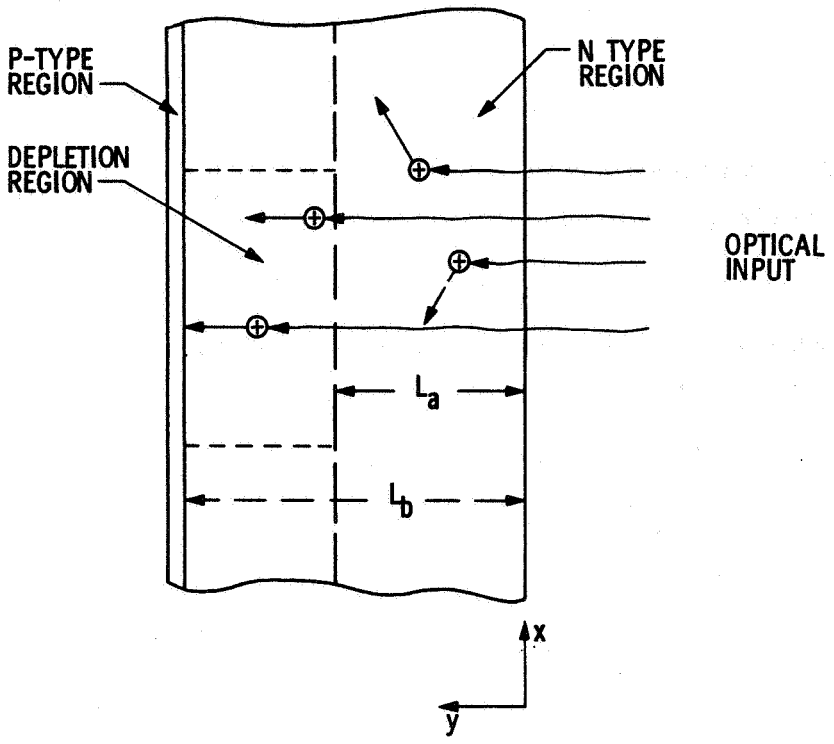

Figure 1. Schematic of simplified model used to calculate η_0 and MTF of a diode array target

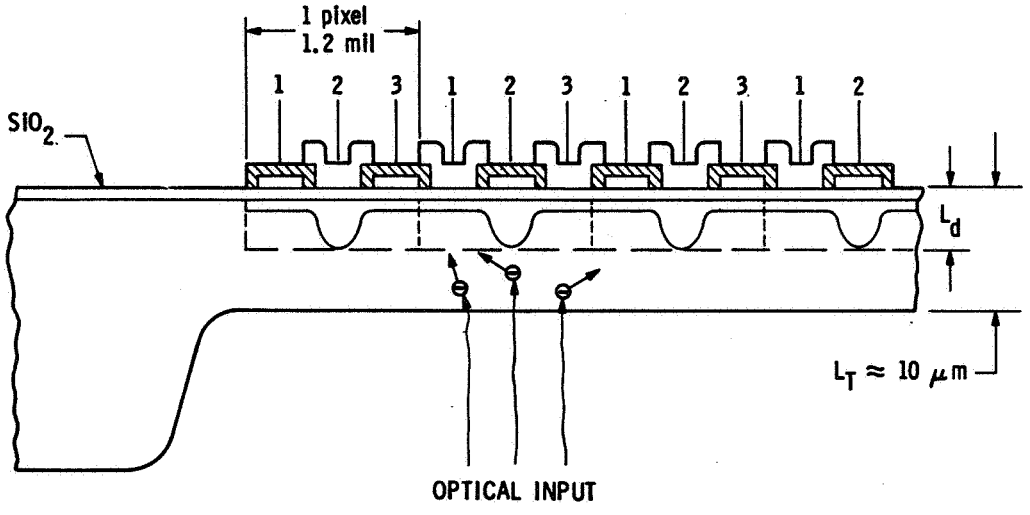

Figure 2. Thinned three-phase anodized AℓCCD (cross section along vertical channel)

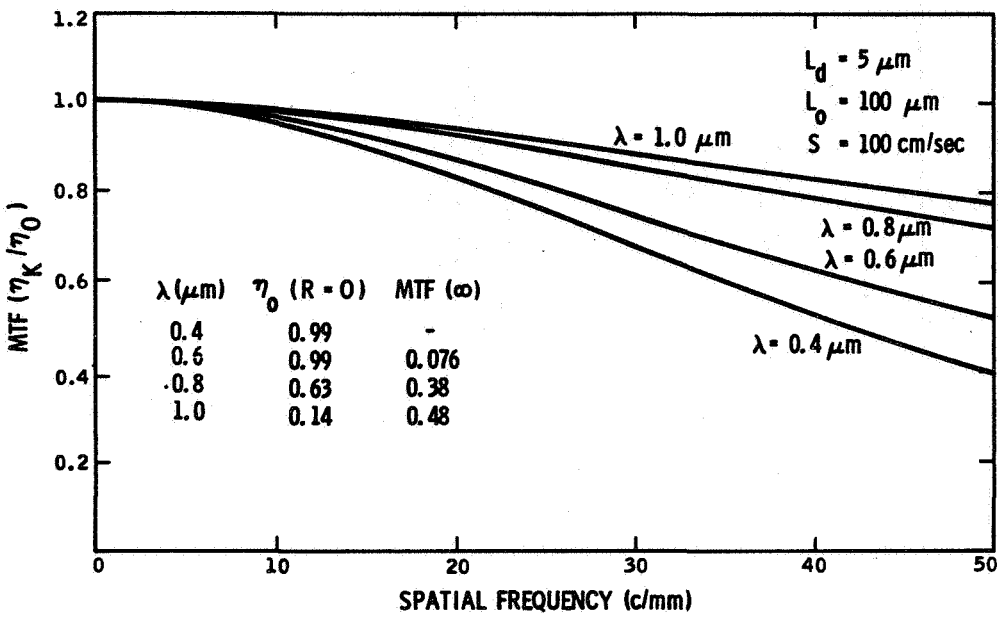

Figure 3. MTF for lateral diffusion (L_T = 10 μm)

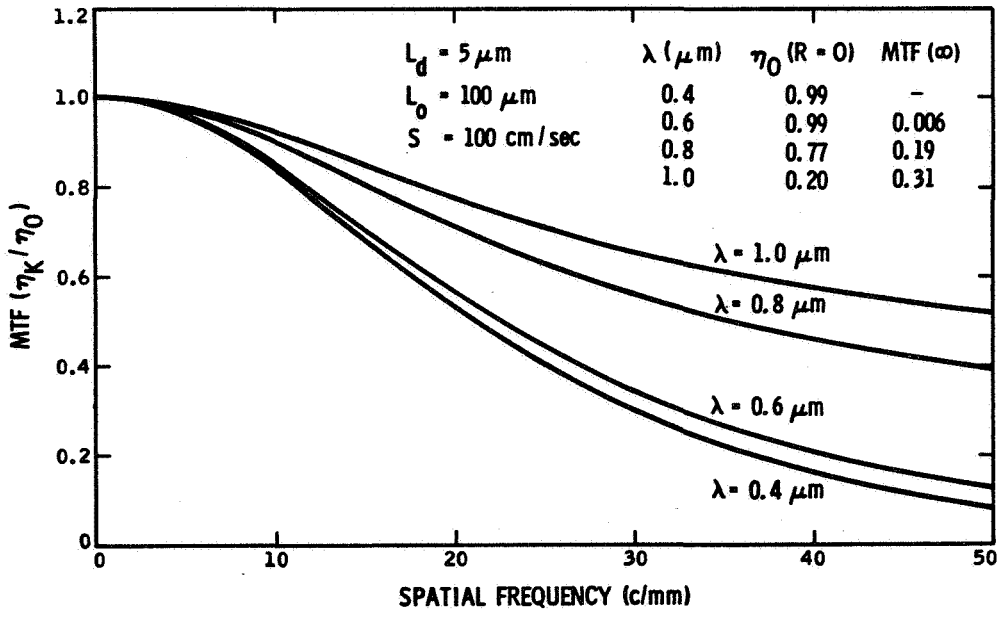

Figure 4. MTF for lateral diffusion (L_T = 15 μm)

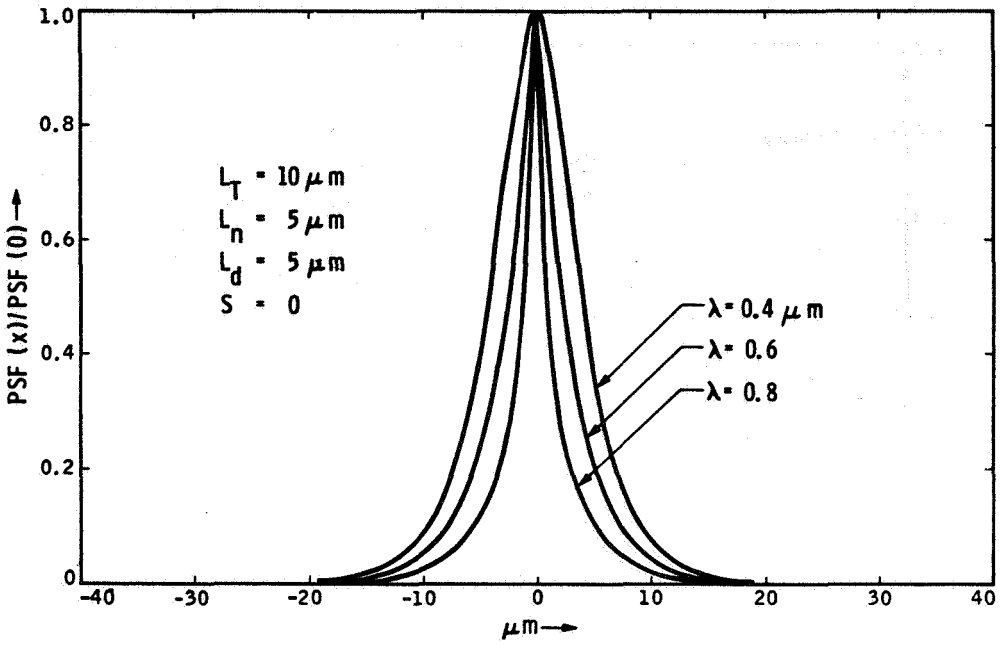

Figure 5. Point-spread function for lateral diffusion $\mathcal{F}^{-1}(\eta_k/\eta_0)C = 0$ (L_T = 10 μm)

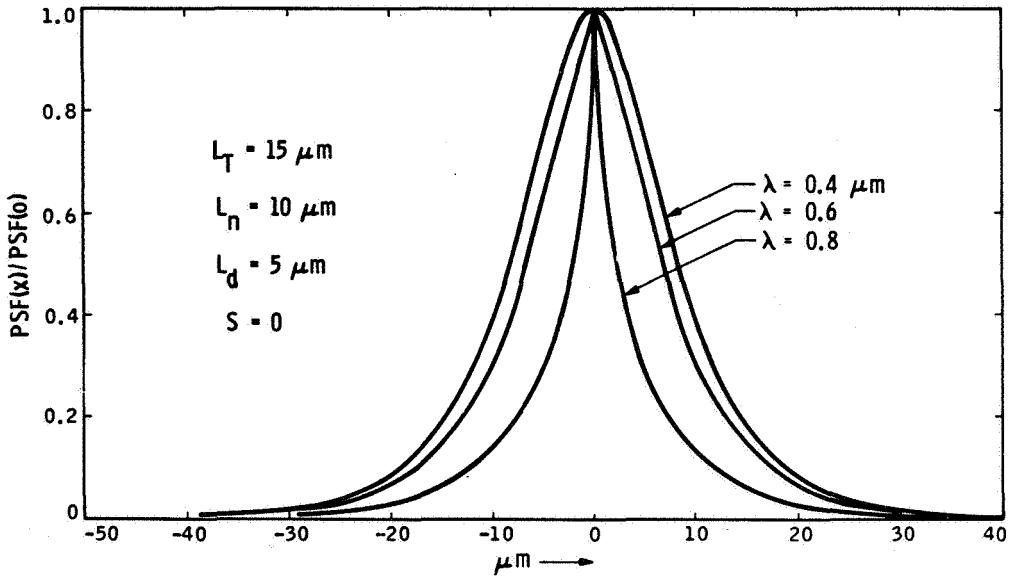

Figure 6. Point-spread function for lateral diffusion $\mathcal{F}^{-1}(\eta_k/\eta_0)C = 0$ (L_T = 15 μm)

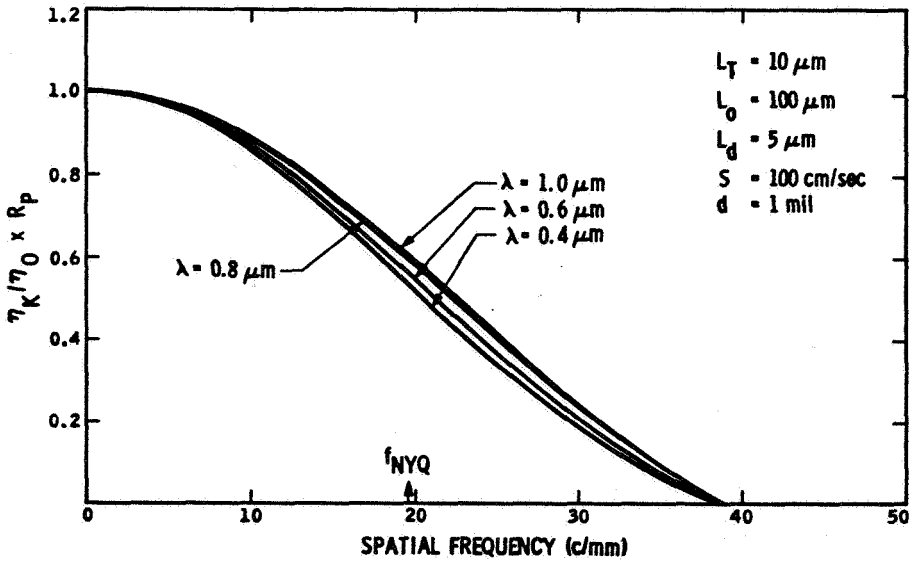

Figure 7. MTF, including the effect of finite pixel size

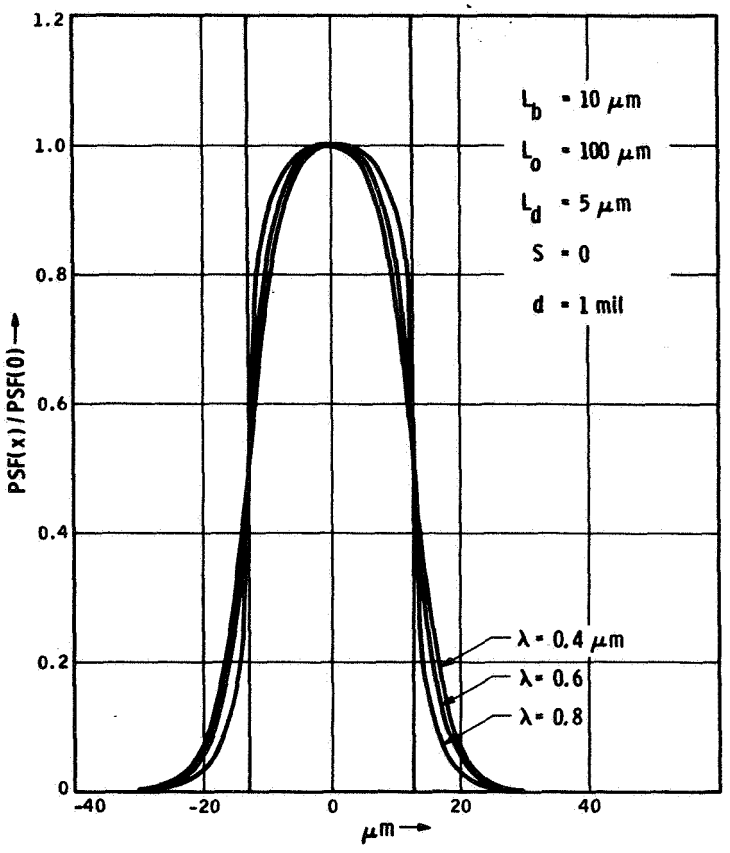

Figure 8. Point-spread function $\mathcal{F}^{-1}(\eta_k/\eta_0 \times R_P)$

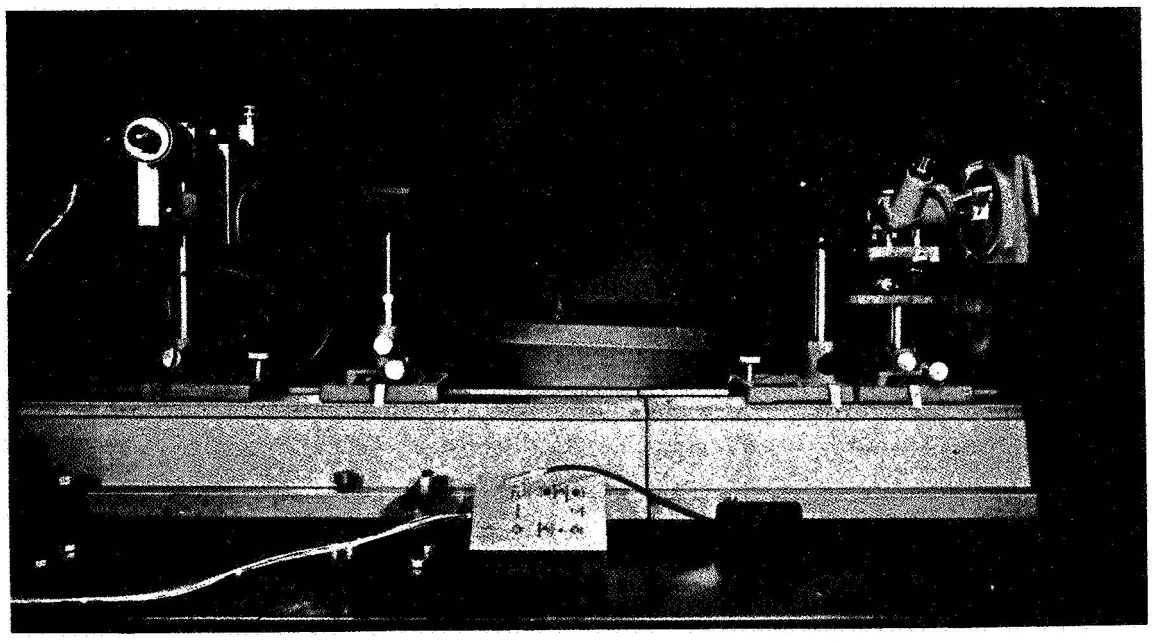

Figure 9. Test setup for sensitivity profile measurements

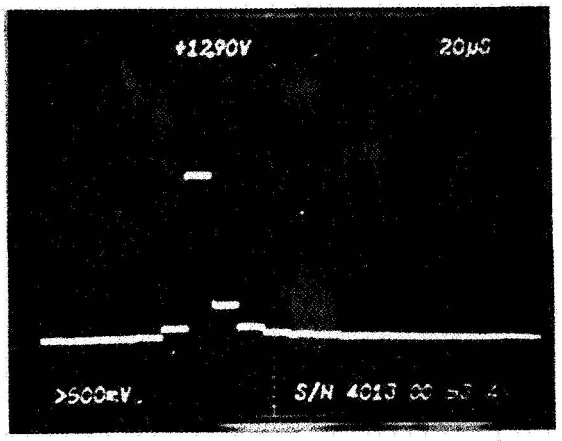

SPOT CENTERED ON PIXEL (25, 7)

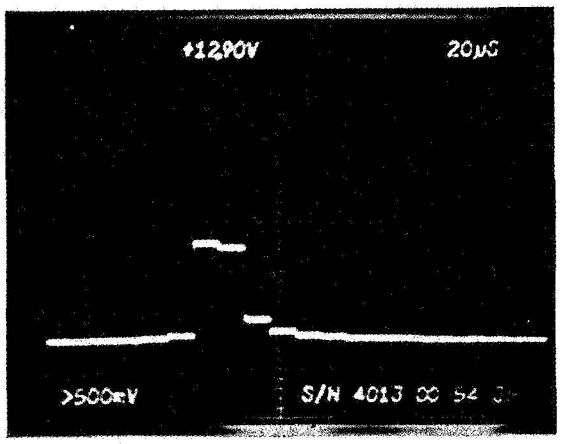

SPOT CENTERED BETWEEN PIXELS (25, 7) AND (26, 7)

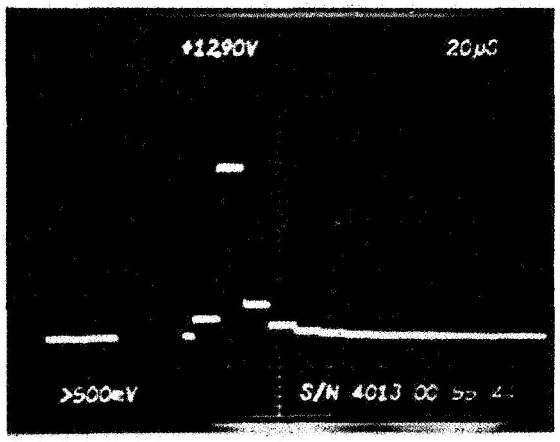

SPOT CENTERED ON PIXEL (26, 7)

Figure 10. Video output from three adjacent pixels vs. spot position (horizontal scan)

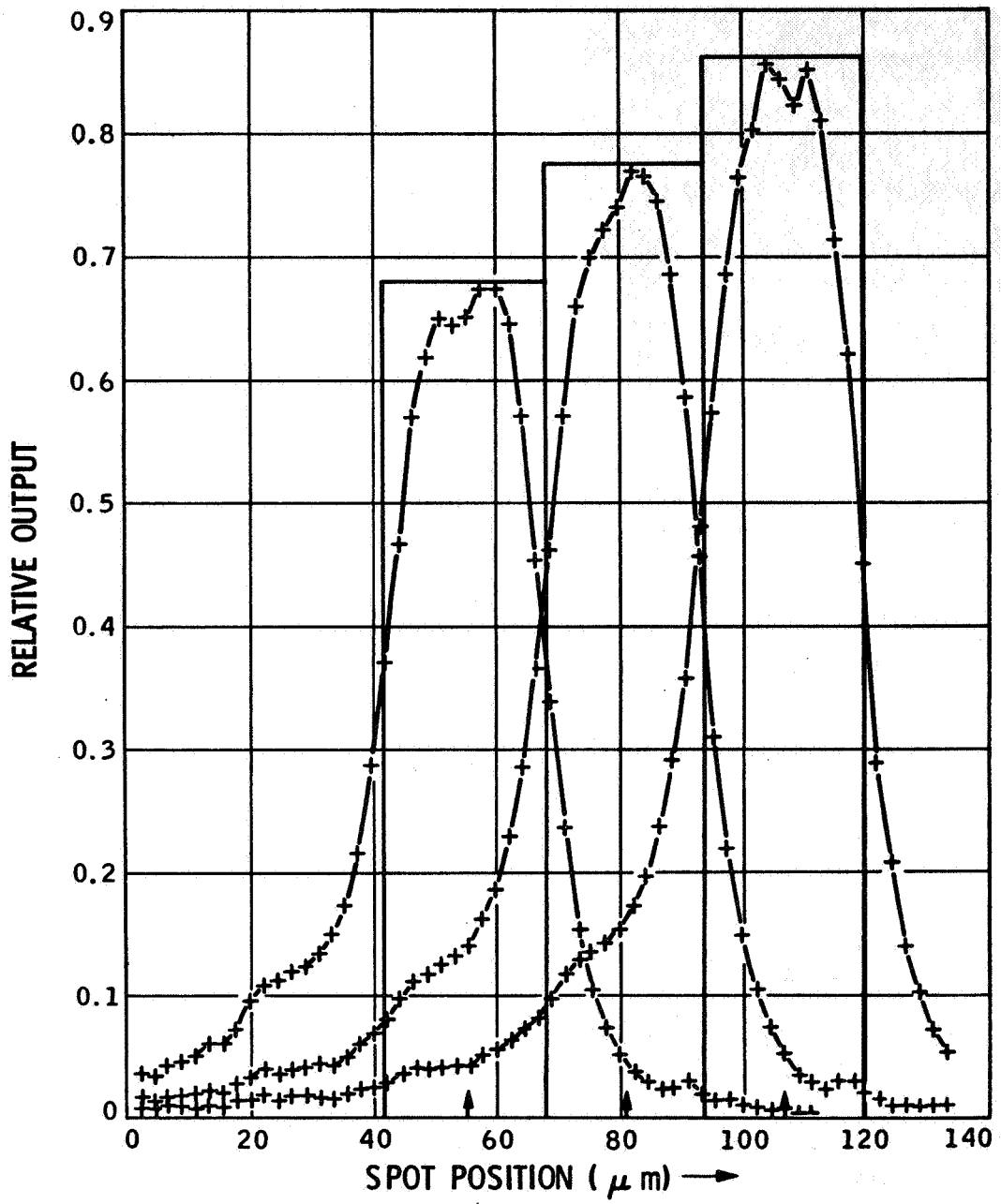

Figure 11. Sensitivity profile for three adjacent pixels (blue filter) (scan ⊥ to vertical channel)

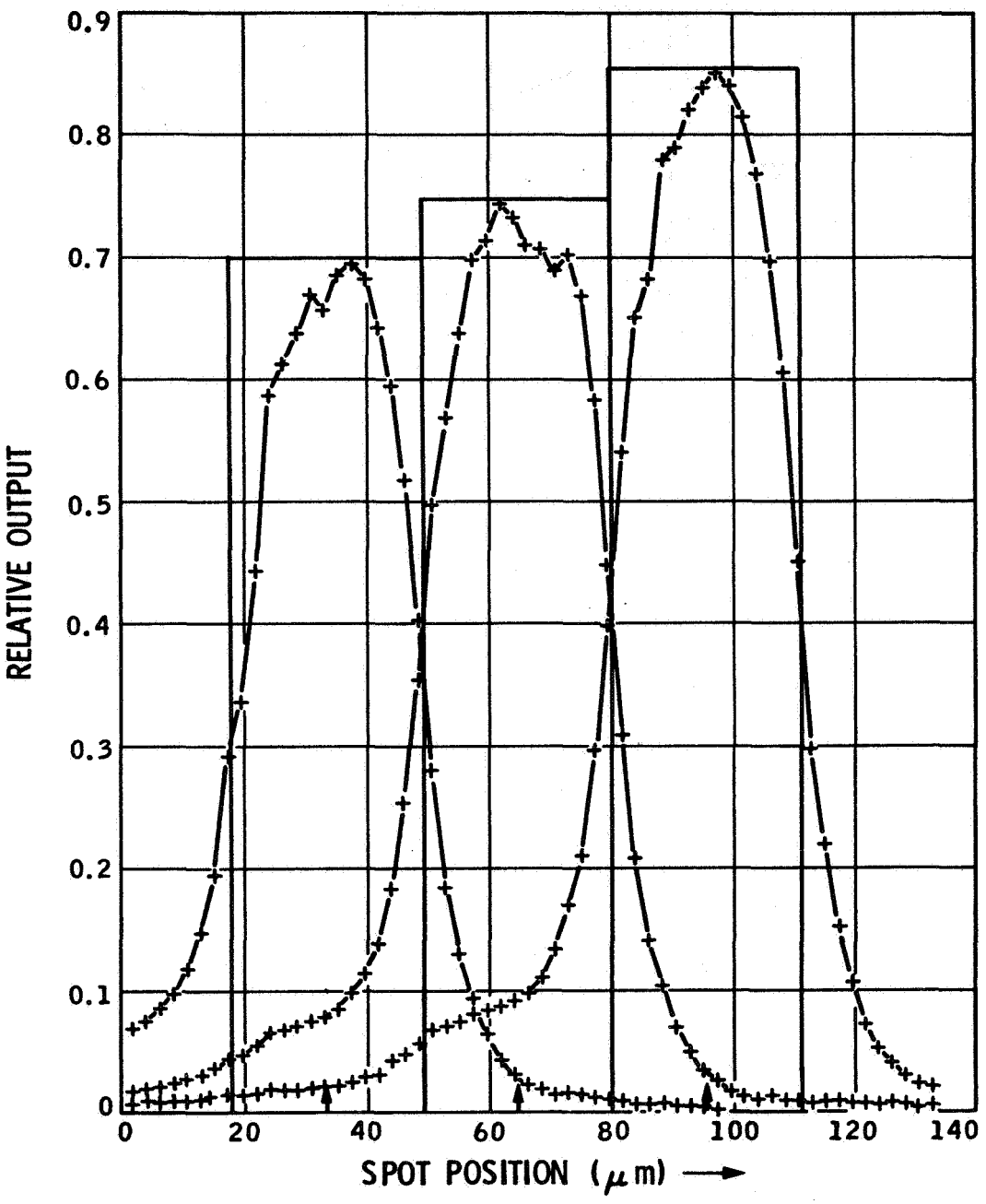

Figure 12. Sensitivity profile for three adjacent pixels (blue filter) (scan || to vertical channel)

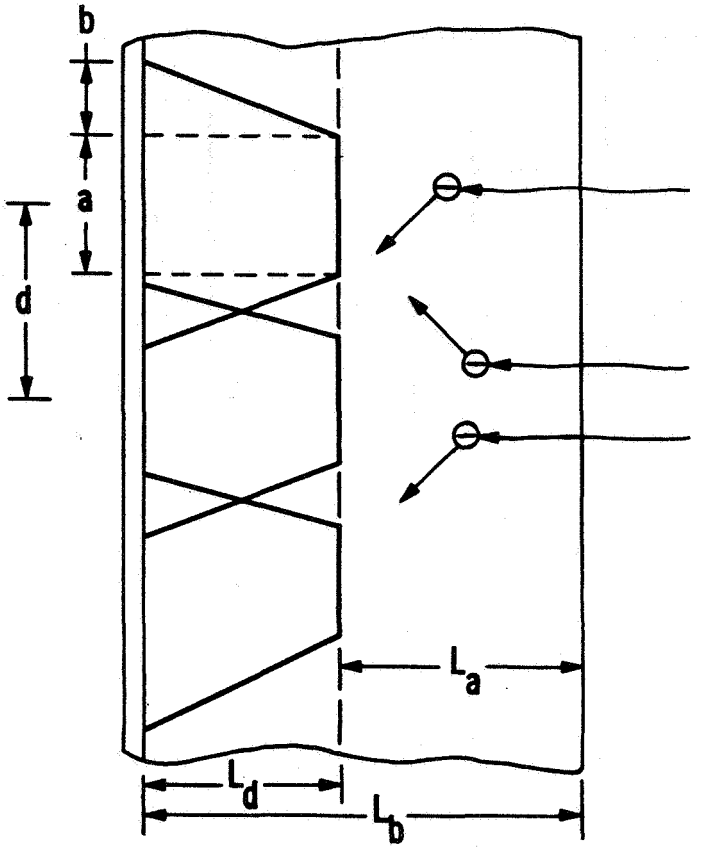

$$MTF = MTF(L.D.) \times R_T$$

$$R_T = \text{sinc}(\omega b/2)\ \text{sinc}(\omega(a+b)/2)$$

Figure 13. Schematic illustrating overlapping depletion collection profile

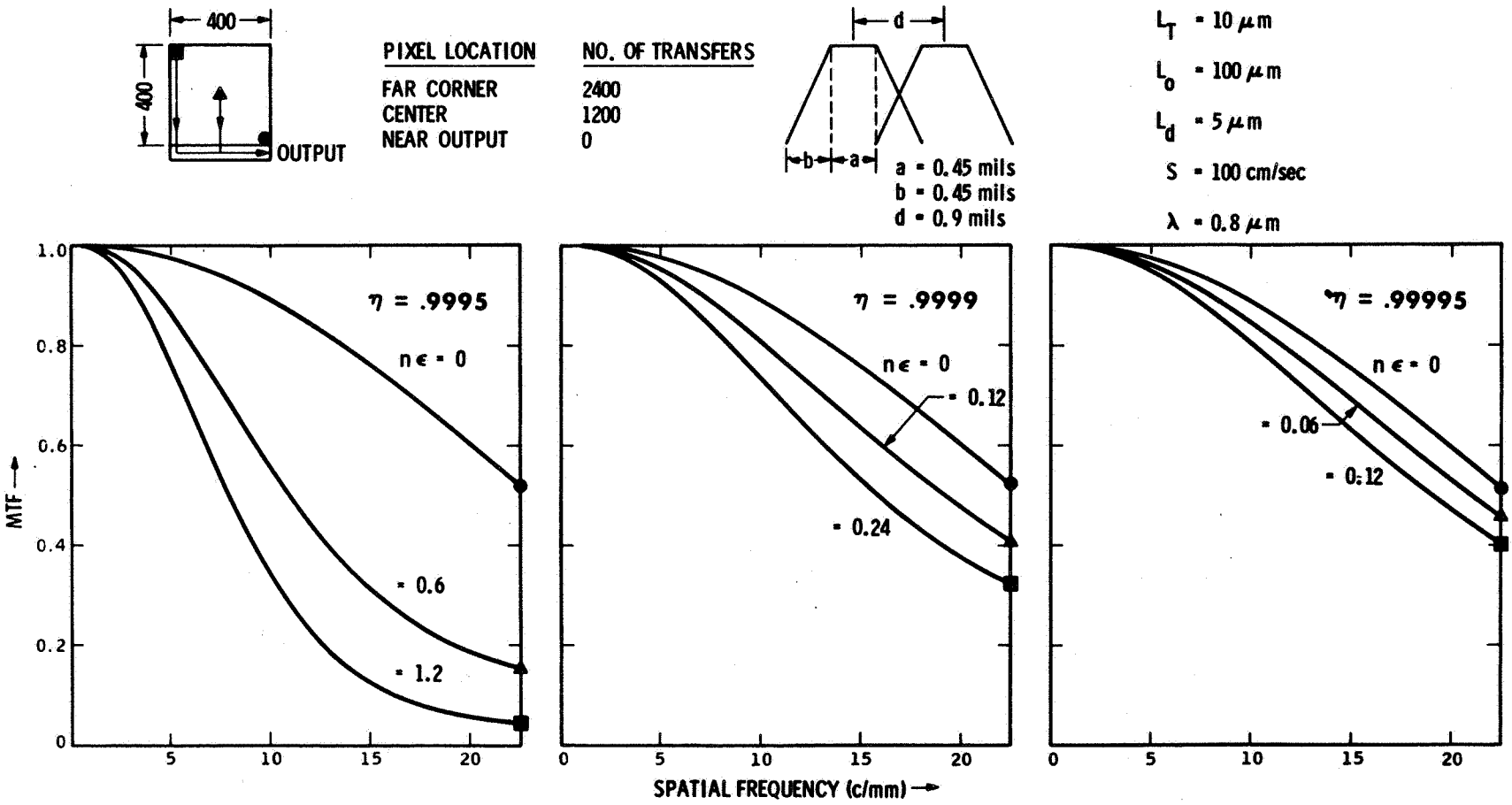

Figure 14. Calculated MTF for a 400 × 400 three-phase CCD imager (MTF = $\eta_k/\eta_0 \times$ MTF (nε) × R_T)

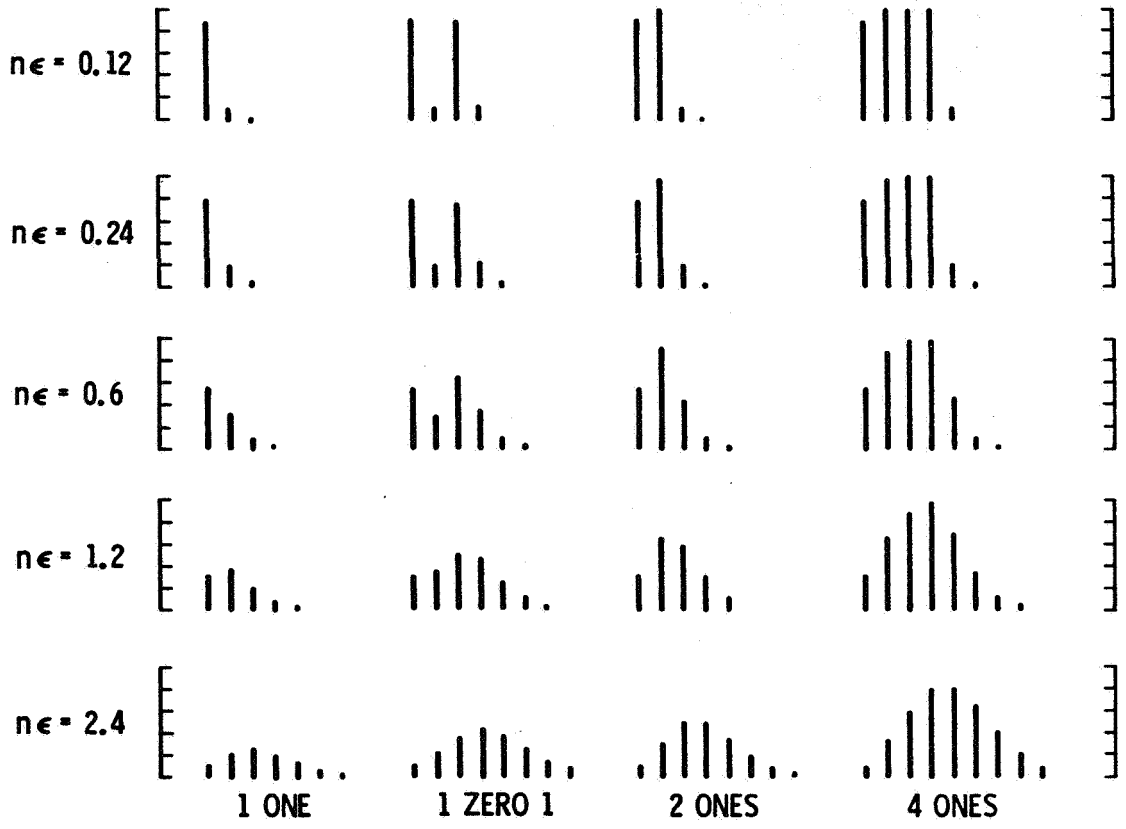

Figure 15. Charge dispersion due to transfer inefficiency (linear model $\eta + \epsilon = 1$)

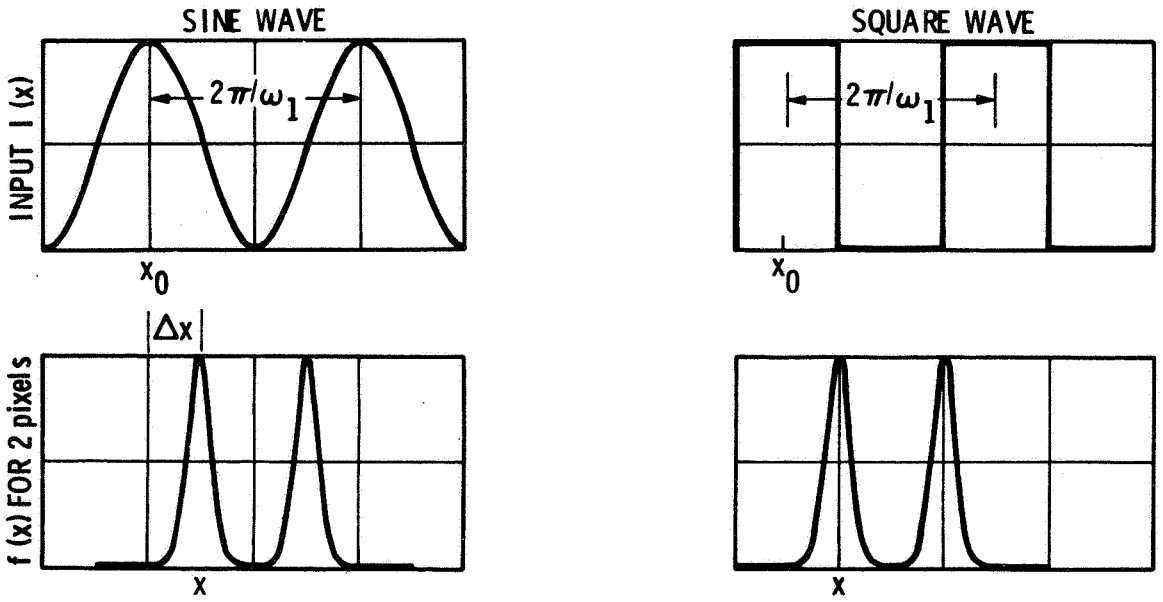

$$R(x)_{\omega=\omega_1} = \int_{-\infty}^{\infty} I(x')f(x' - x)\,dx'$$

$$= \cos \omega_1(\Delta x)F(f(x))\Big|_{\omega=\omega_1}$$

$$= \cos \omega_1(\Delta x)\,MTF(\omega_1)$$

WHERE $\Delta x = x - x_0$

$$R(x)_{\omega=\omega_1} = \int_{-\infty}^{\infty} Sq(x')f(x' - x)\,dx'$$

$$= F^{-1}\left[F(\omega)F(Sq(x))\right]$$

$$= \frac{4}{\pi} \sum_{n=1,3,5\ldots}^{\infty} (-1)^{(n-1)/2} \frac{\cos(n\omega_1\Delta x)}{n} MTF(n\omega_1)$$

Figure 16. Relation between the MTF and device response for sine- and square-wave inputs

EFFECTS OF IONIZING RADIATION ON CCDs*

G. A. Hartsell, D. A. Robinson, and D. R. Collins
Texas Instruments Incorporated
Dallas, Texas

The use of CCD sensors for satellite and deep space probes appears very attractive from the standpoints of size, weight, power, and reliability. One of the factors affecting CCD sensor reliability is the naturally occurring radiation levels encountered in such environments. This paper reports the preliminary results of tests of the effects of 1.2-MeV gamma radiation (Co^{60} source) and 20-MeV electrons (Linac source) on the operational characteristics of CCDs.

The effects of ionizing radiation on the charge transfer efficiency, dark current, and input/output circuitry are described. The improved radiation hardness of buried-channel CCDs is compared to surface-channel results. Both ion-implanted and epitaxial layer buried-channel device results are included. The advantages of using a single-thickness SiO_2 gate dielectric are described. The threshold voltage shifts and surface state density changes of dry, steam, and HCl doped oxides are discussed. Recent results on the recovery times and total dose effects of high-dose-rate pulses of 20-MeV electrons are reported.

*This work is being supported by the Air Force Avionics Laboratory, Wright Patterson Air Force Base under contract F33615-74-C-1054.

I. DESCRIPTION OF TEST DEVICES

All of the CCDs tested have been 4 ϕ double-level aluminum metal n-channel devices having SiO_2 gate oxide and anodized aluminum interlevel metal insulation. These devices have a coplanar overlapping gate structure and a single-thickness uniform gate oxide layer, which is desirable for radiation hardness because the effects of oxide charge buildup are the same under all gates. Although these devices were 4 ϕ type, they had the same gate metal and oxide structure as is being used in the 3 ϕ double-level anodized aluminum imagers developed at Texas Instruments (Ref. 1).

The test chip design used for the test samples contains the following devices: (1) two 150-bit 4 ϕ linear CCD shift registers, one having a precharged diffusion plus source follower output and one having a simple diode output, (2) a MOSFET test transistor with W/L = 10, (3) an MOS gate oxide capacitor, and (4) an MOS gated diode. All of these can be ion-implanted or fabricated on epitaxial material to form buried-channel type devices.

Two groups of test samples have been fabricated for the two series of tests made to date. The first of these included both surface and buried-channel devices, oxide process variations of 950° C steam, 1100° dry, and 1100° HCl-grown oxides. The metallization was e-beam evaporated. Buried-channel devices of both the ion-implanted and epitaxial layer type were included. The second group was mostly buried-channel type, with either 950° C steam or 1000° dry oxide. Diffused chrome doping of the oxide was done on some of the devices. Metallization variations were e-beam evaporated and thermally evaporated metal. PSG gate oxide passivation and a nitride overcoat were used on all devices tested.

II. DESCRIPTION OF RADIATION TESTS

Total dose gamma radiation tests were made using the Co^{60} radiation sources ($\approx$1.2-MeV photons) at Sandia Labs in Albuquerque and at the Nuclear Effects Laboratory, White Sands Missile Range. Dose levels ranged from 10^5 rad to 10^7 rad. In each of the two series of tests made, the test samples were connected in parallel and biased to simulate normal operating conditions in the CCD so that several samples could be irradiated at the same time. This was necessary because a large number of test samples was required due to the number of different process variations that were tested. All the CCD and test

device n-diffusions were reverse biased to +24 volts, and the gates were pulsed with a 50% duty cycle between 0 and +8, +12, or +15 volts.

The dose rate effects tests were made using the Linac source at the Nuclear Weapons Laboratory in the pulsed electron beam mode. The pulse width was 100 ns and electron energy was set at 20 MeV. The CCDs were tested for recovery time after pulses at dose rates of 10^8, 10^9, 10^{10} and 4×10^{10} rad/sec. To measure the recovery time, it was necessary to be able to operate the CCD with normal bias and clock levels and remotely monitor the output during irradiation in the source chamber. A special test set was made to permit driving the CCD clocks through more than 50 feet of cable and monitoring the output at clock rates of up to 10 MHz. This test equipment was also used for the Linac total dose test and was found to be very advantageous for total dose tests in that data can be easily obtained at several dose levels for the same device. This eliminates device-to-device variations when comparing effects at different dose levels.

III. EXPERIMENTAL RESULTS OF THE TOTAL DOSE GAMMA TESTS

Both surface- and buried-channel devices have been tested; the results obtained for the two types were very different. For surface-channel devices, the results can be summarized as follows:

(1) At levels of 10^5 rad or above, the charge transfer efficiency (CTE) was so degraded as to make the device useless.

(2) Relatively low dc threshold shifts occurred in the MOSFETs.

(3) Large increases in CCD leakage current occurred.

(4) The CV curves of the MOS capacitors exhibited large negative shifts at high frequency.

The surface-channel CCDs had pre-irradiation charge transfer efficiencies of 0.9991 to 0.9995 which decreased so much as to become unmeasurable after irradiation. The 1.0-MHz CV curve shift for the test capacitors ranged from 11 volts to over 60 volts after 10^6 rad, depending on the oxide growth process. The CV shifts were very frequency-dependent, as shown in Figure 1. GV measurements indicated surface state trap densities of over 10^{12} per eV-cm^2. This explains the large CTE degradation seen in these devices. However, as shown in Figure 2, there was little shift in the MOSFET dc threshold voltage (except

for the HCℓ-grown oxide), implying very little increase in the fixed surface charge. The HCℓ-grown oxides were much worse than either the steam or dry oxides in regard to surface state and fixed charge buildup. CCD leakage current was initially 100-200 nA/cm^2 and typically increased by a factor of 50 after irradiation. Leakage in the sub-threshold region for the MOSFETs also increased appreciably.

The test results for buried-channel CCDs can be summarized as follows:

(1) While considerable variation has been seen, changes in charge transfer inefficiency (CTI) of $<5 \times 10^{-5}$ have been found in several samples after exposures of 10^6 rad. The variation of CTI frequency is not measurably changed after irradiation.

(2) The full-well capacity is not significantly changed.

(3) Large increases in both fixed charge and surface state trapping effects after irradiation have been seen for devices heavily ion-implanted through the gate oxide.

(4) The surface charge buildup causes input and output threshold voltage shifts.

(5) The surface trapping states have little effect on operation of the buried-channel CCD but may cause significant G_m loss in the MOSFETs in the output circuit.

A plot of the increase in CTI versus dose (Figure 3) shows wide variations, but some samples had increases of 5×10^{-5} or less even after 10^6 rad. Both pre- and post-irradiation measurements were made without externally introduced fat zero. The cause of the CTI increase has not been determined. However, the large fixed charge buildup at the interface may have moved the channel nearer the surface so that the surface state traps affected the charge transfer.

In some devices, breakdown between the channel and the p+ channel stop diffusion occurs after irradiation and results in a large increase in dark current. This breakdown is attributed to the increased channel potential resulting from the fixed charge buildup and can be eliminated by increasing the substrate bias which reduces the potential between the channel and channel stop.

The increase in fixed oxide charge and interface trapping states was determined by pulsed turn-off measurements made on the buried-channel MOSFETs. If the gates of these depletion mode MOSFETs are pulsed from near 0 volts with a negative pulse V_T (pulse) just large enough to overcome the potential due to the fixed charge layer, the source-drain current will be momentarily cut off but will then again start to flow if there were a significant number of filled trapping states which can empty electrons into the channel. This effect is seen in the current waveforms of Figure 4. The size of the negative gate pulse must be increased by an amount $\Delta V_T(ss)$ in order to keep the channel turned off after the traps empty and the total number of surface state traps involved is equal to $\Delta V_T(ss) \cdot C_{ox}/q$, where ΔV_T (pulse) is the change in pulsed threshold after exposure. From these measurements, the increase in fixed charge after 10^6 rad for the ion-implanted BC MOSFETs was found to be 3 to 4 $\times 10^{12}/cm^2$ for both wet and dry grown oxide. The total number of surface state traps ranged from about 1 to 5 $\times 10^{12}/cm^2$.

No correlation was found between the different types of oxide and the increase in fixed charge or surface states for the implanted buried-channel devices tested. Of course, the resulting threshold voltage shift is inversely proportional to the oxide capacitance, and therefore a strong correlation is seen between threshold shifts and oxide thickness. The reason for the much larger buildup of fixed charge in the implanted buried-channel devices has not been fully determined but may be due to the ion implant through the gate oxide. Much smaller fixed charge increases were seen in the epitaxial buried-layer devices, but this may be due to other factors. The input threshold voltage changes seen on buried-channel CCDs is less than the threshold voltage changes of the MOSFETs even though both were biased the same during irradiation.

Noise measurements were made before and after irradiation using a low-noise input technique (Ref. 2) and a correlated double-sampling scheme (Ref. 3) to reduce the noise on the output node. Before irradiation, the noise ranged from 100-300 electrons, and the dominant source was the output source follower. After exposure, the noise increased by an amount equivalent to the shot noise on the increased leakage current.

IV. RESULTS OF THE PULSE RECOVERY TESTS

Waveforms of the CCD output during and after a 100-ns wide, 10^{10}-rad/sec pulse of 20-MeV electrons are shown in Figure 5. Recovery to normal operating levels at the CCD output occurred in from 240 to 310 μs for dose rates of from 10^8 to 4×10^{10} rad/sec and a clock rate of 1 MHz. This recovery time can be divided into two parts. During the first, which starts with the radiation pulse and lasts 50 to 100 μs, the CCD output diode is discharged to near substrate potential due to the large amount of radiation-generated charge present. After this charge is removed by the output drain diffusions of the reset and source follower MOSFETs, normal output circuit levels are reestablished and the excess charge remaining in the CCD channel is clocked out in a period of about 200 μs. For the 4×10^{10} rad/sec level pulses, an increased output leakage was seen, which decayed with a time constant of approximately 1.0 ms. This is thought to be due to the thermal time constant for removal of heat generated by the large photocurrents which flow in the output circuit.

V. LINAC TOTAL DOSE TESTS

Total dose effects tests were made using 100-ns wide, 20-MeV electron pulses of about 80 rad per pulse and 10 pulses per second. The source was turned off and data taken at levels of 0, 5×10^4, 10^5, 3×10^5, and 10^6 rad. The CCD input threshold was found to shift by 3 to 6 volts at 10^6 rad, depending on oxide thickness. Typically, one half of this shift had occurred at a dose of 10^5 rad, and little shift was seen after 5×10^5 rad. The CTI increase was more than that seen in the better devices in the Co^{60} gamma tests. The devices typically had a large increase in leakage current at about 3×10^5 rad, which made CTI measurements difficult. It was later found that this leakage current can be greatly reduced by increasing the substrate bias, as in the case of some of the Co^{60} irradiated devices.

One very different result for these tests was that the source follower gain was degraded much less than was the case for the Co^{60} tests. This is probably due to the fact that for a high dose rate source, the CCD output node is discharged to nearly substrate voltage by the large photocurrent during the radiation. Therefore, the gate bias on the source follower is nearly zero during irradiation compared to a gate bias of about +24 volts for buried-channel devices in the low-dose-rate Co^{60} tests.

VI. CONCLUSIONS

It seems unlikely that total dose hardness to the 10^6-rad range can be achieved with surface-channel CCDs due to large CTE degradation caused by surface state trapping. However, even though several problems remain with the buried-channel devices tested to date, it appears that buried-channel devices can be made using the structure described here that will give good performance after exposure to doses of up to 10^6 rad. The major problems identified are input and output level shifts, increased dark current and associated noise, and output MOSFET gain loss.

REFERENCES

1. G. A. Hartsell and A. R. Kmetz, "Design and Performance of a Three Phase Double Level Metal 160 X 100 Element CCD Imager," International Electron Devices Meeting, December 1974, Washington, D. C. Also, G. A. Antcliffe, et. al., "Large Area CCD Imager for Spacecraft Applications," Proceedings of this Symposium.

2. S. P. Emmons and D. D. Buss, "Techniques for Introducing a Low-Noise Fat Zero in CCDs," Device Research Conference, 26-28 June 1973, Boulder, Colorado.

3. M. H. White, et. al., "Characterization of Surface Channel CCD Image Arrays at Low Light Levels," IEEE J. Solid State Circuits SC-9, 1 (1974).

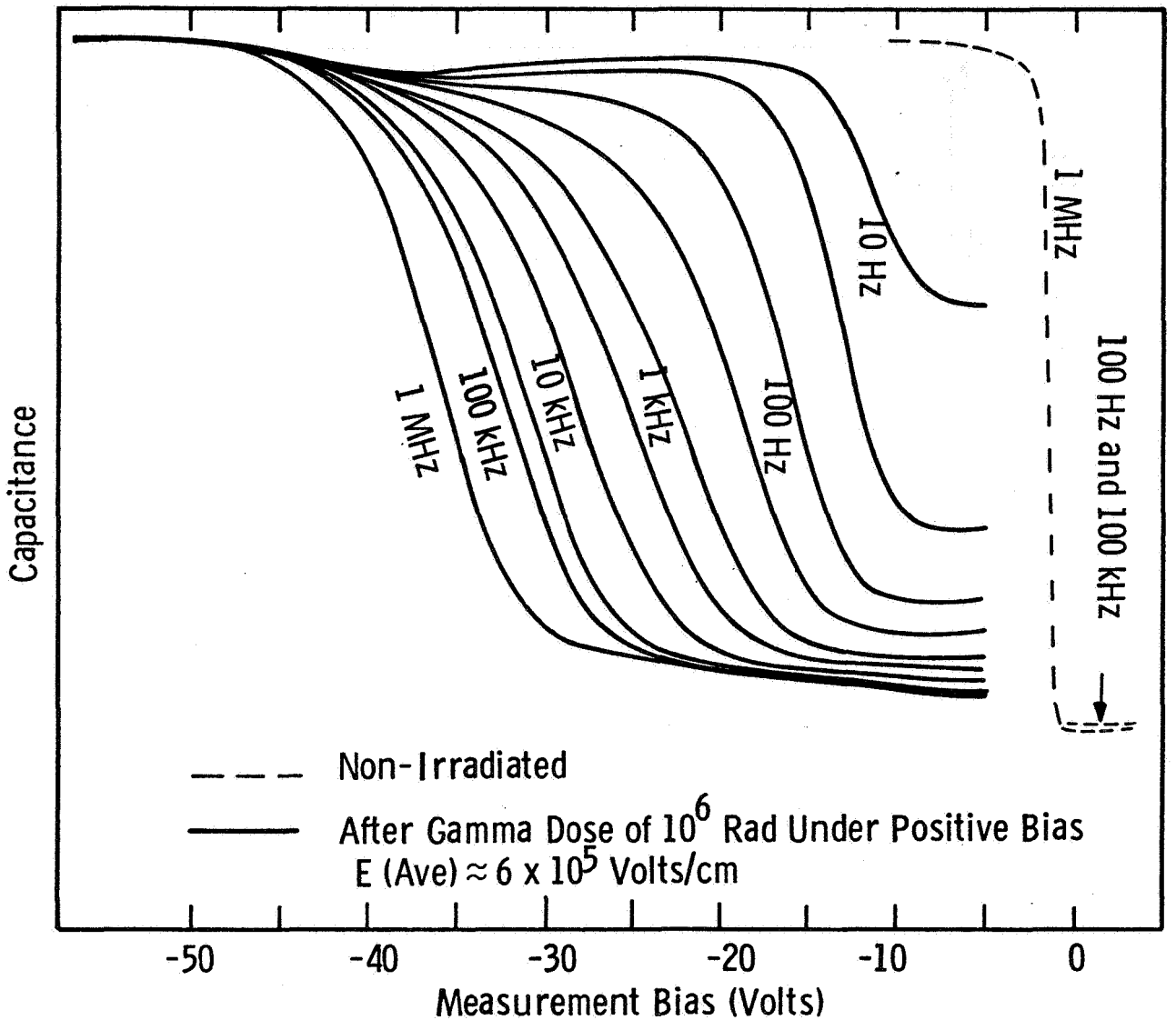

Figure 1. Curves showing CV shift with frequency for surface-channel MOS capacitors with HCℓ oxide

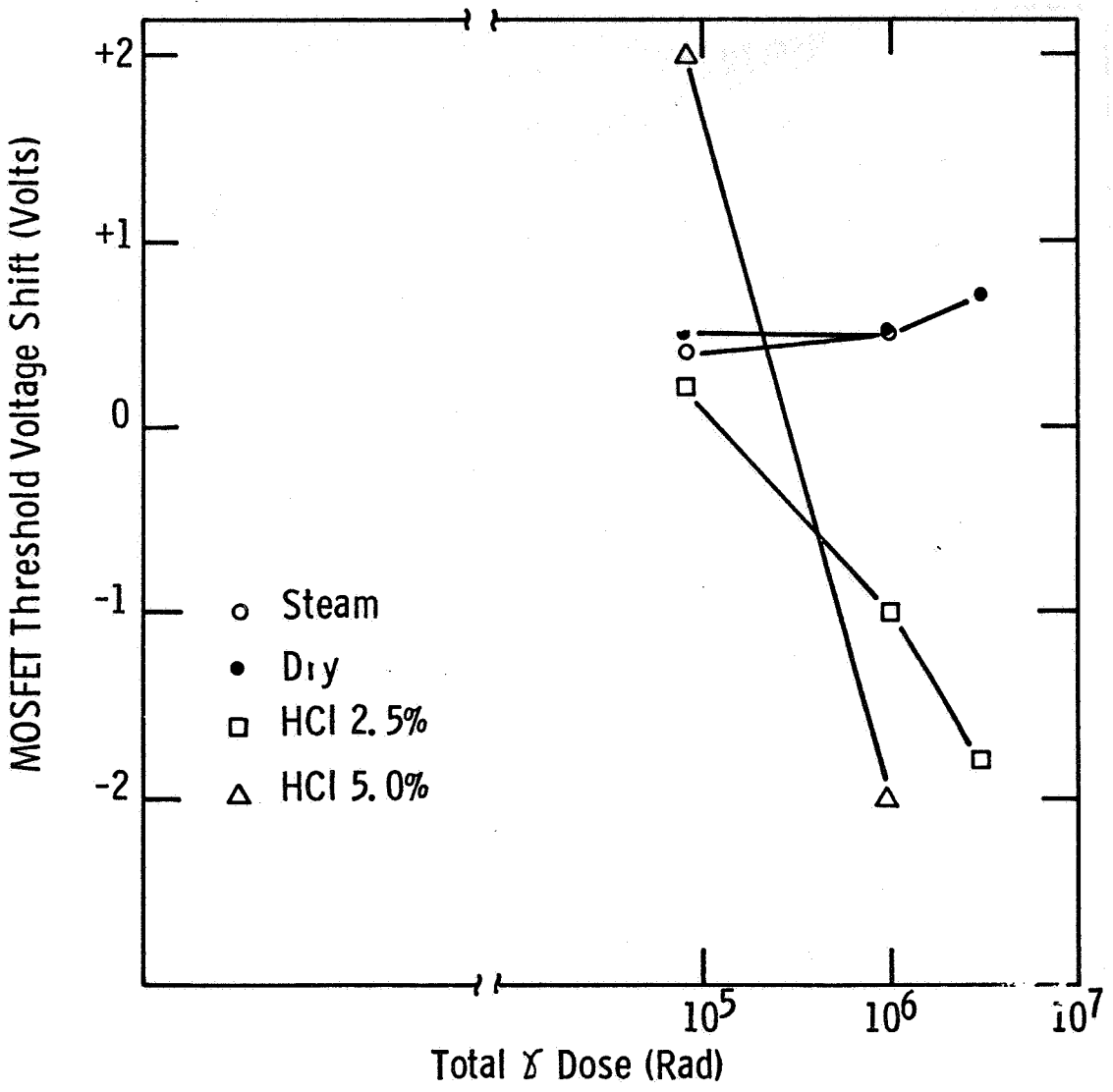

Figure 2. MOSFET threshold variation with gamma dose for surface-channel devices

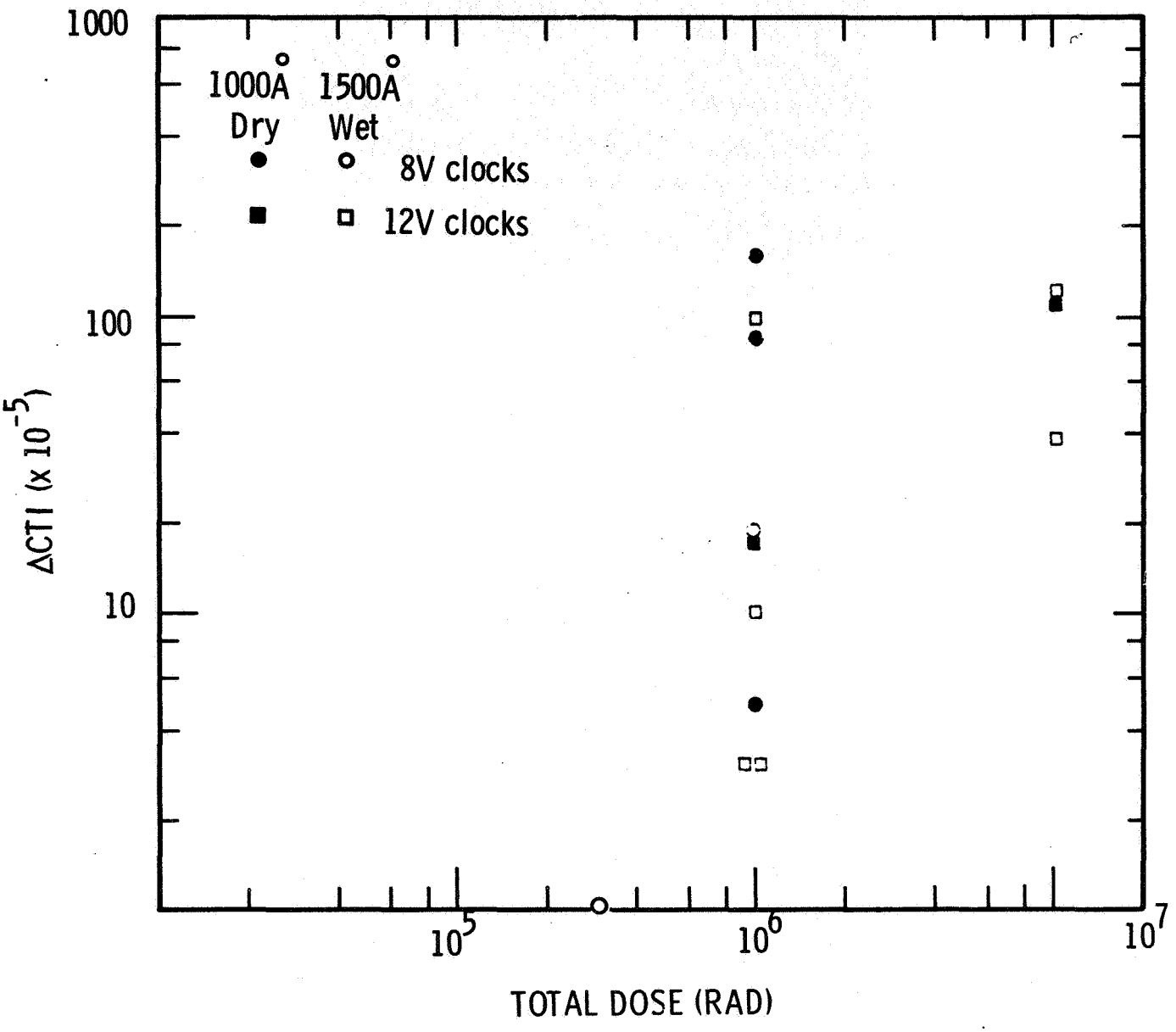

Figure 3. Change in charge transfer inefficiency with gamma dose for buried-channel CCDs

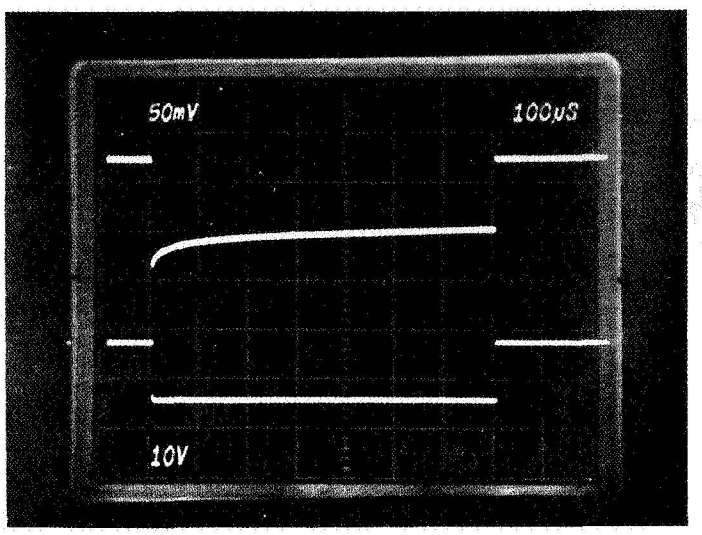

Sample 68-6-66

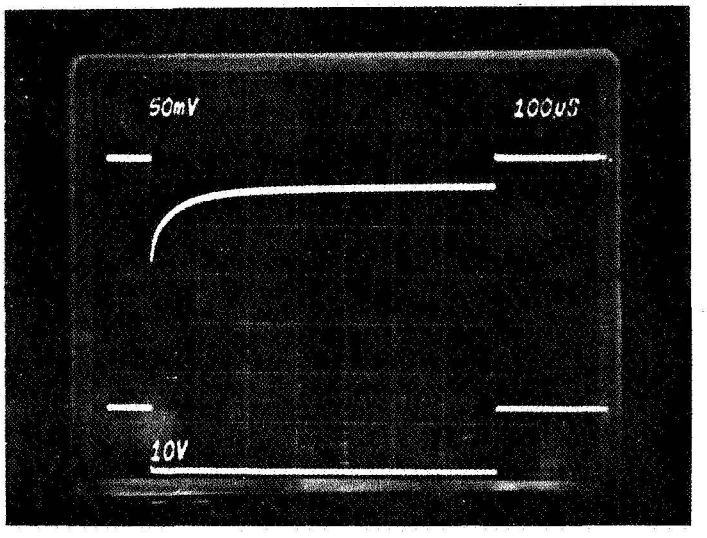

Sample 68-4-157

Figure 4. Variation of MOSFET drain current with time due to emptying of surface state traps [Top trace – I_D (2 ma/div), lower trace – V_G. (10 V/div).]

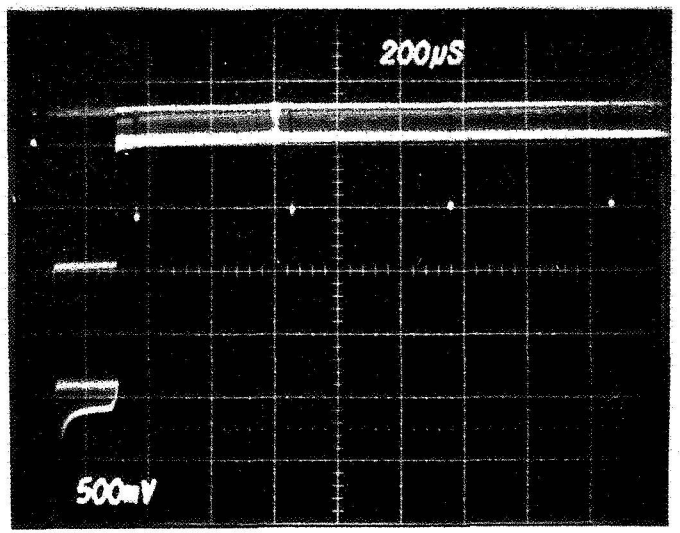

Output waveforms of buried channel CCD showing operation during and after exposure to a 100ns wide pulse of 20 Mev electrons from Linac dose rate is 10^{10} Rad/sec.

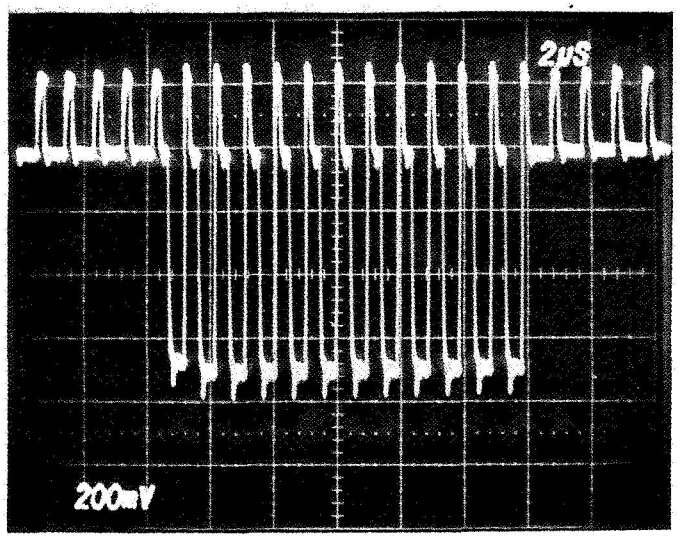

Expanded scale waveform of CCD signal pulse demonstrating good CTE after recovery from saturation caused by photocurrent from radiation pulse.

Figure 5. Waveforms of CCD output showing recovery from 10^{10} rad/sec radiation pulse

EFFECTS OF IONIZING RADIATION ON CHARGE-COUPLED IMAGERS

J. M. Killiany, W. D. Baker, N. S. Saks, and D. F. Barbe
Naval Research Laboratory
Washington, D. C.

The effects of ionizing radiation on three different charge-coupled imagers have been investigated. Device performance was evaluated as a function of total gamma ray dose. The principal failure mechanisms have been identified for each particular device structure. The clock and bias voltages required for high total dose operation of the devices are presented.

I. INTRODUCTION

The recently developed charge-coupled devices (CCDs) are expected to have low cost, small size, low power consumption, and high reliability. Such characteristics make CCDs especially attractive for space flight missions if the devices can be made to operate in a radiation environment. Since no standard CCD design has yet emerged, we have been engaged in a program to evaluate the effects of ionizing radiation on several of the CCD structures currently in use. Our objectives have been to identify the radiation-induced failure mechanisms and to determine whether the clock and bias voltages can be modified to permit higher total dose operation.

The CCD imagers that we have evaluated include: (1) a 256-bit, two-phase linear imager with overlapping polysilicon gates; (2) a 60-bit, three-phase linear imager with planar doped polysilicon electrodes and high-resistivity polysilicon interelectrode isolation; and (3) a 100 X 100 bit area imager with associated two-phase transfer registers. All three types of

imagers were buried-channel devices. No effort was made to process harden any of the devices to radiation.*

II. REVIEW OF CCD OPERATION

Space considerations do not permit an explanation of the manner in which CCD imagers operate. Instead, the reader is directed to a number of tutorial papers (Refs. 1, 2, 3). Those aspects of CCD operation which are important to the treatment of radiation effects were briefly presented by Killiany et al. (Ref. 4). The state-of-the-art in CCD imagers has recently been reviewed by Barbe (Ref. 5).

III. EXPERIMENTAL DETAILS AND RESULTS

A. 256 X 1 Linear Imager

The test device is a 256-bit linear imager employing the double-register parallel transfer readout organization shown in Figure 1a (Ref. 6). The 256 photosites are separated by diffused channel stops and covered by a polysilicon photogate 23 μm wide. The center-to-center spacing of the photosites is 13 μm. The two-phase parallel shift registers have overlapping polysilicon gates and self-aligned ion implanted barriers. The right-left register outputs are interlaced at the output gate and fed into the gated charge integrator. The shift registers are designed to operate at 5 MHz with a resulting 10 MHz output data rate. The on-chip compensation amplifier can be used to suppress the reset clock noise by use of a differential amplifier in the external video circuitry.

A cross-section of the shift register is shown in Figure 1b. The gate insulator is a combination of an oxide and a nitride (Si_3N_4) layer. The self-aligned barrier is formed by means of a boron implant. The shift registers are covered with aluminum to prevent the incident light from going through the polysilicon gates and smearing the image.

The devices were characterized in both the integration mode and the continuous mode of operation. For the integration mode, the photogates are

*The devices were fabricated by Fairchild Semiconductor, R&D Laboratory, Palo Alto, California, and are commercially available. Fairchild's 500-stage linear imager has the same structure as the 60 X 1 test imager.

held at +5 V, and the 1-MHz shift register clocks swing from 0 to +7 V with a 50% duty cycle. Charge is transferred from the photosites to the shift registers by holding the shift register clocks at their high value and pulsing the transfer gate from 0 to +7 V. In the devices available for testing, one of the shift registers was inoperable. Hence, all photosites had to empty into one register. This necessitated the use of a modified timing diagram. The reset pulse frequency was 1 MHz instead of the 2-MHz rate required to interlace the outputs of the parallel registers.

The input diode (ϕ_{SB}) and input gate (GB) were respectively biased to +12 V and 0 V to prevent charge from being introduced into the shift registers electrically. The output gate (OG) was held at +3 V, while both the reset drain and output diode voltage was +15 V.

For continuous mode operation, both the photogate and transfer gates were held at 0 V.

Two devices were irradiated, with Cobalt 60 gamma rays, the first to 4.5×10^4 rads (Si) and the second to 1.88×10^5 rads (Si). The devices were irradiated while being operated as line imagers with normal bias and clock voltages applied. The integration time was 12.8 ms. An unirradiated control device was also recharacterized after each dose increment as a check to the proper operation of the electronics. For total doses less than 5×10^4 rads, a dose rate of 8.2×10^2 rads (Si)/min was employed. The highest dose rate employed was 4.6×10^3 rads (Si)/min. The flat-band voltage shift was determined from 1-MHz C-V curves taken from an on-chip buried-channel capacitor whose gate was biased with the ϕ-1 clock and which had +15 V applied to the buried channel.

The radiation-induced flat-band voltage shift (ΔV_{FB}), shown in Figure 2a, limited device operation with the pre-irradiation clocks and bias to 4.5×10^4 rads (Si). The failure mechanisms resulting from ΔV_{FB} were: (1) buried channel driven out of depletion, (2) reset transistor biased in the conducting state for the entire clock period, and (3) input gate turned on. These three effects will be discussed separately in the following paragraphs.

The first requirement for successful operation of a buried-channel CCD is that, for zero signal, the implanted layer should be entirely depleted of majority carriers. The depletion is accomplished by applying a sufficiently large positive voltage to the output diode at the end of the CCD channel. The effect of the positive charge buildup in the oxide during irradiation is to increase the reverse bias required for total depletion. The minimum reset voltage required to deplete the buried channel is shown in Figure 2b as a function of radiation dose. The maximum reverse bias that can be applied across the output diode of this device is 18 V. Hence, for doses greater than 5×10^4 rads, with the pre-irradiation gate clock and bias voltages previously specified, the reset drain voltage required to deplete the buried channel is greater than the maximum reverse bias which can be applied to the output diode.

The pre-irradiation threshold voltage of the reset drain transistor was +5 V. For doses greater than 4×10^4 rads, the flat-band voltage shift is of sufficient magnitude to cause the reset transistor to be biased into the conducting state for the entire clock period. This has the effect of severely distorting the output signal. Proper reset drain transistor operation can be restored by applying a negative dc offset to the reset gate clock of sufficient magnitude to turn off the transistor between pulses.

The input gate threshold voltage as a function of dose is shown in Figure 2b. For a pre-irradiation input gate voltage of 0 V, the input would be turned on at 4.5×10^4 rads, filling the shift register wells. Saturation of the imager shift register can be avoided by simply increasing the reverse bias on the input diode while biasing the input gate to a negative voltage. In order to apply an analog signal to the shift register, a more sophisticated input scheme which minimizes the effect of the flat-band voltage shift must be employed since the input gate voltage swing between threshold and full-well is only about 0.5 V (Ref. 7).

At doses greater than 2×10^4 rads, the gain of the on-chip FET amplifier began to degrade. After 4×10^4 rads, the voltage output for a full-well signal was reduced to ~70% of its pre-irradiation value. The decrease in the amplifier gain was probably due to a shift in the operating point of the amplifier to large current values with a corresponding smaller transconductance.

The pre-irradiation full-well signal voltage could be restored by increasing the output drain voltage from +15 to +18 V.

The transfer inefficiency as a function of dose for electrically introduced full-well and half-well signals is shown in Figure 3a. The larger increase in the inefficiency for the full-well signal can probably be attributed to increased interface trapping. The interface state density as measured by a G-V technique was $1.3 \times 10^{10}/(cm^2 eV)$ at 0 rads and increased to a value of $6 \times 10^{10}/(cm^2 eV)$ at 4.5×10^4 rads. At 4×10^4 rads, a measurement of inefficiency vs. signal amplitude showed a sharp increase in loss for signals greater than 50% full-well. The inefficiency for 25% full-well was approximately the same as the 50% full-well value. A larger inefficiency for signals greater than 50% full-well is expected since the buried-channel device is operating in the surface-channel mode with increased interface state trapping (Ref. 8).

The increase in the thermally generated charge (dark current) density as a function of dose is shown for both devices in Figure 3b. The 27-fold increase at 4×10^4 rads would restrict operation to short integration times (i.e., the wells are filled with the dark charge in approximately 17 ms) or require cooled operation.

The full-well capacity of both the photosite and shift register wells remained at the pre-irradiation value of 3×10^5 electrons at 4×10^4 rads.

In principle, the minimum reset drain voltage required to totally deplete the buried channel could be reduced to the pre-irradiation value by applying a negative dc offset voltage to all clock and bias gates to compensate for the change in surface potential produced by the trapping of positive charge in the oxide during irradiation. This was confirmed experimentally for device No. 9 at 2×10^4 and 3×10^4 rads by applying offset voltages of -3.5 V and -5 V, respectively.

Device No. 9 was operated for doses greater than 4.5×10^4 rads, with a reset drain bias of 17.5 V, by applying a negative 5-V offset to all gate clocks and bias except the reset transistor gate whose clock had a negative 3-V offset. The input diode voltage was held at the pre-irradiation value, while the output transistor drain bias was increased to 18 V. Device No. 9 was irradiated with these offset voltages for doses greater than 5×10^4 rads and functioned up to

a dose of 9×10^4 rads. Operation at 10^5 rads was restored with the application of a negative 9-V offset to the gate clock and bias voltages. The transfer inefficiency, full-well capacity, and signal amplitude at 7.5×10^4 rads were approximately the same as those measured at 4×10^4 rads. However, the dark current density increased to 2000 nA/cm^2. At 1.25×10^5 rads, the transfer inefficiency for a half full-well signal had increased to 3×10^{-3}.

Unless a capability exists for changing the voltages on the gate clocks and the bias of a device after it has been irradiated, the unirradiated devices must be capable of being operated with those negative offset voltages which are compatible with operation at large doses. Two unirradiated devices were operated as imagers with a -5 V offset on all gate clocks and bias except the reset transistor clock, which has a -3 V offset.

In summary, these devices were operated with the pre-irradiation clock and bias up to 4.5×10^4 rads. The application of negative dc offset voltages to the gates extended the operational range to 1.25×10^5 rads.

B. 60 X 1 Linear Imager

This device, with a structure as illustrated in Figure 4, is a three-phase buried-channel CCD with planar, doped polysilicon electrodes and high-resistivity polysilicon interelectrode isolation. The substrate is 60-95 ohm-cm p-type silicon with <100> orientation. The channel oxide is thermally grown by a dry oxide technique and is 1800 Å thick. Ion implantation of phosphorus through the oxide is used to form a buried-channel 3000 Å thick with an average doping of 3×10^{16} cm^{-3}. A layer of high-resistivity polysilicon about 5000 Å thick is deposited over the channel oxide. The electrode pattern is formed by selective phosphorus diffusion into the polysilicon sheet. A vapor-deposited oxide is used to protect the device from damage.

During operation, the buried channel was kept completely depleted by a reverse bias of nominally 13 V between the channel drain contact and the substrate. (All voltages are referenced to the grounded substrate.) The phase voltage clock swing was between -2 V and +5 V. The imaging gate was held at +5 V during the integration time and was pulsed to -2 V when charge was to be transferred to the vertical registers. The transfer gate was held at -2 V during integration and was pulsed to +5 V when charge was to be

transferred to the vertical registers. The nominal integration time was 1 ms. The aluminum light shield was connected to the substrate.

The flat-band voltage shift under the imaging gate was -5.5 V at 3×10^4 rads. The failure mechanisms resulting from ΔV_{FB} were: (1) buried channel driven out of depletion, (2) channel induced in the undoped polysilicon interelectrode isolation regions. These two effects will be discussed separately in the following paragraphs.

The minimum reset drain voltage (V_{DR}) required to deplete the buried channel was +10 V for an unirradiated device. At a dose slightly greater than 1×10^4 rads, the nominal +13 V reset drain bias was no longer sufficient to totally deplete the channel. Experimentally, after 3×10^4 rads, a reset drain voltage of +15 V was required to operate the CCD.

The resistivity of the undoped polysilicon isolation between the gate electrodes was reduced by a factor of approximately 20 after a total dose of 3×10^4 rads. This drop in the resistance was due to field-induced channeling in the undoped polysilicon as a result of trapped positive charge in the oxide. The lower isolation resistance allowed the various clock and bias voltages to mix together. The principal result of the mixing was that the transfer and imaging gate waveforms were altered such that almost no barrier existed between the photosensitive elements and the vertical transport registers. A cross-section of the device with calculated pre- and post-irradiation potential profiles is shown in Figures 4c through 4e. The barrier reduction allowed almost all of the photo-generated charge under the imaging gate to continuously spill into the vertical registers instead of being collected for an integration time prior to being transferred. As a result, the effective output signal was reduced to approximately 3% of the pre-irradiation full-well capacity. This observed reduction agrees well with that expected from the profile of Figure 4e. Consequently, these devices became inoperative at a total dose of 3×10^4 rads, and operation could not be recovered by adjusting the bias and clock voltages.

Additional details concerning the effects of radiation on these devices have been published (Ref. 9).

C. 100 X 100 Area Imager

The device consists of 10^4 photosensitive sites arranged in 100 columns, each containing 100 sites (see Figure 5a). Adjacent to each column of photosensitive sites is a vertical transfer register. The horizontal shift register is employed to multiplex the signals from the vertical registers. A differential FET amplifier on the chip provides the video output.

During irradiation, the buried channel was kept depleted by applying a reverse bias of nominally 16 V between the channel drain and substrate. The horizontal clock rate was 2 MHz with a voltage swing between +3 V and -7 V. The vertical clock pulses were 10 μs wide with a period of 63 μs. For one of the vertical phases, the pulse swing was from +1.5 V to -7 V and back; for the other, the pulse swing was from -7 V to +1.5 V and back. During integration, the photosensitive sites were held at +4.5 V to collect photoelectrons and then were briefly pulsed to +1.5 V to transfer the charge into the vertical transfer registers. The integration time was about 8 ms.

The device has the structure shown in Figure 5b. It is a two-phase, buried-channel CCD with ion-implanted barriers. The electrodes are doped polysilicon and the interelectrode isolation is high-resistivity polysilicon. The CCD substrate is 60-90 ohm-cm p-type silicon with <100> orientation. The channel oxide is 1200 Å thick and is grown by a dry oxide technique. Ion implantation of arsenic through the oxide is used to form an n-type buried channel with a thickness of about 3000 Å and an average doping of 1×10^{16} cm^{-3}. The barriers necessary for two-phase operation are formed by implanting boron into the channel. A layer of high-resistivity polysilicon is deposited over the channel oxide. The electrode pattern is formed by selective diffusion into the undoped polysilicon sheet. A thick vapor-deposited oxide covers the device. Aluminum light shields are used to cover all of the active region except for the photosensitive areas.

These CCDs were used as the imaging device in a TV operating at a frame rate of 120 frames/second (4 times the conventional TV rate), with a line time of 65 μs. The geometrically calculated limiting resolution for these devices is approximately 16 lp/mm in the vertical direction and 12 lp/mm in the horizontal direction. The experimental values determined with a

resolution target range from 14 to 16 lp/mm vertically and from 11 to 12 lp/mm horizontally. A typical pre-irradiation image is shown in Figure 5c.

For a total dose of 1×10^4 rads, no change in the imaging quality of the devices was observable. At 3×10^4 rads, the image did deteriorate significantly. A qualitative demonstration of this is shown in Figure 5d. The limiting resolution at this total dose decreased to between 6 and 10 lp/mm vertically and between 5 and 6 lp/mm horizontally. At a total dose of 1×10^5 rads, no image at all was obtained with the original clock and bias voltages. After substantial adjustments of the operating conditions, a rather poor image could be recovered.

Measurements on interelectrode resistances indicate that channeling in the polysilicon isolation regions is very likely responsible for the CCD deterioration at higher doses. The dc interelectrode resistance for both the vertical and horizontal clocks was observed to drop to approximately 20% of its pre-irradiation value at 3×10^4 rads and to less than 10% at 1×10^5 rads. The reduced interelectrode resistance allows a mixing of the clocking waveforms with a resulting disturbance in the potential well and barrier shapes. The effect appears to be the same as that seen on the 60 X 1 imagers described in the preceding section.

Additional details concerning the effects of radiation on these devices have been published (Ref. 4).

IV. CONCLUSION

The operating range of a CCD imager in a radiation environment can be extended by carefully choosing the pre-irradiation bias voltages. For the devices tested, the most important consideration was to bias the reset drain so that the buried channel remained depleted after irradiation.

REFERENCES

1. D.F. Barbe, "The Charge-Coupled Concept," Reports of NRL Progress, March 1972, p. 1.

2. M.F. Tompsett, "Charge Transfer Devices," J. Vac. Sci. Tech., 9, 1166 (1972).

REFERENCES (continued)

3. J.E. Carnes and W.F. Kosonocky, "Charge-Coupled Devices and Applications," Solid State Tech., 17, 67 (1974).

4. J.M. Killiany, W.D. Baker, N.S. Saks, and D.F. Barbe, "Effects of Ionizing Radiation on Charge-Coupled Device Structures," IEEE Trans. Nuc. Sci., NS-21, 193 (1974).

5. D.F. Barbe, "Imaging Devices Using the Charge-Coupled Concept," Proc. IEEE, 63, 38 (1975).

6. C.K. Kim, "Two-Phase Charge Coupled Linear Imaging Devices with Self-Aligned Implanted Barrier," Proceedings of the International Electron Device Meeting, Washington, D.C., Dec. 1974, p. 55.

7. S.P. Emmons and D.D. Buss, "Techniques for Introducing a Low Noise Fat Zero in CCD's," Device Research Conference, Boulder, Colorado, June 1973.

8. C.K. Kim, "Design and Operation of Buried Channel Charge-Coupled Devices," Proceedings of the CCD Applications Conference, San Diego, California, Sept. 1973, p. 7.

9. J.M. Killiany, N.S. Saks, W.D. Baker, and D.F. Barbe, "Effects of Radiation on Buried-Channel CCD's with Doped Polysilicon Gates and Undoped Polysilicon Interelectrode Isolation," Appl. Phys. Lett., 24, 506 (1974).

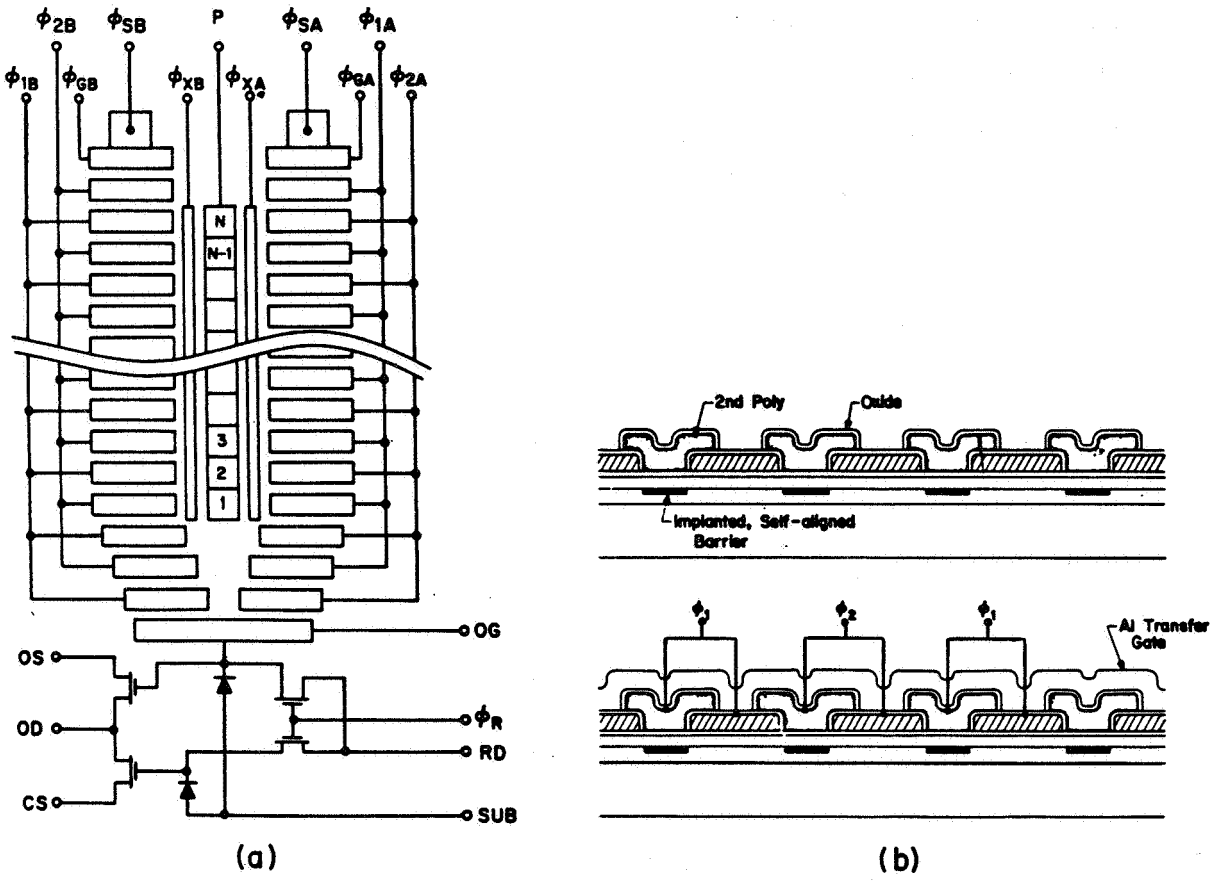

Figure 1. 256 X 1 CCD structure: (a) top view of the device; (b) cross-sectional view along the shift register

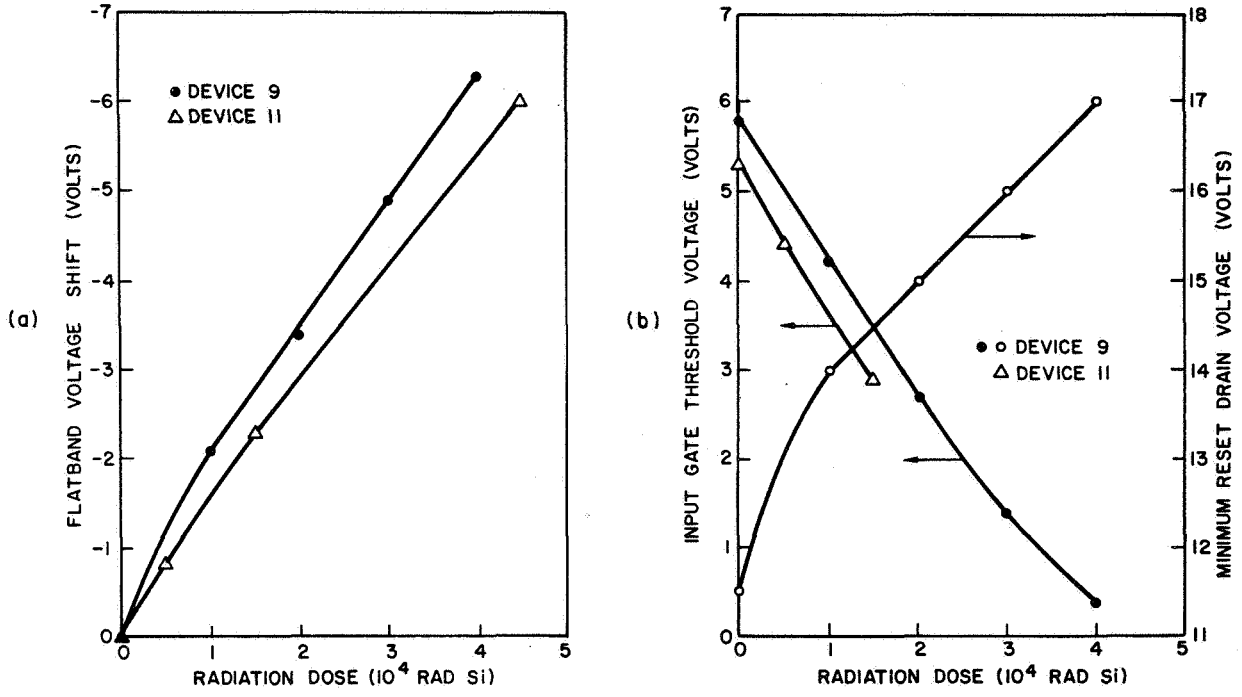

Figure 2. (a) Flat-band voltage shift vs. total dose for 256 X 1; (b) input gate threshold voltage and minimum reset drain voltage vs. total dose for 256 X 1

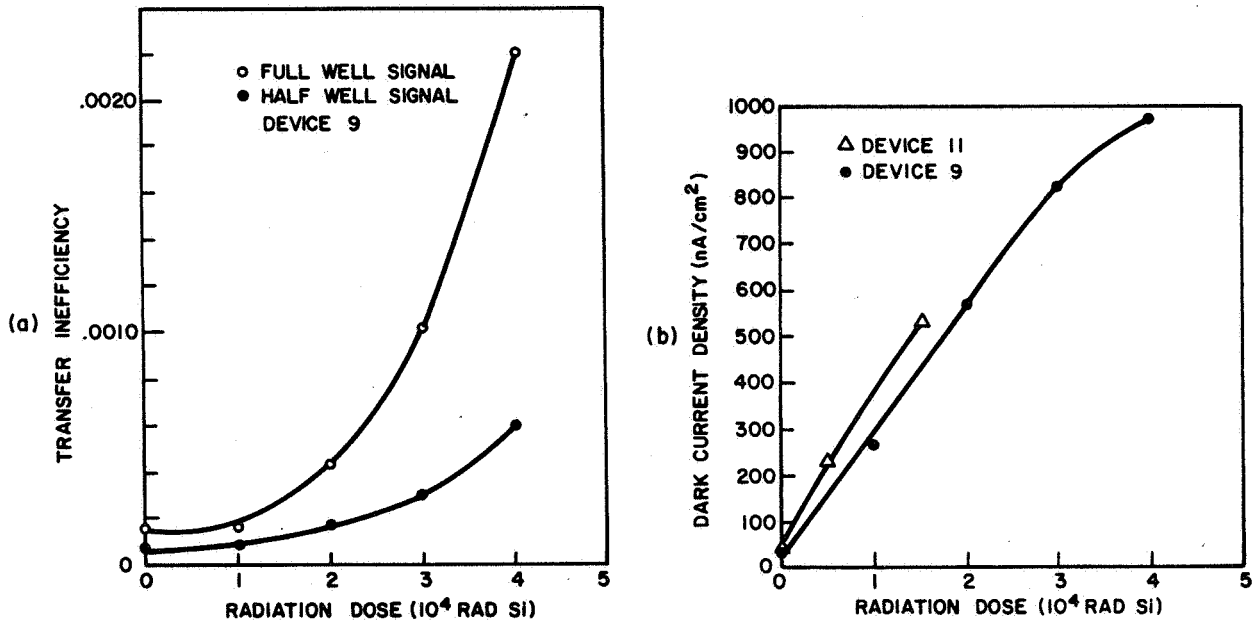

Figure 3. (a) Transfer inefficiency vs. total dose for 256 X 1; (b) dark current density vs. total dose for 256 X 1

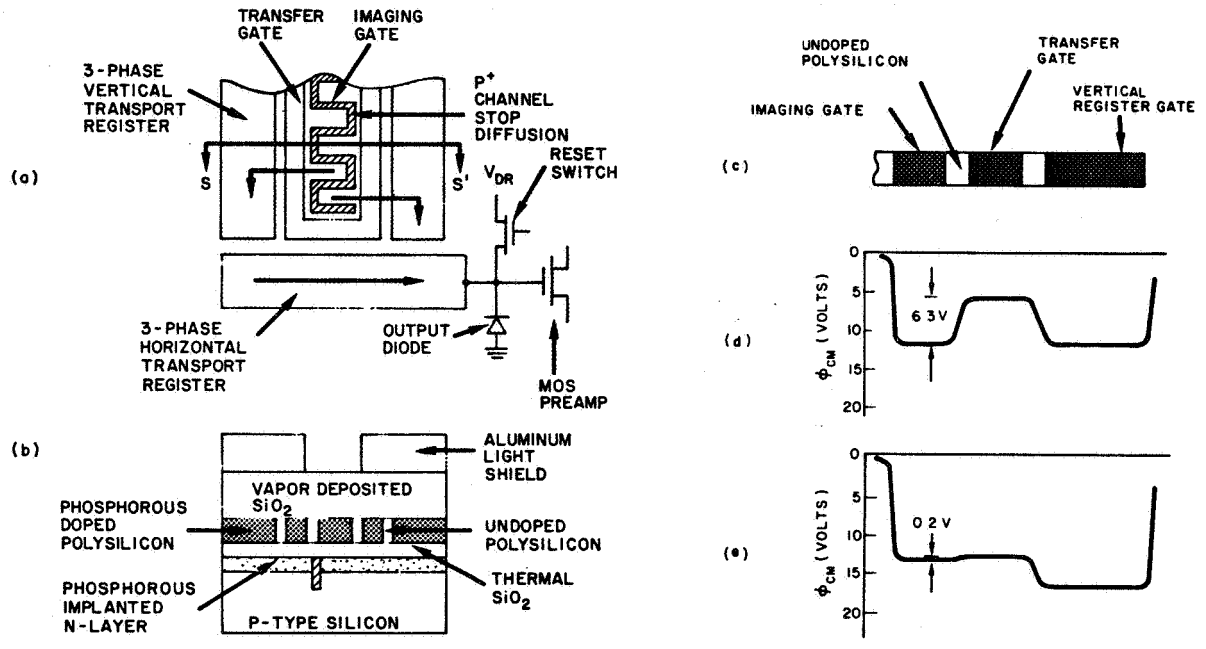

Figure 4. 60 X 1 CCD structure and potential profiles: (a) top view; (b) cross-sectional view; (c) cross-section of the gate structure; (d) pre-irradiation profile of the maximum channel potential; (e) profile of the maximum channel potential after 3×10^4 rads

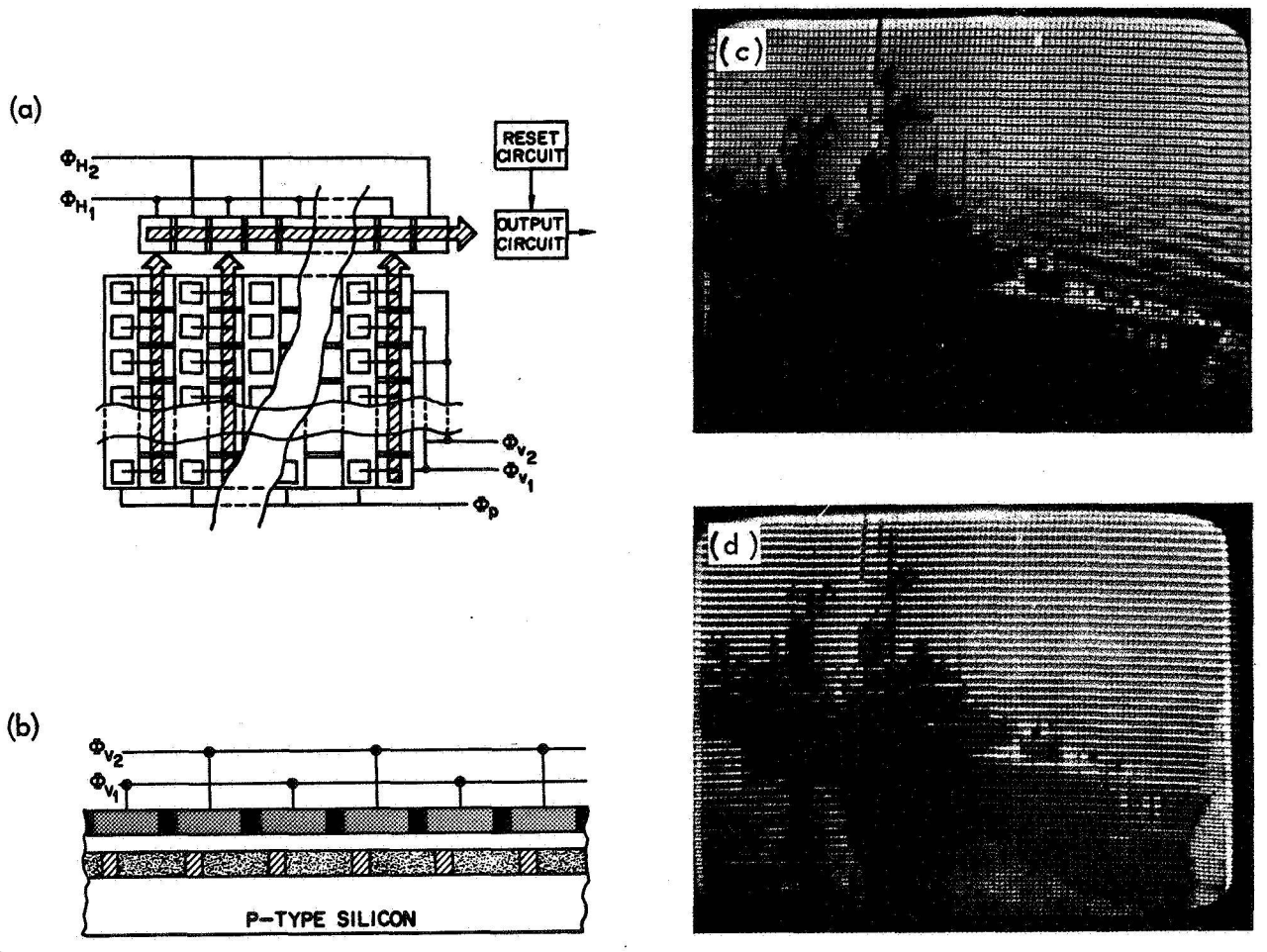

Figure 5. 100 X 100 CCD structure and image quality: (a) top view of the device; (b) cross-sectional view along a vertical transfer register; (c) pre-irradiation image; (d) image after 3×10^4 rads

EFFECTS OF RADIATION ON CHARGE-COUPLED DEVICES*

James E. Carnes, A. Danforth Cope,
Leonard R. Rockett, and Kenneth M. Schlesier
RCA Laboratories
Princeton, New Jersey

The effects of 1-MeV electron irradiation upon the performance of two-phase, polysilicon-aluminum gate CCDs will be reported. Both n- and p-surface channel and n-buried-channel devices were investigated using 64- and 128-stage line arrays. Characteristics measured as a function of radiation dose include: transfer inefficiency, threshold voltage, field effect mobility, interface state density, full-well signal level and dark current. Surface-channel devices were found to degrade considerably at less than 10^5 rads (Si) due to the large increase in the fast interface state density caused by radiation. Buried-channel devices maintained efficient operation to the highest dose levels used [5×10^5 rads (Si)].

I. INTRODUCTION

Since CCDs consist of arrays of MOS capacitors, it is expected that many of the permanent radiation effects seen in MOS devices and circuits will also occur in CCDs; namely, oxide charge (Q_{ox}) buildup and increase in fast interface state density (N_{ss}). However, the effects of these interface changes upon CCD performance are expected to differ considerably from their effect upon MOSFET performance. This is basically because a MOSFET operates in

*This work was supported by the Air Force Cambridge Research Laboratory under Contract F19628-74-C-0039.

thermal equilibrium with an infinite supply of charge from the source, while a CCD operates in nonthermal equilibrium with a fixed amount of charge as a signal. Surface-channel CCDs (SCCCDs) are very sensitive to fast interface state levels but relatively insensitive to threshold voltage changes. Both SCCCDs and buried-channel CCDs (BCCCDs) are sensitive to dark current levels. The situation is just reversed for MOSFETs.

This paper reports the results of a study of the effects of radiation (1-MeV electrons) on CCDs, both surface- and buried-channel, to establish both the nature of the radiation effects and a baseline for the radiation tolerance of present-day (unhardened) CCD technology. The test vehicles used were two-phase linear CCD registers with 64 and 128 stages, with polysilicon-aluminum gate construction (Ref. 1). Figure 1 shows a cross-sectional view of a surface-channel device along with a photomicrograph of a 128-stage register.

II. SURFACE CHANNEL RESULTS

Figure 2 shows a plot of the threshold voltage of the polysilicon and aluminum gates vs. radiation dose for an n-channel SCCCD. The negative shift in threshold voltage indicates a buildup of positive oxide charge of 1.9×10^{11} charges/cm^2 for the polysilicon gates and 2.7×10^{11} charges/cm^2 for the aluminum gates after a dose of 10^5 rads (Si). This oxide charge buildup necessitated changes in dc operating points of the various control gates and phase electrodes to maintain full signal levels and proper fat zero levels. However, since all gates are accessible, it is possible to do this.

More serious, however, is the buildup of fast interface state density. N_{ss} was measured by varying the number of zeros between strings of ones (Ref. 2). N_{ss} is proportional to the slope of ϵ vs. ln (n_{zero}), where n_{zero} is the number of zeros between ones. This type of plot is shown in Figure 3; each curve corresponds to a different dose. Figure 4 is a plot of N_{ss} determined in this manner vs. dose and indicates the sharp increase in N_{ss} from 10^{10} to 10^{11} (cm^2-eV)$^{-1}$ which occurs between 10^4 and 10^5 rads (Si). This increase in N_{ss} results in an increased transfer inefficiency (ϵ), as shown in Figure 5, for all levels of fat zero. Since the lowest inefficiency attainable is limited by edge effect trapping (Ref. 3), it is not surprising that the 30% fat zero curve increases by an order of magnitude when N_{ss} does the same. The seriousness of this effect would be increased when narrower channel devices are used as would be the case

with imagers or memories. This increase in transfer inefficiency due to radiation-induced buildup of N_{ss} severely restricts the usefulness of surface-channel CCDs in a radiation environment. It also suggests that buried-channel devices should be superior in this respect since they are free of interface state trapping effects.

III. BURIED-CHANNEL RESULTS

Similar oxide charge buildup is also observed in BCCDs, as indicated in Figure 6, which is a plot of the channel turn-on voltage vs. dose. While this effect does not affect transfer efficiency, it does affect maximum well size (signal) unless changes are made in the dc operating points of the phase electrodes. This is illustrated in Figure 7, which shows the maximum signal vs. dose for the initial dc conditions and for conditions adjusted for maximum signal. No serious degradation in full-well signal is observed if adjustment is made.

Figure 8 shows transfer inefficiency vs. dose for n-channel BCCDs. No significant increase in ϵ is observed up to 10^5 rads (Si), indicating that no interface trapping is occurring. Some increase is observed at 3×10^5 rads, but the absolute level remains satisfactory for most applications. Finally, Figure 9 shows dark current vs. dose for several different devices as measured by continuous operation and in an integration mode. No serious increases are observed up to 3×10^5 rads (Si). Neutron irradiation and the resulting displacement damage may adversely affect dark current, however.

IV. SUMMARY AND CONCLUSIONS

Typical MOS radiation effects were observed: oxide charge and fast interface state density buildup. The increased interface state density severely degraded transfer efficiency in surface-channel devices but had little or no effect on buried-channel devices. Oxide charge buildup required adjustment of dc operating points to maintain signal level. Since all gates of CCDs are externally accessible, it appears feasible to automatically adjust dc levels using on-chip threshold tracking circuits. If this is done in conjunction with buried-channel devices, it appears that CCDs can be as radiation hard as adjacent MOS circuits and should maintain satisfactory performance at least to the 5×10^5 rad (Si) level. Displacement damage caused by neutron damage could increase dark current levels and should be experimentally investigated.

REFERENCES

1. W. F. Kosonocky and J. E. Carnes, "Two-Phase Charge-Coupled Devices with Overlapping Polysilicon and Aluminum Gates," RCA Review 34, 164, March 1973.

2. J. E. Carnes and W. F. Kosonocky, "Fast Interface States Losses in Charge-Coupled Devices," Appl. Phys. Ltrs. 20, 261, April 1, 1972.

3. M. F. Tompsett, "The Quantitative Effects of Interface States on the Performance of Charge-Coupled Devices," IEEE Trans. on Elec. Dev. ED-20, 45, Jan. 1973.

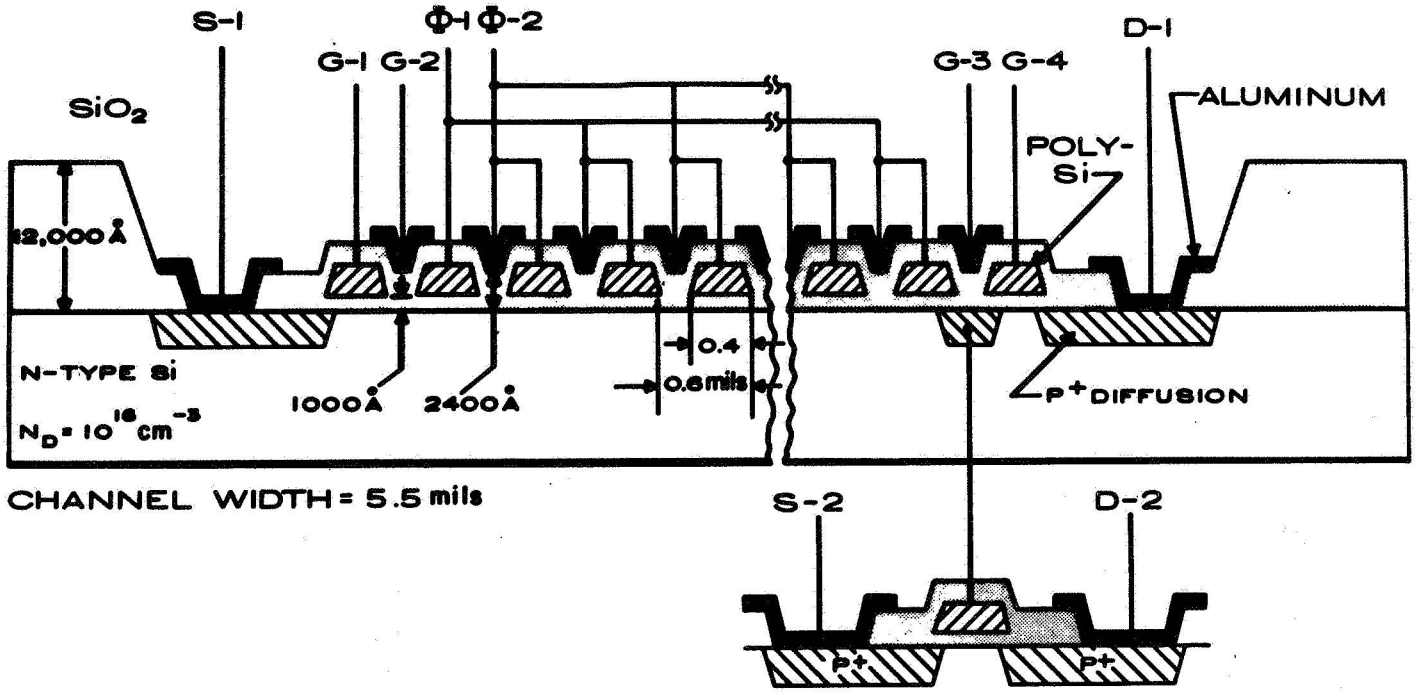

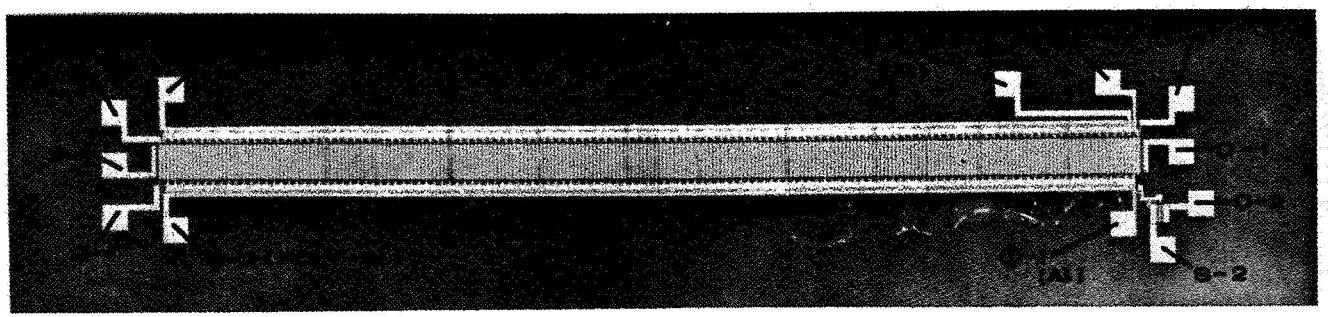

128 STAGE SHIFT REGISTER

Figure 1. Cross section of two-phase surface-channel CCD

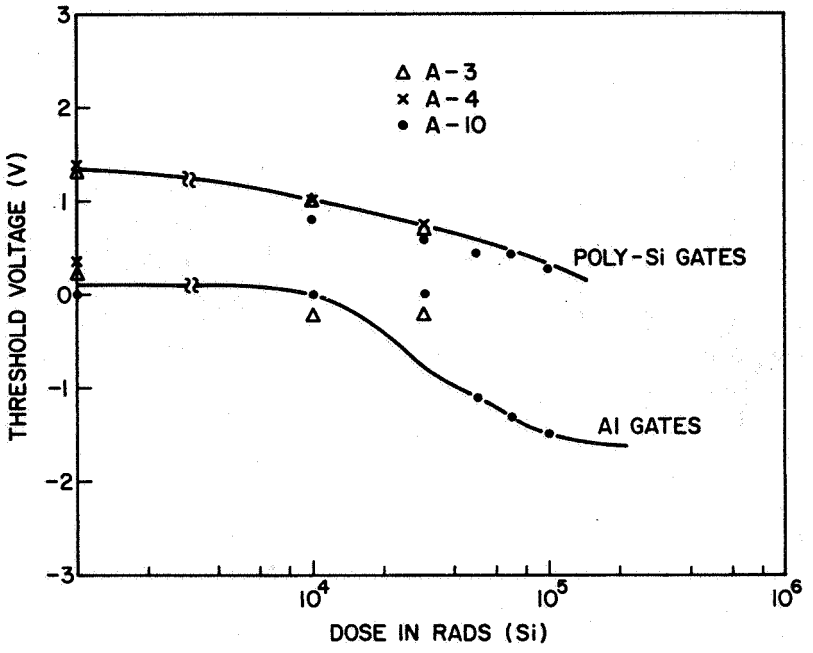

Figure 2. Gate threshold voltage vs. irradiation (n-channel, 128 stages)

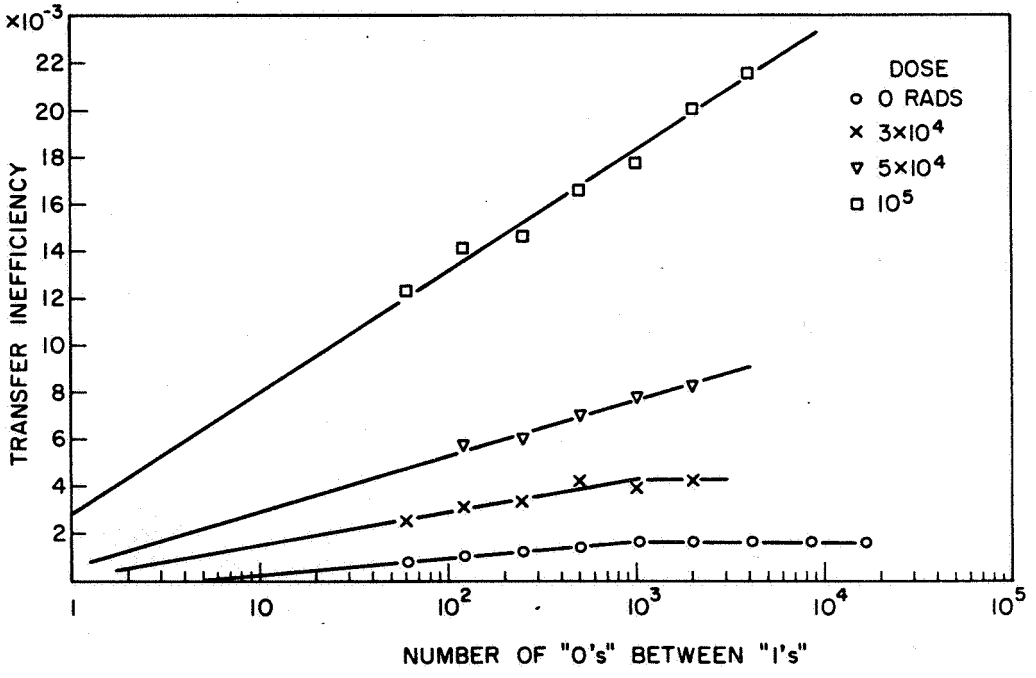

Figure 3. Transfer inefficiency vs. log (n_{zero}) (n-channel, 128 stages, device A10)

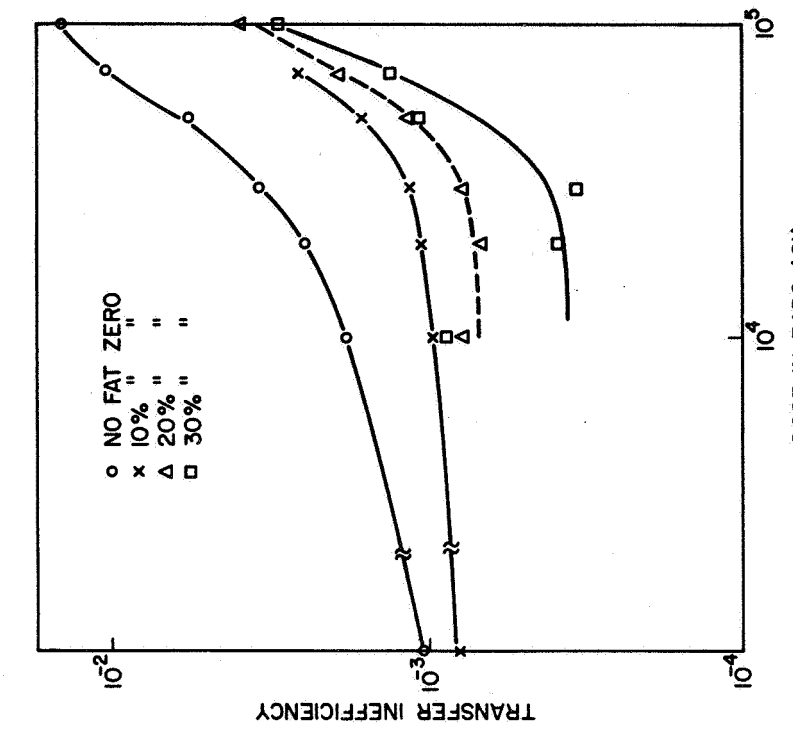

Figure 5. Transfer inefficiency vs. irradiation (n-channel, 128 stages, with fat zero)

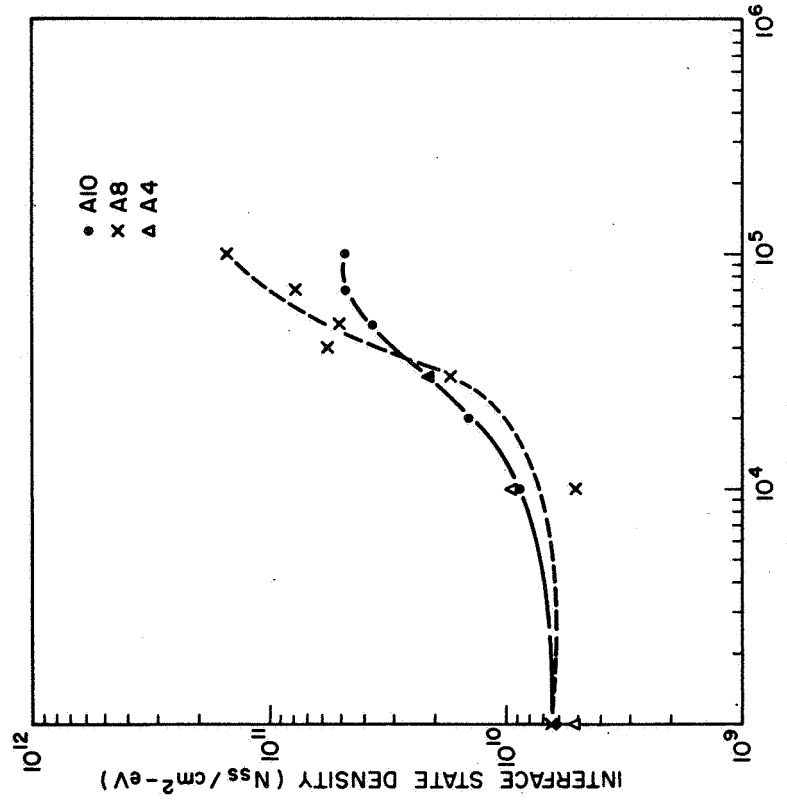

Figure 4. Interface state density vs. irradiation (n-channel, 128 stages)

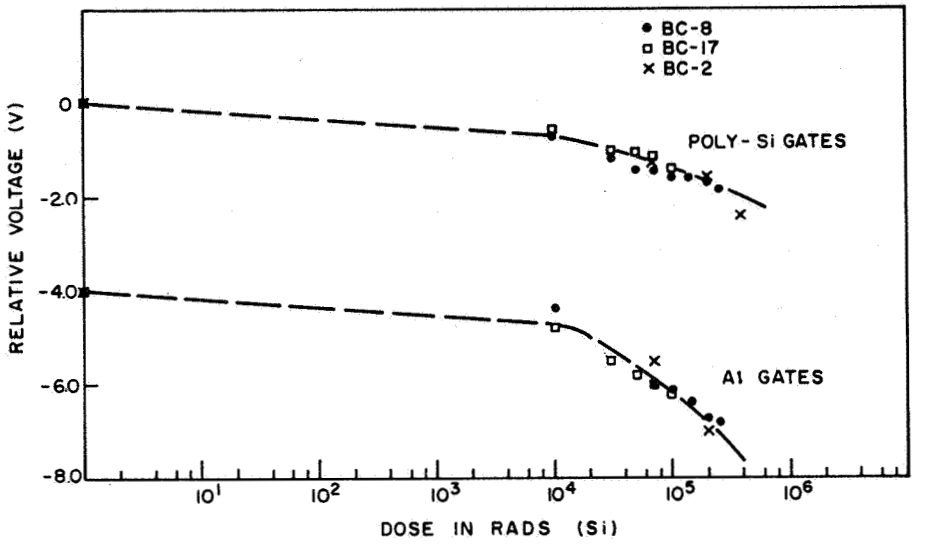

Figure 6. Channel turn-on voltage vs. irradiation (buried channel, 64 stages)

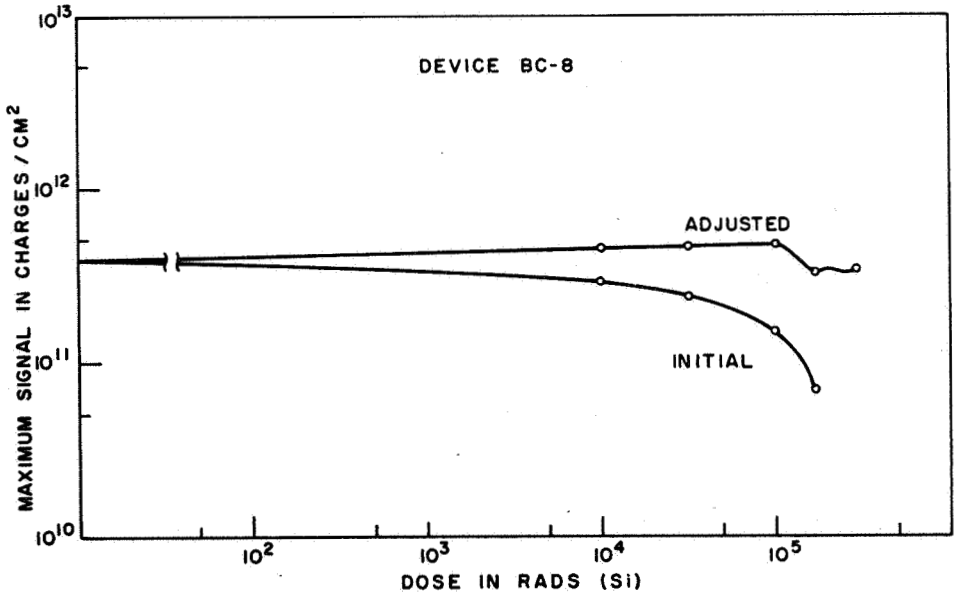

Figure 7. Maximum charge density vs. irradiation (buried-channel device)

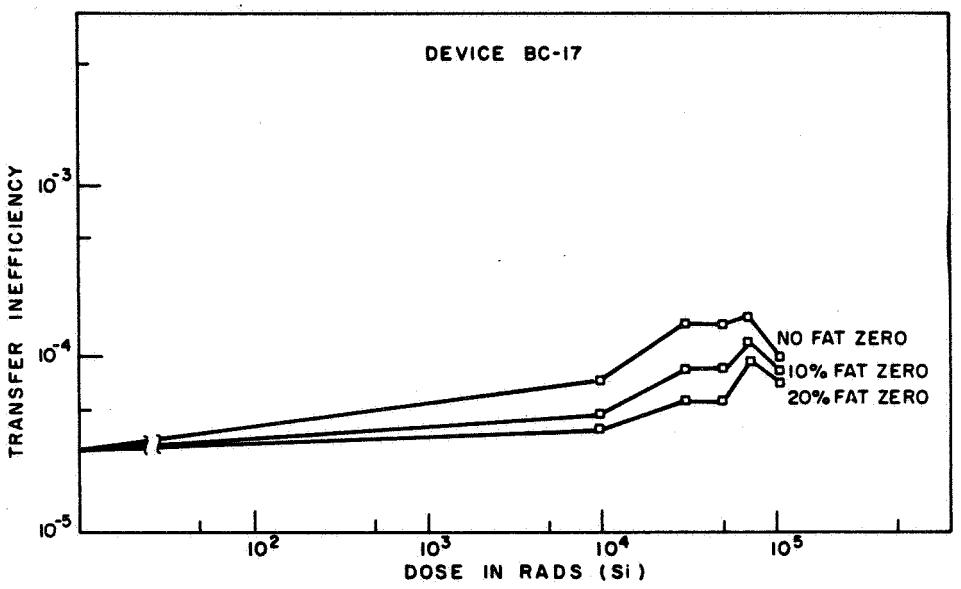

Figure 8. Transfer inefficiency vs. irradiation (buried-channel device)

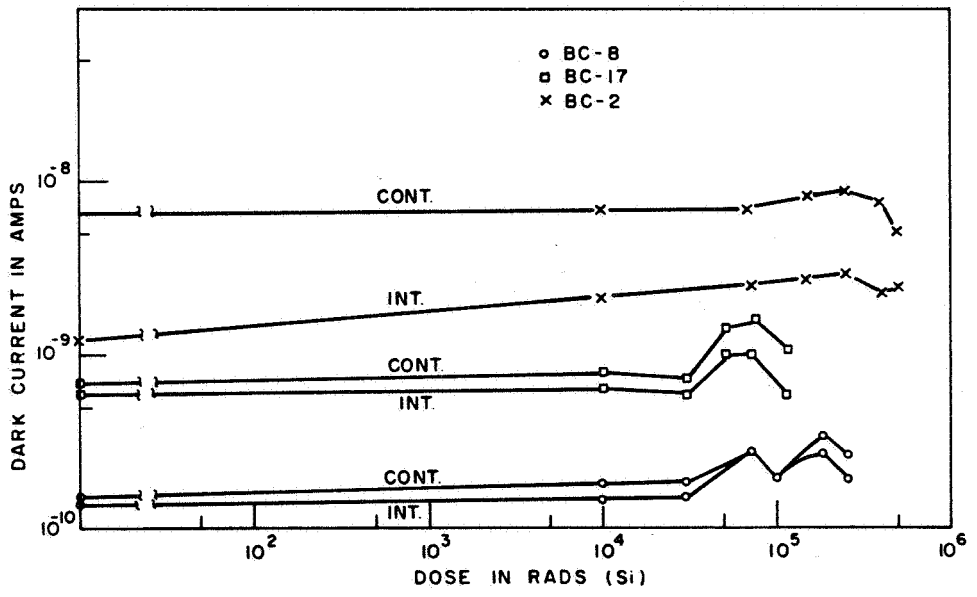

Figure 9. Dark current vs. irradiation (buried channel, 64 stages)

TECHNICAL REPORT STANDARD TITLE PAGE

1. Report No. 43-21	2. Government Accession No.	3. Recipient's Catalog No.
4. Title and Subtitle SYMPOSIUM ON CHARGE-COUPLED DEVICE TECHNOLOGY FOR SCIENTIFIC IMAGING APPLICATIONS		5. Report Date June 10, 1975 6. Performing Organization Code
7. Author(s) M. I. Smokler		8. Performing Organization Report No.
9. Performing Organization Name and Address JET PROPULSION LABORATORY California Institute of Technology 4800 Oak Grove Drive Pasadena, California 91103		10. Work Unit No. 11. Contract or Grant No. NAS 7-100 13. Type of Report and Period Covered Special Publication
12. Sponsoring Agency Name and Address NATIONAL AERONAUTICS AND SPACE ADMINISTRATION Washington, D.C. 20546		14. Sponsoring Agency Code

15. Supplementary Notes

16. Abstract

The Proceedings includes the twenty-one papers presented at the Symposium held at JPL on March 6-7, 1975. Twelve papers are on recent developments in Charge-Coupled Device imaging sensor technology, including descriptions of new area and line arrays and of the results of experiments to determine performance characteristics. Nine papers are on application of CCD imagers to space research and exploration and to astronomy from observatories on earth and in space.

17. Key Words (Selected by Author(s))	18. Distribution Statement
Electronics and Electrical Engineering Spacecraft Instrumentation Astronomy Lunar and Planetary Exploration (Advanced)	Unclassified -- Unlimited

19. Security Classif. (of this report)	20. Security Classif. (of this page)	21. No. of Pages	22. Price
Unclassified	Unclassified	254	

HOW TO FILL OUT THE TECHNICAL REPORT STANDARD TITLE PAGE

Make items 1, 4, 5, 9, 12, and 13 agree with the corresponding information on the report cover. Use all capital letters for title (item 4). Leave items 2, 6, and 14 blank. Complete the remaining items as follows:

3. Recipient's Catalog No. Reserved for use by report recipients.

7. Author(s). Include corresponding information from the report cover. In addition, list the affiliation of an author if it differs from that of the performing organization.

8. Performing Organization Report No. Insert if performing organization wishes to assign this number.

10. Work Unit No. Use the agency-wide code (for example, 923-50-10-06-72), which uniquely identifies the work unit under which the work was authorized. Non-NASA performing organizations will leave this blank.

11. Insert the number of the contract or grant under which the report was prepared.

15. Supplementary Notes. Enter information not included elsewhere but useful, such as: Prepared in cooperation with... Translation of (or by)... Presented at conference of... To be published in...

16. Abstract. Include a brief (not to exceed 200 words) factual summary of the most significant information contained in the report. If possible, the abstract of a classified report should be unclassified. If the report contains a significant bibliography or literature survey, mention it here.

17. Key Words. Insert terms or short phrases selected by the author that identify the principal subjects covered in the report, and that are sufficiently specific and precise to be used for cataloging.

18. Distribution Statement. Enter one of the authorized statements used to denote releasability to the public or a limitation on dissemination for reasons other than security of defense information. Authorized statements are "Unclassified—Unlimited," "U. S. Government and Contractors only," "U. S. Government Agencies only," and "NASA and NASA Contractors only."

19. Security Classification (of report). NOTE: Reports carrying a security classification will require additional markings giving security and downgrading information as specified by the Security Requirements Checklist and the DoD Industrial Security Manual (DoD 5220.22-M).

20. Security Classification (of this page). NOTE: Because this page may be used in preparing announcements, bibliographies, and data banks, it should be unclassified if possible. If a classification is required, indicate separately the classification of the title and the abstract by following these items with either "(U)" for unclassified, or "(C)" or "(S)" as applicable for classified items.

21. No. of Pages. Insert the number of pages.

22. Price. Insert the price set by the Clearinghouse for Federal Scientific and Technical Information or the Government Printing Office, if known.